

---

---

SCALING FOR LOBE AND CLEFT  
PATTERNS IN PARTICLE-LADEN  
GRAVITY CURRENTS

---

---

ANDREW JACKSON, MEng.

*Thesis submitted to the University of Nottingham  
for the degree of Doctor of Philosophy*

JULY 2014



## Abstract

Lobe and cleft patterns are frequently observed at the leading edge of gravity currents, including non-Boussinesq particle-laden currents such as powder snow avalanches. Despite the importance of the instability in driving air entrainment, little is known about its origin or the mechanisms behind its development. In this work we seek to gain a better understanding of these mechanisms from a laboratory scale model of powder snow avalanches using lightweight granular material.

The instability mechanisms in these flows appear to be a combination of those found in both homogeneous Boussinesq gravity currents and unsuspended granular flows, with the size of the granular particles playing a central role in determining the wavelength of the lobe and cleft pattern. When scaled by particle diameter a relationship between Froude number and the wavelength of the lobe and cleft pattern is found, where the wavelength increases monotonically with Froude number. This relationship, in addition to Particle Image Velocimetry analysis, provides evidence for the existence of pairs of counter-rotating vortices at the leading edge of these currents, which play a key role in the development of the lobe and cleft pattern.

The internal pressure of these flows is found to scale with the dynamics of the large vortex-like structure that is observed within the head of the current.





## **Acknowledgments**

A PhD research project is a big undertaking, and although my name is the only one on the front of this thesis, there were many more people involved who I would like to thank.

I have spent the last four years doing something that I love and I am hugely grateful to Dr Barbara Turnbull for giving me this opportunity and for her ongoing advice, support and encouragement. I would also like to thank Dr Rick Munro for all the help he has given me along the way.

I would like to thank the Engineering and Physical Sciences Research Council (EPSRC) for generously funding my Ph.D. research project along with the University of Nottingham.

I would also like to thank my friends and family for all their help and support, especially my wife, Laura, whose love and patience have been an essential constant throughout this project.

Finally, I'd like to dedicate this thesis to my late father, Dr Howard Jackson, who inspired and encouraged me to ask questions and find answers, without which you would not be reading this thesis now.



# Contents

<b>Nomenclature</b>	<b>xv</b>
<b>1 Introduction</b>	<b>1</b>
1.1 Field measurements . . . . .	3
1.2 Physical modelling of avalanches . . . . .	4
1.2.1 Large-scale avalanche models . . . . .	4
1.2.2 Laboratory-scale avalanche models . . . . .	6
1.3 Flow description . . . . .	10
1.4 Frontal instability mechanisms . . . . .	12
1.4.1 Classic lobe-and-cleft instability . . . . .	13
1.4.2 Twin vortices . . . . .	18
1.4.3 Polydispersity . . . . .	21
1.4.4 Rayleigh-Taylor instability . . . . .	22
1.5 Air pressure . . . . .	23
1.6 Summary . . . . .	25
<b>2 Experimental set-up</b>	<b>31</b>
2.1 Air pressure measurements . . . . .	33
2.2 EPS bead properties and processing . . . . .	34

2.2.1	Angle of repose . . . . .	36
2.2.2	Suspension and entrainment . . . . .	38
2.2.3	Chute surface roughness . . . . .	39
2.3	Summary . . . . .	43
<b>3</b>	<b>Imaging and front tracking</b>	<b>45</b>
3.1	Cameras . . . . .	45
3.1.1	Image pixel coordinates . . . . .	46
3.2	Off-the-shelf edge detection functions . . . . .	47
3.3	Front tracking – change-point detection . . . . .	48
3.3.1	Threshold selection method . . . . .	51
3.4	Front tracking – level set method . . . . .	55
3.5	Profile smoothing . . . . .	57
3.6	Coordinates conversion . . . . .	59
3.7	Comparison of front velocity measurements . . . . .	60
3.8	Lobe and cleft detection . . . . .	66
3.8.1	Measurement of lobe and cleft pattern wavelength and amplitude . . . . .	71
3.9	Measurement of flow and nose height . . . . .	72
3.10	Measurement of lobe radius of curvature . . . . .	72
3.11	Summary . . . . .	73
<b>4</b>	<b>Lobe-and-cleft-type patterns in particle-laden gravity currents</b>	<b>75</b>
4.1	Front velocity . . . . .	75
4.2	Flow height measurements . . . . .	80

4.3	Nose height measurements . . . . .	82
4.4	Flow front patterns . . . . .	84
4.5	Scaling of lobe-and-cleft-type patterns . . . . .	102
4.6	Chute surface friction . . . . .	105
4.7	Polydispersity of EPS beads . . . . .	109
4.8	Summary . . . . .	113
<b>5</b>	<b>Air pressure</b>	<b>117</b>
5.1	Air pressure signal noise removal . . . . .	117
5.1.1	Discrete Fourier Transform . . . . .	117
5.1.2	Wavelet analysis . . . . .	123
5.2	Air pressure signals . . . . .	134
5.2.1	Scaling of pressure signals . . . . .	135
5.3	Current front angles . . . . .	141
5.4	Visualisation of pressure signal features . . . . .	146
5.5	Summary . . . . .	148
<b>6</b>	<b>Identification of flow patterns using Particle Image Velocimetry</b>	<b>153</b>
6.1	Particle Image Velocimetry . . . . .	153
6.1.1	Lobe bifurcation . . . . .	160
6.1.2	PIV and pressure signal comparison . . . . .	162
6.2	Summary . . . . .	165
<b>7</b>	<b>Conclusions</b>	<b>167</b>

<b>A The Stationary Wavelet Transform</b>	<b>171</b>
<b>B Published work</b>	<b>173</b>
<b>C Chute design CAD drawings</b>	<b>185</b>

# List of Figures

1.1	A powder snow avalanche, north of Silverton, Colorado, USA. . .	2
1.2	Schematic showing the anatomy of an avalanche. . . . .	2
1.3	Front view of a 550, 000 ping pong ball avalanche at the Miyanomori ski jump from McElwaine and Nishimura [2001]. . . . .	5
1.4	Schematic diagram of a particulate gravity current. . . . .	7
1.5	Flow relative to the head of a typical EPS bead current dur- ing the dense granular flow stage just after release and as a suspended current further down the chute. . . . .	11
1.6	Diagram of the head of a suspended current at a low slope angle and at a high slope angle. . . . .	11
1.7	Examples of lobe-and-cleft type patterns at the leading edge of: a natural powder snow avalanche, a laboratory-scale homo- geneous particle-laden gravity current, and a laboratory-scale unsuspended flow of granular material. . . . .	13
1.8	Initiation of the lobe-and-cleft structure at the head of a gravity current and the evolution of lobes as observed in the experiments of Simpson [1972]. . . . .	14
1.9	Granular flows from the experiments of Nohguchi and Ozawa [2008]. . . . .	19
1.10	Schematic showing plan view of the wave pattern produced at the front of a particle-laden flow. . . . .	19

1.11	Finger-like pattern produced at the leading edge of an unsus- pended granular flow as a result of polydispersity of the granular material, as observed in the experiments of Pouliquen et al. [1997].	22
1.12	A typical air pressure signal obtained from the chute surface of a laboratory scale avalanche. . . . .	24
2.1	Front and side view schematic of the chute used for experiments.	32
2.2	Example of greyscale and binary images used to measure mean equivalent diameter of EPS beads. . . . .	34
2.3	Size distribution of equivalent diameter, $d_e$ , values. . . . .	35
2.4	Angle of repose versus EPS bead diameter. . . . .	37
2.5	Side-on image of an EPS bead gravity current . . . . .	38
2.6	Schematic diagram of process used to measure effective coeffi- cient of friction, $\mu_e$ . . . . .	39
2.7	Effective friction coefficient versus EPS bead diameter for the different chute surface coverings used. . . . .	40
2.8	Effective friction coefficient, $\mu_e$ , versus EPS bead diameter ratio, $\gamma$ . . . . .	42
2.9	Schematic showing sample EPS beads with different values of EPS bead diameter ratio, $\gamma$ , at rest on an EPS bead covered surface. . . . .	42
3.1	Edge detection using MATLAB's Sobel method edge detection algorithm. . . . .	46
3.2	Edge detection using a Moore-Neighbor tracing algorithm. . . .	47
3.3	Comparison of front edges detected for currents consisting of different release volumes of EPS bead. . . . .	49
3.4	Comparison of fronts detected at different stages of a current's motion. . . . .	50



3.5	Typical image taken from an experiment and its corresponding intensity level histogram. . . . .	51
3.6	Within class variance, $\sigma_W^2$ , versus threshold value , $\Theta$ , for the histogram shown in Figure 3.5. . . . .	53
3.7	Comparison of fronts detected for currents consisting of different release volumes of EPS bead, thresholded using clustering and $I_{max}$ -based methods. . . . .	54
3.8	Comparison of fronts detected at different stages of a current's motion, thresholded using clustering and $I_{max}$ -based methods. .	54
3.9	Comparisons of change-point and level set methods detecting deep clefts. . . . .	55
3.10	Front and side contours produced using level set method. . . . .	56
3.11	(a) Individual, unsuspended EPS beads moving ahead of a flow front (b) An image with salt and pepper noise. . . . .	57
3.12	Front detection: without filter, with median filter and with Gaussian filter. . . . .	58
3.13	Typical air pressure signals obtained from experiments. . . . .	61
3.14	Correlation plots of (a) $U_{f(P)}$ versus $U_{f(D)}$ , (b) $U_{f(I)}$ versus $U_{f(D)}$ and (c) $U_{f(P)}$ versus $U_{f(I)}$ . . . . .	63
3.15	Individual residual plots for (a) $U_{f(P)}$ and $U_{f(D)}$ comparison, (b) $U_{f(I)}$ and $U_{f(D)}$ comparison and (c) $U_{f(P)}$ and $U_{f(i)}$ comparison. .	64
3.16	Vector field showing the gradient of the level set taken from an experiment. . . . .	67
3.17	Divergence of the vector field shown in Figure 3.16. . . . .	68
3.18	Front profile contours with all lobe and cleft locations identified from the corresponding matrix of divergence values marked. . .	69
3.19	Front profile contours with consolidated lobe and cleft locations marked. . . . .	70

3.20	A single front edge profile with detected lobe and cleft positions marked. . . . .	71
3.21	Side profile contour with current height, $h_c$ , and current nose height, $h_n$ , measurements. . . . .	72
4.1	Schematic diagrams of a particulate gravity current. . . . .	76
4.2	Front velocity versus time plots taken from two experiments conducted using different release volumes. . . . .	76
4.3	Non-dimensionalised front velocity ( $\tilde{U}_{f_{V_i}}$ ) versus time ( $\tilde{t}_{V_i}$ ) plots. . . . .	77
4.4	Ensemble averaged non-dimensional front velocity ( $\tilde{U}_{f_{V_i}}$ ) versus time ( $\tilde{t}_{V_i}$ ) plots. . . . .	78
4.5	Mean non-dimensionalised front velocity taken at $\tilde{t}_{V_i} = 10$ versus slope angle ( $\theta$ ) for experiments conducted using different values of EPS bead diameter. . . . .	79
4.6	Current head height ( $h_c$ ) versus slope angle ( $\theta$ ) for currents consisting of different sized EPS beads. . . . .	81
4.7	Side-on image of an EPS bead gravity current with superimposed general profile shape of a gravity current taken from Lawson [1971]. . . . .	82
4.8	Dimensionless nose height, $\frac{h_n}{h_c}$ , versus Reynolds number. . . . .	83
4.9	Video stills taken at 0.2 s intervals from experiments conducted using different sized EPS beads. . . . .	85
4.10	Video stills taken at $\tilde{t}_{d_p} = 50$ from experiments conducted using different sized EPS beads. . . . .	85
4.11	Non-dimensional lobe and cleft pattern amplitude ( $\tilde{a}_{d_p}$ ) versus non-dimensional time ( $\tilde{t}$ ). . . . .	86
4.12	Non-dimensional lobe and cleft pattern amplitude ( $\tilde{a}_\lambda$ ) versus non-dimensional time ( $\tilde{t}$ ). . . . .	87
4.13	Front profiles at 0.05 s intervals. . . . .	89

4.14	Vector fields showing the gradient of the level set $T_{ij}$ . . . . .	89
4.15	Curvature ( $\kappa$ ) of the level set $T_{ij}$ . . . . .	90
4.16	Average wavelength ( $\lambda$ ) versus distance from line release ( $\frac{y}{S}$ ) for experiments using different release volumes of EPS beads. . . . .	90
4.17	Average wavelength ( $\lambda$ ) versus distance from line release ( $\frac{y}{S}$ ) for experiments using different sized EPS beads. . . . .	91
4.18	Average wavelength ( $\lambda$ ) 1 m from the line release versus slope angle ( $\theta$ ). . . . .	92
4.19	Comparison of wavenumber, $1/\lambda$ , versus Grashof number, $Gr_{hc}$ , for Boussinesq and non-Boussinesq gravity currents. . . . .	94
4.20	Comparison of Froude number, $Fr_{hc}$ , versus Grashof number, $Gr_{hc}$ , for Boussinesq and non-Boussinesq gravity currents. . . . .	95
4.21	Radius of curvature, $r$ , of lobes versus EPS bead diameter, $d_p$ , at different values of $\tilde{t}_{d_p}$ . . . . .	97
4.22	Mean non-dimensional radius of curvature, $\tilde{r}_{d_p}$ versus non-dimensional time, $\tilde{t}_{d_p}$ . . . . .	98
4.23	Variation in radius of curvature of a lobe $r$ as wavelength $\lambda$ increases. . . . .	99
4.24	Variation in radius of curvature of a lobe $r$ of wavelength $\lambda$ as amplitude $a$ increases for $\tilde{t}_{d_p} < \approx 50$ . . . . .	100
4.25	Pattern of extended lobes and clefts observed at $\tilde{t}_{d_p} > \approx 50$ . . . . .	100
4.26	Radius of curvature, $r$ , of lobes versus EPS bead diameter, $d_p$ , at maximum available values of $\tilde{t}_{d_p}$ . . . . .	101
4.27	Non-dimensional wavelength ( $\tilde{\lambda}_{d_p}$ ) versus Froude number ( $Fr_{d_p}$ ). . . . .	104
4.28	Dimensionless nose height, $\frac{h_n}{h_c}$ versus effective friction coefficient, $\mu_e$ for experiments conducted using different chute surfaces. . . . .	106
4.29	Wavelength, $\frac{\lambda}{W}$ , versus distance from line release, $\frac{y}{S}$ for experiments conducted on different chute surfaces. . . . .	107

4.30	Wavelength, $\lambda$ , versus EPS bead diameter, $d_p$ for experiments conducted using different chute surfaces. . . . .	108
4.31	Comparison of wavelength versus distance results from experiments conducted using quasi-monodisperse and polydisperse EPS beads. . . . .	110
4.32	Comparison of non-dimensionalised amplitude versus time results from experiments conducted using quasi-monodisperse and polydisperse EPS beads. . . . .	111
4.33	Motions of particles within (a) unsuspended and (b) suspended flows. . . . .	112
5.1	Example of an unprocessed pressure signal obtained from one of the pressure sensors mounted on the chute. . . . .	118
5.2	Single-sided power spectrum of $p(t)$ . . . . .	120
5.3	Pressure versus time plots using data obtained from inverse DFT. . . . .	122
5.4	Daubechies Db5 wavelet function. . . . .	124
5.5	Approximation ( $A$ ) and wavelet ( $w$ ) coefficients resulting from a multiscale SWT decomposition of a pressure signal. . . . .	126
5.6	Comparison of wavelet db5 and centre frequency based approximation. . . . .	127
5.7	Histogram of wavelet scale $w_{1,k}$ coefficient values corresponding to electronic noise with a normal (Gaussian) density function fitted to the data. . . . .	129
5.8	Original and de-noised wavelet coefficients at all scales. . . . .	130
5.9	Original signal, de-noised signal, and residuals of the de-noised signal. . . . .	131
5.10	De-noised and interval-filtered wavelet coefficients at all scales. . . . .	132
5.11	De-noised signal, interval-filtered signal and residuals of the interval-filtered signal. . . . .	133

5.12	Air pressure measurements from five 3300 cm <sup>3</sup> of 2.7 mm diameter EPS bead currents at a slope angle of 80° . . . . .	135
5.13	Ensemble mean air pressure signals collected from experiments.	136
5.14	Non-dimensional air pressure signals collected from experiments.	138
5.15	Ensemble mean non-dimensional air pressure signals collected from experiments. . . . .	139
5.16	Non-dimensional air pressure signals. . . . .	140
5.17	Current front edge profile with discretization applied. . . . .	141
5.18	Current front angle, $\phi$ , versus distance distance from foremost point of the current, $s$ , for a front edge profile. . . . .	142
5.19	Current front angle, $\phi$ , versus slope angle, $\theta$ . . . . .	144
5.20	Kernel density estimate plots of the front angle data for each slope angle. . . . .	145
5.21	Wavelet-based visualisation of flow features. . . . .	147
5.22	Ensemble wavelet-based visualisation of flow features. . . . .	148
6.1	Velocity and vorticity fields obtained from PIV analysis of images obtained from the early stages of an experiment conducted using 2.1 mm diameter EPS beads. . . . .	156
6.2	Velocity and vorticity fields obtained from PIV analysis of images obtained from the later stages of an experiment conducted using 2.1 mm diameter EPS beads. . . . .	157
6.3	Velocity and vorticity fields obtained from PIV analysis of images obtained from the early stages of an experiment conducted using 5.0 mm diameter EPS beads. . . . .	158
6.4	Velocity and vorticity fields obtained from PIV analysis of images obtained from the later stages of an experiment conducted using 5.0 mm diameter EPS beads. . . . .	159

6.5	Vorticity Fields from PIV analysis of image sequence showing a bifurcating lobe. A small region of opposing vorticity that develops into a new lobe is circled at $t = 1.025$ s . . . . .	161
6.6	Comparison of air pressure signal and PIV analysis data between $t = 0.03$ – $0.0325$ s for an experiment conducted using 5 mm diameter EPS beads. . . . .	163
6.7	Comparison of non-dimensional air pressure signals corresponding to lobe and cleft locations. . . . .	164

# Nomenclature

$A_{j,k}$	Approximation coefficient
$A_{j,k}^{\circ}$	Periodized approximation coefficient
$A_r$	Area of image region representing an EPS bead
$a$	Average amplitude of lobe and cleft pattern
$\tilde{a}_{d_p}$	Non-dimensional amplitude of lobe and cleft patterns – EPS bead diameter scaled
$a_i$	Amplitude of a single lobe/cleft
$a_{l_i}$	Amplitude of a cleft to the left of a given lobe
$a_{r_i}$	Amplitude of a cleft to the right of a given lobe
$\tilde{a}_{\lambda}$	Non-dimensional amplitude of lobe and cleft patterns – Wavelength scaled
$\alpha_{1,n}$	Data set for root-mean-squared relative error calculation
$b$	Release hopper width
$C_c$	Current pixel class
$C_d$	Coefficient of drag
$C_s$	Chute surface pixel class
$D_p(k)$	Wavelet de-noised pressure signal
$d_e$	Equivalent diameter of EPS bead
$d_p$	EPS bead diameter
$d_{p_{\text{surface}}}$	Diameter of EPS bead attached to chute surface
$d_{p_{\text{sample}}}$	Diameter of EPS bead sample used for measurement of effective friction coefficient, $\mu_e$
$\Delta$	Wavelet sampling period
$\Delta t$	Time elapsed between pressure signal peaks
$\delta_v$	Velocity boundary layer thickness
$\epsilon$	Root-mean-squared relative error
$\eta$	Distance between pressure sensor and the moving front of the current

$F_c$	Centre frequency
$F_j$	Pseudo-frequency
$F_p(k)$	Wavelet interval-filtered pressure signal
$Fr$	Froude number
$Fr_{dp}$	Froude number – EPS bead diameter scaled
$Fr_{hc}$	Froude number – Current height scaled
$Gr$	Grashof number
$Gr_{hc}$	Grashof number – Current height scaled
$g$	Gravitational acceleration
$g'$	Reduced gravity
$g_l$	DWT low pass (scaling) filter
$\tilde{g}_{j,l}$	SWT low pass (scaling) filter
$\gamma$	Ratio of $d_{psample}$ to $d_{psurface}$
$h(x_i, y_j)$	Gaussian filter
$h_c$	Current height (perpendicular to slope)
$h_g(x_i, y_j)$	Gaussian convolution function
$h_l$	DWT high pass (wavelet) filter
$\tilde{h}_{j,l}$	SWT high pass (wavelet) filter
$\tilde{h}_{j,l}^\circ$	Periodized SWT high pass (wavelet) filter
$h_n$	Nose height
$I$	Light intensity
$\bar{I}_c$	Current class mean light intensity level
$I_{max}$	Maximum light intensity
$\bar{I}_s$	Surface class mean light intensity level
$I_\tau$	Total number of light intensity levels
$\bar{I}_\tau$	Total mean light intensity level
$\hat{\mathbf{i}}$	$x$ -direction (lateral) unit vector
$\hat{\mathbf{j}}$	$y$ -direction (longitudinal) unit vector
$\kappa$	Curvature of level set
$L$	Characteristic length scale
$l_f$	Distance from where current height is maximum to the nose of the current
$l_r$	Distance from where current height is maximum to the rear of the current
$\Lambda$	Quadrature mirror filter width
$\lambda$	Average wavelength of frontal pattern



$\lambda_{c_j}$	Lateral distance between a pair of clefts on a given front edge profile contour
$\lambda_{l_i}$	Lateral distance between a pair of lobes on a given front edge profile contour
$\lambda_{\max}$	Maximum wavelength
$\lambda_{\min}$	Minimum wavelength
$\lambda_p$	Preferred wavelength of classic lobe and cleft instability
$\tilde{\lambda}_{d_p}$	Non-dimensional wavelength
$m$	Mass of individual EPS bead
$\mu$	Dynamic viscosity of ambient fluid
$\mu_e$	Effective coefficient of friction
$M$	Number of pixel rows in images
$N$	Number of pixel columns in images
$n_c$	Total number of detected clefts on a given front edge profile contour
$n_l$	Total number of detected lobes on a given front edge profile contour
$N_\tau$	Total number of pixels in an image
$N_p$	Length of pressure signal
$n_I$	Number of pixels at intensity level $I$
$n_\tau$	Number of data points in a series
$\nu$	Kinematic viscosity
$\omega_c$	Current class occurrence probability
$\omega_s$	Surface class occurrence probability
$P(j)$	DFT of a pressure signal
$\mathcal{P}_I$	Probability distribution of pixel intensity
$p$	Pressure
$\tilde{p}$	Non-dimensional pressure
$p(k)$	Discretised pressure signal
$p(t)$	Time-variant pressure signal
$\Phi$	DFT filter threshold value
$\phi$	Acute angle that the moving front of a current makes with the chute surface
$\psi$	Mother wavelet function
$R$	Reaction force of an individual EPS bead
Re	Reynolds number

$Re_p$	Particle Reynolds number
$Ri$	Richardson number
$\bar{\mathcal{R}}$	Mean residual
$\mathcal{R}_n$	Residual
$r$	Radius of curvature of a lobe
$\tilde{r}_{d_p}$	Non-dimensional Radius of curvature of a lobe – EPS bead diameter scaled
$\rho$	Current density
$\rho_a$	Density of air
$\rho_p$	EPS bead bulk density
$S$	Total length of chute
$St$	Stokes number
$s$	Distance into the current from the nose
$\sigma_c^2$	Current class variance
$\sigma_g$	Standard deviation of gaussian distribution
$\sigma_s^2$	Surface class variance
$\sigma_W^2$	Within class variance
$T_{ij}$	Matrix of front edge first arrival times
$t$	Time after release
$\tilde{t}_{d_p}$	Non-dimensional time – EPS bead diameter scaled
$\tilde{t}_p$	Non-dimensional time – Current height scaled
$\tilde{t}_{V_i}$	Non-dimensional time – Initial release volume scaled
$\Theta$	Threshold value for flow front detection
$\theta$	Slope Angle
$\theta_c$	Critical angle (friction test)
$\theta_r$	Angle of repose
$U_f$	Front velocity
$U_{f(D)}$	Front velocity – Dynamic pressure method
$\tilde{U}_{fV_i}$	Non-dimensional front velocity – Initial release volume scaled
$U_{f(I)}$	Front velocity – image data method
$U_{f(P)}$	Front velocity – Pressure signal peaks method
$u$	Velocity
$u_b$	Buoyancy velocity
$V$	Ratio of $V_i/V_c$
$V_c$	Current volume
$V_i$	Initial release volume/Release hopper volume
$v_t$	Settling velocity of EPS beads

$W$	Total width of the chute
$w_{j,k}$	Wavelet coefficient
$w_{j,k}^{\circ}$	Periodized wavelet coefficient
$x$	Lateral chute coordinates
$y$	Longitudinal chute coordinates
$y_p$	Longitudinal pressure sensor position
$z$	Coordinates perpendicular to the $x$ - $y$ plane of the chute
$x_i$	Lateral pixel coordinates
$x_l$	Lateral position of a lobe centre
$x_r$	Lateral width of region used for measurement of lobe radius of curvature
$y_j$	Longitudinal pixel coordinates



# Chapter 1

## Introduction

Avalanches can be highly destructive and dangerous events, especially if they occur near built up areas. Large flows of dense granular material will cause large amounts of damage to structures, but the cloud of powder snow that forms can also do significant damage. The powder cloud, referred to as a powder snow avalanche, can cause large changes in pressure over very short time periods which will subject a structure to high stresses. Powder snow avalanches are a naturally occurring example of a particle-driven gravity current (Figure 1.1). Other examples of naturally occurring particle-driven gravity currents include pyroclastic ash flows down volcano slopes and turbidity currents of silt in oceanic trenches, which are capable of being equally destructive within their respective environments. Whilst the primary focus of this work is powder snow avalanches, the physical similarity shared by all of these flows implies that any development of concepts relating to the flow properties of powder snow avalanches will also be applicable to the other forms of particle-driven gravity current. These currents take the form of a cloud of particles kept in suspension by turbulence in the carrier fluid, entrained from the surrounding ambient fluid. The suspension of particles increases the density of the cloud compared to the surrounding ambient fluid, creating a driving buoyancy force. As the current entrains more of the surrounding ambient fluid the density difference decreases, leading to a reduction in the driving force unless the current is supplied with more particles [Simpson, 1997]. In the case of a powder snow avalanche, dilution caused by entrainment of air is counteracted by entrainment of snow particles from the snow cover, maintaining the driving density difference (Figure 1.2).



Figure 1.1: A powder snow avalanche, north of Silverton, Colorado, USA.  
Photo: R.L. Armstrong, NSIDC.

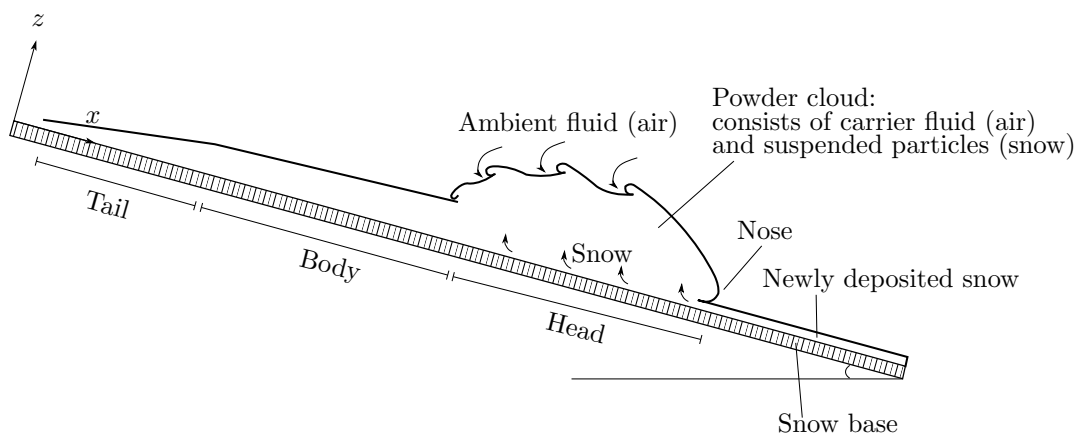


Figure 1.2: Schematic showing the anatomy of an avalanche.

## 1.1. FIELD MEASUREMENTS

---

Powder snow avalanches usually start as a dense granular flow of snow down a slope. Ambient air entrains snow at the upper surface and front of the flow and a powder cloud is formed. If enough snow becomes suspended and the level of turbulence is high enough to maintain the suspension, the powder cloud will flow down the slope as a gravity current. The powder cloud often travels above the dense granular flow, however the two components have distinct dynamics and are linked only by an exchange of snow between them. Also, powder clouds often run metres in front of the dense granular flow and sometimes continue for significant distances after the dense granular avalanche has stopped. They have even been observed to follow different routes to the granular flow [Margreth, 2000].

The entrainment of ambient air into the powder cloud is likely to have significant effects on the development and dynamics of a powder snow avalanche. Whilst some of the mechanisms that cause ambient air to become entrained, such as through Kelvin-Helmholtz billows that form at the upper surface of the current [Simpson, 1972, 1997], are reasonably well understood, others are less clear. One such mechanism is the instability which causes the formation of a three-dimensional wavy pattern at the moving front of the powder snow avalanche. Whilst it is highly likely that the formation and development of this pattern will have a significant effect on the entrainment of ambient air into the current, little is known about the instability that causes it. The primary focus of this work is to gain a better understanding of the mechanisms behind, and the development of the patterns that form at the leading edge of particle-laden gravity currents. We seek to achieve this through the physical modelling of powder snow avalanches.

## 1.1 Field measurements

The unpredictability of when and where an avalanche will occur make collecting dynamic data from naturally occurring avalanches practically impossible. However facilities do exist in mountainous regions of countries such as Switzerland and Russia where avalanches can be artificially triggered and field data collected [Turnbull and McElwaine, 2007, Bozhinskiy and Sukhanov, 1998]. These measurements are useful both for providing more information about avalanche dynamics and for validating and calibrating physical and theoretic-

cal models [Vallet et al., 2004, Bozhinskiy and Sukhanov, 1998, Turnbull and McElwaine, 2007, Turnbull et al., 2007]. However, there are some serious drawbacks to using field experiments to collect data. They are costly and logistically difficult to run owing to both the damage caused by the avalanches being measured, and to the harsh weather conditions in the places where the avalanches occur. Reproducibility of the experiments and interpretation of the data is also difficult due to the lack of control over the initial and boundary conditions. It is therefore desirable to physically model avalanches in conditions that are more hospitable and easily repeatable.

## 1.2 Physical modelling of avalanches

### 1.2.1 Large-scale avalanche models

Avalanches have been physically modelled on a large scale by releasing large numbers ( $\approx 10^5$ ) of ping pong balls on a ski jump landing slope (Figure 1.3, McElwaine and Nishimura [2001]). This model provides greater repeatability and control over parameters/variables such as vertical distance ( $\approx 50$  m), slope angle ( $\approx 35^\circ$ ) and volume of initial release. Ping pong balls have also been shown to model the interaction between snow particles and ambient air relatively well, reaching terminal velocity in only a few metres, and thus allowing fully developed flows to occur even on short slopes. However, these experiments only produce a saltation layer (individual particles are removed from a surface and travel a short distance in a parallel plane before returning to the surface) on top of a dense granular flow and do not fully model the transition to a fully suspended flow. This transition is likely to have significant effects on the dynamics of a powder snow avalanche and ideally should be accounted for by any physical model. Whilst cheaper and more accessible than field experiments, these large scale experiments potentially still cause problems in terms of access to appropriate facilities and logistical problems caused by the large number of ping pong balls involved. Furthermore, although the repeatability and control over conditions is more straightforward than in field experiments, some variables, such as slope angle, are fixed and cannot be easily adjusted.



## 1.2. PHYSICAL MODELLING OF AVALANCHES

---

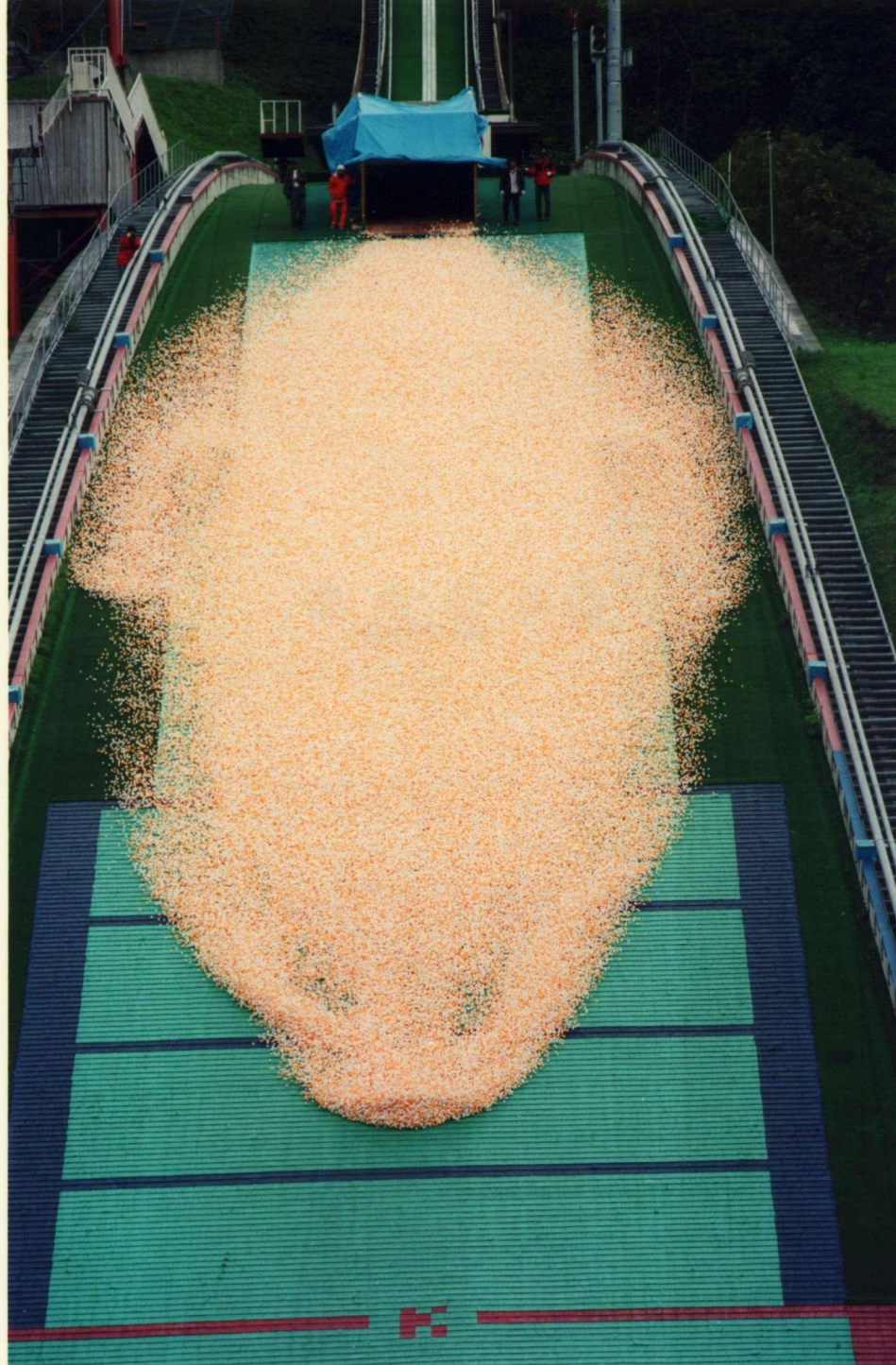


Figure 1.3: Front view of a 550,000 ping pong ball avalanche at the Miyanomori ski jump [McElwaine and Nishimura, 2001]. The horizontal lines are 5 m apart.

### 1.2.2 Laboratory-scale avalanche models

The difficulties and limitations associated with field and large-scale experiments may be overcome by using physical models that allow suspension currents, similar to powder-snow avalanches, to be generated in the laboratory in a systematic and repeatable manner. Many attempts at modelling particulate gravity currents on a laboratory scale used water as the ambient fluid [Ancey, 2004, Beghin et al., 1981, Hermann et al., 1987, Hampton, 1972, Hopfinger and Tochon-Danguy, 1977]. For such experiments the density ratio between the current and the ambient fluid is usually very low, typically only a few percent, and these currents are in the Boussinesq regime. The Boussinesq approximation [Boussinesq, 1897] neglects density differences except in buoyancy terms, and is often used to simplify the equations of motion and analysis of fluid behaviour. This approximation does not hold for solid particles in the air as soon as the solid concentration exceeds a few percent; the flow is then said to be in a non-Boussinesq regime. Powder snow avalanches are non-Boussinesq, with the relatively heavy snow particles carrying a significant proportion of the current's momentum, and therefore density differences will be important in both dynamic and buoyancy terms. Currents with low density ratios, such as those where water is used as the ambient fluid, will therefore not model the dynamics and mixing within a powder snow avalanche well as the particles' momentum is very small relative to that of the ambient fluid.

Additionally, few laboratory scale experiments have considered the transition from a dense flow to a suspension current and have not attempted to model the saltation and suspension mechanisms. Most either just focus on dense, unsuspended flows [Nohguchi and Ozawa, 2008, Hutter et al., 1989, Pouliquen, 1999] or use dense ambient fluid or premixed turbulent suspensions to model the dynamics of developed suspension currents [Hermann et al., 1987, Beghin and Olagne, 1991]. As previously mentioned, the transition from dense flow to suspension current may have significant effects on the dynamics of a powder snow avalanche and should be accounted for in a comprehensive physical model. Of the laboratory scale experiments that could be identified and that do consider the transition from dense flow to suspension current, only three have density ratios that fall within the non-Boussinesq regime; the sawdust and aluminium mixture-air currents of Bozhinskiy and Sukhanov [1998], the snow-air and the polystyrene-air currents of Turnbull and McElwaine [2008].

## 1.2. PHYSICAL MODELLING OF AVALANCHES

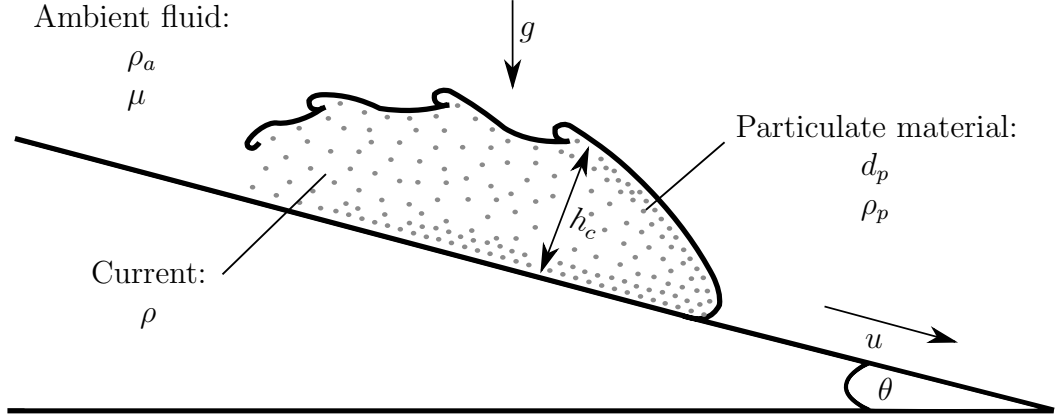


Figure 1.4: Schematic diagram of a particulate gravity current of height  $h_c$ , density  $\rho$  and velocity  $u$  travelling down an inclined plane. Ambient fluid has density  $\rho_a$  and viscosity  $\mu$ , and individual particles have a diameter  $d_p$  and density  $\rho_p$ .

The particle Reynolds number

$$\text{Re}_p = \frac{\rho_a u d_p}{\mu}, \quad (1.1)$$

is the ratio of the viscous and form drag forces (per unit volume) of a particle with diameter  $d_p$  and velocity  $u$  in ambient fluid of viscosity  $\mu$  and density  $\rho_a$  (Figure 1.4). The particle Reynolds number determines whether the drag is dominated by viscous or pressure forces. Powder snow avalanches typically have a  $\text{Re}_p \approx 3000$  meaning viscous drag forces play a minor role compared with the form drag of the particle. For values  $500 < \text{Re}_p < 10^5$  the drag coefficient for a spherical particle is essentially independent of  $\text{Re}_p$  [Massey, 2006] and so within this range of  $\text{Re}_p$  drag forces in powder snow avalanches will be well modelled. It should be noted that both the natural and model powder snow particles are henceforth assumed to be spherical. While it is unlikely that the particles are perfectly spherical, a particle's eccentricity will only have an effect on its drag coefficient when  $\text{Re}_p > \approx 10^5$  [Massey, 2006], which is well above the typical values of  $\text{Re}_p$  observed in natural powder snow avalanches.

Turnbull and McElwaine's [2008] snow-air and polystyrene-air models have a  $\text{Re}_p \approx 150$  due to the currents reaching much lower speeds than powder snow avalanches. Therefore viscous forces between the air and snow/polystyrene particles will have a greater effect on these flows than in a powder snow

## 1.2. PHYSICAL MODELLING OF AVALANCHES

---

avalanche. However, for this model  $\text{Re}_p$  is still large enough that form drag will be dominant and viscous drag forces can be considered small, especially compared with Bozhinskiy and Sukhanov's experiments ( $\text{Re}_p \approx 0.1$ ), where the particles are so fine that drag force is dominated by viscous forces.

The transition to, and subsequent maintenance of, a suspended state within the snow-air and polystyrene-air currents used in Turnbull and McElwaine's experiments is due to the matching of Richardson number ( $\text{Ri}$ ), between the laboratory and real world currents. The Richardson number is the ratio of potential energy to kinetic energy of particles at the sheared interface between two fluids. The Richardson number for a layer of height  $h_c$  and velocity  $u$  on a slope at angle  $\theta$  to the horizontal is

$$\text{Ri} = \frac{g' h_c \cos \theta}{u^2}. \quad (1.2)$$

The reduced gravity is  $g' = g\Delta\rho/\rho_a$ , where  $\Delta\rho = \rho - \rho_a$  with  $\rho$  and  $\rho_a$  the densities of the current and the ambient fluid respectively (Figure 1.4). The Richardson number provides an indication of the stability of the flow [Ellison and Turner, 1959]. If the  $\text{Ri}$  value is low, a dense flow will entrain air on the upper surface and become suspended. If the  $\text{Ri}$  value remains low the current will maintain the particles in suspension and further entrain air. Due to the lower velocities of the snow-air and polystyrene-air flows, very high slope angles have to be used in order to achieve values of  $\text{Ri}$  identical to those observed in powder-snow avalanches. Matching the low  $\text{Ri}$  values found in powder-snow avalanches ensures that air is entrained on the upper surface of the current and that the snow or polystyrene particles become suspended.

The Stokes number is a measure of the interaction between the particles and the fluid and whether the suspension behaves as a single phase or two phase flow [Ancy, 2007]. This depends on the drag regime and is defined in terms of the particle drag timescale and the timescale of the flow. For a form drag regime the Stokes number is

$$\text{St} = \frac{\rho_p d_p}{\rho_a h_c}, \quad (1.3)$$

where  $\rho_p$  is particle density (Figure 1.4). The snow-air and polystyrene-air models' Stokes numbers ( $\text{St} = 10$  &  $1$  respectively) are higher than a powder snow avalanche's ( $\approx 0.02$ ) because the current is so much smaller. However,

## 1.2. PHYSICAL MODELLING OF AVALANCHES

---

for polystyrene-air currents this value is within the range where the motion of the particles and fluid are strongly linked and the suspension behaves as a single phase [Ancey, 2007].

Polystyrene-air currents also offer a significant advantage over snow-air currents in that they allow much more control over initial conditions. Dry snow metamorphoses and sinters into clumps within seconds, and therefore has to be broken up with a sieve before being dropped on to the chute, greatly restricting control over initial conditions of the flow.

The Reynolds number

$$\text{Re} = \frac{\rho u h_c}{\mu}, \quad (1.4)$$

which determines the degree of turbulence in the flow, of the polystyrene-air currents ( $\text{Re} \approx 10^4$ ) is lower than that of a powder snow avalanche ( $\text{Re} \approx 10^9$ ). However, this is also true of all of the other laboratory-scale flows previously mentioned, and the Re value for polystyrene-air currents is within a turbulent regime, and therefore can be expected to provide similar flow characteristics to natural powder snow avalanches.

One process that is not accounted for by this model is the entrainment of additional particulate material through the base of the current (Figure 1.2). Over a long distance this lack of addition of dense material will result in the current becoming increasingly dilute by the continual entrainment of air, eventually resulting the flow ‘slumping’ (a significant decrease in flow height) and/or slowing down due to the decrease in driving buoyancy force. However, providing suitably large initial volumes of polystyrene beads are released it is unlikely that these effects and their subsequent influence on flow dynamics will be observed over the distances applicable to laboratory-scale flows.

The close matching of the relevant similarity criteria (Richardson number and density ratio) means that the polystyrene-air model is very well suited to modelling entrainment effects and the transition from dense granular flow to suspension current. The other similarity criteria are not exactly matched, but are within a range where the same flow behaviour and dynamics are expected. For these reasons polystyrene-air (EPS bead-air) currents will be used in this study to create laboratory-scale experiments that model natural powder snow avalanches.

## 1.3 Flow description

Between 1 and 3 litres of EPS beads were released from a line hopper, to flow down a steep slope (angles  $65^\circ - 85^\circ$ ) in air (described in detail in Chapter 2). Initially gravity accelerates granular material down the chute as a dense granular flow (Figure 1.5). Pressure forces arising from the particles' interaction with the ambient air, referred to as form drag, causes the front of the flow to form a crescent shape (in the  $y$ - $z$  plane), the foremost point of which is referred to as the nose. The nose of the current is slightly raised from the chute surface due to friction at the chute surface. Initially the driving gravity force is much larger than the form drag and basal drag caused by the chute surface and the flow continues to accelerate. A small amount of the ambient air will be forced underneath the nose of the flow and will be overrun by it. The majority of the ambient fluid will pass over the top of the flow. As it does so Kelvin-Helmholtz instabilities lead to the formation of turbulent eddies in the ambient air, which entrain particles from the upper surface [Simpson, 1997]. This is the main method by which air becomes mixed into the granular flow and causes the top surface to rise up perpendicular to the slope. Some ambient air will also become mixed into the flow through the formation of lobes and clefts at the front of the flow. Additionally a small amount of air will also enter the flow from the overrun layer as it rises due to buoyancy [Simpson, 1972]. The introduction of this air fluidises the granular flow by causing some of the EPS beads to become suspended. As the amount of air entrained increases more EPS beads from the bottom of the flow become suspended. As more air is entrained the driving buoyancy decreases until it balances the retarding forces of the EPS bead-air mixture, at this point dynamic equilibrium is reached and the front of the flow travels at constant velocity.

The motion of the flow within the head is thought to be dominated by a large-scale vortical structure [Bozhinskiy and Losev, 1998, McElwaine, 2004]. The driving component of gravity accelerates the EPS beads and air downslope towards the front of the flow. At the front of the flow this acceleration is countered by drag from the ambient air. Turbulent eddies forming along the top surface of the flow entrain air and slow the flow at the top of the current (Figure 1.5). Moving back from the front the turbulence decreases and the denser EPS beads begin to settle and fall towards the chute. This forms a denser layer close to the chute surface which then accelerates towards the front

### 1.3. FLOW DESCRIPTION

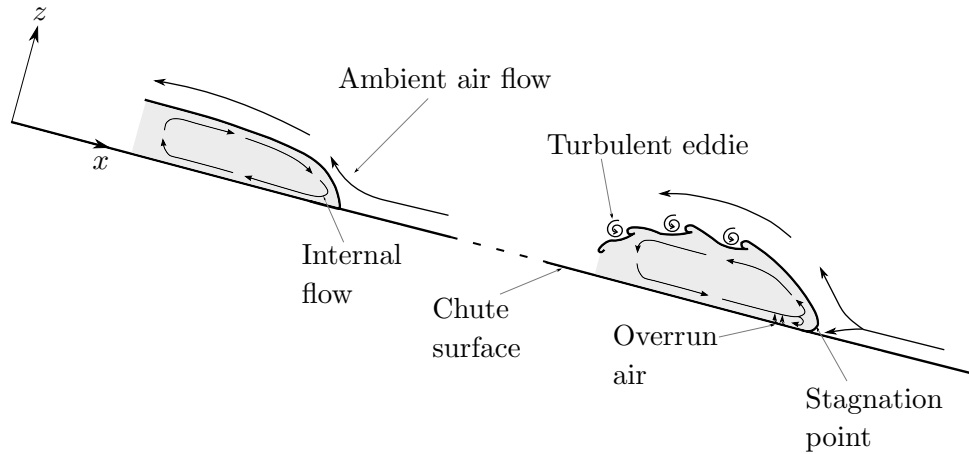


Figure 1.5: Flow relative to the head of a typical EPS bead current during the dense granular flow stage just after release (left) and as a suspended current further down the chute (right).

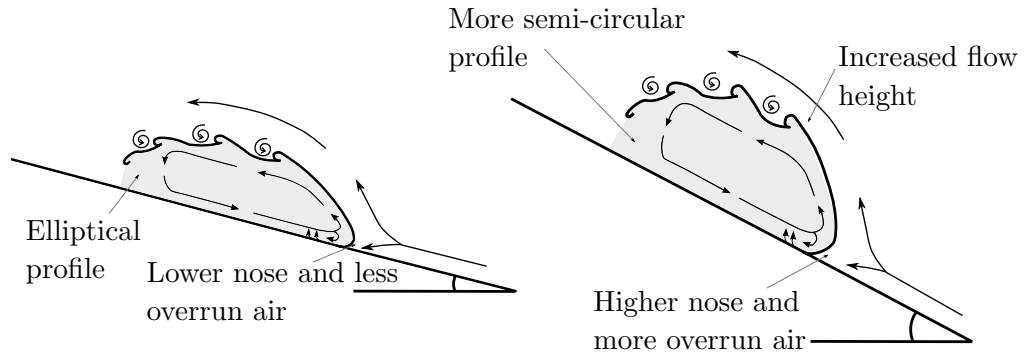


Figure 1.6: Diagram of the head of a suspended current at a low slope angle (left) and at a high slope angle (right).

due to its greater driving buoyancy force. The process then repeats creating a recirculating flow inside the head. Most of the particles will move up towards the top of the flow after reaching the front and circulate in that direction, however a small amount of particles will move down towards the chute surface creating a small region of flow circulating in the opposite direction close to the ground at the front.

Increasing the slope angle alters the evolution of the chute flows in several ways. Firstly the basal friction from the chute surface will decrease due to the decreased reaction force normal to the surface. This will be more important during the early stages when a large number of particles are in contact with the surface, however form drag will still be the dominant resistive force. Increasing the slope angle also increases the driving gravity component causing increased acceleration of the EPS beads. The particles therefore reach higher velocities

at an earlier stage in the motion. Larger velocities mean larger form drag forces. As the slope angle increases so does the level of air entrainment, this is due to the interface between the upper surface of the flow and the ambient air becoming less stable. This decrease in stability is caused by the decrease in gravitational force normal to the chute surface and therefore any particle leaving the dense flow is less likely to be pulled back into it by gravity. This increased entrainment counters the increased fall velocity. Thus the velocity at which the flow reaches dynamic equilibrium is approximately independent of slope angle. For shallow angles only a few particles enter suspension and the base of the current remains a dense granular flow. The head of the flow is only slightly deeper than the following tail. At larger angles most or all of the particles enter suspension. Increased entrainment of air means the head is much deeper than the following flow and is semi-elliptical or even (at very steep angles) semi-circular (Figure 1.6). As the level of suspension increases the dense granular flow at the base of the current becomes shallower and more ambient air is overrun causing the nose of the current to rise.

## 1.4 Frontal instability mechanisms

Powder snow avalanches typically feature characteristic three-dimensional wavy patterns at their leading edge (as illustrated by Figure 1.7(a)). Examples of this instability can also be found at the leading edges of both homogeneous particle-laden gravity currents and flows of unsuspended granular material (Figures 1.7(b) & 1.7(c)). Although it is thought that this lobe-and-cleft-type structure contributes significantly to air entrainment [Simpson and Britter, 1979], and thus the dynamics of powder snow avalanches, relatively little is known about the mechanisms that cause the formation of these patterns. One of the main aims of this study is to gain a better understanding of the instability at the leading edge of particle-laden flows. Several instability mechanisms have been identified in gravity currents and unsuspended granular flows that may also play a role in powder snow avalanches.



## 1.4. FRONTAL INSTABILITY MECHANISMS

---

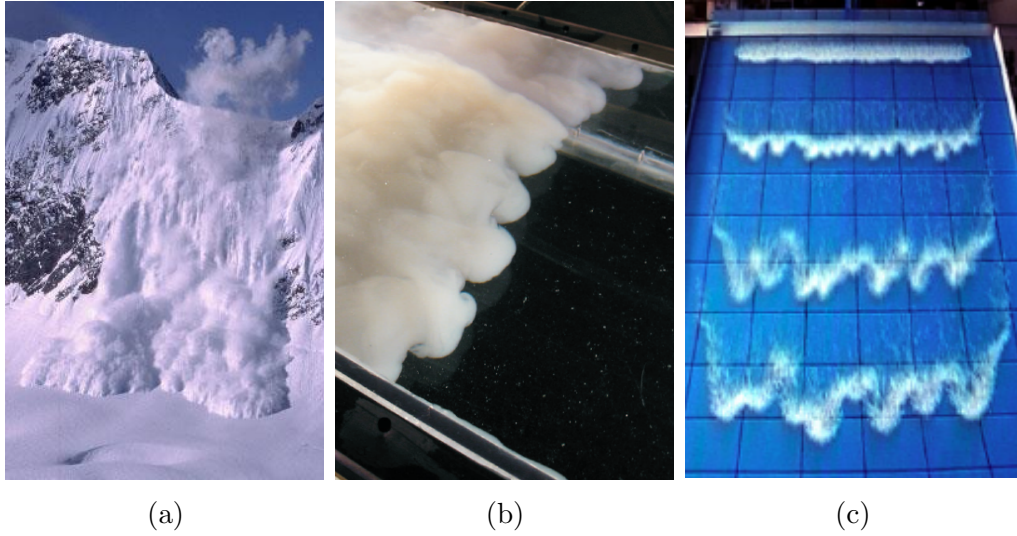


Figure 1.7: Examples of lobe-and-cleft type patterns at the leading edge of: (a) a natural powder snow avalanche (photograph reproduced by courtesy of Brad White and the Avalanche.org), (b) a laboratory-scale homogeneous particle-laden gravity current [Neufeld, 2002], and (c) a laboratory-scale unsuspended flow of granular material [Nohguchi and Ozawa, 2008].

### 1.4.1 Classic lobe-and-cleft instability

For homogenous Boussinesq gravity currents flowing along a horizontal surface a shifting pattern of lobes and clefts has been observed at the leading edge [Simpson, 1972, Neufeld, 2002, Härtel et al., 2000]. Simpson [1972] studied the evolution of the lobe and cleft structure (Figures 1.8(a) & 1.8(b)) in experiments using a volume of saline solution released under controlled conditions into a tank of water in order to produce a gravity current. He noted that in the early stages of the flow a regular structure of filaments formed at the front of the gravity current. Simpson points out that these filaments indicate the existence of an initially preferred lobe size. This filamentary structure then persists for a short distance downstream before collapsing into a more irregular pattern of shifting lobes and clefts. It was found that clefts do not disappear but may absorb or be absorbed by their neighbours since all the lobes are either swelling or shrinking in width. There is a maximum size possible for a lobe, and when this is reached, a new cleft forms in it. In this rapidly shifting system the number of lobes and clefts can remain almost constant. A dependence of nose height and of lobe size on Reynolds number for the whole flow was observed.

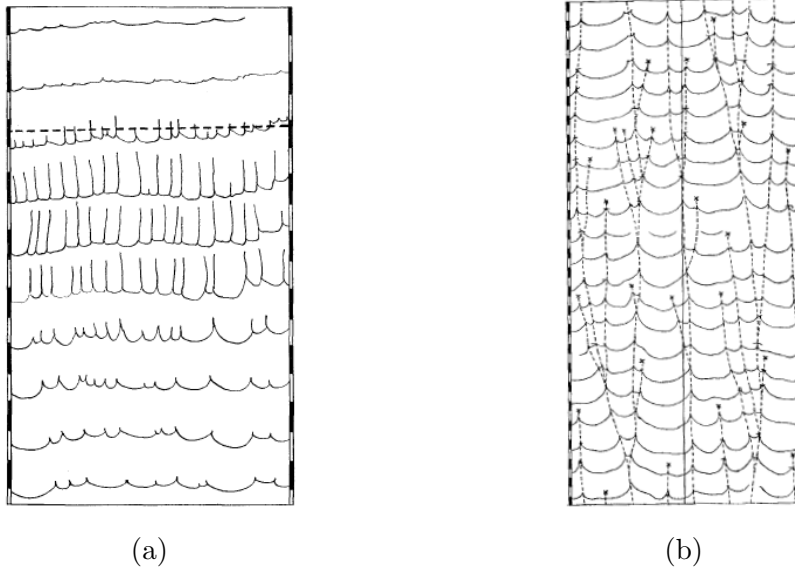


Figure 1.8: (a) Initiation of the lobe-and-cleft structure at the head of a gravity current as observed in the experiments of Simpson [1972]. Plan view at intervals of  $\frac{1}{3}$  s. The flow direction is from top to bottom at a Reynolds number of approximately 4500. Initially the floor underneath the front was moved with the front giving an almost two-dimensional flow structure at the leading edge. At the position of the dashed horizontal line the floor was suddenly brought to rest. The rapid transition to a filamentary structure, which precedes the final breakdown into lobes and clefts is clearly recognized. (b) Drawing from shadowgraph series showing the evolution of lobes as observed in the experiments of Simpson [1972]. - - -, continuity of clefts;  $\times$ , points where new clefts appear. Time interval 0.5 s, scale in cm,  $\Delta\rho/\rho = 1\%$  and the flow direction is from top to bottom.

#### 1.4. FRONTAL INSTABILITY MECHANISMS

---

McElwaine and Patterson [2004] have also carried out experiments and analysis on lobe and cleft formation using saline solution in water in order to produce a gravity current. In agreement with Simpson, McElwaine and Patterson note that as lobes between clefts increase in size and decrease in curvature they become dynamically unstable and an indentation forms in them. After propagating a distance of the radius of curvature of the indentation a cleft appears. This results in a process of clefts continually forming, then merging, but never disappearing.

The raised nose of a gravity current causes some of the less dense ambient fluid to be forced underneath the nose and overrun by the gravity current. Simpson conducted experiments in order to investigate the role played by this overrunning of less dense fluid in causing the lobe and cleft instability. In his experiments Simpson found that it is possible to suppress the formation of the lobe and cleft structure. One method prevented the overrunning of light fluid by laying down a thin layer of dense fluid ahead of the current, ensuring that all the overrunning fluid was no longer lighter than the gravity current fluid. The other method involved a section of the floor underneath the current being moved in the direction of the current, creating a slip boundary. Increasing the speed of the floor caused the profile of the front to become flatter and the nose to approach the ground. As the speed of the floor approached the speed of the head fewer lobes formed and at a speed slightly above that of the head, no lobes formed. Stopping the floor caused a nose to form once more and the lobe and cleft pattern immediately returned.

Simpson proposed that the lobe and cleft structure at the head of a gravity current arises from a convective instability produced by light liquid which has been overrun by the denser liquid of a gravity current. However, no sufficiently detailed measurements were available to reveal details of the structure and location of the frontal instability.

McElwaine and Patterson disagree with Simpson's suggestion that the instability is due to the overrunning of ambient fluid. They point out that compared to environmental flows, experiments and simulations are performed at very low Reynolds numbers, where flows are only barely turbulent. At higher Reynolds numbers the overrunning layer will increase in size relative to the trapped ambient layer, making the trapped ambient layer less important. Lobes and clefts are still observed in these flows so there must be at least

one other source of instability. Therefore an alternative explanation offered for Simpson's observations is that the presence of a slip boundary results in much less turbulence in the flow. This would mean that much higher Reynolds numbers would have to be achieved in order to observe the instability.

Härtel et al. [2000] have carried out a stability analysis of the flow at the head of a gravity current in order to closer examine the lobe-and-cleft instability. They approach the problem by looking at two-dimensional fronts and seeing if they are unstable to small three-dimensional disturbances, aiming to identify the primary and three-dimensional linear instability that drives an initially two-dimensional flow into a three-dimensional state. The primary instability is the structure of filaments observed by Simpson, however Härtel et al. suggest that, as this occurs at the foremost part of the flow, the two-to-three dimensional transition at the head is caused by an instability that acts locally at the leading edge, rather than by a buoyancy induced rise of overrun fluid. In order to test this hypothesis a linear-stability analysis is carried out on the direct numerical simulation (DNS) results of two-dimensional lock-exchange flows over a range of Reynolds numbers that extended to about 14 000.

A key observation from Härtel et al.'s simulation was that the stagnation point of the flow is located below and slightly behind the foremost part of the front. Therefore some of the ambient fluid will temporarily enter the region below the nose, before flowing around the nose and ending up above the current. This creates a localized region of unstable stratification at the leading edge that does not involve the light fluid eventually overrun by the current. This is in marked contrast to Simpson's suggestion that the stagnation point and the foremost point of a front coincide.

The other key finding from the analysis is that the head of a gravity current is linearly unstable to three-dimensional disturbances over the range of Reynolds numbers examined and at high Reynolds numbers the breakdown of a two-dimensional flow to a three-dimensional one will be very abrupt. The linear-stability analysis revealed that the spacing of the initial filaments is closely related to the preferred wavenumber of a vigorous instability that has not been recognised before. The preferred wavenumber was found to increase with increasing Grashof number of the flow. The Grashof number is a dimensionless parameter that represents the ratio of buoyancy to viscous forces, and

#### 1.4. FRONTAL INSTABILITY MECHANISMS

---

is defined as

$$\text{Gr} = \left( \frac{u_b L}{\nu} \right)^2, \quad (1.5)$$

where the buoyancy velocity  $u_b = \sqrt{g' L}$  and  $L$  is a lengthscale, in this case the channel half-height of the lock-exchange flow being modelled. The Froude number,

$$\text{Fr} = \frac{u}{\sqrt{g' L}}, \quad (1.6)$$

which is a dimensionless parameter representing the ratio of inertial forces (i.e. front velocity) to buoyancy forces, was also found to increase as Grashof number increases. The Reynolds number of the flow can be evaluated using the relationship

$$\text{Re} \propto \text{Fr} \sqrt{\text{Gr}}. \quad (1.7)$$

The linear stability analysis predictions were compared with the filament spacings from Simpson's experimental results and a good agreement was shown. These results have also since been verified experimentally by Neufeld [2002].

It was found that the region most affected by this leading-edge instability is located between the nose and stagnation point. The fact that it is most pronounced in this unstably stratified region suggests that it is caused by buoyancy forces. In order to examine more specifically the role that buoyancy plays, part of the analysis was repeated using simplified stability equations in which the gravity term was dropped. No unstable modes were found, providing evidence that the mechanism triggering the breakdown of the front into a lobe and cleft pattern is indeed a gravitational instability. In order to show that this instability is not related to the unstable stratification between the heavy fluid within the head and the thin layer of light fluid that the front overruns, the stability properties of the near-wall flow beneath the head were also examined. The analysis showed that in this region further gravitational instabilities may exist, but their contribution to the frontal breakdown is negligible.

To further validate their findings Härtel et al.'s two-dimensional linear-stability results were compared with results from a three-dimensional DNS. Härtel et al.'s DNS exhibits all the characteristic features of gravity currents, including the lobe-and-cleft structure at the leading edge, which previous simulations had not been able to achieve. However their simulation was only able to reach a Reynolds number of about 750, due to computer processor limitations. The three-dimensional DNS showed good agreement with the linear

stability analysis and that the dominant mode of instability is the same as that in the two-dimensional analysis.

In this study we will henceforth refer to this instability as the classical lobe-and-cleft instability. For clarity it should be pointed out that we will refer to the wavy patterns observed at the front of the flows as lobe-and-cleft-type patterns, however the formation of these patterns is not necessarily caused by the classic lobe-and-cleft instability. There are several other mechanisms that could cause the formation of a lobe-and-cleft-type pattern, which we shall now introduce.

### 1.4.2 Twin vortices

In contrast to homogenous Boussinesq gravity currents, flows of dense unsuspended granular material moving down an inclined plane exhibit different forms of lobe-and-cleft-type patterns at their leading edge [Nohguchi and Ozawa, 2008, Pouliquen et al., 1997]. While it is possible that the classic lobe-and-cleft instability causes the initial fluctuations in the moving front, the aforementioned continuously shifting pattern of lobes and clefts is not present in these cases. Instead a more stable pattern develops with lobes developing into fingers that accelerate downslope ahead of the remainder of the flow.

Nohguchi and Ozawa [2008] have speculated that the formation mechanism of the wave pattern observed at the fronts of granular flows under the influence of air drag force may be related to the classic lobe-and-cleft instability.

Using EPS beads and an inclined chute, Nohguchi and Ozawa have investigated the role of particle size on the wavelength produced in unsuspended granular flows. Two different starter hoppers were used in order to release the particles and start the flow, one linear and one half-spherical.

Lobe-and-cleft-type patterns in the flow fronts were observed for both the linear and half-spherical starter hopper experiments. The radius of curvature, in the  $x$ - $y$  plane, of the lobes increased with increasing particle diameter in both cases. With the half-spherical starter hopper, the flow always had a single ‘tail’ at the rear end and a number of ‘heads’, or lobes, at the front (Figure 1.9). The smaller the particles the greater the number of lobes that formed, suggesting a scaling law that relates particle diameter to the size of the lobes.

#### 1.4. FRONTAL INSTABILITY MECHANISMS

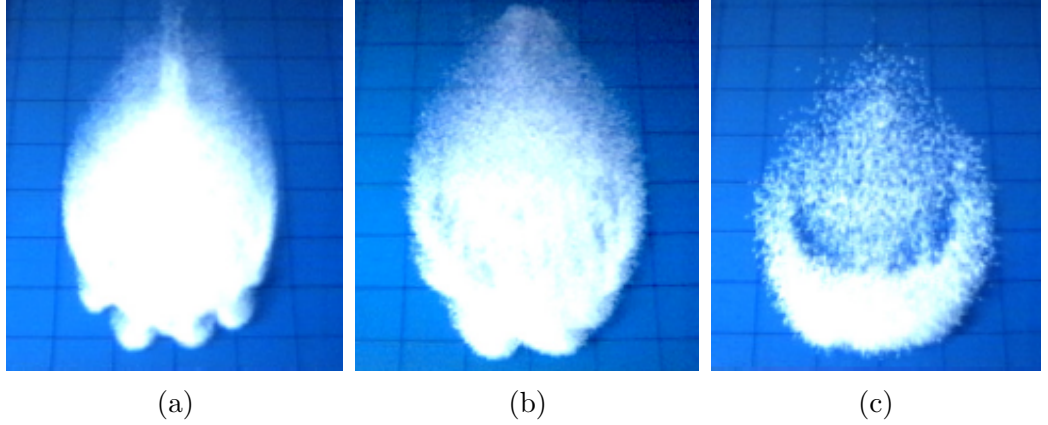


Figure 1.9: Granular flows from the experiments of Nohguchi and Ozawa [2008], released from a half-spherical starter using EPS beads of diameter: (a)  $d_p = 1.9$  mm, (b)  $d_p = 4.2$  mm and (c)  $d_p = 7.4$  mm.

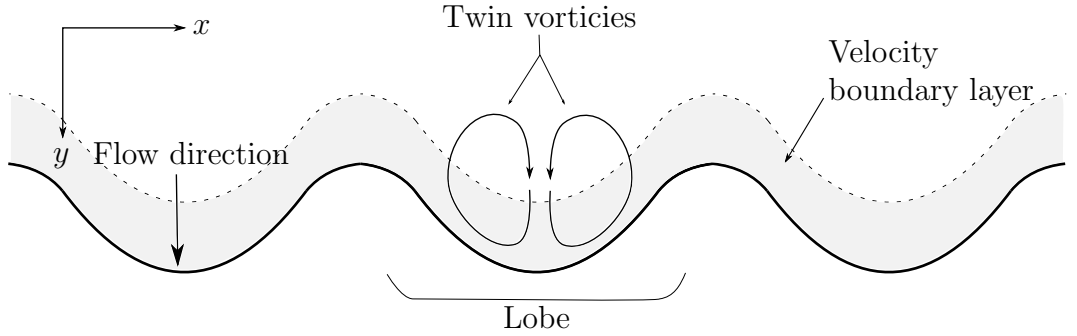


Figure 1.10: Schematic showing plan view of the wave pattern produced at the front of a particle-laden flow.

The mean velocity of the moving front was found to be faster for the smaller particles. Although the terminal velocity of each single particle is slower for the smaller particles, the smaller particles tend to produce a sharper (i.e. smaller radius of curvature in the  $x$ - $y$  plane) lobe at the moving front. This is subject to a weaker drag force and thereby attains a higher terminal velocity.

Analysis of the image data obtained from the experiments revealed twin vortices behind each lobe. The rotation takes place in a manner that reduces the relative wind velocity at the system's surface (Figure 1.10), therefore reducing the air drag force exerted on the system. This results in a rapid increase in front velocity just after the formation of the lobes.

Nohguchi and Ozawa suggest that a velocity boundary layer exists around the edge of the flow (Figure 1.10). This is caused by the fact that the air inside

## 1.4. FRONTAL INSTABILITY MECHANISMS

---

the flow is moving at the mean flow velocity, whilst the air outside the flow is stationary. This leads to a transitional region over which the air and particle velocity significantly differ. In this region the particles are strongly affected by the air drag force, thereby changing their velocity. This contrasts with particles in the central part of the flow, which experience reduced air drag. This results in a difference in particle velocity between the velocity boundary layer and the central part of the flow. This difference causes the circulating motion observed in the particle-laden flows. Nohguchi and Ozawa [2008] hypothesise that pairs of vortices form between clefts in the front of a granular flow. These vortices rotate in a manner that reduces the air drag at the leading edge, causing the vortices to grow and deform the initial perturbation into a finger-like pattern. The thickness of the velocity boundary layer is assumed to be equal to the distance that a single particle travelling at the flow velocity can move against the drag force of the static air. The velocity boundary layer thickness  $\delta_v$  is therefore defined by Nohguchi and Ozawa [2008] as

$$\delta_v = \frac{2\rho_p d_p}{3C_d \rho_a}, \quad (1.8)$$

where  $\rho_p$  and  $\rho_a$  are the densities of the particle and the surrounding air respectively,  $d_p$  is the diameter of a single particle, and  $C_d$  is the drag coefficient. In order to maintain steady-state vortex motion the radius of each lobe would need to be twice the thickness of the velocity boundary layer. This then suggests that the size of the lobes will be related to the drag forces acting on the particles as drag force plays a key role in determining the velocity boundary layer thickness.

Comparison of experimental and theoretical results shows reasonable agreement, despite some rough approximation assumed in the analysis (gravity terms and interaction between particles in the velocity boundary layer were neglected). The agreement of the results suggests that the concept of a velocity boundary layer can provide a first-order estimate for the size of vortices at the moving front of granular particles. However more studies are required to clarify the exact flow patterns of vortex motion.

Nohguchi and Ozawa state that it is likely to be the same classic lobe-and-cleft instability found in the leading edges of homogenous Boussinesq gravity currents that plays a role in the initiation of front fluctuations in the moving fronts of granular flows. However, after initiation, the non-linear feedback



## 1.4. FRONTAL INSTABILITY MECHANISMS

---

growth of the vortices deforms the initial fluctuations to produce a wavy pattern associated with these vortices. The emergent pattern shows a dependency on particle size as this determines the size of the velocity boundary layer, which in turn determines the size of the vortices.

This is in contrast with Simpson's observations of homogenous Boussinesq gravity currents where, as the front propagates, clefts merge but never disappear. As the lobes between clefts increase in size new clefts appear, resulting in a rapidly shifting system in which the total number of lobes and clefts remains almost constant. The front of the flow is irregular and unstable with no emergent pattern.

### 1.4.3 Polydispersity

A further mechanism that leads to the formation of lobe-and-cleft-type patterns is caused by polydispersity of the granular medium [Pouliquen et al., 1997, Pouliquen and Vallance, 1999].

It has been found that in inclined chute flows of unsuspended polydisperse granular material, the larger particles rise to the free surface through a statistical sieving mechanism [Drahn and Bridgewater, 1983, Savage and Lun, 1988]. Higher velocities at the free surface result in the larger particles being transported to the leading edge of the flow. Upon reaching the front the larger particles stop on the chute surface, while the rest of the leading edge continues to propagate down the slope. The larger particles are thus re-injected into the body of the flow, the segregation process is repeated, and a recirculation motion is established.

If a small perturbation occurs at the front, the trajectories of the large particles arriving at the front are deflected towards the cleft of the deformation, following the steepest slope of the free surface. However, the return trajectories of the larger particles when they have just left the leading edge remain approximately straight lines. A uniform concentration of large particles arriving at the free surface thus leads to a non-uniform distribution at the chute surface with high concentration at the cleft in the leading edge.

The high concentration of large particles located in the vicinity of a cleft leads to a local increase of the friction in these areas. The material thus

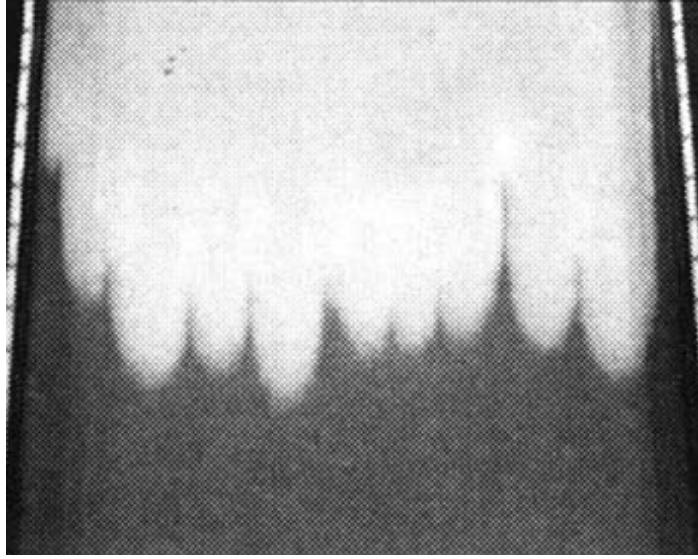


Figure 1.11: Finger-like pattern produced at the leading edge of an unsuspended granular flow as a result of polydispersity of the granular material, as observed in the experiments of Pouliquen et al. [1997].

locally slows down, amplifying the perturbation and leading to the formation of extended lobes or ‘fingers’ (Figure 1.11). The recirculation motion of the large particles amplifies this phenomenon as the larger particles tend to accumulate in lines behind the clefts.

No fingering was observed by Pouliquen et al. [1997] in flows consisting of quasi-monodisperse granular material, for which the range of variation in particle diameter was  $\pm 11\%$  of the mean particle diameter. However, the addition of material with mean diameter 14% larger than the mean diameter of the quasi-monodisperse granular material was enough to induce the instability. Pouliquen et al. [1997] found that the addition to the bulk quasi-monodisperse granular material of just 5% by volume of larger particles was enough to induce the fingering instability, whilst introduction of the same percentage by volume of smaller particles had no effect.

### 1.4.4 Rayleigh-Taylor instability

The Rayleigh-Taylor instability is a fingering instability that occurs at an interface between two fluids of different density, for example a heavy fluid initially lying on top of light fluid in a gravitational field [Rayleigh, 1900,

## 1.5. AIR PRESSURE

---

Taylor, 1950]. For inviscid fluids the interface will always be unstable, with the growth rate of the unstable modes increasing as their wavelengths decrease [Chandrasekhar, 1961].

Most experimental studies of the Rayleigh-Taylor instability focus on liquid-liquid or sediment-liquid interfaces and it has been shown that factors such as viscosity, surface tension and diffusivity inhibit short wavelength perturbations [Chandrasekhar, 1961, Duff et al., 1962, Sharp, 1984, Youngs, 1984, Völtz et al., 2001], resulting in a most unstable wavelength which is dependent on the properties of the fluids involved. Vinningland et al. [2007, 2010] have conducted Rayleigh-Taylor instability experiments and numerical simulations using a gas-grain interface. The Rayleigh-Taylor instability induced structures were found to be size invariant when scaled with grain diameter. However the sizes of the grains used ( $70\text{--}570\,\mu\text{m}$ ) are so small that the effects of viscous drag are likely to be significant. This is confirmed by a theoretical analysis conducted by Vinningland et al. [2010] that predicts that this size invariance will only hold for grain diameters of approximately  $140\,\mu\text{m}$ .

## 1.5 Air pressure

Front velocities and flow heights of both field and laboratory avalanches are typically found using video data of the flows. However air pressure measurements (Figure 1.12) provide information about a flow's internal structure. These measurements have been made in large natural snow avalanches [Nishimura et al., 1995, Turnbull and McElwaine, 2007, Nishimura and Ito, 1997] and laboratory avalanches [Turnbull and McElwaine, 2008, 2010]. Additionally theoretical analysis of the pressure distribution through a gravity current has also been conducted and models have been developed [von Kármán, 1940, McElwaine, 2004].

Early analytical work assumed that inside the flow the pressure distribution was hydrostatic and that the front of the gravity current should make an angle of  $60^\circ$  to the horizontal [von Kármán, 1940]. Later analytical studies agree with the front angle result, but suggest that the hydrostatic assumption is incorrect and a new model based on the dynamic pressure of the gravity current was proposed [McElwaine, 2004]. The validity of this model has been tested and confirmed using experimental data. Turnbull and McElwaine [2008] found

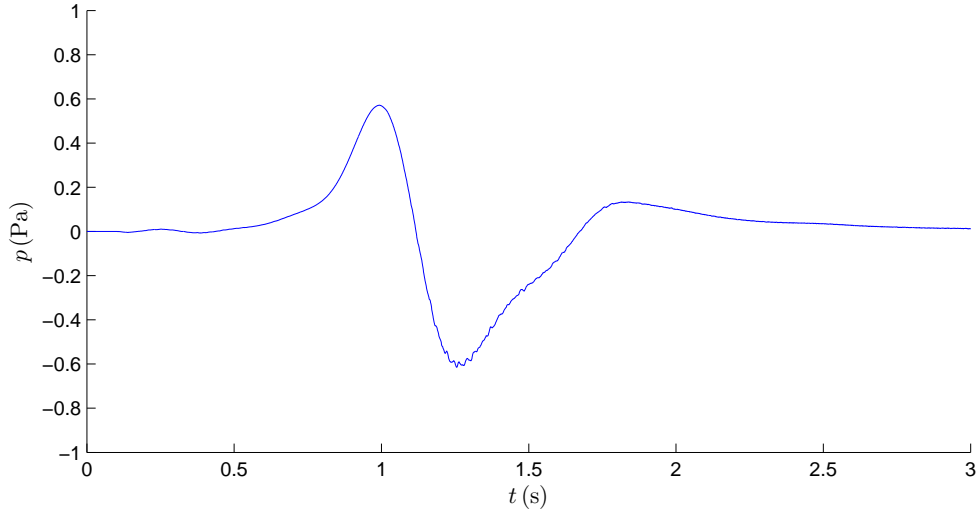


Figure 1.12: A typical air pressure signal obtained from the chute surface of a laboratory scale avalanche.

that as the front of a current passes over a pressure sensor there is a positive pressure peak, corresponding to the change in air velocity caused by the flow. This is followed by a sharp drop in pressure over a very short period of time inside the head of the current. The more suspended the current is the greater the negative pressure peak. When the flow is fully suspended this negative peak is of similar magnitude to the positive peak. This large negative pressure inside the head indicates a high degree of internal motion, with internal vertical velocities of similar magnitude to the front velocity and thus confirming the hypothesis that the head dynamics are dominated by a large vortex [Bozhinskiy and Losev, 1998]. After reaching the negative peak, the air behind the head becomes turbulent and the pressure returns to zero as the flow has passed.

This negative pressure peak has important implications for estimating the maximum bulk stresses avalanches can exert on structures. Guidelines suggest that the pressure a powder snow avalanche can exert on a structure is the stagnation pressure. This corresponds to the positive pressure peak at the nose of the flow. The fact that the negative peak is of similar size to the positive peak implies that the internal velocities are of the same magnitude as the front velocity of the flow. Therefore the largest velocities may be as much as double the front velocity, resulting in peak pressures up to four times higher than the stagnation pressure [Turnbull and McElwaine, 2010]. The negative pressure will also provide a strong influence for the entrainment of snow particles from underneath the powder cloud, allowing the avalanche to

## 1.6. SUMMARY

---

grow and accelerate [Louge et al., 2011].

Analysis and comparison to video data is complicated by inhomogeneities in the snow-air flow. Larger clumps of snow mix with ambient air less well than smaller particles, leading to wide variations in velocities within the flow [Turnbull and McElwaine, 2010]. More accurate and reproducible experiments could be carried out with EPS bead-air flows, additionally the theoretical result of a front angle of  $60^\circ$  has not been fully confirmed experimentally.

## 1.6 Summary

In this work we attempt to gain a better understanding of the dynamics of powder snow avalanches, with a specific focus on the mechanisms behind, and the development of the lobe-and-cleft-type pattern at the leading edge of these particle-laden gravity currents. Several frontal instability mechanisms have been identified that may lead to the formation of lobe-and-cleft-type patterns at the leading edge of various types of flow: the classic lobe-and-cleft instability, twin vortices, polydispersity and Rayleigh-Taylor. A key aim of this work is to ascertain which, if any, of these instabilities play a role in these non-Boussinesq, fully-suspended, particle-laden flows.

This is achieved through the physical modelling of powder snow avalanches on a laboratory scale using gravity currents consisting of expanded polystyrene (EPS) beads and air, which have been demonstrated to have to the required similarity criteria to well model powder snow. Video and air pressure data is used to track and quantify lobe-and-cleft-type patterns in the leading edge of these currents as they develop, investigate the effects of their formation on the dynamics of the flow (and vice-versa) and identify how these patterns are dependent on, and scale with key parameters.

## Bibliography

C. Ancey. Powder snow avalanches: Approximation as non-Boussinesq clouds with a Richardson number-dependent entrainment function. *Journal of Geophysical Research*, 109(F01005), 2004. doi:10.1029/2003JF000052.

- C. Ancey. Plasticity and geophysical flows: A review. *Journal of Non-Newtonian Fluid Mechanics*, 142(4-35), 2007.
- P. Beghin and X. Olagne. Experimental and theoretical study of the dynamics of powder snow avalanches. *Cold Regions Science and Technology*, 19:317–326, 1991.
- P. E. Beghin, E. J. Hopfinger, and R. E. Britter. Gravitational convection from instantaneous sources on inclined boundaries. *Journal of Fluid Mechanics*, 107:407–422, 1981.
- J. Boussinesq. *Thorie de l’coulement tourbillonnant et tumultueux des liquides dans les lits rectilignes a grande section*, volume 1. Gauthier-Villars, Paris, 1897.
- A. N. Bozhinskiy and K. S. Losev. *The fundamentals of avalanche science*. Eidgenössisches Institut für Schnee- und Lawinenforschung, Davos, Switzerland, 1998.
- A. N. Bozhinskiy and L.A. Sukhanov. Physical modelling of avalanches using an aerosol cloud of powder material. *Annals of Glaciology*, 26:242–394, 1998.
- S. Chandrasekhar. *Hydrodynamic and Hydromagnetic Stabiltiy*. Oxford University Press, Oxford, UK, 1961.
- J. A. Drahn and J. Bridgewater. The mechanisms of free surface segregation. *Powder Technology*, 36:39–53, 1983.
- R. E. Duff, F. H. Harlow, and C. W. Hirt. Effects of diffusion on interface instability between gases. *Physics of Fluids*, 5:417–425, 1962.
- T. Ellison and J. Turner. Turbulent entrainment in stratified flows. *Journal of Fluid Mechanics*, 6(423-448), 1959.
- M. A. Hampton. The role of sub-aqueous debris flow in generating turbidity currents. *Journal of Sedimentary Petrology*, 42:775–793, 1972.
- C. Härtel, F. Carlsson, and M. Thunblom. Analysis and direct numerical simulation of the flow at a gravity-current head. Part 2. The lobe-and-cleft instability. *Journal of Fluid Mechanics*, 418:213–229, 2000.

## BIBLIOGRAPHY

---

- F. Hermann, J. Hermann, and K. Hutter. Laboratory experiments on the dynamics of powder snow avalanches. In *International Symposium on Avalanche Formation, Movement and Effects, Proceedings of the Davos Symposium, Sept. 1986*, volume IAHS-Publ. No. 162, pages 431–439, 1987.
- E. J. Hopfinger and J. C. Tochon-Danguy. A model study of powder snow avalanches. *Journal of Glaciology*, 81:343–356, 1977.
- K. Hutter, S. B. Savage, and Y. Nohguchi. Numerical, analytical, and laboratory experimental studies of granular avalanche flows. *Annals of Glaciology*, 13:109–116, 1989.
- M. Y. Louge, C. S. Carroll, and B. Turnbull. Role of pore pressure gradients in sustaining frontal particle entrainment in eruption currents - the case of powder snow avalanches. *Journal of Geophysical Research: Earth Surface*, 116(F04030), 2011. doi:10.1029/2011JF002065.
- S. Margreth. Gutachten betreffend unglückslawinen in Galtür vom 23.2.1999 und in Valzur vom 24.2.1999. In *SLF Gutachten G2000*, pages 15–18. Swiss Federal Institute for Snow and Avalanche Research (SLF), Davos Dorf, Switzerland, 2000. In German.
- B. S. Massey. *Mechanics of Fluids*. Taylor & Francis, Abingdon, UK, 8th edition, 2006.
- J. N. McElwaine. Rotational flow in gravity current heads. *Philosophical Transactions of the Royal Society*, 363:1603–1623, 2004.
- J. N. McElwaine and K. Nishimura. *Particulate Gravity Currents*, volume 31 of *Special Publication of the International Association of Sedimentologists*, chapter Ping-pong Ball Avalanche Experiments, pages 135–148. Blackwell Science, Malden, Massachusetts, USA, 2001.
- J. N. McElwaine and M. D. Patterson. Lobe and cleft formation at the head of a gravity current. Technical report, Department of Applied Mathematics and Theoretical Physics, Centre for Mathematical Sciences, University of Cambridge, 2004.
- J. Neufeld. Lobe-cleft patterns in the leading edge of a gravity current. Master’s thesis, Department of Physics, University of Toronto, Toronto, Canada, 2002.

- K. Nishimura and Y. Ito. Velocity distribution in snow avalanches. *Journal of Geophysical Research*, 102(B12):27297–27303, 1997.
- K. Nishimura, F. Sandersen, K. Kristensen, and K. Lied. Measurements of powder snow avalanche - Nature. *Surveys in Geophysics*, 16(5-6), 1995.
- Y. Nohguchi and H. Ozawa. On the vortex formation at the moving front of lightweight granular particles. *Physica D*, 238:20–26, 2008. doi:10.1016/j.physd.2008.08.019.
- O. Pouliquen. Scaling laws in granular flows down rough inclined planes. *Physics of Fluids*, 11(3):542–548, 1999.
- O. Pouliquen and J. W. Vallance. Segregation induced instabilities of granular fronts. *Chaos*, 9(3):621–629, 1999.
- O. Pouliquen, J. Delour, and S. B. Savage. Fingering in granular flows. *Nature*, 386:816–817, 1997.
- Lord Rayleigh. Investigation of the character of the equilibrium of an incompressible heavy fluid of variable density. In *Scientific Papers*, volume II, page 200. Cambridge University Press, Cambridge, UK, 1900.
- S. B. Savage and C. K. K. Lun. Particle size segregation in inclined chute flow of dry cohesionless granular solids. *Journal of Fluid Mechanics*, 189: 311–335, 1988.
- D. H. Sharp. An overview of Rayleigh-Taylor instability. *Physica D*, 12:3–18, 1984.
- J. E. Simpson. Effects of the lower boundary on the head of a gravity current. *Journal of Fluid Mechanics*, 53(4):759–768, 1972.
- J. E. Simpson. *Gravity Currents in the Environment and the Laboratory*. Cambridge University Press, 2nd edition, 1997.
- J. E. Simpson and R. E. Britter. The dynamics of the head of a gravity current advancing over a horizontal surface. *Journal of Fluid Mechanics*, 94(3): 477–495, 1979.
- G. I. Taylor. The instability of liquid surfaces when accelerated in a direction perpendicular to their planes, I. *Proceedings of the Royal Society A*, 201: 192–6, 1950.



## BIBLIOGRAPHY

---

- B. Turnbull and J. N. McElwaine. A comparison of powder-snow avalanches at Vallée de la Sionne, Switzerland, with plume theories. *Journal of Glaciology*, 53(180):30–40, 2007.
- B. Turnbull and J. N. McElwaine. Experiments on the non-Boussinesq flow of self-igniting suspension currents on a steep open slope. *Journal of Geophysical Research*, 113(F01003), 2008. doi:10.1029/2007JF000753.
- B. Turnbull and J. N. McElwaine. Potential flow models of suspension current air pressure. *Annals of Glaciology*, 51(54), 2010.
- B. Turnbull, J. N. McElwaine, and C. Ancey. Kulikovskiy-Sveshnikova-Beghin model of powder snow avalanches: Development and application. *Journal of Geophysical Research*, 112(F01004), 2007. doi:10.1029/2006JF000489.
- J. Vallet, B. Turnbull, S. Joly, and F. Dufour. Observations on powder snow avalanches using videogrammetry. *Cold Regions Science and Technology*, 39: 153–159, 2004.
- J. L. Vinningland, Ø. Johnsen, Flekkøy E. G., R. Toussaint, and K. J. Måløy. Experiments and simulations of a gravitational granular flow instability. *Physical Review E*, 76(051306), 2007.
- J. L. Vinningland, Ø. Johnsen, Flekkøy E. G., R. Toussaint, and K. J. Måløy. Size invariance of the granular Rayleigh-Taylor instability. *Physical Review E*, 81(041308), 2010.
- C. Völtz, W. Pesch, and I. Rehberg. Rayleigh-Taylor instability in a sedimenting suspension. *Physical Review E*, 65(011404), 2001.
- T. von Kármán. The engineer grapples with nonlinear problems. *Bulletin of the American Mathematical Society*, 46:615–683, 1940.
- D. L. Youngs. Numerical simulation of turbulent mixing by Rayleigh-Taylor instability. *Physica D*, 12:32–34, 1984.

## BIBLIOGRAPHY

---

## Chapter 2

### Experimental set-up

In order to study the development of lobe-and-cleft-type patterns at the leading edge of powder snow avalanches, experiments that created repeatable, laboratory scale avalanches were conducted using line releases of expanded polystyrene (EPS) beads in air. The use of a line release on a planar surface creates a pseudo two-dimensional release, enabling the study of instabilities that occur where freedom in the transversal direction exists in addition to that in the flow direction [Nohguchi and Ozawa, 2008]. The following section describes the experimental set-up that was used to create these laboratory scale avalanches and capture video and air pressure data, whilst also allowing key parameters, such as slope angle, surface roughness and size and volume of material released, to be varied.

The experiments detailed in this thesis were conducted on a 1 m wide, 1.9 m long, flat, open sided wooden chute (Figure 2.1). The chute could be inclined at any angle between  $60^\circ$  and  $90^\circ$ , where  $\theta$  denotes the angle between the chute and the horizontal. Lateral spreading at the edges of the flow is minimal, negating the need for sidewalls on the chute.

To create a pseudo two-dimensional line release, the lightweight granular material was released from a linear hopper which had a semi-elliptical cross section with aspect ratio 0.9 and a length of 0.85 m. Three different-sized line release hoppers were used, to achieve release volumes ( $V_i$ ) of  $1000 \text{ cm}^3$ ,  $2100 \text{ cm}^3$  and  $3300 \text{ cm}^3$ . The origin of the  $x$ ,  $y$  and  $z$  coordinates is located in the centre of the front edge of the release hopper. The coordinates  $(x, y, z)$  are defined as shown in Figure 2.1, with the origin located at the centre of the

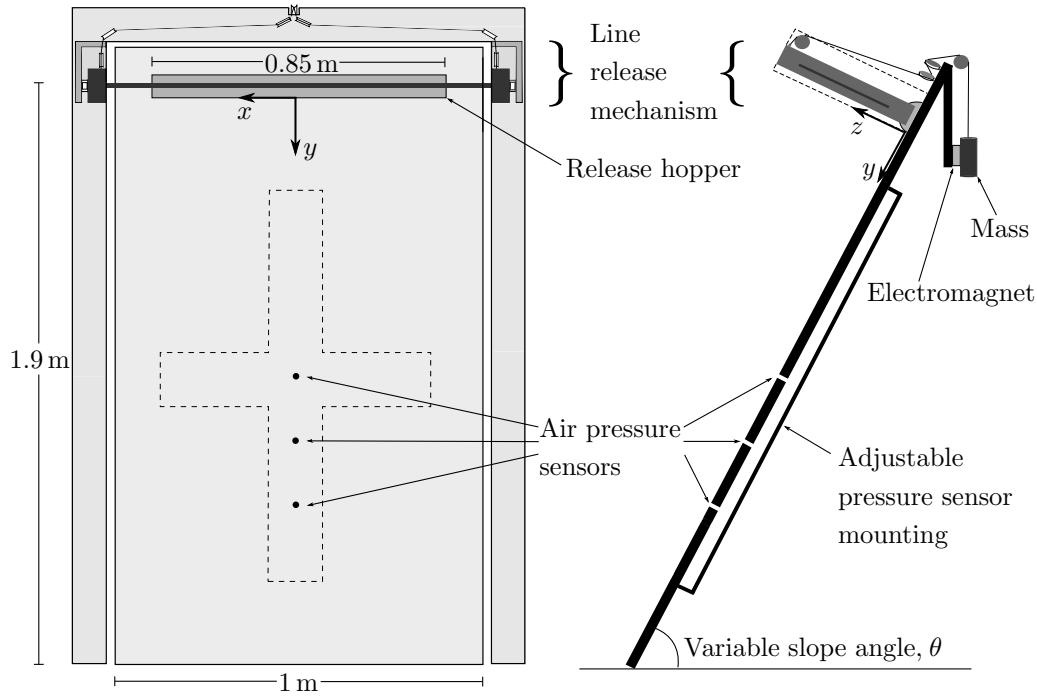


Figure 2.1: Front and side view schematic of the chute used for experiments.

front edge of the release hopper, with  $z = 0$  corresponding to the plane of the chute<sup>1</sup>.

Initially the hopper was attached to a manually operated pull-string release mechanism, which in turn was fixed to the top of the chute. However, preliminary tests showed that the operation of the mechanism caused significant vibration of the chute surface which affected the readings from the sensitive pressure sensors attached to the chute (§2.1).

To prevent vibrations being transmitted to the chute, the mechanism was redesigned. The release mechanism was removed from the chute and instead attached to a completely separate structure that surrounded the top and side edges of the chute. This meant that prior to release the only part of the mechanism that was in contact with the chute was the release hopper itself. As soon as the mechanism was operated all contact between the chute and the mechanism was broken (Figure 2.1 and Appendix C). To synchronise the initiation of the release with the data acquisition instrumentation, the manual release was replaced by an electromagnetically controlled release mechanism.

<sup>1</sup>Note the unconventional orientation of the  $x$  coordinates used is necessary in order to provide the right-handed system of coordinates required for the measurement of vorticity in Chapter 6

## 2.1. AIR PRESSURE MEASUREMENTS

---

An electromagnet was used to release a suspended mass, which provided the downward force to operate the pull-string mechanism. The power supply to the electromagnet was controlled via a data acquisition (DAQ) device, which also provided a trigger for starting data acquisition (pressure sensors and cameras). The pressure sensors (described in §2.1) were held in an adjustable mounting fixed to the underside of the chute (Figure 2.1 and Appendix C), which allowed the pressure sensors to be positioned anywhere in the  $x$ - $y$  plane of the chute.

## 2.1 Air pressure measurements

The air flow in front of and inside the flows was measured using three calibrated pressure transducers mounted in the surface of the chute (Figure 2.1). The dynamics and structure of high Reynolds number flows, such as powder snow avalanches, are determined by their interaction with the ambient air. Taking air pressure measurements allows comparison with measurements obtained from full-scale natural snow avalanches [Nishimura and Ito, 1997, Turnbull and McElwaine, 2007], medium-scale ping-pong ball experiments [McElwaine and Nishimura, 2001] and similar laboratory-scale experiments [Turnbull and McElwaine, 2008]. The pressure sensors used were Validyne DP 103 differential pressure transducers with a range of 0 to 35 Pa. Similar to the experiments conducted by McElwaine and Nishimura [2001], the sampling frequency of the sensors was set at 1 kHz. Given the mean velocity of the flows,  $u \approx 2 \text{ m s}^{-1}$ , both the range and sampling rate of the pressure sensors are high enough to adequately capture the flow features including any turbulent fluctuations ( $\approx 10u$  [Turnbull and McElwaine, 2008]).

To maximize the frequency response each of the sensors was connected to the chute using a very short tube ( $\approx 40 \text{ mm}$ ) with resonant frequency approximately 2 kHz, which is significantly higher than the frequency of any features of the flow that we might expect to observe. The pressure sensors were connected to the same DAQ device as the electromagnet that controls the release mechanism, allowing acquisition of data from the pressure sensors to be synchronised with the release of the EPS beads.

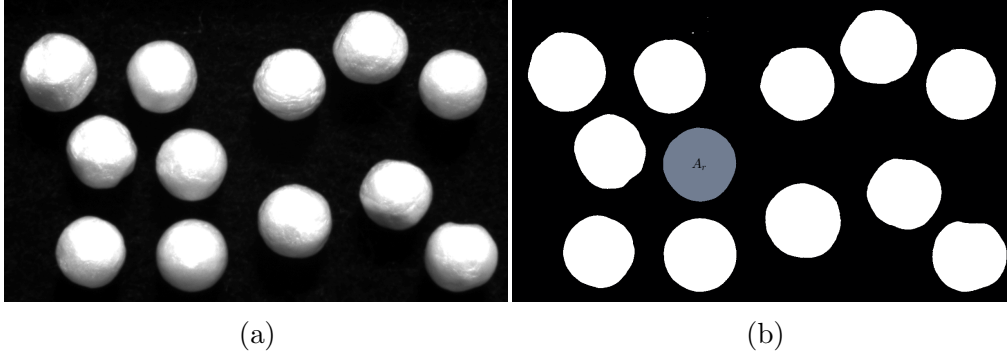


Figure 2.2: (a) An example of one of the images used to measure mean equivalent diameter of EPS beads. (b) Binary version of the image shown in Figure 2.2(a), with one of the identified regions used to calculate  $A_r$  highlighted.

## 2.2 EPS bead properties and processing

The lightweight granular material used in this study is expanded-polystyrene (EPS) bead which has been shown [Turnbull and McElwaine, 2008] to provide a good model for powder-snow avalanches by matching important similarity criteria such as: Richardson number, Reynolds number, Stokes number and particle Reynolds number. The bulk density of the EPS bead is  $\rho_p \approx 20 \text{ kg m}^{-3}$ , with a relative density  $\rho_p/\rho_a \approx 17$ , where  $\rho_a = 1.20 \text{ kg m}^{-3}$  denotes air density (at  $20^\circ\text{C}$  and 1 atm) and is here assumed throughout to be a constant. The relative density of the EPS beads, while lower than that of powder snow (typically  $\approx 30\text{--}100$ ), is still non-Boussinesq and means that the relatively high level of momentum carried by the snow particles in a powder-snow avalanche is well modelled.

To minimise the effects of polydispersity (§1.4.3) the EPS beads were sieved into narrow size-ranges. To accurately measure the average diameter of the beads in each size range, a digital camera was used to take close-up images of several ( $\approx 10$ ) beads at a time (Figure 2.2). The images were then converted to binary images and a flood-fill based algorithm was used to identify regions of connected components that represent the EPS beads. The equivalent diameter,  $d_e$ , of each bead is then calculated using  $d_e = \sqrt{4A_r/\pi}$ , where  $A_r$  is the area of each identified region. This method was chosen over measuring the diameters directly because the beads were not always perfectly spherical (average eccentricity of beads in images =  $0.25 \pm 0.09$ ). The mean equivalent diameter was then calculated for each size range and used as the value for EPS bead diameter,  $d_p$ . Figure 2.3 shows the size distribution of equivalent

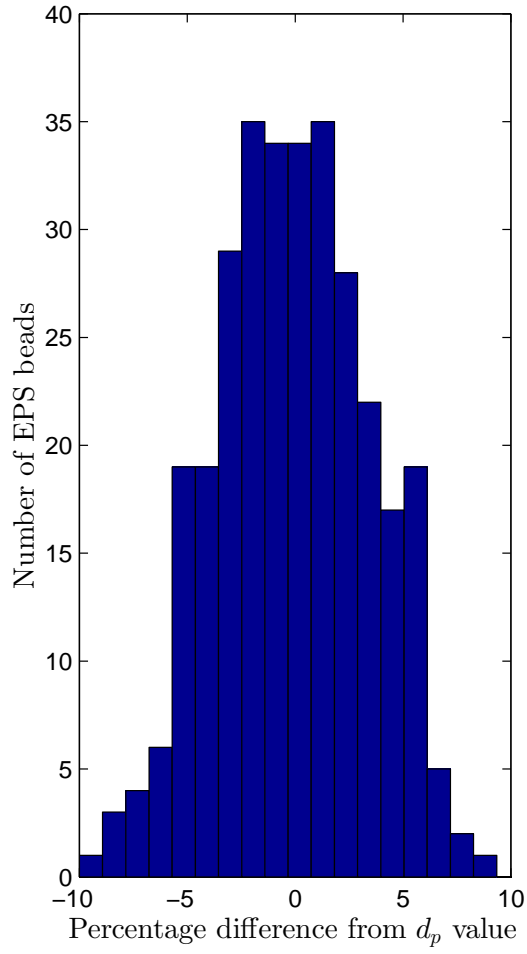


Figure 2.3: Size distribution of equivalent diameter,  $d_e$ , values.  $d_e$  values are presented as the percentage difference from the mean value,  $d_p$ , for the corresponding size range.

## 2.2. EPS BEAD PROPERTIES AND PROCESSING

Diameter <sup>a</sup> $d_p$ (mm)	Bulk density $\rho_p$ (kg m <sup>-3</sup> )	Particle Reynolds no. <sup>a,b</sup> $Re_p$	Settling velocity <sup>a,c</sup> $v_t$ (m s <sup>-1</sup> )
$1.3 \pm 0.05$	22	$175 \pm 15$	$0.5 \pm 0.05$
$1.5 \pm 0.06$	22	$200 \pm 17$	$0.6 \pm 0.06$
$1.8 \pm 0.09$	21	$225 \pm 22$	$0.7 \pm 0.07$
$2.1 \pm 0.07$	21	$250 \pm 24$	$0.7 \pm 0.07$
$2.5 \pm 0.09$	20	$325 \pm 28$	$0.8 \pm 0.07$
$2.7 \pm 0.08$	19	$325 \pm 29$	$0.8 \pm 0.09$
$5.0 \pm 0.13$	11	$525 \pm 51$	$1.1 \pm 0.08$
$6.8 \pm 0.20$	10	$750 \pm 72$	$1.1 \pm 0.09$

<sup>a</sup>Mean value  $\pm 1$  standard deviation

<sup>b</sup>The value of velocity  $u$  used to calculate  $Re_p$  is the average steady state front velocity measured in the reported experiments for flows consisting of EPS beads of the corresponding size.

<sup>c</sup>Settling velocity is measured as the average steady state velocity reached by an individual EPS bead at a slope angle of  $\theta = 90^\circ$ .

Table 2.1: Properties of EPS beads used in the experiments.

diameters, where each value of  $d_e$  is presented in terms of its percentage difference from  $d_p$  for the size range it is taken from. Eight different sizes of particles were used in the experiments, the properties of which are shown in Table 2.1. The particle Reynolds number (Equation 1.1) determines whether the drag acting on the particle is dominated by viscous or pressure forces. Particle Reynolds numbers for powder snow avalanches are typically of the order  $Re_p = 3 \times 10^3$  [Turnbull et al., 2007] and the drag force exerted on the snow particles from the ambient fluid will largely be due to the form drag of the particles. For values  $500 < Re_p < 10^5$  the drag coefficient for a spherical particle is essentially independent of the particle Reynolds number [Massey, 2006]. Typical values of  $Re_p$  for the EPS beads used in the experiments reported are shown in Table 2.1, and lie on the lower boundary of this range, but correspond to the case where the pressure forces are dominant compared to the viscous forces. The dynamic viscosity,  $\mu$ , of the ambient fluid, taken to be  $\mu = 1.81 \times 10^{-5} \text{ kg s}^{-1} \text{ m}^{-1}$  (air at 20° C and 1 atm of pressure) for these calculations and throughout the remainder of this work.

### 2.2.1 Angle of repose

The angle of repose,  $\theta_r$ , gives an indication of the friction forces between individual particles. These forces are likely to be more significant where the



## 2.2. EPS BEAD PROPERTIES AND PROCESSING

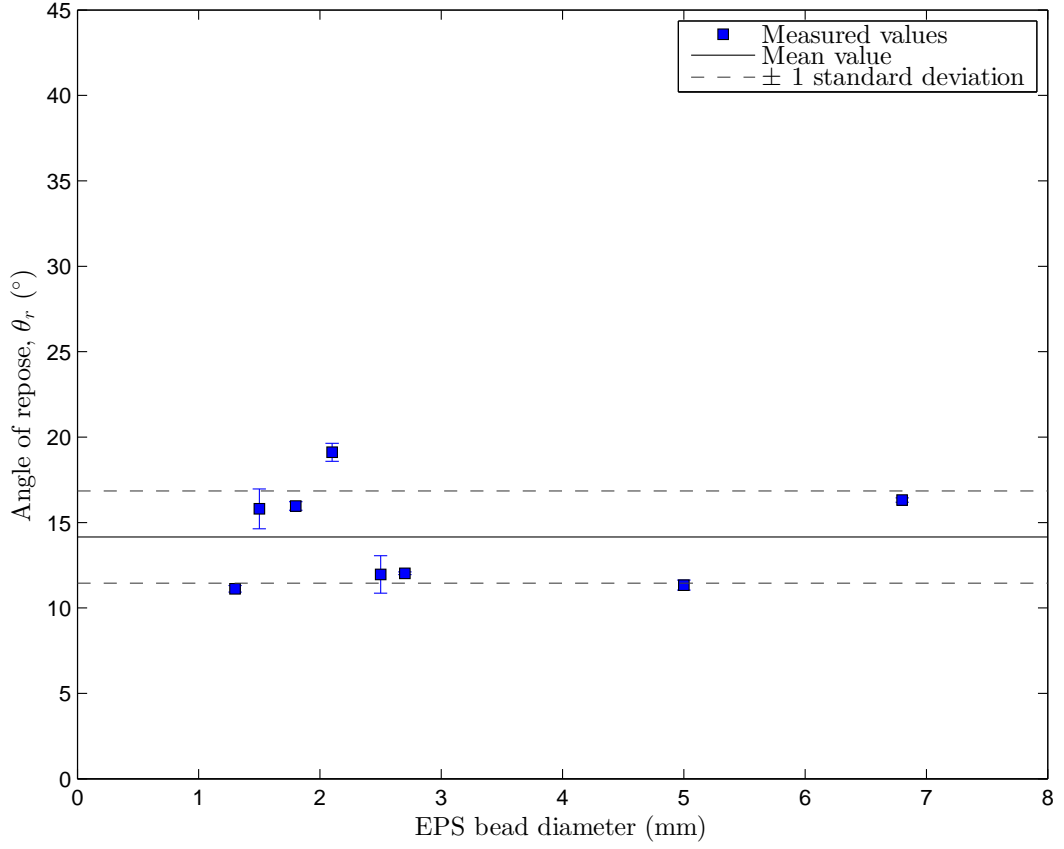


Figure 2.4: Angle of repose versus EPS bead diameter. Markers represent the mean of the measured values for each EPS bead size, with error bar length equal to  $\pm 1$  standard deviation. The solid line represents the mean of all measured values across all EPS bead sizes with dashed lines at  $\pm 1$  standard deviation.

flow is relatively dense, such as during the early stages after release when the flow is still unsuspended and at the base of fully developed flows.

The angle of repose was measured by carefully pouring a fixed volume ( $\approx 100 \text{ cm}^3$ ) of each size of EPS bead into a conical pile on a level surface. A side-on image of the pile was then taken using a digital camera and the slope of the pile was measured from the image. This process was then repeated several times and mean values were calculated for each EPS bead size. The mean of all values of  $\theta_r$  across all EPS bead sizes was also calculated.

There was little variation in angle of repose for the different EPS bead sizes (Figure 2.4) and the average value for all EPS bead sizes is relatively low when compared with other granular materials (dry sand  $\approx 35^\circ$ , gravel  $\approx 40^\circ$ ). This

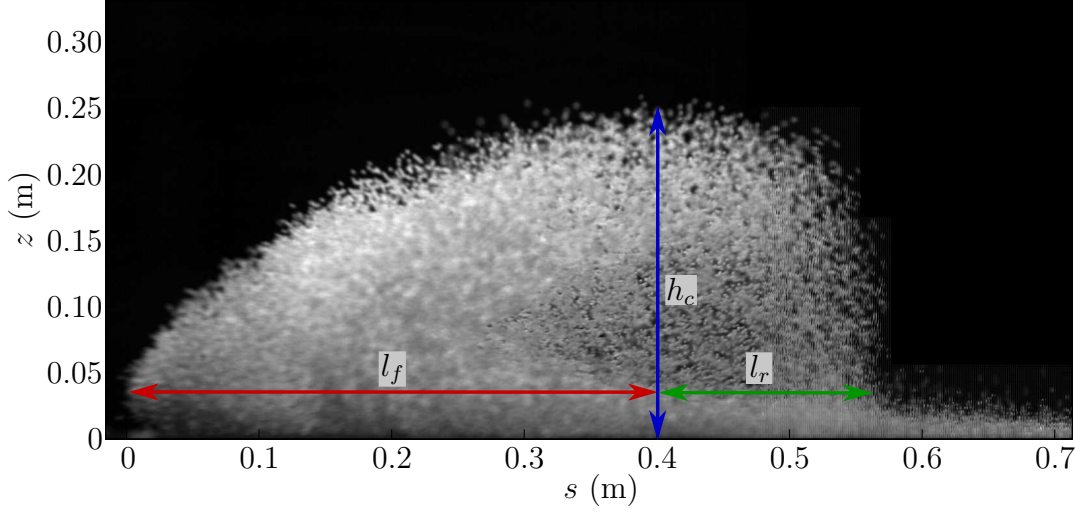


Figure 2.5: Side-on image of an EPS bead gravity current taken from an experiment conducted using  $V_i = 3300 \text{ cm}^3$  of 2.7 mm diameter EPS beads on a slope of angle,  $\theta = 65^\circ$ .  $s$  is the distance into the current from the nose, where at the foremost point of the nose,  $s = 0$ .  $h_c$  is the height of the current,  $l_f$  is the distance from where current height is maximum to the nose of the current and  $l_r$  is the distance from where current height is maximum to the rear of the current.

suggests that friction forces between individual particles are unaffected by the size of the EPS beads used here and will be insignificant even at times and locations where the flow is relatively dense.

### 2.2.2 Suspension and entrainment

By using steep slope angles the values of Richardson number (Equation 1.2) in our experiments ( $\text{Ri} \approx 2$ ) were comparable to those observed in full-scale powder-snow avalanches ( $\text{Ri} \approx 1$ ). The head of a powder snow avalanche is often modelled as being semi-elliptical in cross section, the aspect ratio of which is dependant on slope angle  $\theta$  [Batchelor, 1967, Beghin and Brugnol, 1983, Turnbull et al., 2007]. Fully suspended ( $\theta \approx 80^\circ$ ) laboratory scale snow-air currents, have been shown to have heads that are approximately semi-circular (aspect ratio = 1) in cross section [Turnbull and McElwaine, 2010].

Whilst the heads formed in the EPS-air currents used in this work (Figure 2.5) are not semi-circular or semi-elliptical ( $h_c \neq l_f \neq l_r$ ), the cross sectional area of the head is approximately equal to that of a semi-circle of radius  $h_c$  as  $l_f + l_r \approx 2h_c$  for all values of slope angle used. Therefore in order to calculate

## 2.2. EPS BEAD PROPERTIES AND PROCESSING

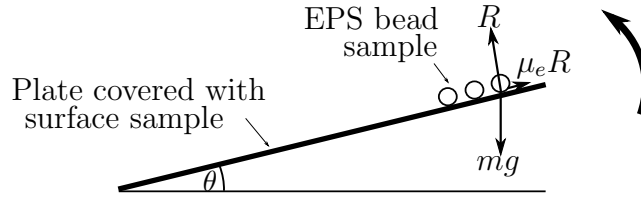


Figure 2.6: Schematic diagram of process used to measure effective coefficient of friction,  $\mu_e$ .

$\rho$ , the head of the current is assumed to be semi-circular in cross section, with radius equal to the current head height,  $h_c$ . The volume of the current can then be approximated as  $V_c = (\pi b h_c^2)/2$  where  $b$  is the width of the release hopper. In Figure 2.5 it can also be seen that some of the EPS beads are detrained from the rear of the head. Qualitatively the amount of material detrained from the rear was observed to be relatively small, and is difficult to accurately quantify as the current progresses down the chute. Therefore, for the purpose of calculating  $\rho$  it is also assumed that all of the EPS beads released are contained within the current head, meaning that the proportion of  $V_c$  made up of EPS beads will be equal to  $V_i$ . The proportion of  $V_c$  that is made up of entrained air is then obtained by subtracting the initial release volume,  $V_i$  from  $V_c$ . The density of the current is then calculated as  $\rho = [(1 - V)\rho_a + V\rho_p]$ , where  $V = V_i/V_c$ .

### 2.2.3 Chute surface roughness

Friction between a current and the surface that it flows over has been shown to play an important role in both the classic lobe-and-cleft (§1.4.1) and polydispersity (§1.4.3) instability mechanisms. Therefore in order to investigate the effects of surface friction on the flows modelled in this study, three different surface coverings were prepared for the chute. One of the surface coverings consisted of a felt cloth, providing a relatively smooth surface for the chute. The other two surface coverings consisted of a layer of painted EPS beads adhered to the surface with diameter 2.7 mm or 5.0 mm.

Due to the approximately spherical shape of the EPS beads, the coefficient of friction between the beads and the surfaces will be dependent on a combination of both the rolling resistance of the beads and the static or kinetic friction force [Hibbeler, 2007]. To reflect this, the friction coefficient between

## 2.2. EPS BEAD PROPERTIES AND PROCESSING

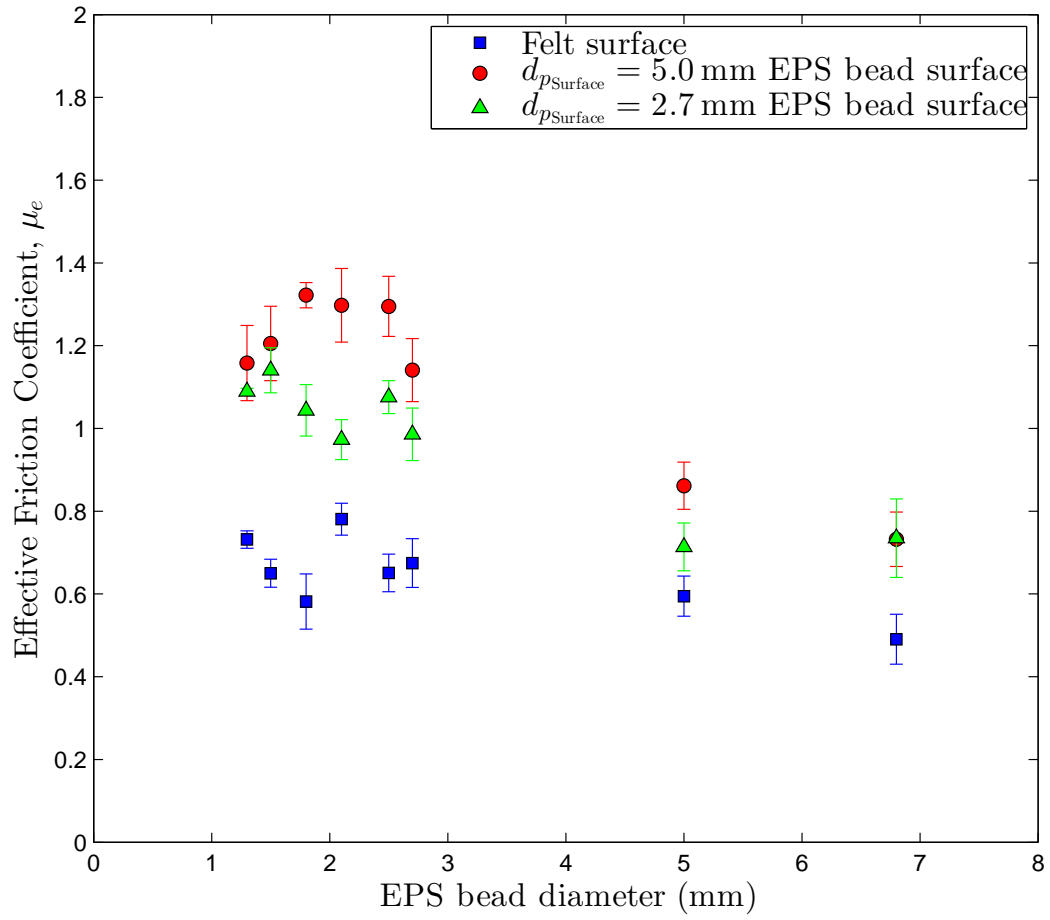


Figure 2.7: Effective friction coefficient versus EPS bead diameter for the different chute surface coverings used. Error bars have length equal to  $\pm 1$  standard deviation from the mean.

## 2.2. EPS BEAD PROPERTIES AND PROCESSING

---

the beads and the surfaces will henceforth be referred to as the effective friction coefficient,  $\mu_e$ . The effective friction coefficient for each size of the EPS beads and each surface was calculated by covering a plate with the surface material and then placing a sample ( $\approx 10$ ) of the EPS bead on the surface at one end of the plate (Figure 2.6). The other end of the plate was hinged to allow it to be tilted at an angle,  $\theta$ , to the horizontal. Using a digital camera, recordings were made of the plate being slowly tilted until the EPS beads started to move down the plate. The frame at which the EPS beads started to move was captured. The critical angle,  $\theta_c$ , between the inclined plate and the horizontal surface was then measured from this image. The forces acting on an EPS bead (Figure 2.6) will be balanced when the slope angle  $\theta = \theta_c$ , and when resolved in the plane of, and perpendicular to the chute give:

$$\mu_e R = mg \sin \theta_c \quad (2.1)$$

and

$$R = mg \cos \theta_c \quad (2.2)$$

respectively, where  $m$  is the mass of an individual EPS bead and  $R$  is equal to the normal reaction force. Substituting equation 2.2 into equation 2.1 gives the effective friction coefficient,

$$\mu_e = \tan \theta_c. \quad (2.3)$$

This method does not take into account any contribution made to the effective friction coefficient by kinetic friction, as accurate measurement of this property is extremely difficult in this situation. Instead static friction is used, which provides a maximum value of  $\mu_e$ , as coefficient of kinetic friction is usually less than the coefficient of static friction for the same materials [Meriam and Kraige, 2002]. It is assumed that the relationship between static and kinetic friction is consistent for all EPS bead sizes and surface coverings. This method was repeated several times for each EPS bead size and surface covering, with mean results shown in Figure 2.7.

It can be seen from Figure 2.7 that the effective coefficient of friction between the EPS bead and the felt surface covering increases by approximately 15% as the diameter of the EPS beads decreases. The small and large EPS bead covered surfaces also increase the effective coefficient of friction for decreasing EPS bead diameters, with the larger bead covering causing a greater

## 2.2. EPS BEAD PROPERTIES AND PROCESSING

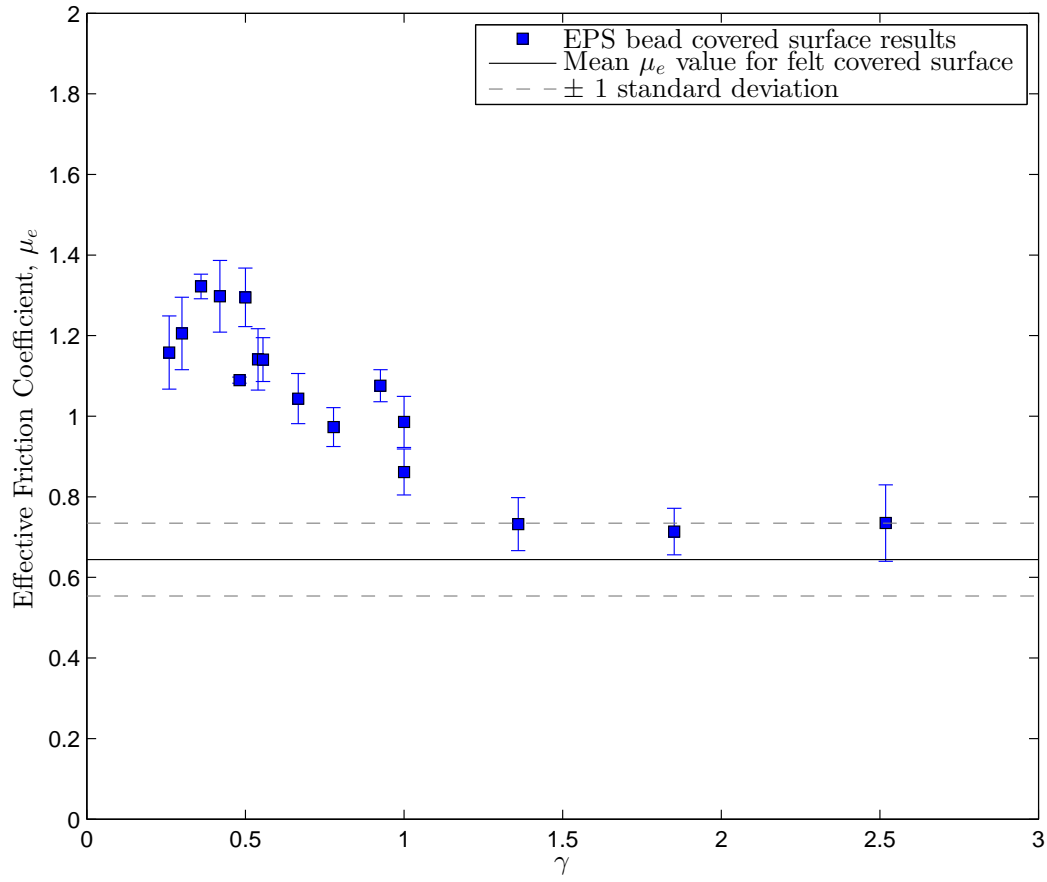


Figure 2.8: Effective friction coefficient,  $\mu_e$ , versus EPS bead diameter ratio,  $\gamma$ . Error bars have length equal to  $\pm 1$  standard deviation from the mean.

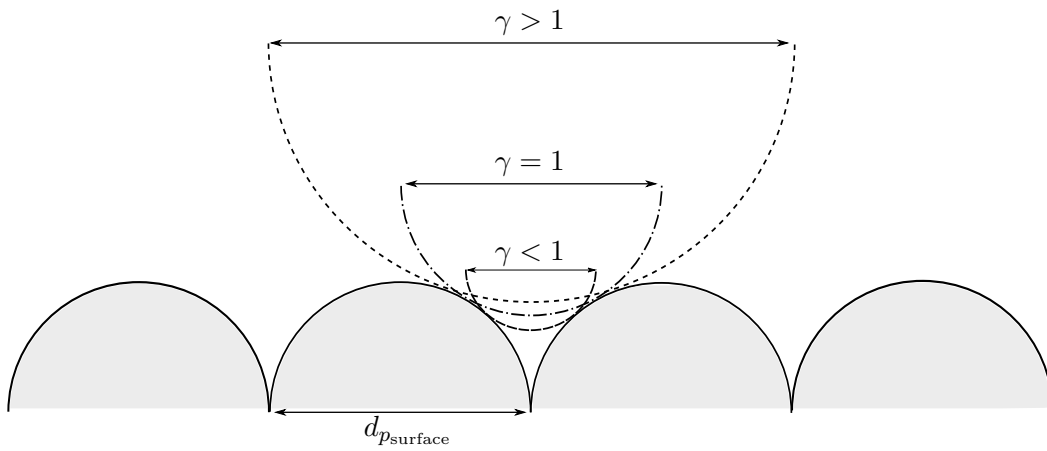


Figure 2.9: Schematic showing sample EPS beads with different values of EPS bead diameter ratio,  $\gamma$ , at rest on an EPS bead covered surface.

## 2.3. SUMMARY

---

increase. However, the factor that appears to have the most significant effect on the effective coefficient of friction is the ratio

$$\gamma = \frac{d_{p_{\text{sample}}}}{d_{p_{\text{surface}}}}, \quad (2.4)$$

where  $d_{p_{\text{sample}}}$  is the diameter of the EPS bead sample, and  $d_{p_{\text{surface}}}$  the diameter of the EPS bead attached to the surface. As can be seen in Figure 2.8, if  $\gamma \leq 1$ ,  $\mu_e$  is significantly larger than it is for the felt surface and when  $\gamma > 1$ , there is little or no effect on  $\mu_e$ . The dependance of  $\mu_e$  on  $\gamma$  is likely to be caused by the spaces between the EPS beads attached to the chute surface. As shown in Figure 2.9, when  $\gamma < 1$  the sample EPS beads lie much deeper in the gaps between the surface EPS beads and therefore require a greater slope angle in order for them to start moving.

## 2.3 Summary

The equipment and experimental procedure described in this chapter allows repeatable, laboratory scale avalanches to be created using line releases of expanded polystyrene in air. The expanded polystyrene and air currents have been shown to model powder snow avalanches well, including the transition from dense granular flow to fully suspended gravity current and the formation of lobe-and-cleft type patterns at the leading edge. These experiments enable the capture of detailed video and air pressure data, whilst also allowing key parameters, such as slope angle, surface roughness and size and volume of material released, to be varied.

## Bibliography

- G. K. Batchelor. *An Introduction to Fluid Mechanics*. Cambridge University Press, Cambridge, UK, 1967.
- P. Beghin and G. Brugnot. Contribution of theoretical and experimental results to powder-snow avalanche dynamics. *Cold Regions Science and Technology*, 8:63–73, 1983.

- R. C. Hibbeler. *Engineering Mechanics: Statics and Dynamics*. Pearson, Prentice Hall, 11th edition, 2007.
- B. S. Massey. *Mechanics Of Fluids*. Taylor & Francis, Abingdon, UK, 8th edition, 2006.
- J. N. McElwaine and K. Nishimura. *Particulate Gravity Currents*, volume 31 of *Special Publication of the International Association of Sedimentologists*, chapter Ping-pong Ball Avalanche Experiments, pages 135–148. Blackwell Science, Malden, Massachusetts, 2001.
- J. L. Meriam and L. G. Kraige. *Engineering Mechanics: Statics*, page 330. Wiley and Sons, 2002.
- K. Nishimura and Y. Ito. Velocity distribution in snow avalanches. *Journal of Geophysical Research*, 102(B12):27297–27303, 1997.
- Y. Nohguchi and H. Ozawa. On the vortex formation at the moving front of lightweight granular particles. *Physica D*, 238:20–26, 2008. doi:10.1016/j.physd.2008.08.019.
- B. Turnbull and J. N. McElwaine. A comparison of powder-snow avalanches at Vallée de la Sionne, Switzerland, with plume theories. *Journal of Glaciology*, 53(180):30–40, 2007.
- B. Turnbull and J. N. McElwaine. Experiments on the non-Boussinesq flow of self-igniting suspension currents on a steep open slope. *Journal of Geophysical Research*, 113(F01003), 2008. doi:10.1029/2007JF000753.
- B. Turnbull and J. N. McElwaine. Potential flow models of suspension current air pressure. *Annals of Glaciology*, 51(54), 2010.
- B. Turnbull, J. N. McElwaine, and C. Ancey. Kulikovskiy-Sveshnikova-Beghin model of powder snow avalanches: Development and application. *Journal of Geophysical Research*, 112(F01004), 2007. doi:10.1029/2006JF000489.



## Chapter 3

# Imaging and front tracking

In order to study the flow dynamics and the formation and evolution of the lobe-and-cleft type patterns that form at the moving front of the laboratory scale avalanches generated, the front position of the flows needs to be accurately tracked. Additionally, due to the large number of experiments conducted and the wide range of variables in this work, application of the front position detection method needs to be automated whilst still able to produce accurate results in all conditions. The methods and techniques used to achieve this are detailed in the following section.

### 3.1 Cameras

The EPS currents were observed using two IDT Nanosense high-speed digital video cameras with 1280x1024 pixel resolution and sampling at 400 Hz. One camera was positioned normal to the  $x$ - $y$  plane of the chute, capturing the plan view of the flow with the full width of the release hopper and the full length of the chute in view. The second camera was positioned to capture the side view, aligned normal to the  $y$ - $z$  plane of the chute, which allowed the head-height of the avalanche to be measured. Individual EPS beads were  $\approx 4$  pixel diameters in the plan view images and  $\approx 10$  pixels in the side view images. Both cameras were triggered by a signal sent from the DAQ device that was connected to the electro-magnetic release mechanism and pressure sensors. This allowed the cameras to be synchronised with each other and also with the release of the EPS beads and the pressure sensor acquisition. The chute surface coverings

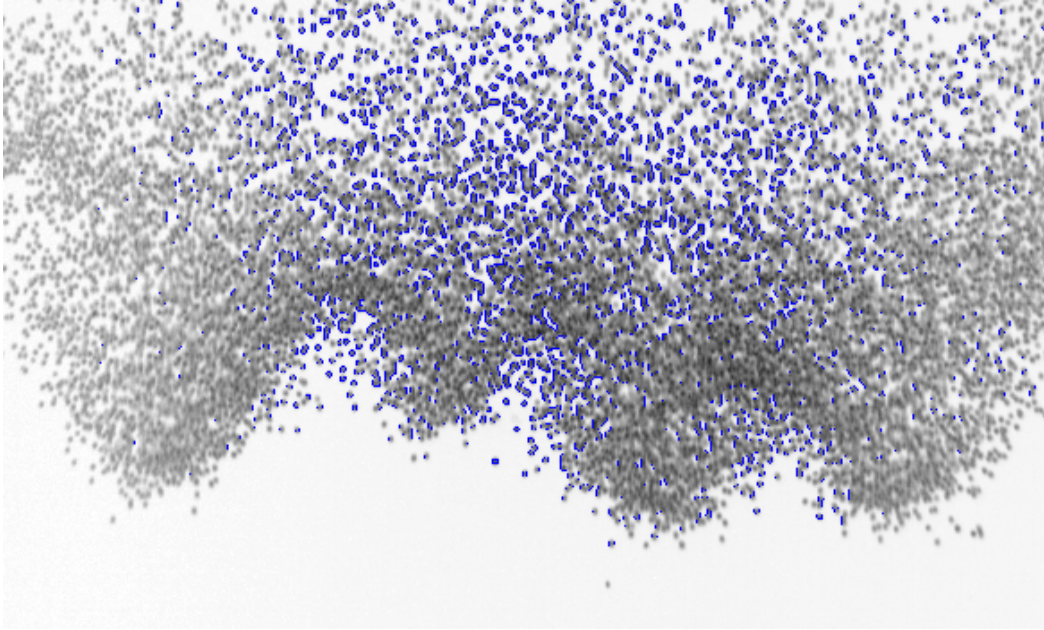


Figure 3.1: Edge detection using MATLAB’s Sobel method edge detection algorithm. Detected edges shown in blue. Prewitt, Roberts, Laplacian of Gaussian and Canny method edge detection algorithms produced similar results. Note to increase clarity of the detected edges the image intensity,  $I$ , has been inverted using  $I_{\text{invert}}(x_i, y_j) = 255 - I(x_i, y_j)$  in all images throughout this chapter.

used were matt black, to optimise contrast with the white EPS beads.

#### 3.1.1 Image pixel coordinates

The captured images consist of  $M$  rows and  $N$  columns of pixels, with the resolution of the cameras such that  $M = 1280$  and  $N = 1024$ . The position of each pixel can be described as  $(x_i, y_j)$  where  $i = 1, \dots, N$  and  $j = 1, \dots, M$ . Pixel  $(x_1, y_1)$  represents the top left-hand corner of the image, and pixel  $(x_N, y_M)$  the bottom right-hand corner. The 2-D continuous spatial signal of light intensity,  $I(x, y)$ , falling on the camera’s CCD sensor is therefore represented by  $I(x_i, y_j)$ .

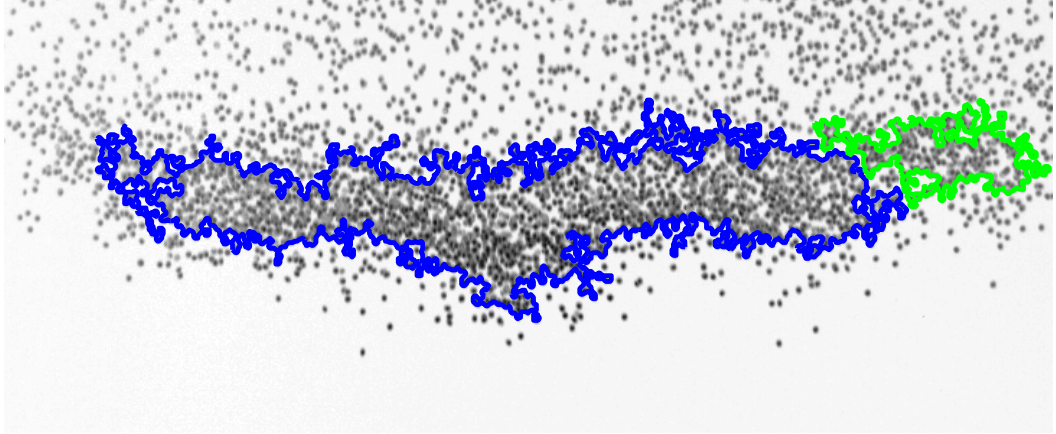


Figure 3.2: Edge detection using a Moore-Neighbor tracing algorithm.

## 3.2 Off-the-shelf edge detection functions

MATLAB's Image Processing Toolbox provides a function, *edge*, that detects colour contrasts in an image using various edge-detection algorithms. Attempts were made to use this function in order to detect the front edge of the flow in the images obtained from the experiments (Figure 3.1). However, because of their particulate composition, the front of the flow does not have a continuous edge and the algorithms used by the *edge* function detect it as a series of small unconnected sections. Groups of particles within the flow also get detected as edges by the algorithms.

In addition to the *edge* function, MATLAB's function *bwboundaries* based on a Moore-Neighbor tracing algorithm, was also applied to the images. This function first converts the grayscale image into a binary image, assigning pixels with luminance greater than a threshold value with the value 1 (white) and replaces all other pixels with the value 0 (black). It then identifies objects within the images by searching for regions of connected pixels with the value 1 and traces the exterior boundaries of these objects. This function was better able to identify the edges of the flow than the *edge* function (Figure 3.2), however the particulate make-up of the flows still caused problems with consistent detection of the whole flow front as a continuous edge. For some flows (especially those with smaller volumes) gaps between the particles result in the flow being detected as several objects rather than one object. The fact that this function also detects the rear facing boundary of the flow leads to some complication when automating front edge detection. Further analysis of

the identified boundary would need to be carried out in order to identify which sections of the boundary correspond to the front, sides and rear of the flow.

### 3.3 Front tracking using a change-point detection based algorithm

In order to accurately detect and track the front of the flows a custom-made algorithm was required. A change-point detection [Serra, 1982] based algorithm was developed to derive the front position and flow height at each time frame. This worked by analysing each vertical column of pixels in the image and identifying the location at which the pixels change from being dark (chute background) to light (EPS bead). At each time, this boundary identifies the position of the front edge of the flow. A threshold value,  $\Theta$ , needs to be set which determines whether a pixel corresponds to part of the chute or part of the flow. Accurate detection of the front edge of the flow is highly dependant on the selection of a suitable value for this threshold. Due to slight variations in illumination and contrast of the images for the different experiments conducted, selection of one universal value that could be applied to all experiments was not possible. An attempt to address this problem was made by identifying the maximum intensity,  $I_{\max}$ , in each pixel column of the image's pixel matrix. The threshold for each column was then set as a fixed percentage of the maximum intensity value for that column. However, inconsistencies in the ability to accurately detect the position of the front edge of the flow using a fixed percentage threshold were observed. These inconsistencies occurred both when comparing edge detection at different times within an individual experiment and also between experiments where the volume of EPS bead released was changed.

The maximum intensity is found where the depth of the current is greatest, at approximately the centreline of the current. This centreline intensity increases if the release volume is increased due to the flows being deeper and containing more EPS beads. While using a percentage of the maximum intensity value accounts for this increase, what is not accounted for by this method is the rate at which the intensity decreases as you move from the centre of the flow towards the front edge.

### 3.3. FRONT TRACKING – CHANGE-POINT DETECTION

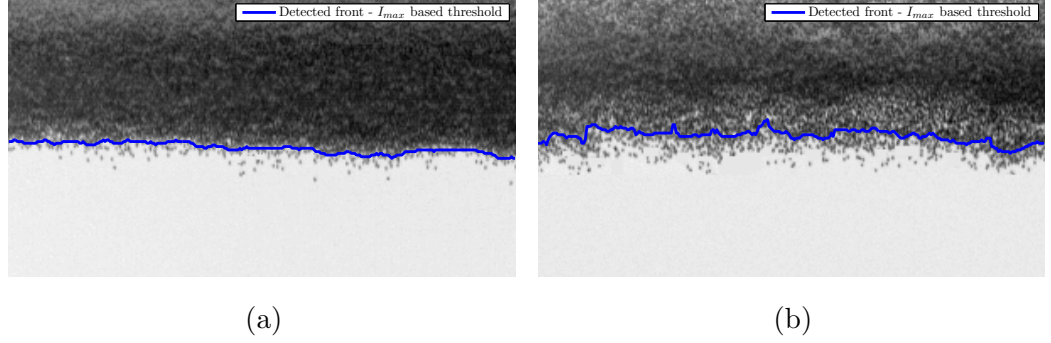


Figure 3.3: Comparison of front edges detected for currents consisting of (a)  $1000 \text{ cm}^3$  and (b)  $3300 \text{ cm}^3$  of  $2.1 \text{ mm}$  diameter EPS bead on a  $65^\circ$  slope and  $t = 0.3 \text{ s}$ , thresholded using  $I_{\max}$ -based method,  $\Theta = 0.5I_{\max}$ . Note the front edges shown in these figures and the remainder of figures shown in this chapter have had the profile smoothing algorithm described in §3.5 applied to them.

For flows containing a large volume of EPS beads the intensity steeply decreases as you move towards the front edge, whereas for flows containing a smaller volume of EPS bead the rate of decrease in intensity is much less. The results of applying the same fixed percentage threshold to flows of differing release volume are shown in Figure 3.3. It can be seen that when applied to the larger volume flow (Figure 3.3(a)) the value selected for the percentage threshold is suitable and the edge is accurately detected. However when the same threshold is applied to the flow with smaller volume (Figure 3.3(b)), the detected edge is actually slightly behind the edge of the flow.

As a current progresses down the chute its length in the  $y$ -direction increases, this also has the effect of changing the rate at which intensity decreases as you move from the centre to the front edge. Figure 3.4 shows the results of applying the same fixed percentage threshold to a current soon after release (Figure 3.4(a)) and at a later stage in its motion down the chute (Figure 3.4(b)). Whilst the selected value gives good results for the early stages, as it progresses down the chute a larger amount of the EPS beads appear below (larger  $y_j$ -value) the detected front edge. Some of these are part of the current and not stray EPS beads moving in front of it and therefore the true position of the front edge is under-detected.

Due to the small number of different release volumes used in these experiments, it would be relatively straightforward to overcome the inconsistencies caused by the differing volumes by simply using a volume dependant percent-

### 3.3. FRONT TRACKING – CHANGE-POINT DETECTION

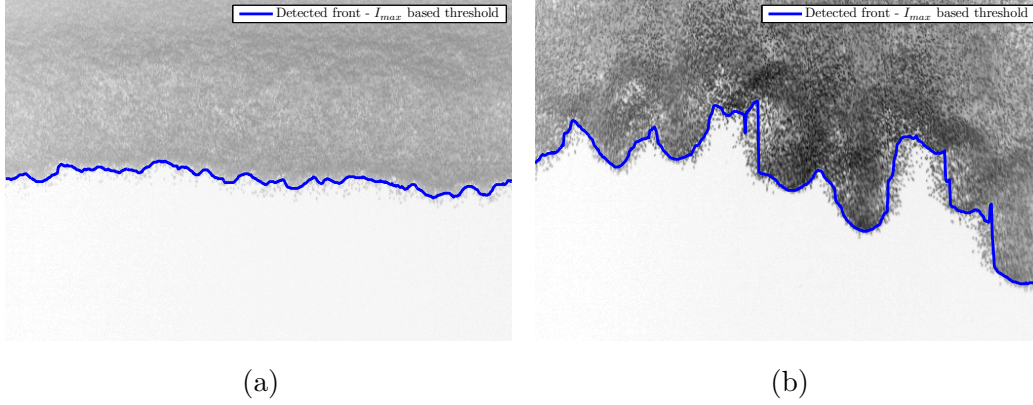


Figure 3.4: Comparison of fronts detected at (a)  $t = 0.4$  s and (b)  $t = 0.9$  s for a current consisting of  $3300 \text{ cm}^3$  of 2.1 mm diameter EPS bead on a  $80^\circ$  slope, thresholded using  $I_{\max}$ -based method,  $\Theta = 0.6I_{\max}$ .

age threshold value. However the inconsistencies caused by the  $y$ -directional lengthening of the currents are much harder to overcome as the amount and rate of lengthening is highly variable and is affected by a combination of variables such as: slope angle, release volume, surface roughness and EPS diameter. Therefore this method is unsuitable for large numbers of experiments as accurate detection of the front edge would require manual adjustment of the percentage value for different experiments.

To address the shortcomings of the previous technique, a nonparametric and fully automated method of threshold selection based on the variance of intensity values of an individual image was sought. To do this the histogram of image intensity is used in order to identify two distinct modes - one for the EPS beads and one for the chute surface. The simplest method of achieving this would be to find the local maxima on the histogram that correspond to each of the modes, then find the minima between them and set the threshold equal to the value of intensity at this location. There are however two problems with this approach. Firstly, the histogram may be noisy, thus causing many local minima and maxima. Secondly, the sum of two separate distributions, each with their own mode, may not produce a distribution with two distinct modes (i.e a unimodal distribution). A typical image taken during one of the experiments in this study and its intensity histogram are shown in Figure 3.5, and it can be seen that the histogram is both unimodal and noisy.

Difficulties with thresholding occur because the image consists of two groups



### 3.3. FRONT TRACKING – CHANGE-POINT DETECTION

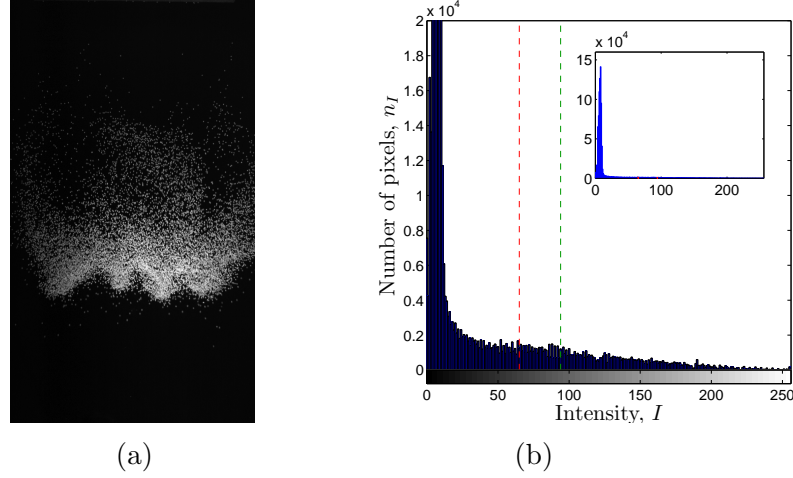


Figure 3.5: (a) Typical image taken from an experiment and (b) its corresponding intensity level histogram. (b) Insert: Intensity level histogram with full range y-axis. (b) Main plot: Intensity level histogram with reduced y-axis for clarity, dashed lines indicate threshold intensity levels identified by both clustering [Otsu, 1979] ( $\Theta = 65$ ) and  $I_{\max}$  ( $\Theta = 0.5 I_{\max} = 94$ ) based methods. Note for the purpose of this illustration the value of  $\Theta = 0.5 I_{\max}$  presented is the mean value of  $I_{\max}$  taken across all values of  $x_i$ .

of pixels with different, but often overlapping, ranges. The aim is to minimise the error of classifying a chute surface pixel as an EPS bead pixel or vice versa. This can be achieved by minimising the area under the histogram for one region that lies on the other region's side of the threshold. However, only the histogram for the combined regions is available and not the histograms for each region. If the values in the two regions are considered as two clusters, the threshold can be set so as to try and make each cluster as tight as possible, thus minimizing their overlap. The following method, developed by Otsu [1979] was used to achieve this.

#### 3.3.1 Threshold selection method

Let the pixels of a image taken from an experiment be represented in  $I_\tau$  intensity levels  $[1, 2, \dots, I_\tau]$ . The number of pixels at level  $I$  is denoted by  $n_I$  and the total number of pixels by  $N_\tau = n_1 + n_2 + \dots + n_{I_\tau}$ . For simplification, the intensity level histogram is normalised and regarded as a probability

### 3.3. FRONT TRACKING – CHANGE-POINT DETECTION

distribution,

$$\mathcal{P}_I = \frac{n_I}{N_\tau}, \quad \mathcal{P}_I \geq 0, \quad \sum_{I=1}^{I_\tau} \mathcal{P}_I = 1. \quad (3.1)$$

The pixels are next dichotomised into two classes  $C_s$  and  $C_c$  (representing chute surface and current respectively) by a threshold at level  $\Theta$ ;  $C_s$  denotes pixels with levels  $[1, \dots, \Theta]$ , and  $C_c$  denotes pixels with levels  $[\Theta + 1, \dots, I_\tau]$ . Then the probabilities of class occurrence and the class mean levels, respectively, are given by

$$\omega_s = \Pr(C_s) = \sum_{I=1}^{\Theta} \mathcal{P}_I = \omega(\Theta) \quad (3.2)$$

$$\omega_c = \Pr(C_c) = \sum_{I=\Theta+1}^{I_\tau} \mathcal{P}_I = 1 - \omega(\Theta) \quad (3.3)$$

and

$$\bar{I}_s = \sum_{I=1}^{\Theta} I \Pr(I | C_s) = \sum_{I=1}^{\Theta} \frac{I \mathcal{P}_I}{\omega_s} = \frac{\bar{I}(\Theta)}{\omega\Theta} \quad (3.4)$$

$$\bar{I}_c = \sum_{I=\Theta+1}^{I_\tau} I \Pr(I | C_c) = \sum_{I=\Theta+1}^{I_\tau} \frac{I \mathcal{P}_I}{\omega_c} = \frac{\bar{I}_\tau - \bar{I}(\Theta)}{1 - \omega\Theta}, \quad (3.5)$$

where

$$\omega(\Theta) = \sum_{I=1}^{\Theta} \mathcal{P}_I \quad (3.6)$$

and

$$\bar{I}(\Theta) = \sum_{I=1}^{\Theta} I \mathcal{P}_I \quad (3.7)$$

are the zeroth- and the first-order cumulative moments of the histogram up to the  $\Theta$ th level, respectively, and

$$\bar{I}_\tau = \sum_{I=1}^{I_\tau} I \mathcal{P}_I \quad (3.8)$$

is the total mean level of the original image. The following relation can be verified for any choice of  $\Theta$ :

$$\omega_s \bar{I}_s + \omega_c \bar{I}_c = \bar{I}_\tau, \quad \omega_s + \omega_c = 1. \quad (3.9)$$



### 3.3. FRONT TRACKING – CHANGE-POINT DETECTION

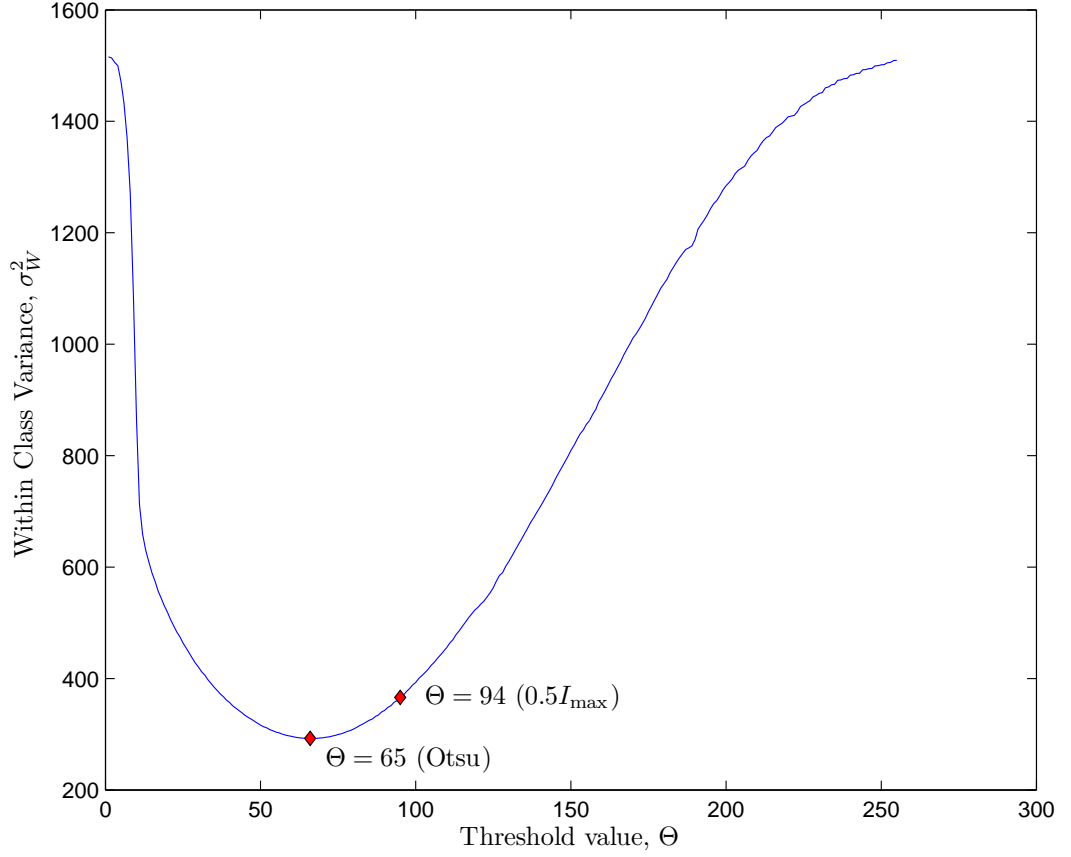


Figure 3.6: Within class variance,  $\sigma_W^2$ , versus threshold value,  $\Theta$ , for the histogram shown in Figure 3.5(b). Results of clustering [Otsu, 1979] and  $I_{\max}$  based methods are marked,  $\diamond$ .

The class variances are given by

$$\sigma_s^2 = \sum_{I=1}^{\Theta} (I - \bar{I}_s)^2 \Pr(I | C_s) = \sum_{I=1}^{\Theta} \frac{(I - \bar{I}_s)^2 \mathcal{P}_I}{\omega_s} \quad (3.10)$$

$$\sigma_c^2 = \sum_{I=\Theta+1}^{I_\tau} (I - \bar{I}_c)^2 \Pr(I | C_c) = \sum_{I=\Theta+1}^{I_\tau} \frac{(I - \bar{I}_c)^2 \mathcal{P}_I}{\omega_c}. \quad (3.11)$$

Which can then be used to calculate the within-class variance

$$\sigma_W^2 = \omega_s \sigma_s^2 + \omega_c \sigma_c^2. \quad (3.12)$$

Within class variance is the measure of the spread of the values within the two classes created by the threshold. Therefore by minimising within class variance, any overlap between the two classes is also minimised, thus reducing

### 3.3. FRONT TRACKING – CHANGE-POINT DETECTION

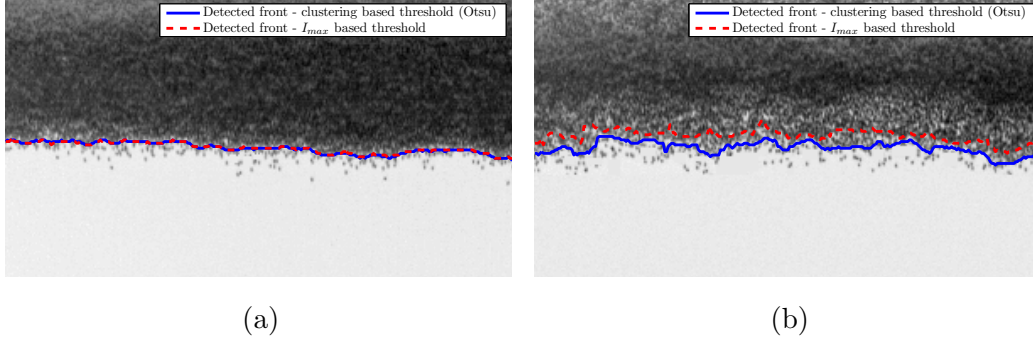


Figure 3.7: Comparison of fronts detected for currents consisting of (a) 1000 cm<sup>3</sup> and (b) 3300 cm<sup>3</sup> of 2.1 mm diameter EPS bead on a 65° slope, thresholded using clustering [Otsu, 1979] and  $I_{max}$ -based methods.

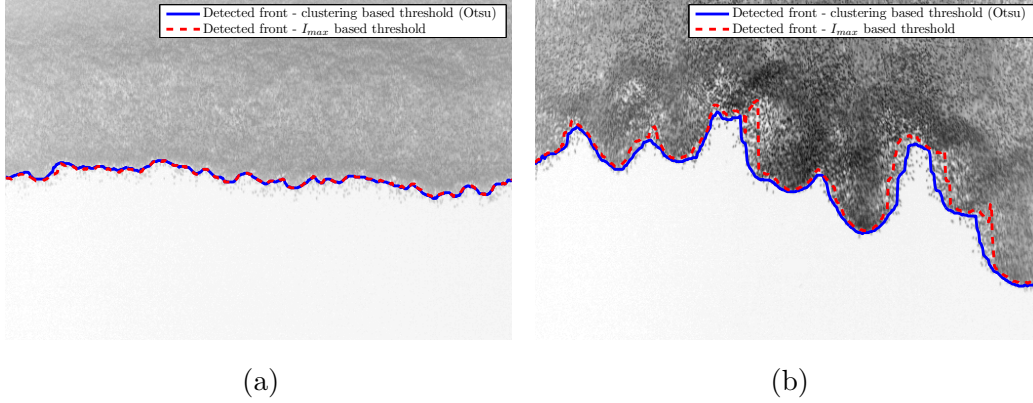


Figure 3.8: Comparison of fronts detected at (a)  $t = 0.4$  s and (b)  $t = 0.9$  s for a current consisting of 3300 cm<sup>3</sup> of 2.1 mm diameter EPS bead on a 80° slope, thresholded using clustering [Otsu, 1979] and  $I_{max}$ -based methods.

the chances of a surface pixel being identified as a current pixel or vice versa. The method used iterates through all possible threshold values and identifies the threshold value where the within class variance is minimised. Using data taken from the histogram (Figure 3.5), within-class variance,  $\sigma_W^2$ , is plotted against threshold value,  $\Theta$ , in Figure 3.6, where it can be seen that  $\sigma_W^2$  is minimised when  $\Theta = 65$ .

When applied to images from different experiments this thresholding algorithm was found to be consistently accurate in detecting the true position of the front edge of the currents, regardless of release volume,  $V_i$ , or time after release,  $t$  (examples of which are shown in Figures 3.7 & 3.8).

### 3.4. FRONT TRACKING – LEVEL SET METHOD

---

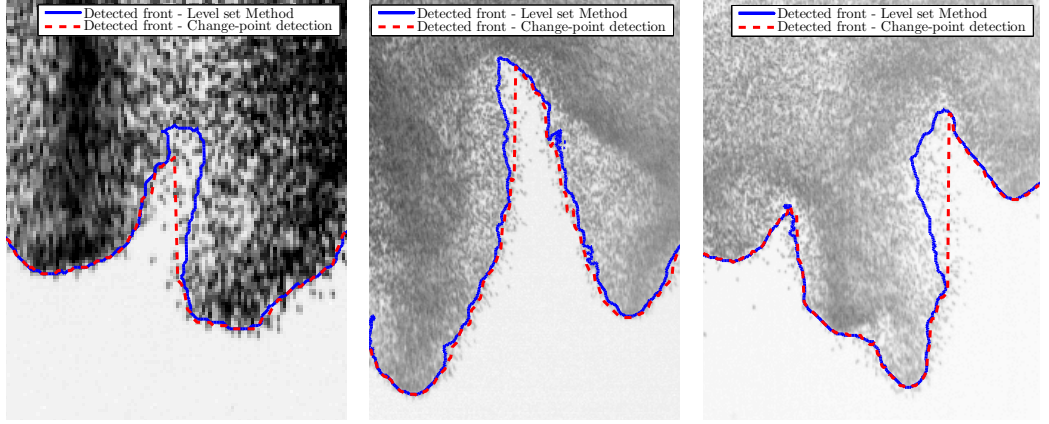


Figure 3.9: Comparisons of change-point and level set methods detecting deep clefts.

### 3.4 Level set method for front tracking

Whilst appropriate threshold selection greatly improved the performance of the front tracking method, it was found that this method was unable to accurately detect deep clefts that are not aligned with the vertical columns of pixels that make up the image. The limitation of the method is that for each column of pixels ( $x_i$ ) it only detects the first point at which the threshold is exceeded, i.e. for a given value of  $x_i$  it is only possible to have one value of  $y_j$ . If further up (lower values of  $y_j$ ) the column the intensity values drop below, then rise above the threshold value again, this is not detected as part of the front edge. The effects of this can be seen in Figure 3.9 in the form of relatively large, almost vertical sections of front edge profile, where small changes in  $x_i$  are accompanied by a large change in  $y_j$  ( $\Delta y_j \gg \Delta x_i$ ).

To overcome this limitation a level-set method [McElwaine et al., 2004] was instead used to track the front edge of the flow. For each sequence of images the arrival time  $T_{ij} = T(x_i, y_j)$  of the front edge of the flow is detected for each pixel. The same change-point technique used in the previous method is used to detect the arrival of the front edge of the flow, but is applied on a pixel by pixel basis rather than to each vertical column of pixels. The matrix  $T_{ij}$  of first arrival times is classified as a level set, with the contours  $T_{ij} = t$  corresponding to the front edge of the flow at a particular time,  $t$ . This technique was applied to both the plan view and side view images, typical results of which are shown in Figure 3.10. As shown in Figure 3.9, this technique is much better suited to

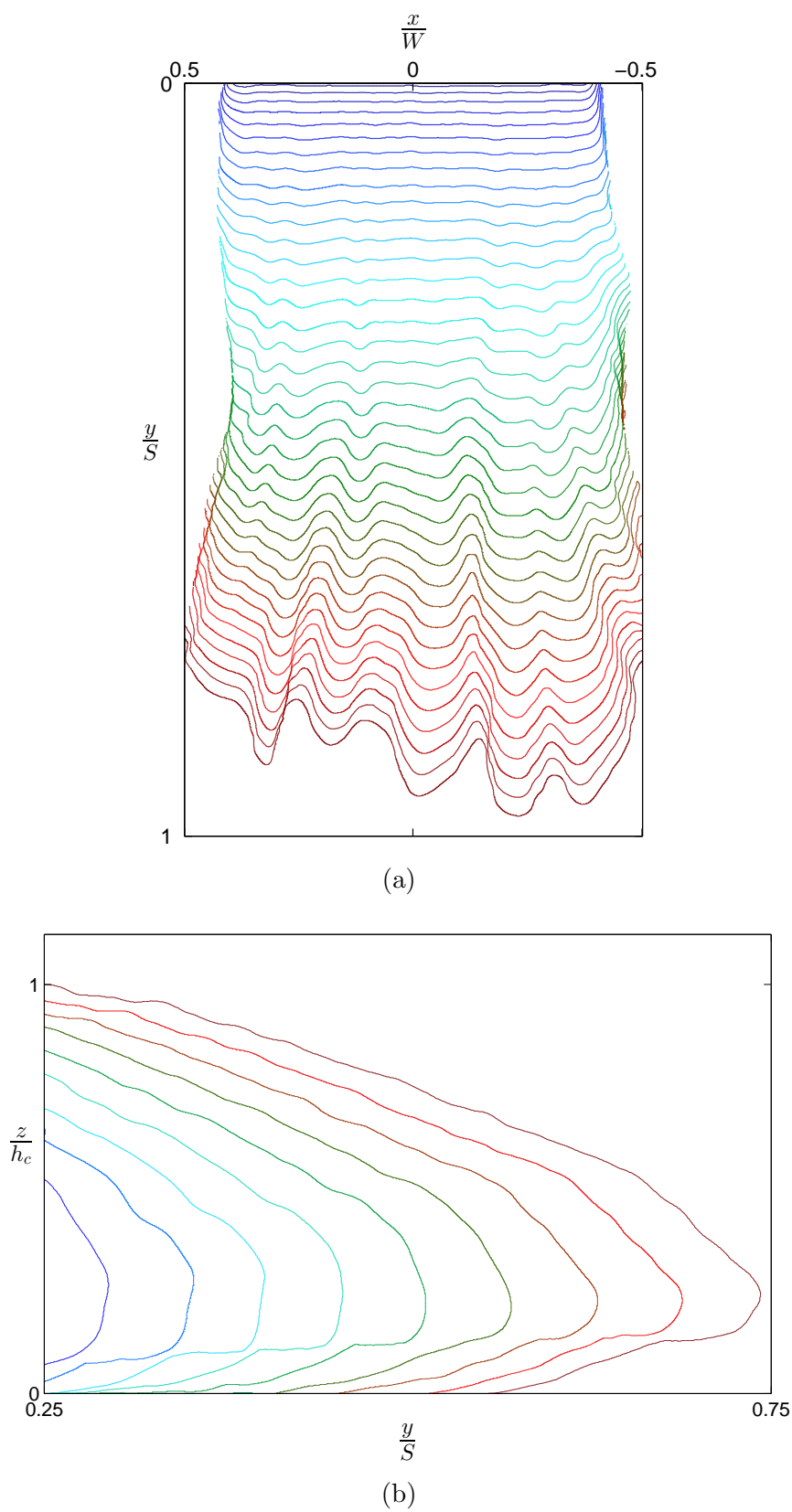


Figure 3.10: (a) Front and (b) side contours produced using level set method.

### 3.5. PROFILE SMOOTHING

---

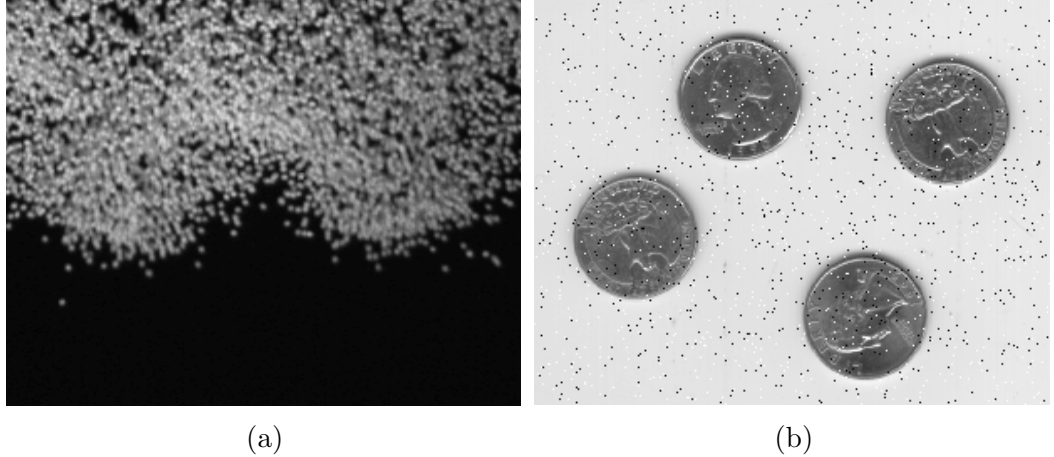


Figure 3.11: (a) Individual, unsuspended EPS beads moving ahead of a flow front (b) An image with salt and pepper noise.

detect the deep clefts than the initial technique, as it is now possible for there to be more than one value of  $y_j$  for a given value of  $x_i$ , allowing the front edge profile to effectively ‘track back’ on itself in the x-direction. Thus avoiding the relatively large, almost vertical sections of front edge profile that the initial technique produced, and which do not accurately reflect the true position of the front edge.

## 3.5 Profile smoothing

When released, a few of the EPS beads do not enter suspension and roll down the chute ahead of the front (Figure 3.2 & 3.11(a)). In order to avoid these beads being detected by the front tracking algorithm a filtering mask is applied to the images before they are processed. The small regions (or ‘spikes’) of intensity fluctuation caused by the individual EPS beads that don’t enter suspension are similar to the salt-and-pepper electronic noise that can occur in digital images (Figure 3.11(b)). This type of electronic noise is normally caused by errors in data transmission. The corrupted pixels are either set to the maximum or minimum value, resulting in intensity spikes and giving the image a ‘salt-and-pepper’ like appearance. ‘Median filters’ have been shown to be particularly effective at removing this kind of noise whilst preserving edges in the image [Lim, 1990]. The median filter works by running through the image pixel by pixel and replacing each intensity value with the median of the

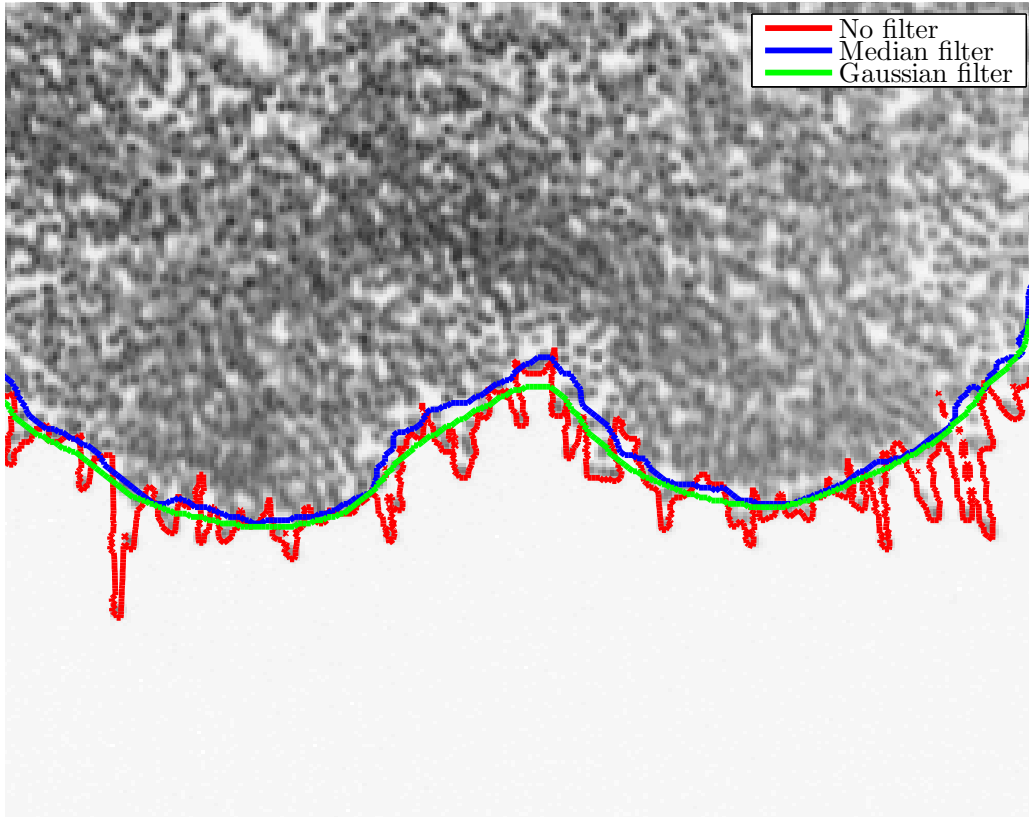


Figure 3.12: Front detection: without filter, with median filter and with Gaussian filter.

neighbouring entries. The number and pattern of neighbouring entries used is called the window, which slides, pixel by pixel, over the entire image. By specifying an appropriate size and shape for the window, the intensity spikes can be filtered out as they did not have a significant effect on the median value. In this situation the spikes are the same size as an individual EPS bead and therefore the window needs to be a square of side greater than two EPS bead diameters. For the plan view images, the largest EPS beads used were approximately 6 pixels in diameter and a  $15 \times 15$  pixel window was found to give good results (as shown in Figure 3.12), while for the side view images the largest beads were approximately 15 pixels in diameter and a  $32 \times 32$  pixel window was used. Additionally, when the images were filtered they were padded symmetrically at the boundaries, meaning mirror reflections of the image's pixels were added to each edge of the image. This was done to minimise distortion at the edges of the image.

### 3.6. COORDINATES CONVERSION

---

For comparison a Gaussian lowpass filter was also used on the images. The Gaussian filter works by convolving the image with a Gaussian function to remove the high frequency fluctuations in image intensity. A Gaussian filter is created using

$$h_g(x_i, y_j) = e^{\frac{-(x_i^2 + y_j^2)}{2\sigma_g^2}} \quad (3.13)$$

$$h(x_i, y_j) = \frac{h_g(x_i, y_j)}{\sum_{x_i} \sum_{y_j} h_g}, \quad (3.14)$$

where  $x_i$  and  $y_j$  are the horizontal and vertical dimensions of the filtering window respectively and  $\sigma_g$  is the standard deviation of the Gaussian distribution. As with the median filter, the parameters were determined by the size of individual EPS beads used. To filter out the intensity spikes caused by individual ‘stray’ EPS beads,  $\sigma_g$  was set to a value equal to two EPS bead diameters. This in turn determined the size of the filtering window, as setting the filter size to  $3\sigma_g$  in each direction means that the filter decays to nearly zero at the edges, avoiding discontinuities in the filtered image.

Whilst the Gaussian filter was effective at filtering out the stray EPS beads in front of the flow, it also caused significant blurring of the front edge of the flow, giving less accurate results (Figure 3.12). This is because the intensity values of the pixels corresponding to the stray EPS beads are much higher than the surrounding pixels that correspond to the chute surface. The  $\sigma_g$  value therefore has to be relatively high to ensure that the high intensity values from the stray EPS beads don’t caused the mean value of the convolution window to rise above the threshold value. A high  $\sigma_g$  value results in having to use a large convolution window, which leads to increased blurring and loss of detail. Therefore in order to increase accuracy a median filter was selected to be applied to the images throughout this work.

## 3.6 Coordinates conversion

In order to measure properties of the flows such as front position and velocity, the pixel coordinates of the video sequences had to be converted to physical coordinates. Before each experiment was conducted calibration grids were placed on the chute. For the camera capturing the plan view of the chute a grid was

### 3.7. COMPARISON OF FRONT VELOCITY MEASUREMENTS

---

placed flat on the plane of the chute, while for the camera capturing the side view a grid was placed along the centreline of the chute, perpendicular to its surface. An image was then taken and used to obtain the pixel coordinates of selected points on the calibration grid. Using an inverse affine transformation the pixel coordinates for the entire image are scaled to physical coordinates [Solomon et al., 2010]. For the plan view images the  $(x, y)$  coordinates were defined relative to the front edge of the release hopper ( $y$ ) and the cross-plane position of the pressure sensors ( $x$ ) (Figure 2.1). The slope normal ( $z$ ) coordinate in the side-view images was defined relative to the chute surface. In some experiments the edge of the release hopper was not visible in the side-view images. In these situations the longitudinal ( $y$ ) coordinates are first zeroed on the longitudinal ( $y$ ) position of the middle pressure sensor, the distance from the hopper release to the middle sensor was then obtained from the plan view calibration image and added to the values. The positions of the release hopper edge in the plan view images and the chute surface in the side images were calculated by selecting points on the respective surfaces then applying a least squares straight-line fit, which was then be extended across the entire width of the image.

The same coordinates conversion technique was also used when measuring: effective coefficient of friction, angle of repose, settling velocity and average EPS bead diameters.

### 3.7 Comparison of front velocity measurements obtained from pressure signal and image data

The experimental set-up detailed in Chapter 2 allows the front velocity,  $U_f$ , of a current to be measured using three different methods. One method utilises the profiles of the front edge of the current obtained from the image data, while the other two make use of the air pressure data. The arrival of the front at each sensor causes a peak in pressure (Figure 3.13). The front velocity,  $U_{f(P)}$ , can be calculated by dividing the distance between consecutive sensors by the time difference ( $\Delta t$ ) between pressure peaks observed at the sensors. The other air pressure based method uses the peak pressure value and the



### 3.7. COMPARISON OF FRONT VELOCITY MEASUREMENTS

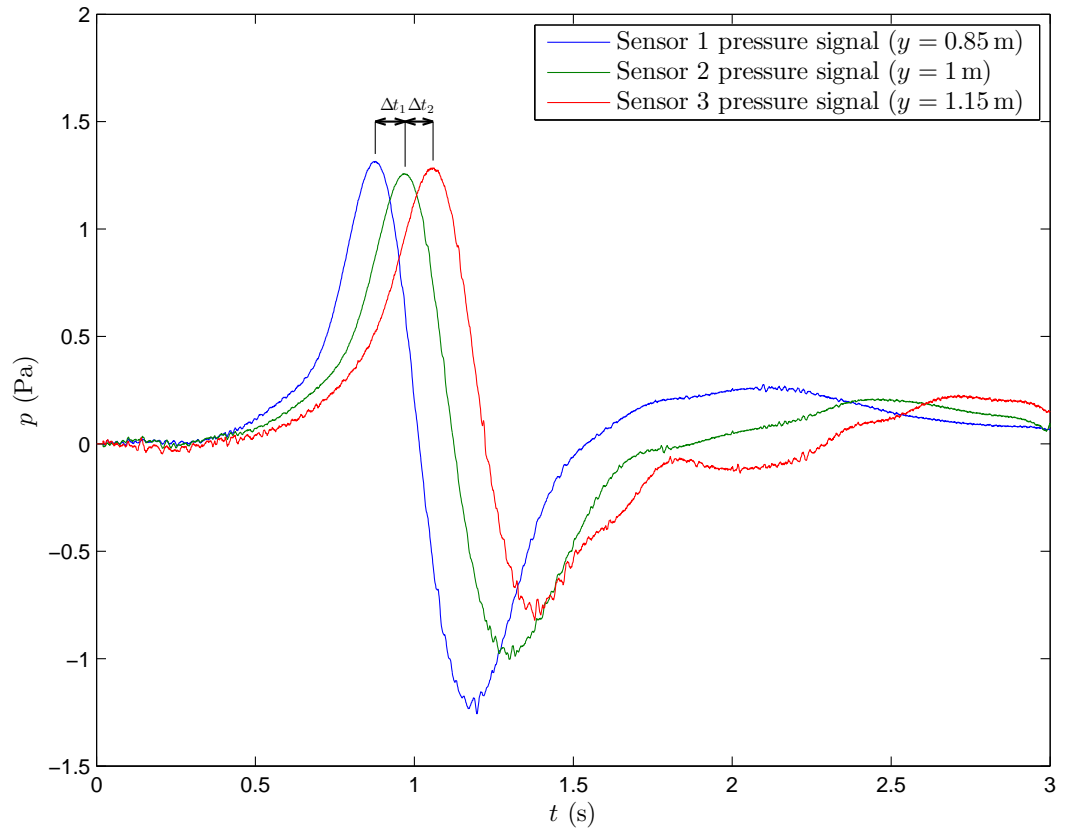


Figure 3.13: Typical air pressure signals obtained from experiments. Pressure sensors are located 0.15 m apart and  $\Delta t =$  time between pressure peaks.

### 3.7. COMPARISON OF FRONT VELOCITY MEASUREMENTS

dynamic pressure,

$$p = \frac{1}{2}\rho_a u^2, \quad (3.15)$$

where  $\rho_a$  is the density of air, in order to calculate the velocity,  $U_{f(D)}$ , of the front at each sensor location. For comparison with the air pressure data, the position of a section of the front edge of the flow, detected using the image data, was used to calculate the front velocity,  $U_{f(I)}$ . The width of section used was 5 mm and was centred at  $x = 0$ , which corresponds to the location and width of the tubes attached to the pressure sensors. Front velocity,  $U_{f(I)}$  was then calculated by dividing the distance travelled by the section between images by the time difference between images.

Correlations of front velocities calculated using each of these three methods for each experiment are shown in Figure 3.14. The velocities plotted represent the average velocity of the current between two laterally centred points on the chute with distances from the release point of  $y = 0.95$  m and  $y = 1.25$  m respectively. For  $U_{f(P)}$  this average was calculated by taking the mean of the value between sensors 1 ( $y = 0.95$  m) and 2 ( $y = 1.10$  m), and the value between sensors 2 and 3 ( $y = 1.25$  m). For  $U_{f(D)}$ , the mean of the values calculated at each of the three sensor locations is used.  $U_{f(I)}$  is the mean of the values calculated for all of the images where the position of the front section is greater than 0.95 m and less than 1.25 m.

For each comparison of front velocity measurements a line with gradient = 1 is shown, indicating where the the corresponding values in each data set are equal. The root-mean-squared relative error between two data sets,  $\alpha_{1,n}$  and  $\alpha_{2,n}$ , is

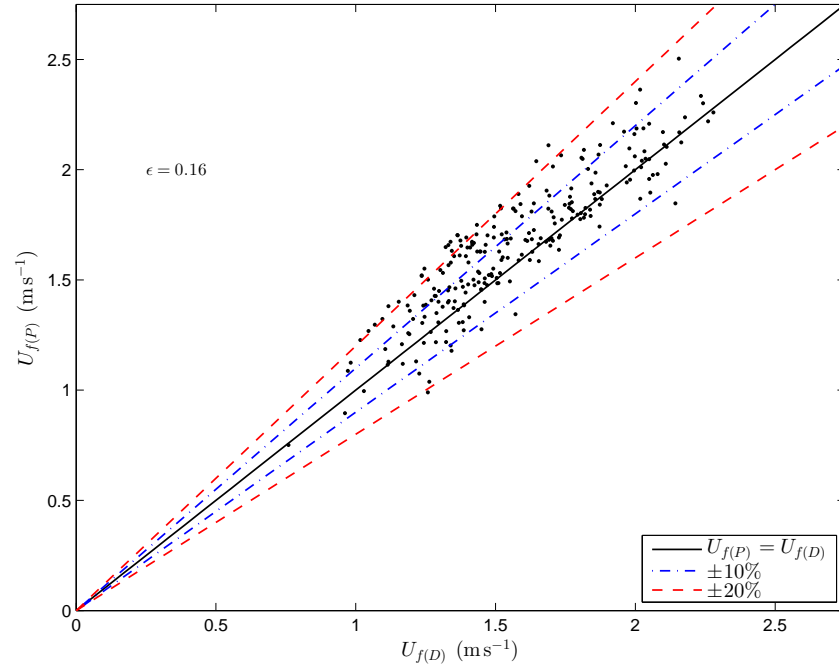
$$\epsilon = \sqrt{\frac{1}{n_\tau} \sum_{n=1}^{n_\tau} (\alpha_{1,n} - \alpha_{2,n})^2}, \quad (3.16)$$

where  $n_\tau$  is the number of data points in each series. The value of  $\epsilon$  is found to vary little between the correlations of the three data sets, although one of the drawbacks of this method of error analysis is that only the magnitude of the differences in values between the data sets is considered and information about the sign of these differences is lost. The individual residuals,

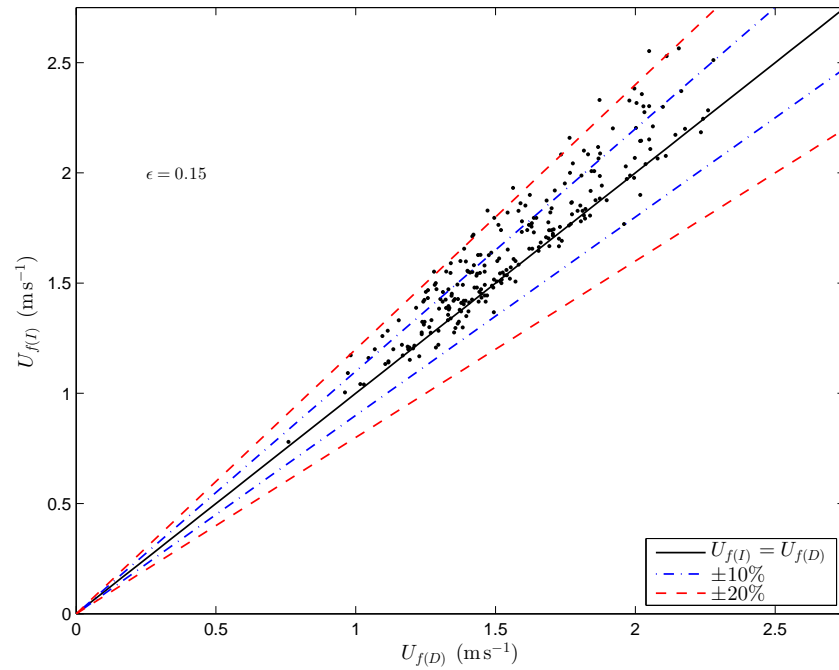
$$\mathcal{R}_n = \alpha_{1,n} - \alpha_{2,n}, \quad (3.17)$$

show that when compared with  $U_{f(P)}$  and  $U_{f(I)}$ ,  $U_{f(D)}$  is on average approx-

### 3.7. COMPARISON OF FRONT VELOCITY MEASUREMENTS



(a)



(b)

Figure 3.14: Correlation plots of (a)  $U_{f(P)}$  versus  $U_{f(D)}$  and (b)  $U_{f(I)}$  versus  $U_{f(D)}$ .

### 3.7. COMPARISON OF FRONT VELOCITY MEASUREMENTS

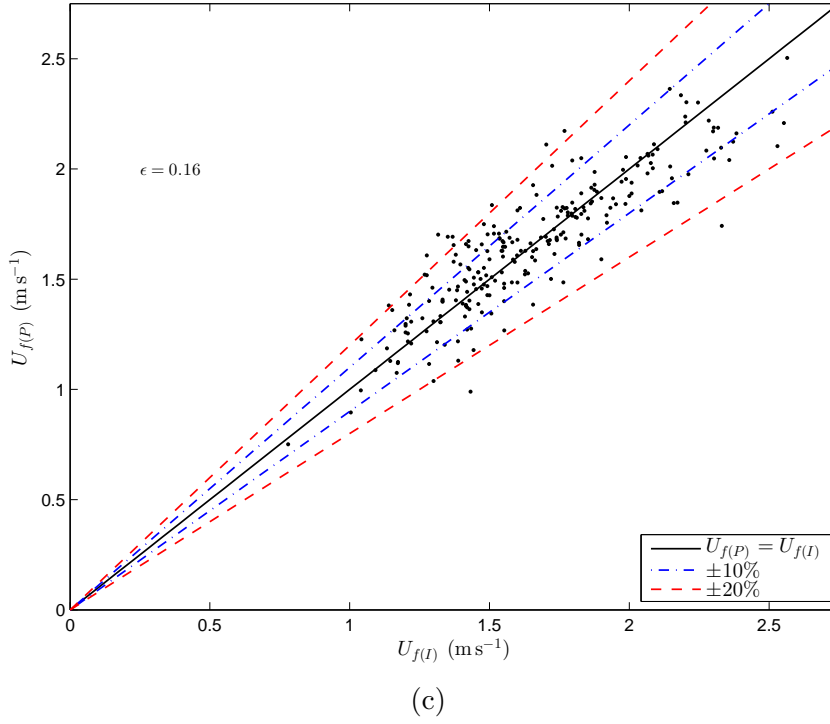


Figure 3.14: (c) Correlation plot of  $U_{f(P)}$  versus  $U_{f(I)}$ .

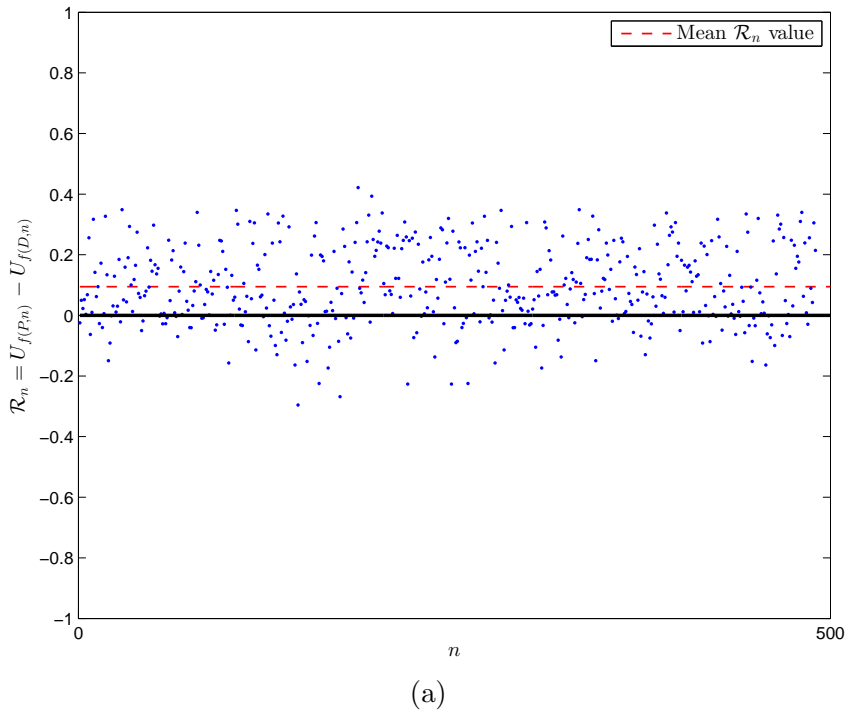
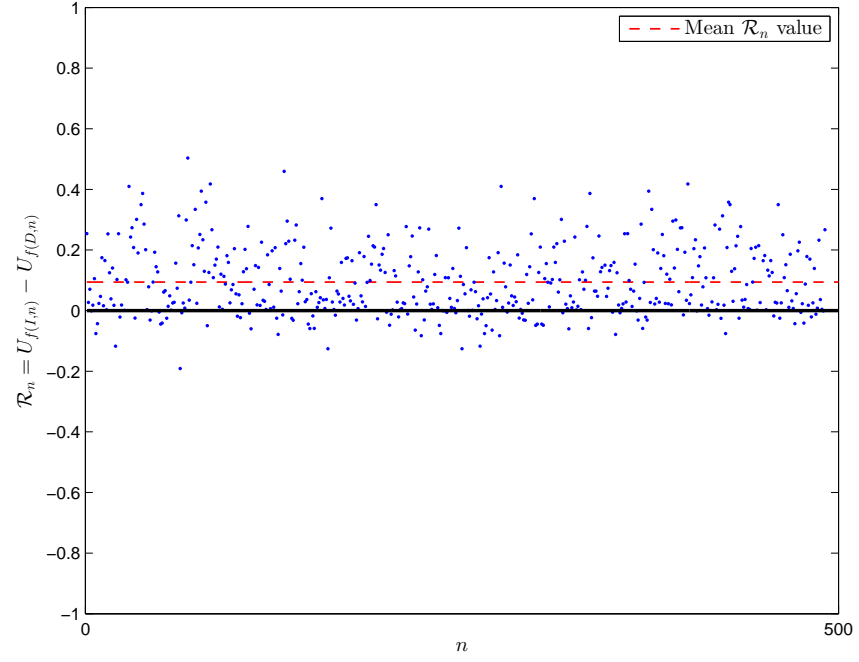
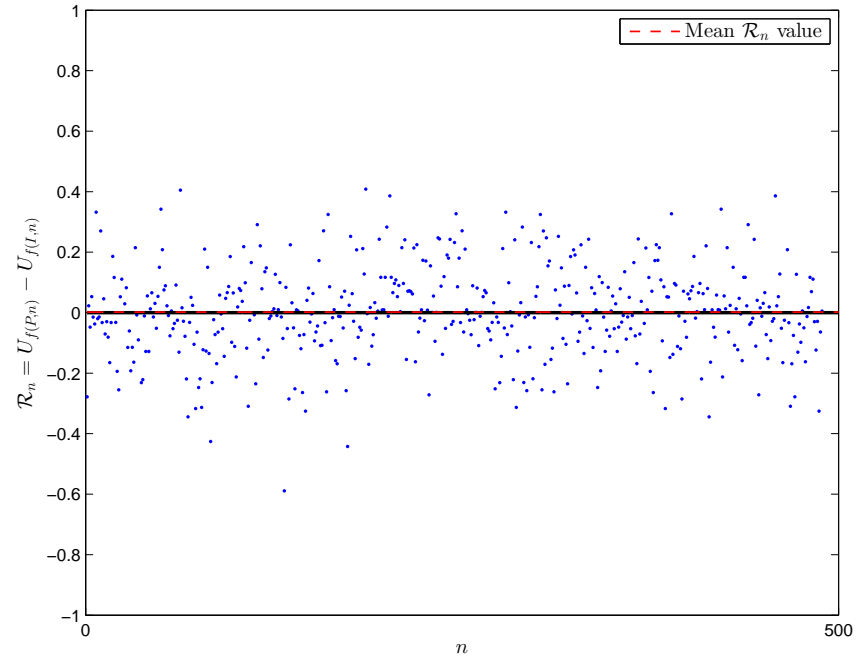


Figure 3.15: (a) Individual residual plot for  $U_{f(P)}$  and  $U_{f(D)}$  comparison.

### 3.7. COMPARISON OF FRONT VELOCITY MEASUREMENTS



(b)



(c)

Figure 3.15: Individual residual plot for (b)  $U_{f(I)}$  and  $U_{f(D)}$  comparison and (c)  $U_{f(P)}$  and  $U_{f(I)}$  comparison.

imately 10% smaller (Figures 3.15a & 3.15b). This under-prediction of front velocity when calculated using the dynamic pressure value is most likely to be caused by the stagnation point at the front of the current missing the pressure sensor. The stagnation point is located somewhere between the nose of the current and where the leading edge meets the chute (§1.4.1), meaning that the stagnation point will pass a small distance above the pressure sensors, which are positioned flush with the chute surface. The pressure has been shown to quickly decrease with distance from the stagnation point [Turnbull and McElwaine, 2010], resulting in lower values being measured by the pressure sensors. Despite some scatter in the correlation of  $U_{f(P)}$  and  $U_{f(I)}$  (Figure 3.14c), the mean individual residual value is approximately zero (mean  $\mathcal{R}_n = 0.0018$ ) (Figure 3.15c), indicating good agreement between the two methods of front velocity measurement. This comparison with the pressure signal data validates the accuracy of the front tracking method that is applied to the image data. Unless otherwise stated, data obtained from the image-based front tracking method will be used for calculations relating to the current's position and velocity throughout this work, as these data accurately capture the current at all positions throughout its motion down the chute and not just at the locations where the pressure sensors are located.

## 3.8 Lobe and cleft detection

The level set matrix  $T_{xy}$  produced using the plan view images for each experiment (§3.4) was used to detect and track the lobes and clefts that formed at the moving front. To do this the gradient,

$$\nabla T_{ij} = \frac{\partial T_{ij}}{\partial x} \hat{\mathbf{i}} + \frac{\partial T_{ij}}{\partial y} \hat{\mathbf{j}} \quad (3.18)$$

of the level set is first calculated, producing a vector field where each vector is normal to the surface of the moving front. Plotting this vector field provides a useful method of visualizing the movement of the leading edge (Figure 3.16), with large arrows representing regions where the front has large magnitude curvature (clefts) and small arrows representing regions of small magnitude curvature (lobes).

When calculating the gradient of  $T_{ij}$ , careful attention needs to be paid to

### 3.8. LOBE AND CLEFT DETECTION

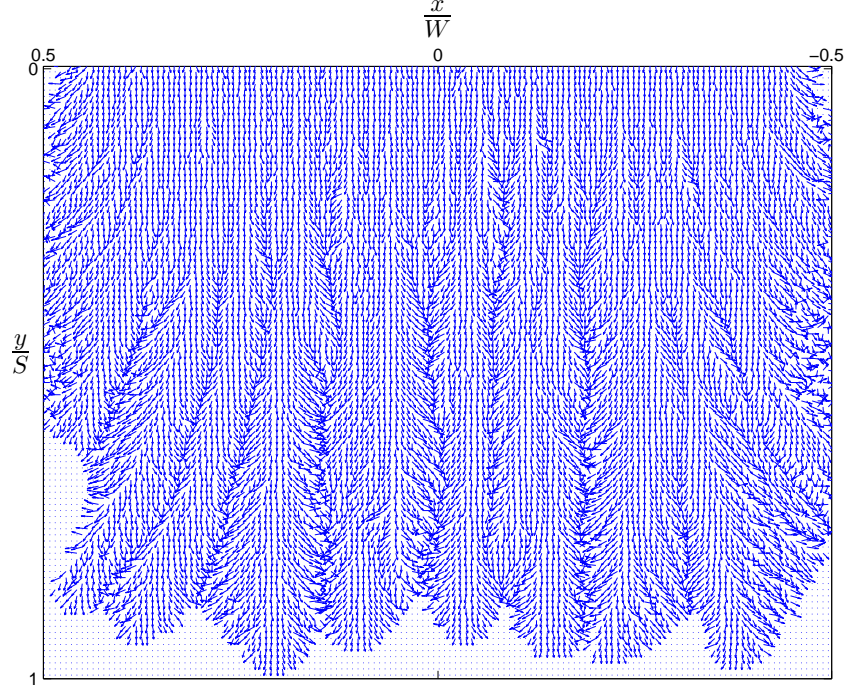


Figure 3.16: Vector field showing the gradient of the level set taken from an experiment using  $2100 \text{ cm}^3$  of 1.8 mm diameter EPS bead on a  $65^\circ$  slope.

selecting appropriate values for the sizes of  $\delta x$  and  $\delta y$ . If the values are too small, changes in  $T_{ij}$  will be too small to detect and changes in position of the front edge of the flow won't be clearly identified, whereas setting the values too high will result in loss of detail. Suitable values for  $\delta x$  and  $\delta y$  were found to be dependant on the size of the EPS beads used in the experiment, with the optimum value for both  $\delta x$  and  $\delta y$  equal to twice the diameter of the EPS beads used.

The divergence of the vector field can be used to calculate the curvature of the level set,

$$\kappa = \nabla \cdot \frac{\nabla T_{ij}}{|\nabla T_{ij}|}. \quad (3.19)$$

Large regions with positive curvature will correspond to the location of lobes, and regions of large negative curvature to the location of clefts. Displaying the divergence of the level set allows the formation and development of lobes and clefts at the moving front to be clearly visualized (Figure 3.17). However, in order to measure properties of the lobe-and-cleft-type pattern, such as wavelength, the precise location of the lateral centre of the lobes and clefts needs to be identified. To achieve this the values in each row of the divergence matrix

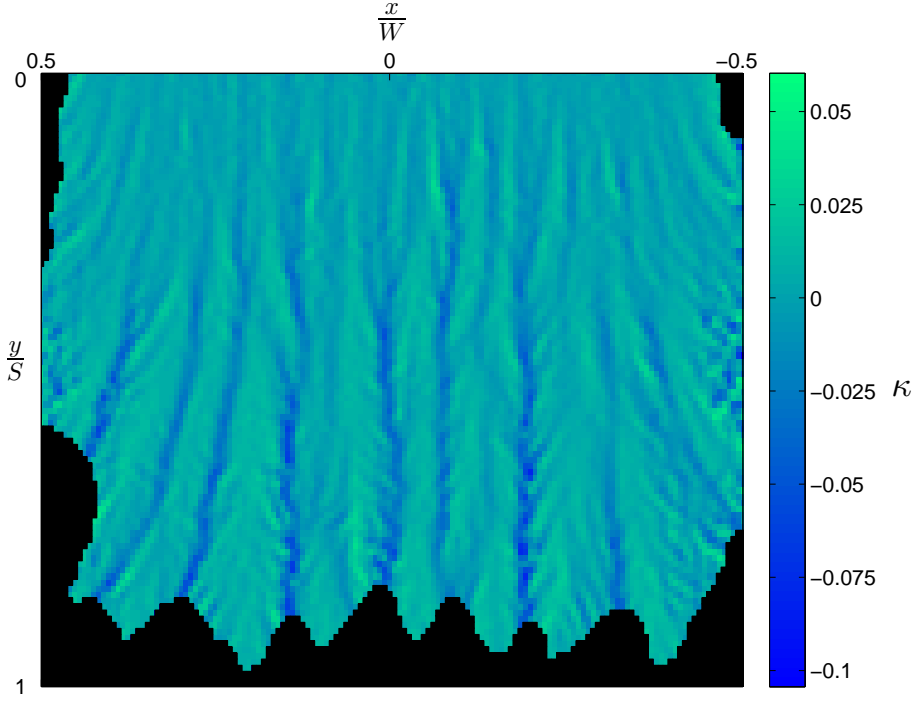


Figure 3.17: Divergence of the vector field shown in Figure 3.16.

were differentiated and the stationary points identified. Each stationary point was further analysed to identify it as either a local maxima, minima or saddle point. Local maxima were then classified as clefts and local minima as lobes.

The location of the lobes and clefts identified within the matrix of divergence values then had to be mapped onto the front profile contours  $T_{xy} = t$  from the level set. This first meant interpolating the matrix of lobe and cleft locations so that it was equal in size to the level set. This means that each identified lobe or cleft location now corresponds to an area equal in size to one element of the grid used for the initial discretization (i.e  $2d_p \times 2d_p$ ). Thus highlighting the importance of using the minimum values of  $\delta x$  and  $\delta y$  that still give meaningful results when calculating the gradient of the level set. Next the matrix of lobe and cleft locations is compared with each front profile contour, and locations on the contour that coincide with a lobe or cleft are noted (Figure 3.18).

The fact that the area of each lobe and cleft location has been expanded during this process sometimes results in a contour coinciding with several locations of the same lobe or cleft. When neighbouring locations on a contour were identified as all being either lobes or clefts the algorithm would select the lo-



### 3.8. LOBE AND CLEFT DETECTION

---

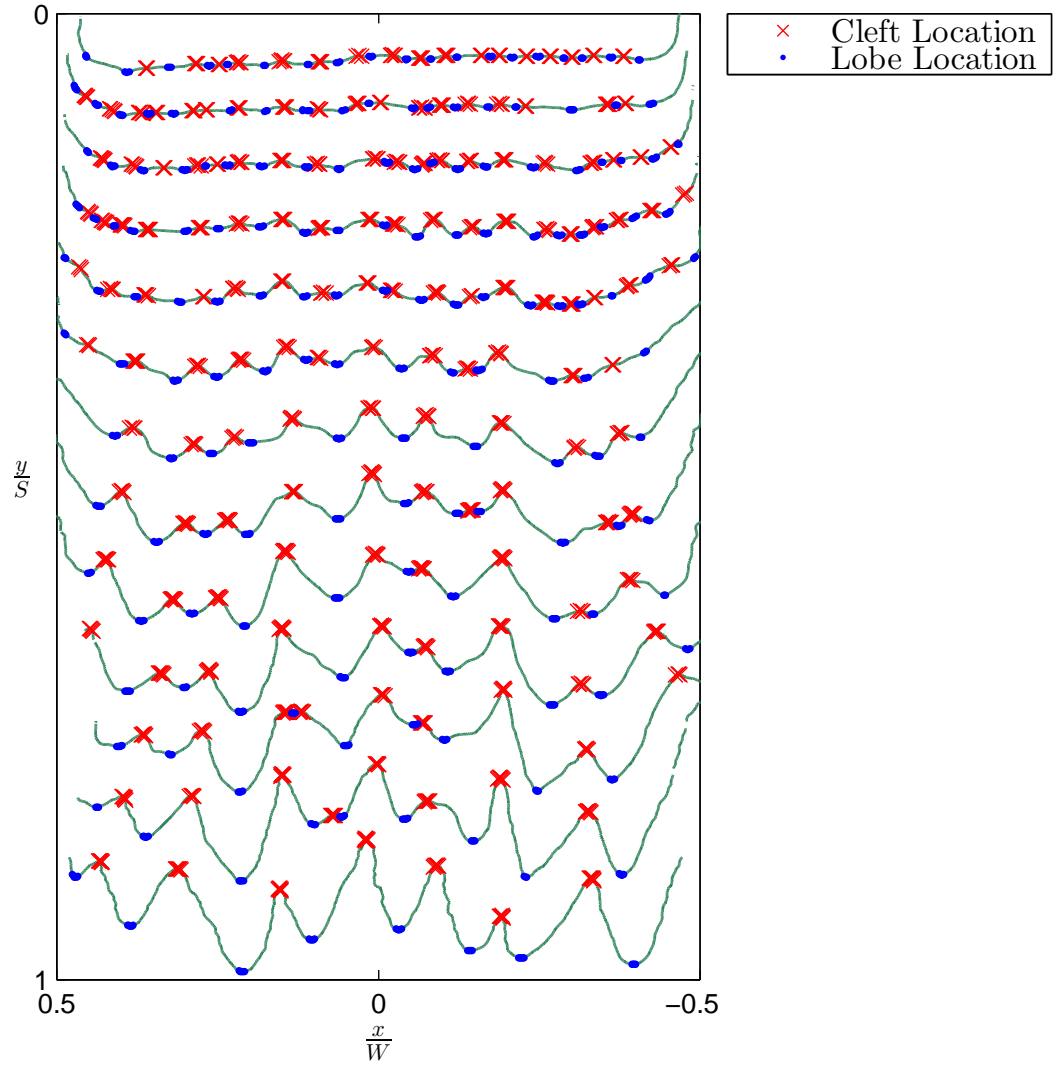


Figure 3.18: Front profile contours with all lobe and cleft locations identified from the corresponding matrix of divergence values marked.

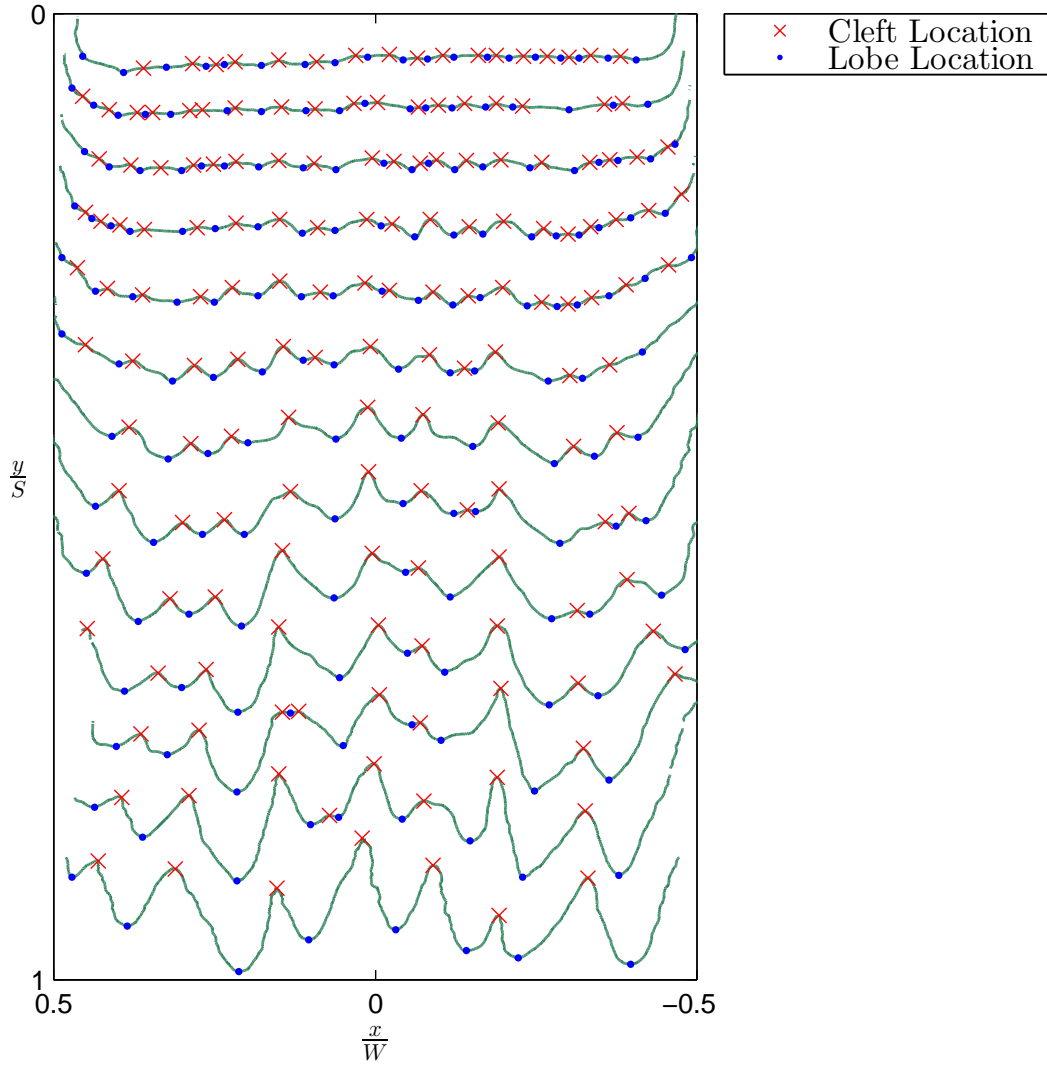


Figure 3.19: Front profile contours, taken from the same experiment as those shown in Figure 3.18, with consolidated lobe and cleft locations marked.

### 3.8. LOBE AND CLEFT DETECTION

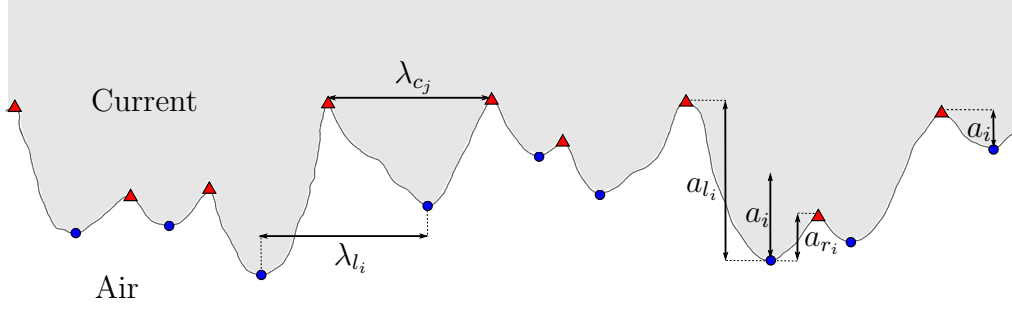


Figure 3.20: A single front edge profile taken from Figure 3.19 with detected lobe ( $\circ$ ) and cleft ( $\triangle$ ) positions marked.

cation in the group with either the highest (lobes) or lowest (clefts) downslope position and remove the other occurrences (Figure 3.19).

#### 3.8.1 Measurement of lobe and cleft pattern wavelength and amplitude

Once the positions of lobe and clefts had been mapped on to the front edge profile contours, the wavelength  $\lambda$  and amplitude  $a$  of the lobe-and-cleft-type pattern at a particular time  $t$  could be measured. For each contour the lateral ( $x$ ) distances between the  $n_l$  adjacent pairs of lobes,  $\lambda_{l_i}$ , and between the  $n_c$  adjacent pairs of clefts,  $\lambda_{c_j}$ , were measured (Figure 3.20) and the mean distance,

$$\lambda = \frac{1}{n_l + n_c} \left( \sum_{i=1}^{n_l} \lambda_{l_i} + \sum_{j=1}^{n_c} \lambda_{c_j} \right) \quad (3.20)$$

was calculated in order to obtain the average wavelength,  $\lambda$ .

The amplitude of the lobe-and-cleft-type pattern,  $a$ , for each contour is calculated by measuring the longitudinal ( $y$ ) distance between lobes and clefts. However, of the  $n_l$  lobes found on a given contour, most are positioned between two clefts, the longitudinal distances to which are not equal. When this is the case the longitudinal distances between the lobe and the cleft to the left ( $a_{l_i}$ ) and the cleft to the right ( $a_{r_i}$ ) are measured (Figure 3.20) and the mean of both distances used as the value of amplitude,  $a_i$ , for that lobe. Where there is only one cleft on either side of a lobe, usually at the ends of a contour, then

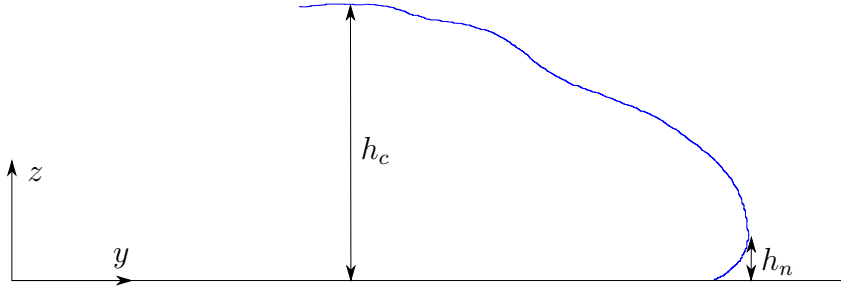


Figure 3.21: Side profile contour with current height,  $h_c$ , and current nose height,  $h_n$ , measurements.

the longitudinal distance from the lobe to that cleft is taken as the value of amplitude,  $a_i$ . The mean,

$$a = \frac{1}{n_l} \sum_{i=1}^{n_l} a_i \quad (3.21)$$

is then calculated in order to obtain the average amplitude,  $a$ , for each contour.

## 3.9 Measurement of flow and nose height

Measurements of the current height,  $h_c$ , and the current nose height,  $h_n$ , were obtained using the contours of the level set matrices produced from the side-on images (Figure 3.21). For a particular value of  $t$ , the corresponding contour of the level set was identified and the current height measured as the maximum value of  $z$  along the contour. The current nose height was measured as the value of  $z$  at the point along the contour where the value of  $y$  was maximum.

## 3.10 Measurement of lobe radius of curvature

For comparison with the results of Nohguchi and Ozawa [2008], the radius of curvature

$$r = \frac{1}{\kappa} \quad (3.22)$$

of each lobe, at each point in time, was calculated. For each lobe location, values of curvature,  $\kappa$ , can be obtained from the level set matrix using the

### 3.11. SUMMARY

---

method described in §3.8. The detected lobe location corresponds to the lateral centre of the lobe; in order to improve the accuracy and reliability of the results, the value of  $\kappa$  used was the mean value of the curvature along a region of the contour that the lobe was located on. The region extended a distance either side (i.e. both increasing and decreasing values of  $x$ ) of the lateral centre of the lobe. It is important to select an appropriate value for the distance that this region extends. It should be big enough that it covers most of the lobe, allowing an accurate and reliable measurement to be obtained. However, if it is too large it may include neighbouring clefts which will adversely effect the accuracy of the results. In order to select an appropriate region size, lobe and cleft wavelength data collected from the contour was used. In theory the lateral width of the region,  $x_r$ , could be set at a value just below the average wavelength for the contour ( $\lambda$ ). This is especially true in the early stages of the flow's motion when the clefts are laterally narrow in comparison to the width of the lobes. However, as the flow progresses the comparative width of the clefts increases, this coupled with the variations of individual lobe wavelength relative to the average wavelength, make values of  $x_r$  that are close to  $\lambda$  an unsuitable choice. The lateral width of the region,  $x_r$ , was therefore set as  $1/2\lambda$ , centred on the lateral position of the lobe centre  $x_l$ .

## 3.11 Summary

The image processing techniques and methods demonstrated in this chapter allow the position of the leading edge of a flow to be accurately tracked using image data collected from experiments conducted with EPS beads. The leading edge profiles that are detected using a level set-based technique can be used in order to detect and track the positions of lobes and clefts; features of the lobe-and-cleft-type pattern such as wavelength, amplitude and lobe radius of curvature can also be measured. Additionally, the leading edge profiles enable the measurement of various other flow features, including front velocity and flow and nose height.

## Bibliography

- J. S. Lim. *Two-Dimensional Signal and Image Processing*, pages 469–476. Prentice Hall, Englewood Cliffs, NJ, 1990.
- J. N. McElwaine, M. D. Patterson, and S. B. Dalziel. Lobe and cleft formation at the head of a gravity current. *Proceedings of the XXI International Congress of Theoretical and Applied Mechanics*, pages 15–21, 2004.
- Y. Nohguchi and H. Ozawa. On the vortex formation at the moving front of lightweight granular particles. *Physica D*, 238:20–26, 2008. doi:10.1016/j.physd.2008.08.019.
- N. Otsu. A threshold selection method from gray-level histograms. *IEEE Transactions on Systems, Man, and Cybernetics*, 9(1):62–66, 1979.
- J. P. Serra. *Image analysis and mathematical morphology*. Academic Press, London, 1982.
- C. Solomon, S. Gibson, and T. Breckon. *Fundamentals of Digital Image Processing: A Practical Approach Using MATLAB*. Wiley, Hoboken, New Jersey, USA, 2010.
- B. Turnbull and J. N. McElwaine. Potential flow models of suspension current air pressure. *Annals of Glaciology*, 51(54), 2010.

## Chapter 4

# Lobe-and-cleft-type patterns in particle-laden gravity currents

The experimental set-up described in Chapter 2 and the image processing techniques described in Chapter 3 enabled the adjustment and measurement of various flow parameters, some of which are shown in Figure 4.1. The effect that these variables have on the dynamics of the flows shall be discussed in this chapter, with particular focus on the development and scaling of lobe-and-cleft-type patterns at the leading edge of the flows.

### 4.1 Front velocity

Figure 4.2 shows velocity-time plots for two experiments with release volumes of  $3300\text{ cm}^3$  and  $1000\text{ cm}^3$ , both conducted using EPS beads with diameter  $d_p = 2.7\text{ mm}$  on a slope of angle  $\theta = 75^\circ$ . Front velocity,  $U_f$ , is calculated using the average downslope position  $y$  taken across the entire width  $b$  of the current. The time origin  $t = 0$  is the time when the release mechanism is operated. The flows quickly reach an approximately constant acceleration which exists for a short distance ( $\approx 0.5 - 0.75\text{ m}$ ) before reaching an approximately constant velocity. It can be seen that the flow with the larger initial volume of release  $V_i$  reaches a higher velocity ( $U_f \approx 2\text{ m s}^{-1}$ ) than the flow with the smaller initial volume of release ( $U_f \approx 1.6\text{ m s}^{-1}$ ), and that both of these values are considerably higher than the settling velocity of an individual EPS bead ( $0.8\text{ m s}^{-1}$ ). The magnitudes of the approximately constant velocities reached

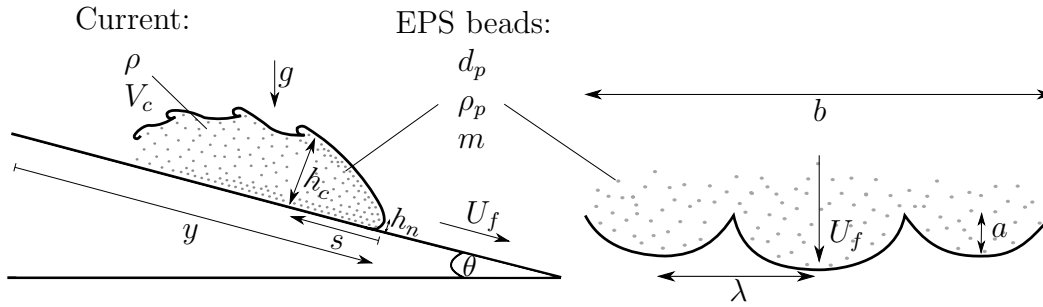


Figure 4.1: Schematic diagrams of a particulate gravity current of height  $h_c$ , width  $b$ , density  $\rho$ , volume  $V_c$  travelling a distance  $y$  down an inclined plane with a front velocity  $U_f$ . The current has a raised ‘nose’ of height  $h_n$  which is the foremost point of the flow, and from which the distance behind the moving front  $s$  is measured. Individual particles have a diameter  $d_p$ , density  $\rho_p$  and mass  $m$ . A lobe and cleft pattern with wavelength  $\lambda$  and amplitude  $a$  forms at the moving front.

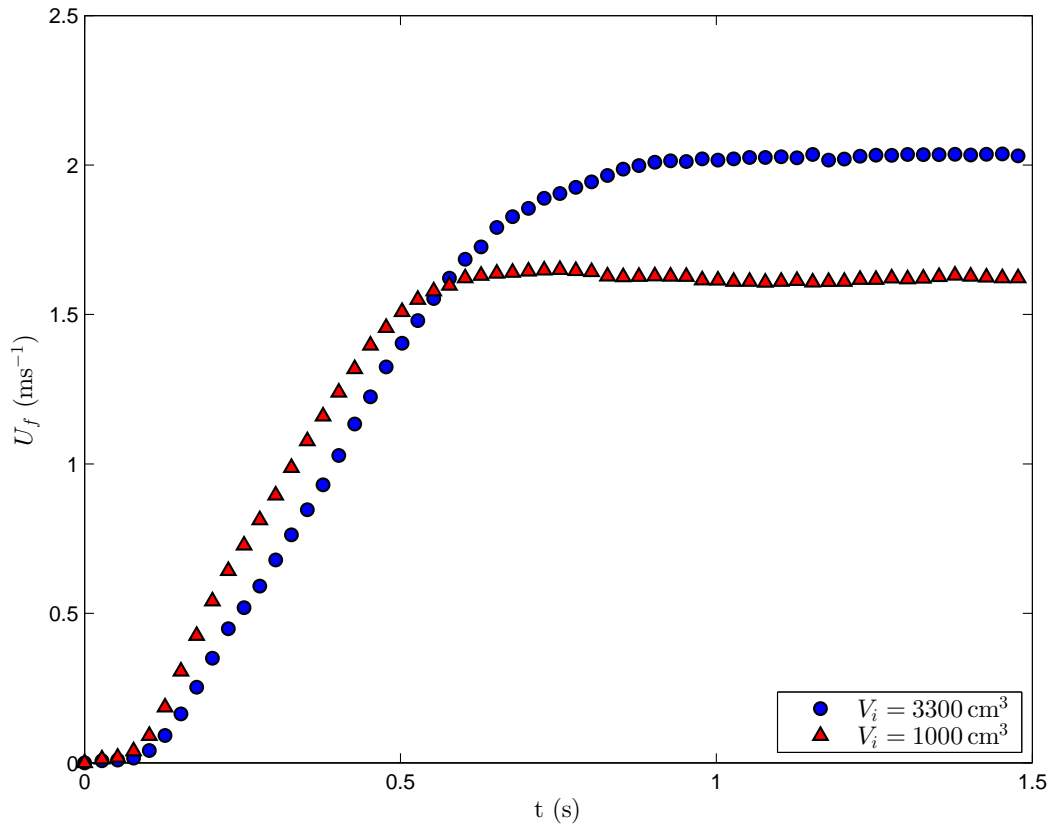


Figure 4.2: Front velocity ( $U_f$ ) versus time plots taken from two experiments conducted using release volumes,  $V_i = 3300 \text{ cm}^3$  and  $V_i = 1000 \text{ cm}^3$ , of 2.7 mm diameter EPS beads on a slope of angle  $\theta = 75^\circ$ .



#### 4.1. FRONT VELOCITY

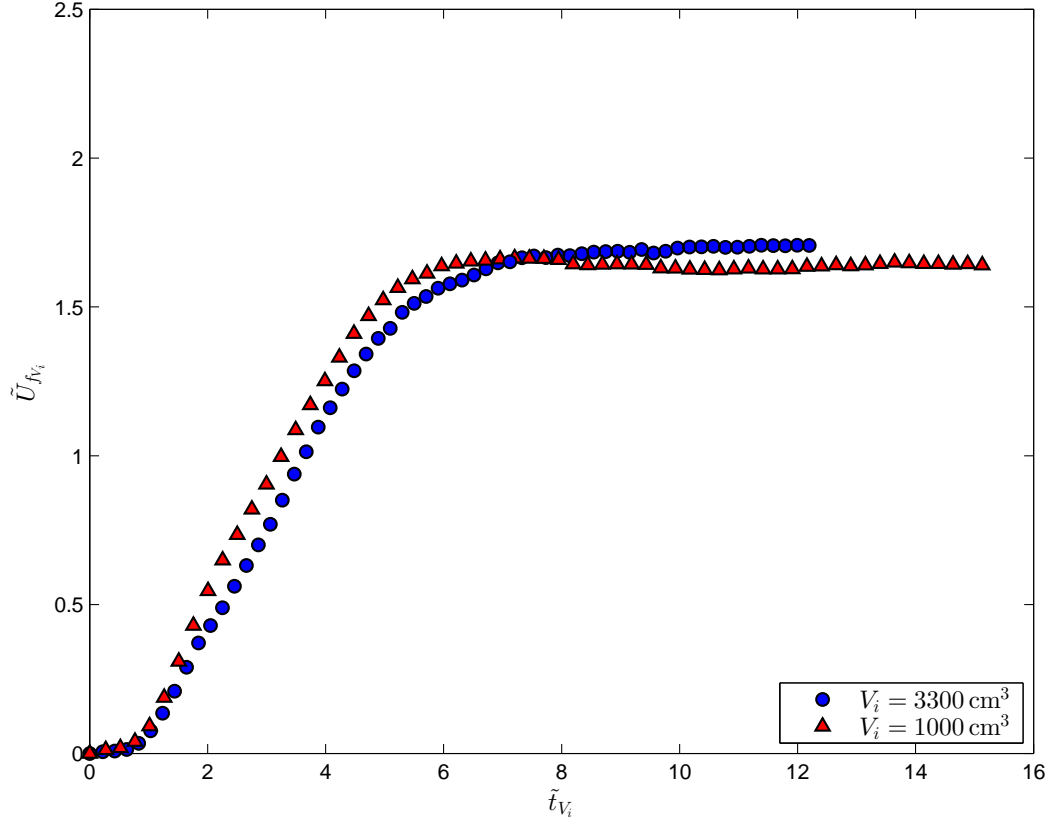


Figure 4.3: Non-dimensionalised front velocity ( $\tilde{U}_{f_{V_i}}$ ) versus time ( $\tilde{t}_{V_i}$ ) plots produced using the data shown in Figure 4.2.

by the flows were found to be reasonably consistent, with the typical standard deviation  $\approx \pm 6\%$  of the mean velocity of all experiments with a particular configuration of variables.

The length scale that characterizes the release volume,  $(\frac{V_i}{b})^{\frac{1}{2}}$ , can be used to calculate the non-dimensional front velocity,

$$\tilde{U}_{f_{V_i}} = \frac{U_f}{\sqrt{(\frac{V_i}{b})^{\frac{1}{2}} g}}, \quad (4.1)$$

where  $g$  is the acceleration due to gravity ( $g = 9.81 \text{ ms}^{-2}$ ). Similarly a non-dimensional timescale can be calculated using the release volume-based length scale,

$$\tilde{t}_{V_i} = \frac{t}{\sqrt{(\frac{V_i}{b})^{\frac{1}{2}} g^{-1}}}. \quad (4.2)$$

Applying this non-dimensionalisation to the data from the individual ex-

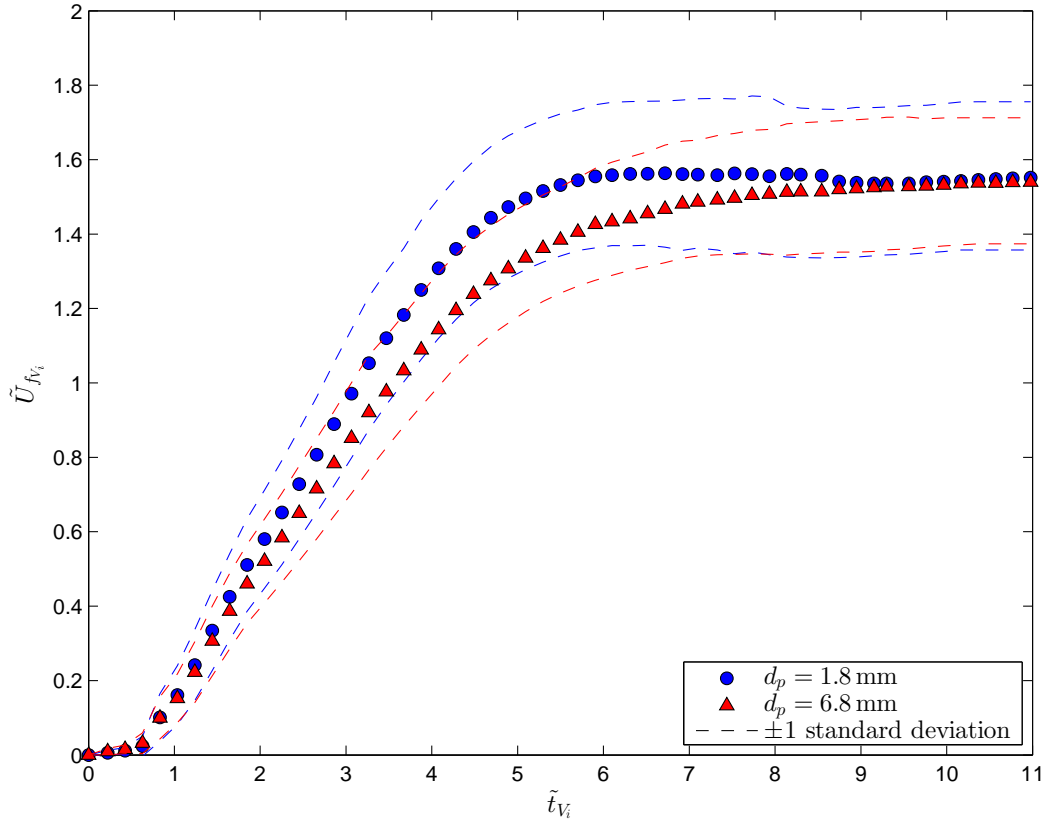


Figure 4.4: Non-dimensionalised front velocity ( $\tilde{U}_{f_{V_i}}$ ) versus time ( $\tilde{t}_{V_i}$ ) plots for experiments conducted using 1.8 mm and 6.8 mm diameter EPS beads. Data is taken from 150 experiments conducted using these EPS bead diameters, including all release volumes and slope angles used, and is presented as an ensemble average for each EPS bead diameter. Solid lines indicate ensemble average data and dashed lines indicate  $\pm 1$  standard deviation from this average.

#### 4.1. FRONT VELOCITY

---

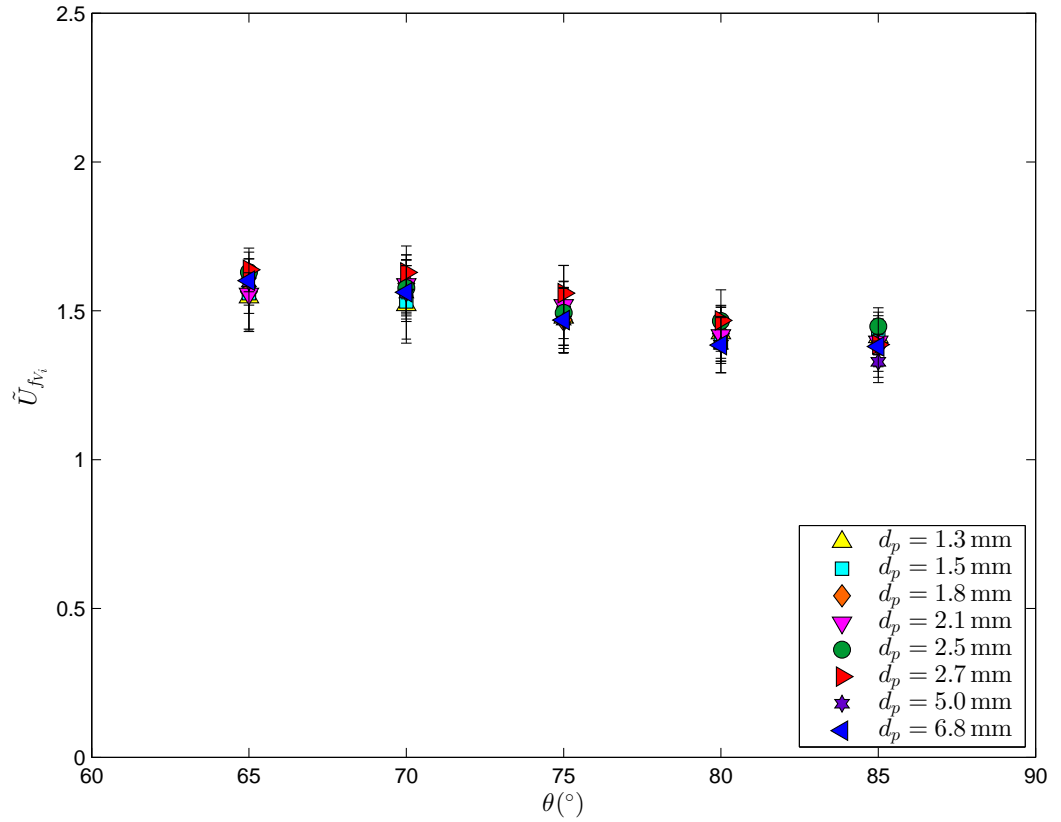


Figure 4.5: Non-dimensionalised front velocity ( $\tilde{U}_{f_{V_i}}$ ) versus slope angle ( $\theta$ ) for experiments conducted using different values of EPS bead diameter. Markers represent the mean non-dimensionalised front velocity taken at  $\tilde{t}_{V_i} = 10$  from experiments conducted using all available values of slope angle and release volume. Error bars have length equal to  $\pm 1$  standard deviation from the mean.

periments shown in Figure 4.2, there appears to be a good collapse of the data (Figure 4.3), in agreement with other laboratory experiments conducted using EPS bead [Turnbull and McElwaine, 2008]. This data collapse is confirmed when applied to all experiments conducted for the largest and smallest EPS bead sizes (Figure 4.4) and it is also indicated that the steady velocity reached by the flow front is independent of EPS bead diameter,  $d_p$ . In Figure 4.5 average front velocities for experiments conducted at different slope angles  $\theta$  and using different sizes of EPS bead  $d_p$  are shown. The velocity is measured at  $\tilde{t}_{V_i} = 10$ , ensuring that the flows have reached an approximately steady velocity, and it can be seen that front velocity is independent of both EPS bead diameter and slope angle. The latter observation being in agreement with other laboratory experiments conducted using both EPS bead-air [Turnbull and McElwaine, 2008], and continuous, homogenous gravity currents [Britter and Linden, 1980] travelling on an incline. This agreement confirms not only the validity of the experimental set-up used in this study, but also the accuracy and reliability of the automated detection and analysis techniques applied to the data collected.

## 4.2 Flow height measurements

Current head heights (§3.9) for flows consisting of 1.8 mm and 6.8 mm diameter EPS beads are shown for each release volume and slope angle in Figure 4.6. Several trends can be seen in the data; current height increases monotonically with increasing slope angle and release volume, but with decreasing particle diameter. That is, currents consisting of smaller particles have larger heads due to the particles' lower settling velocities resulting in lower rates of particle sedimentation. Larger heads are observed at higher slope angles as the component of the particles' settling velocity normal to the slope is reduced. The data in Figure 4.6 shows agreement with qualitative observations of detrainment levels at the rear of the flow. That is, it was observed that as the release volume was increased, higher levels of rear detrainment were observed, especially for currents consisting of smaller diameter EPS beads. Increased detrainment was also observed at higher slope angles. These observations are supported by Figure 4.6 where the data for the smaller particles shows a much smaller increase in current head height between the middle and largest size of release volume than that between the smallest and middle size. For both

## 4.2. FLOW HEIGHT MEASUREMENTS

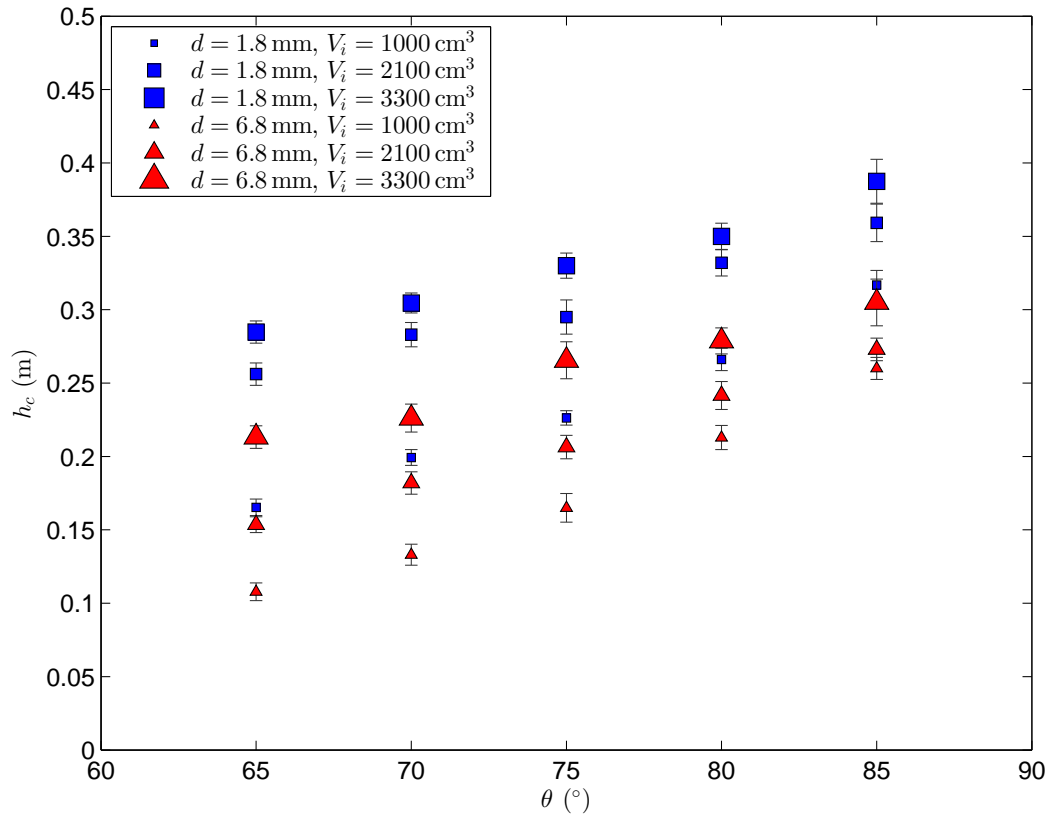


Figure 4.6: Current head height ( $h_c$ ) versus slope angle ( $\theta$ ) for currents consisting of 1.8 mm or 6.8 mm diameter EPS beads. Head height was measured at a distance of 1 m from the line release. Error bars have length equal to the standard deviation from the mean.

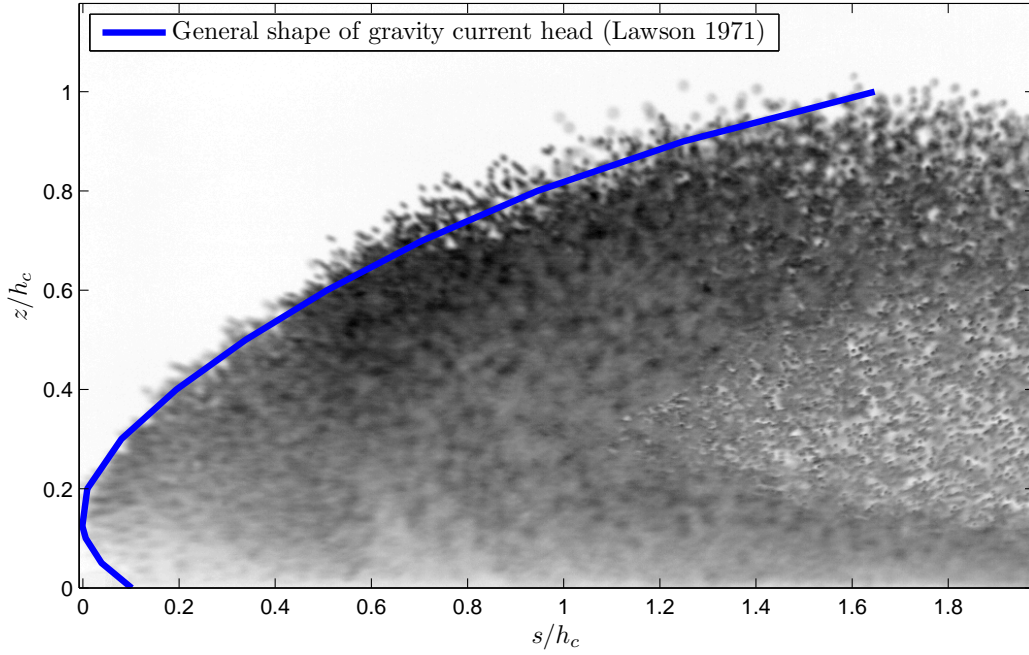


Figure 4.7: Side-on image of an EPS bead gravity current taken from an experiment conducted using  $V_i = 3300 \text{ cm}^3$  of 2.7 mm diameter EPS beads on a slope of angle,  $\theta = 65^\circ$ . Colours have been inverted for clarity. The solid line represents general profile shape of a gravity current taken from Lawson [1971].  $s$  = distance into the current from the nose, where at the foremost point of the nose,  $s = 0$ .

particle sizes the difference in current head height between the three release volume sizes decreases as slope angle increases. These observations and results indicate that there may be a limit to the amount of material that can be suspended within the head of the current, and as this limit is approached the amount of material detrained from the rear of the head increases.

### 4.3 Nose height measurements

Previous laboratory experiments [Keulegan, 1957, Middleton, 1966] have reported a general profile shape for the head of a gravity current [Lawson, 1971]. This general profile shape is based on the ratios of both the vertical height and the horizontal distance from the front, with the maximum vertical height of the current. When applied to images taken from EPS bead-air gravity current experiments a reasonable agreement can be seen with the general profile shape

### 4.3. NOSE HEIGHT MEASUREMENTS

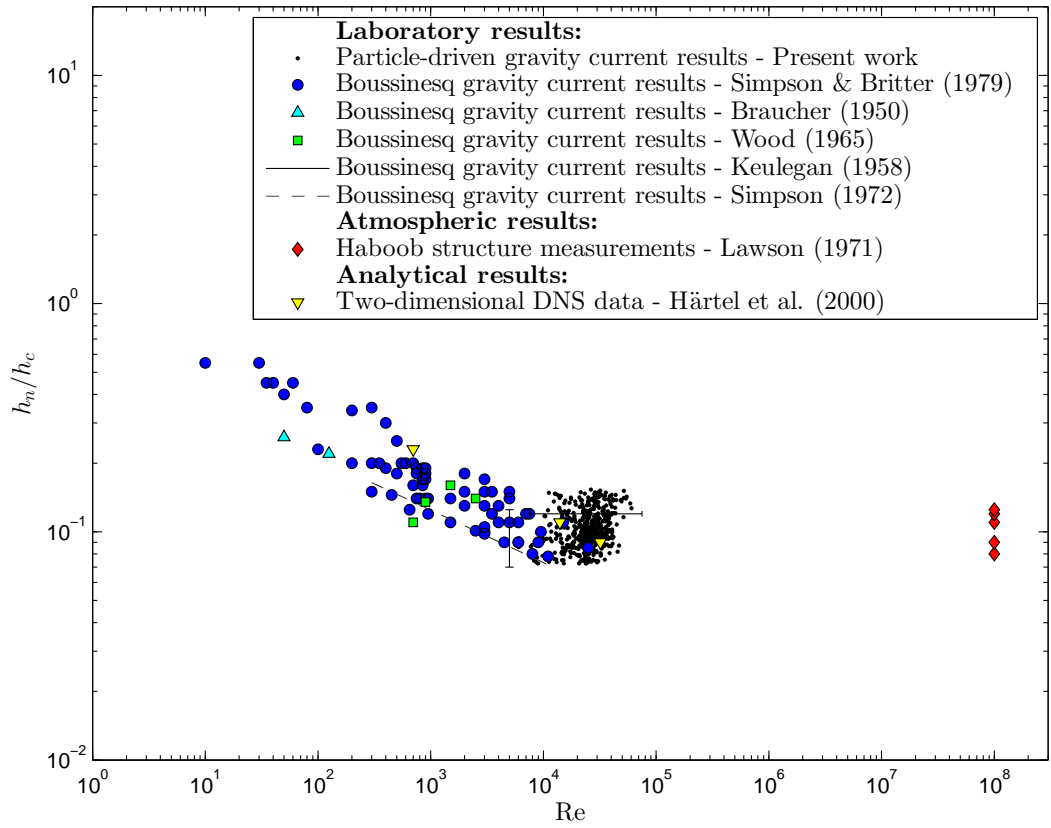


Figure 4.8: Dimensionless nose height,  $\frac{h_n}{h_c}$ , versus Reynolds number,  $Re$ , where  $Re = \frac{U_f h_c}{\nu}$ .

(Figure 4.7).

Measurements of the height of the foremost point of the head, or ‘nose’, of gravity currents have been made in the laboratory and in the atmosphere and some results are shown in Figure 4.8. A non-dimensional nose height  $h_n/h_c \approx \frac{1}{8}$ , independent of Reynolds number for values greater than  $10^3$  has been suggested [Simpson, 1997] and results from the EPS bead-air gravity current experiments support this.

It has been shown by Härtel et al. [2000] that the stagnation point of a gravity current with a raised nose is located between the nose and where the front meets the chute surface. There is a region of unstable stratification in this region and it is believed that this is where the classic lobe-and-cleft instability originates [Härtel et al., 2000]. It is therefore significant that the particle-driven gravity currents exhibit a similar region, and it is interesting to note whether the instability observed in these currents correlates with the classic lobe-and-cleft instability found in Boussinesq gravity currents.

## 4.4 Flow front patterns

Although the particles start from a pseudo two-dimensional linear distribution, a wavy pattern quickly appears in the moving front. As the fronts continue to propagate downslope these fluctuations grow in amplitude. Clear qualitative differences can be observed between the two flows shown in Figure 4.9. One of the most striking is the difference in wavelength of the lobe-and-cleft-type pattern created by the fluctuations in the moving front during the later stages of the flows motion. That is, the lobe and cleft structure in Figure 4.9(a) (for  $d_p = 1.8$  mm), has a noticeably shorter wavelength than that observed for the larger particles shown in Figure 4.9(b) (for  $d_p = 5.0$  mm).

By taking particle diameter  $d_p$  as our length scale, a non-dimensional timescale can be calculated,

$$\tilde{t}_{d_p} = t/\sqrt{d_p/g}. \quad (4.3)$$

Images taken at the same non-dimensional time,  $\tilde{t}_{d_p} = 50$ , from four experiments using the same release volume, but different sized particles are shown



#### 4.4. FLOW FRONT PATTERNS

---

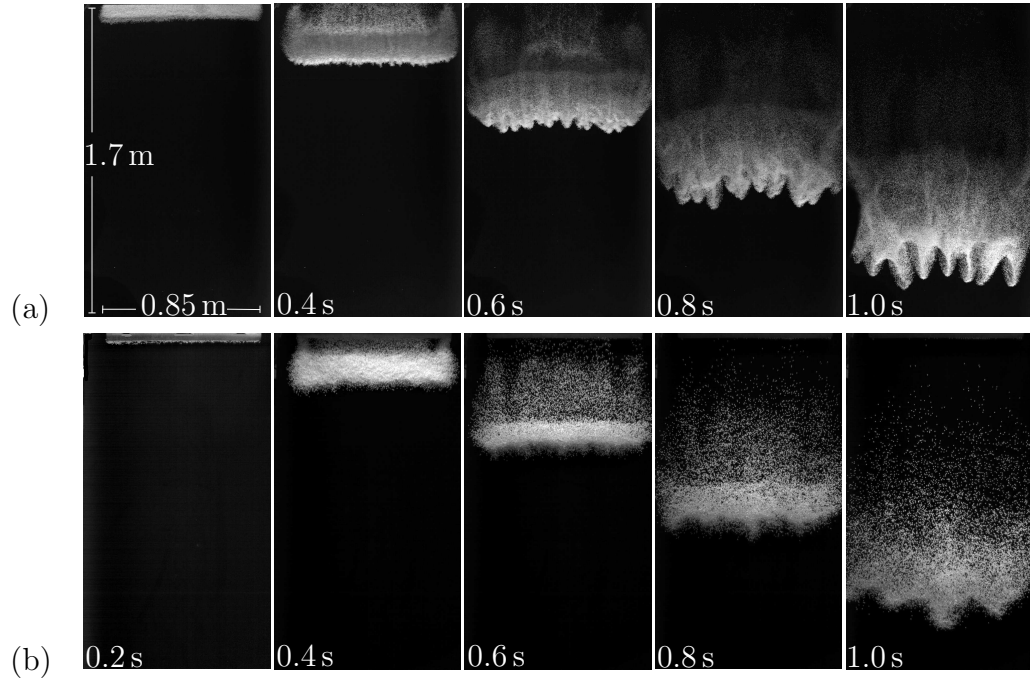


Figure 4.9: Video stills taken at 0.2 s intervals from experiments conducted on a felt surface at an angle of 65° using: (a) 2100 cm³ of 1.8 mm diameter EPS beads and (b) 3300 cm³ of 5.0 mm diameter EPS beads.

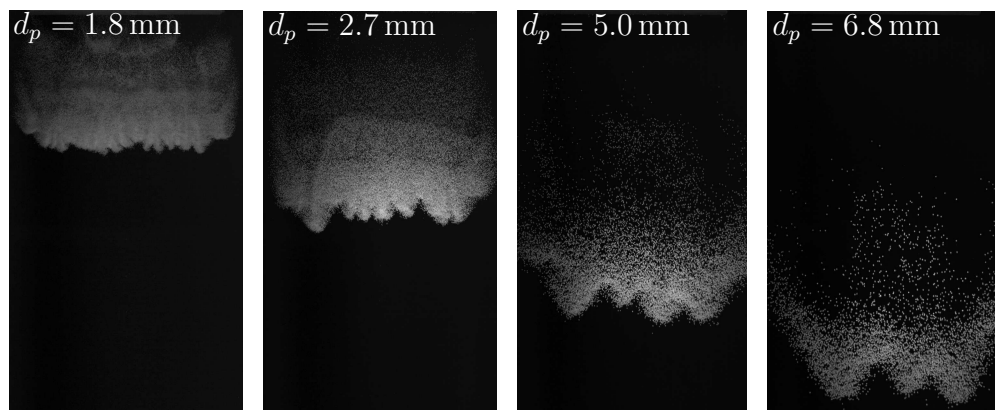


Figure 4.10: Video stills taken at  $\tilde{t}_{d_p} = 50$  from experiments conducted at a slope angle of 65° using 2100 cm³ of: 1.8 mm, 2.7 mm, 5.0 mm and 6.8 mm diameter EPS beads.

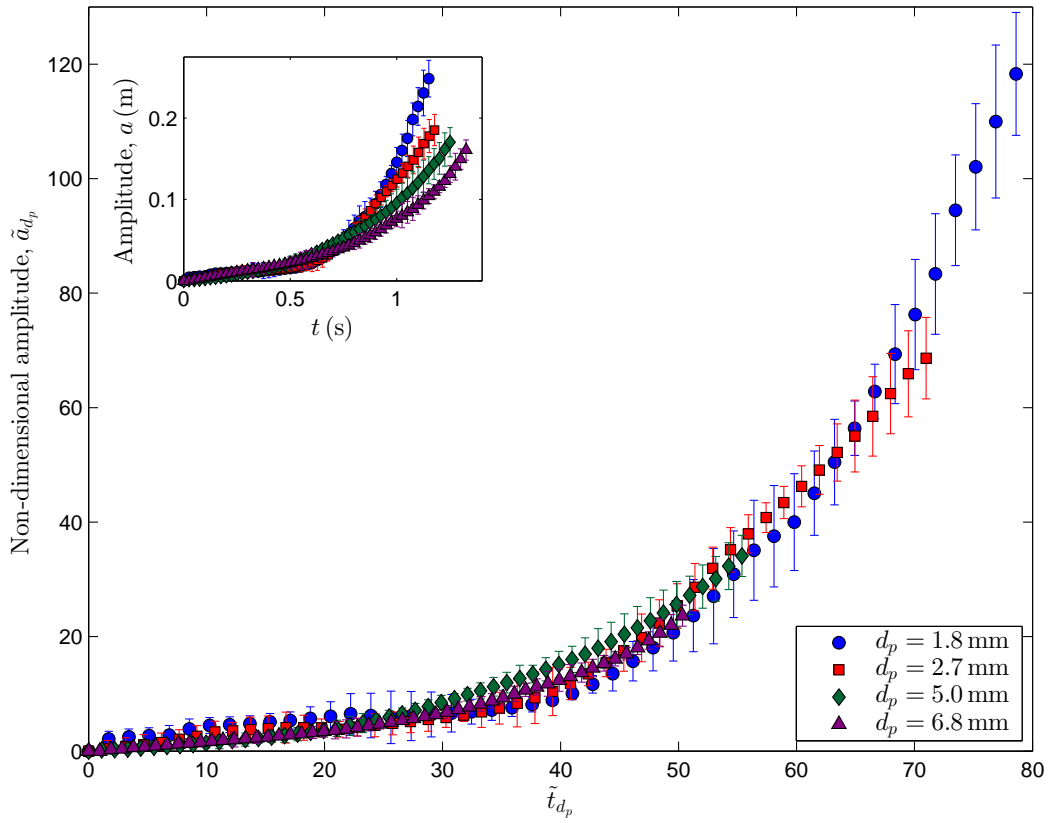


Figure 4.11: Non-dimensional lobe and cleft pattern amplitude ( $\tilde{a}_{d_p}$ ) versus non-dimensional time ( $\tilde{t}$ ) for flows shown in Figure 4.10. Error bars have length equal to  $\pm 1$  standard deviation from the mean.

#### 4.4. FLOW FRONT PATTERNS

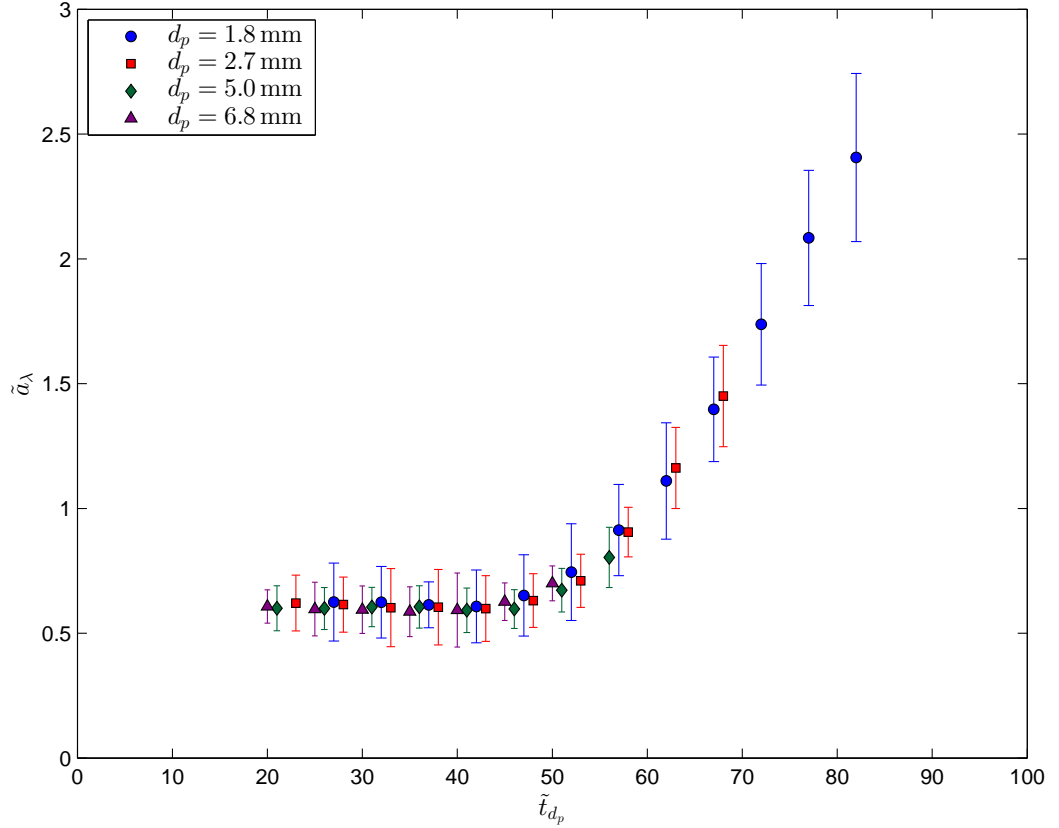


Figure 4.12: Non-dimensional lobe and cleft pattern amplitude ( $\tilde{a}_{d_\lambda}$ ) versus non-dimensional time ( $\tilde{t}$ ) for flows shown in Figure 4.10. Error bars have length equal to  $\pm 1$  standard deviation from the mean.

in Figure 4.10. It can be seen that for a given value of  $\tilde{t}_{d_p}$ , as particle diameter increases the wavelength of the lobe-and-cleft-type pattern and the downslope position of the front also increase.

Both the dimensional,  $a$ , and non-dimensional,  $\tilde{a}_{d_p} = a/d_p$ , amplitudes (§3.8.1) of the lobe-and-cleft-type patterns are shown in Figure 4.11. When viewed dimensionally (Figure 4.11 (inset)) the currents consisting of smaller particles have larger amplitude lobe and cleft patterns. However when scaled with particle diameter (Figure 4.11 (main)), amplitude and its rate of growth appears to be the same for all particle sizes. The currents consisting of smaller particles achieve larger amplitudes due to the fact that, when scaled with particle diameter, the chute appears longer to these currents and they therefore flow over longer  $\tilde{t}_{d_p}$  timescales.

In the images shown at  $\tilde{t}_{d_p} = 50$  (Figure 4.10), the ratio of amplitude to

#### 4.4. FLOW FRONT PATTERNS

wavelength,  $\frac{a}{\lambda}$ , appears to be approximately constant for all EPS bead sizes. When wavelength-scaled amplitude,  $\tilde{a}_\lambda = \frac{a}{\lambda}$ , is calculated for a range of values of  $\tilde{t}_{d_p}$  (Figure 4.12), it can be seen that for values of  $\tilde{t}_{d_p} < \approx 50$  the ratio of amplitude to wavelength remains constant. Since the rate of amplitude growth is increasing (Figure 4.11) during this period, the wavelength must also be increasing at the same rate. For values of  $\tilde{t}_{d_p} > \approx 50$ , the rate of amplitude growth appears to become constant and the ratio of amplitude to wavelength increases, suggesting that during this period the wavelength stays constant whilst amplitude continues to increase. Qualitative observations of this effect were made during the experiments, with the currents consisting of smaller EPS beads forming much more elongated lobes during the later stages of the flow. The size of the chute used meant that while this effect was clearly observable for the currents consisting of smaller particles ( $d_p = 1.3 - 2.7$  mm), the currents consisting of larger particles ( $d_p = 5.0 - 6.8$  mm) reached the bottom of the chute before values of  $\tilde{t}_{d_p} \gg 50$ , and it would be of interest to conduct more experiments using a longer chute in order to fully verify this observation. However, for any future studies conducted using a longer chute, care would have to be taken in order to ensure that the lack of dense material being entrained into the base of the current does not significantly affect the flow dynamics.

Front profiles generated from the two flows in Figures 4.9(a) & 4.9(b) are shown in Figure 4.13, with the gradient and curvature of the corresponding level sets shown in Figures 4.14 & 4.15 respectively. These figures show an initially shifting pattern of lobes and clefts. Lobes develop and grow in size, occasionally bifurcating, whilst clefts regularly merge together. This indicates that the classic lobe-and-cleft instability is dominant during the early phases of the flow. In the later stages of the flow, the position of the lobes is much more stable and there is less merging and bifurcation. As already noted, at later times the amplitude of the lobes has increased, this is particularly apparent for the flows consisting of smaller particles. This indicates that the fingering instabilities observed in unsuspended granular flows become more dominant in the later phases of the flow.

In order to investigate the effects of changing the release volume, wavelength against average distance from the line release for two particle sizes (2.7 mm & 5.0 mm) is shown in Figure 4.16. Results from each of the three different release volumes are plotted separately and it can be seen that the

#### 4.4. FLOW FRONT PATTERNS

---

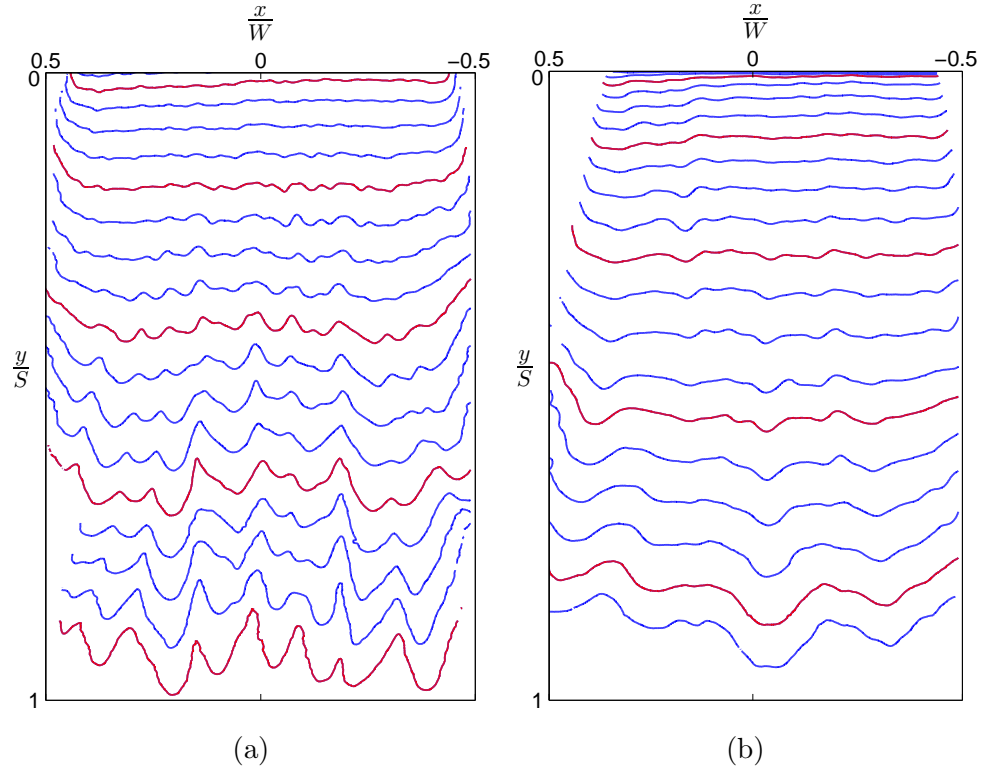


Figure 4.13: (a) & (b) Front profiles at 0.05 s intervals taken from the flows shown in Figures 4.9(a) & (b) respectively. The highlighted profiles correspond to the position of the fronts at the times shown in Figure 4.9.

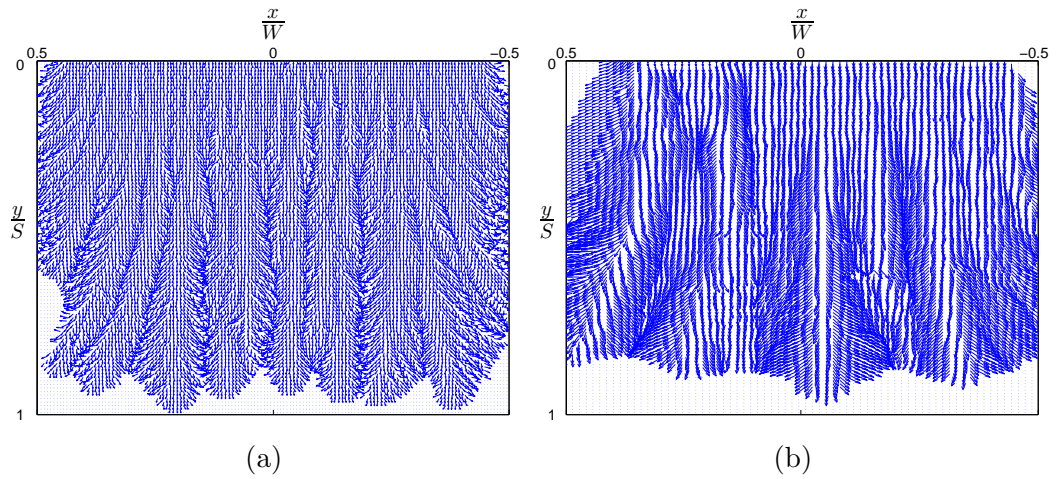


Figure 4.14: (a) & (b) Vector fields showing the gradient of the level set  $T_{ij}$  calculated from the flows shown in Figures 4.9(a) & (b) respectively.

#### 4.4. FLOW FRONT PATTERNS

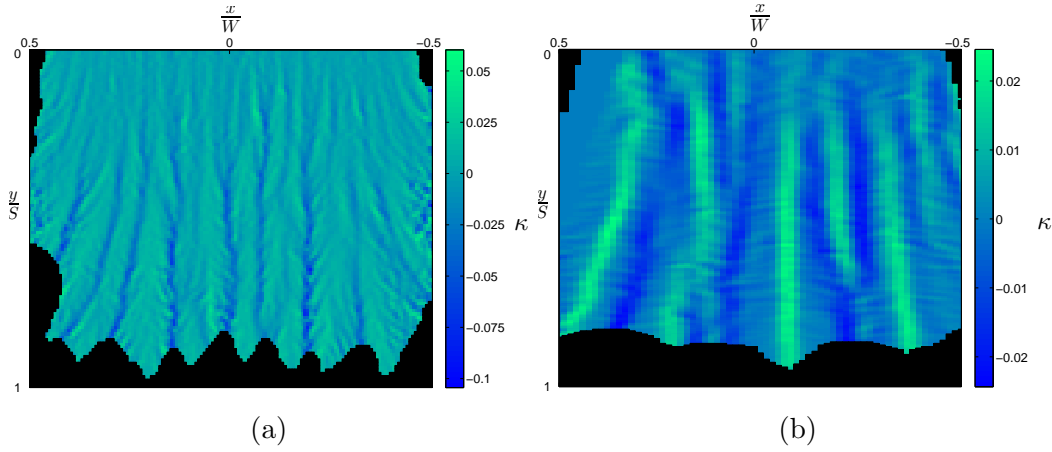


Figure 4.15: (a) & (b) Curvature ( $\kappa$ ) of the level set  $T_{ij}$  calculated from the flows shown in Figures 4.9(a) & (b) respectively. Areas of negative curvature (dark) indicate the location of clefts, whilst areas of positive curvature (light) indicate the location of lobes.

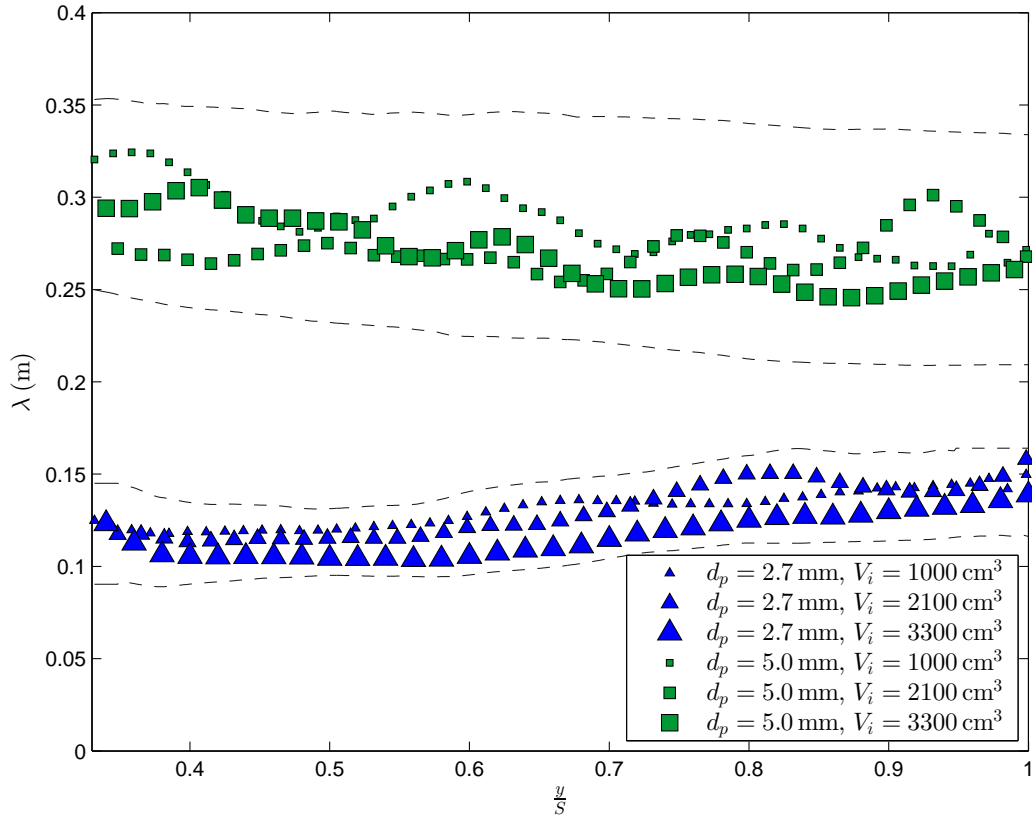


Figure 4.16: Average wavelength ( $\lambda$ ) versus distance from line release ( $\frac{y}{S}$ ) for experiments using 2.7 mm and 5.0 mm diameter particles,  $\pm 1$  standard deviation from the mean (dashed lines). Values of ( $\frac{y}{S}$ ) correspond to the region of the chute where the front of the current is travelling at an approximately constant velocity.

#### 4.4. FLOW FRONT PATTERNS

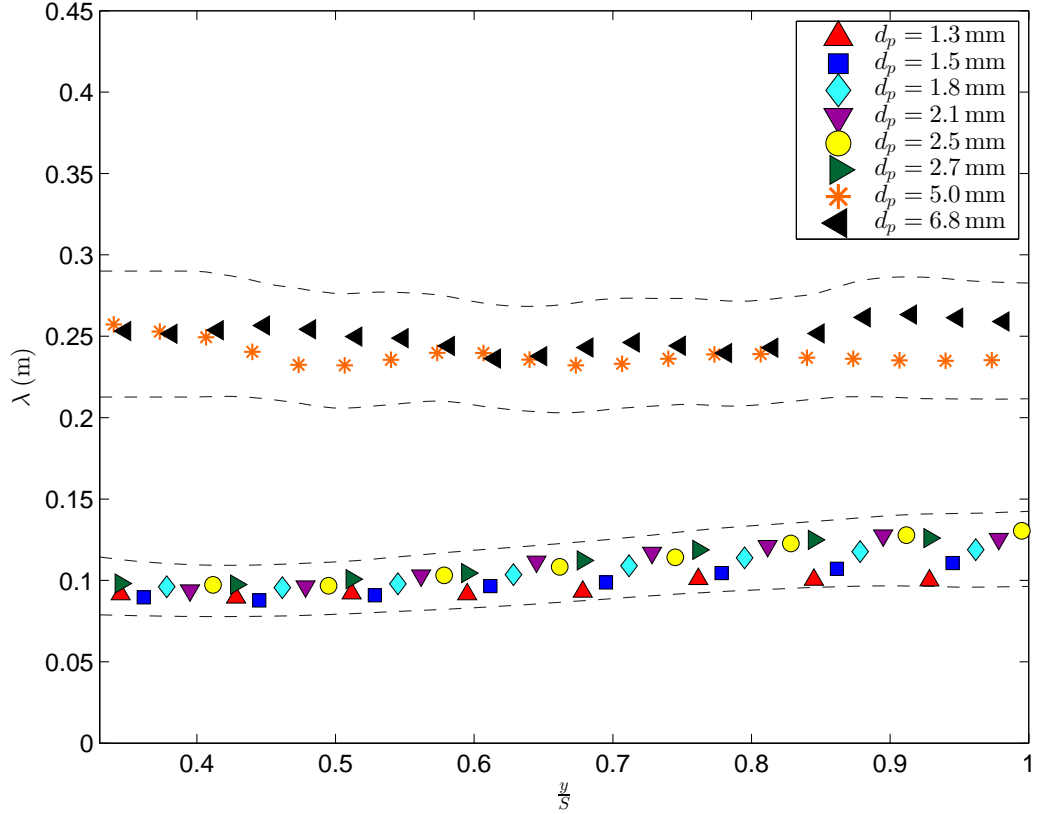


Figure 4.17: Average wavelength ( $\lambda$ ) versus distance from line release ( $\frac{y}{S}$ ),  $\pm 1$  standard deviation from the mean (dashed lines). Values of ( $\frac{y}{S}$ ) correspond to the region of the chute where the front of the current is travelling at an approximately constant velocity.

volume of granular material released has little effect on the wavelength of the pattern in the moving front. However, the data does show that for the currents consisting of larger particles there are regular oscillations in wavelength as the current proceeds down the chute. Such oscillations in wavelength appear to be consistent with the action of classic lobe-and-cleft instability, whereby lobes grow to a certain size before bifurcating into smaller lobes which then grow again and repeat the process. The fact that these oscillations are only observed further down the chute ( $\frac{y}{S} > 0.4$ ) for currents consisting of larger particles again indicates that the classic lobe-and-cleft instability is only dominant during the early stages of the currents' motion, as the currents consisting of larger particles are flowing over much shorter  $\tilde{t}_{d_p}$  timescales than those consisting of smaller particles.

Figure 4.17 shows average wavelength ( $\lambda$ ) plotted against average distance

#### 4.4. FLOW FRONT PATTERNS

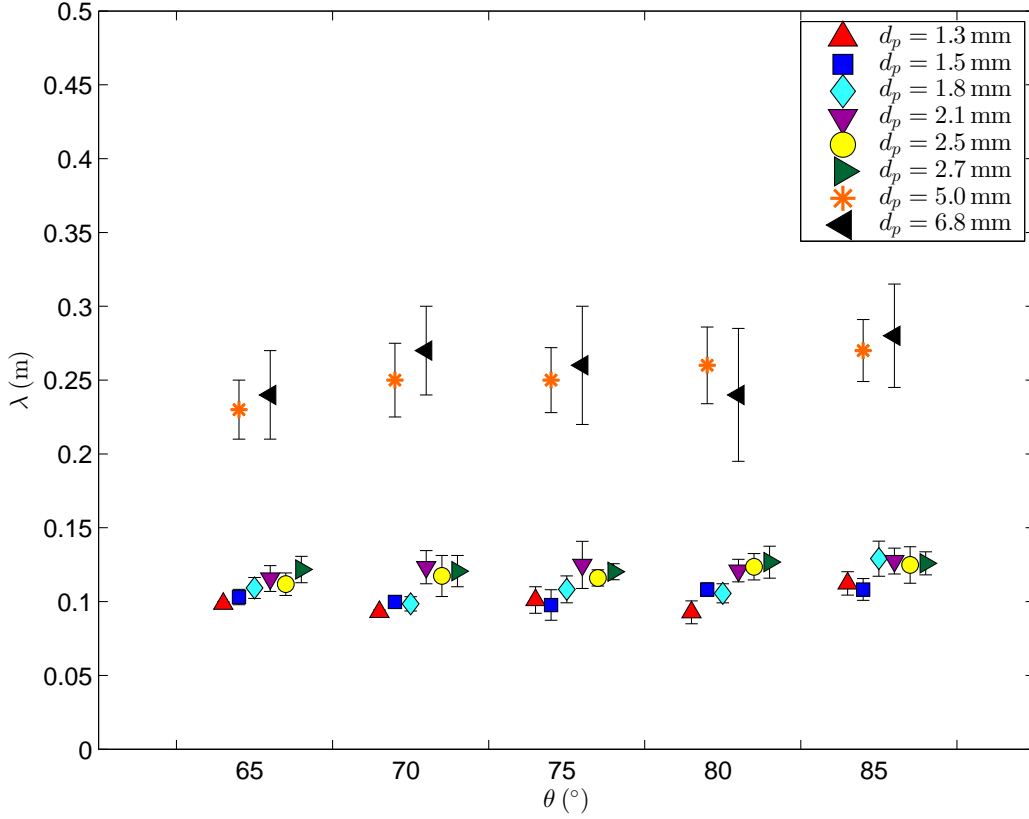


Figure 4.18: Average wavelength ( $\lambda$ ) 1 m from the line release versus slope angle ( $\theta$ ). Error bars have length equal to  $\pm 1$  standard deviation from the mean. Results are offset horizontally for clarity.

from the line release for each particle size. The wavelength values for each particle size are obtained by taking the average from experiments conducted using the three release volumes. The results verify the observation that the pattern observed in the flows made up of smaller particles had a shorter wavelength than those made up of larger particles. It can also be seen that the wavelength remains relatively stable once the flow has reached an approximately constant velocity.

In Figure 4.18 the average wavelength is plotted against slope angle for each of the particle sizes used. Average wavelength was measured at a distance of  $y = 1$  m from the line release, this distance was selected as it is well within the region of the chute where all flows have reached an approximately constant front velocity. It was observed during the experiments that increasing the angle of the slope increased the level of suspension within the flow. At higher slope angles, more air was entrained into the current and its height ( $h_c$ ) per-



#### 4.4. FLOW FRONT PATTERNS

---

pendicular to the slope visibly increased. As the slope angle becomes steeper, the increased component of gravity driving the current is counteracted by an increase in air entrainment [Turnbull and McElwaine, 2007]. However, it can be seen from Figure 4.18 that the wavelength of the pattern is independent of the slope angle, indicating that level of suspension or air entrainment has no effect on the formation of the pattern.

Interestingly, in Figures 4.17 & 4.18 there appears to be a bifurcation in the data between the smaller particles ( $d_p = 1.5 - 2.7$  mm) and the larger particles ( $d_p = 5.0 - 6.8$  mm). This bifurcation could be due to the higher levels of polydispersity of the smaller particles (standard deviation  $\approx 5\%$  of mean particle diameter) compared with the larger particles (standard deviation  $\approx 2.5\%$  of mean particle diameter). Whilst it is possible that the polydispersity-induced granular fingering mechanism observed by Pouliquen et al. [1997] could play a more significant role in the flows consisting of smaller particles, this seems unlikely as in the experiments conducted by Pouliquen et al. this mechanism was only observed when the standard deviation of the mean particle diameter was greater than 10%. Another potential explanation for the bifurcation in the data could be the role played by viscous drag forces for the different particle sizes. As previously mentioned (§2.2), the values of  $Re_p$  are high enough for pressure drag forces to constitute the bulk of the total drag force. However, whilst the larger particles  $Re_p$  values are within the region where the drag coefficient for a spherical particle is independent of  $Re_p$ , the smaller particles values lie just below this region. Therefore, although pressure drag forces are still dominant, viscous forces will have a more significant effect on the drag force acting on the particles.

#### Classic lobe-and-cleft instability mechanisms

When compared with analytical and experimental results obtained using Boussinesq gravity currents consisting of two homogenous fluids (Figure 4.19), the frontal wavelength of the non-Boussinesq EPS bead-air gravity currents shows reasonable agreement with the Grashof number-dependent relationship exhibited by the classic lobe-and-cleft instability [Härtel et al., 2000]. Splitting the EPS bead-air gravity current results according to upper ( $y = 0.5$  m) and lower ( $y = 1$  m) chute position reveals much closer agreement for the upper chute results (RMSE = 0.12) than for the lower chute results (RMSE = 0.37), with the

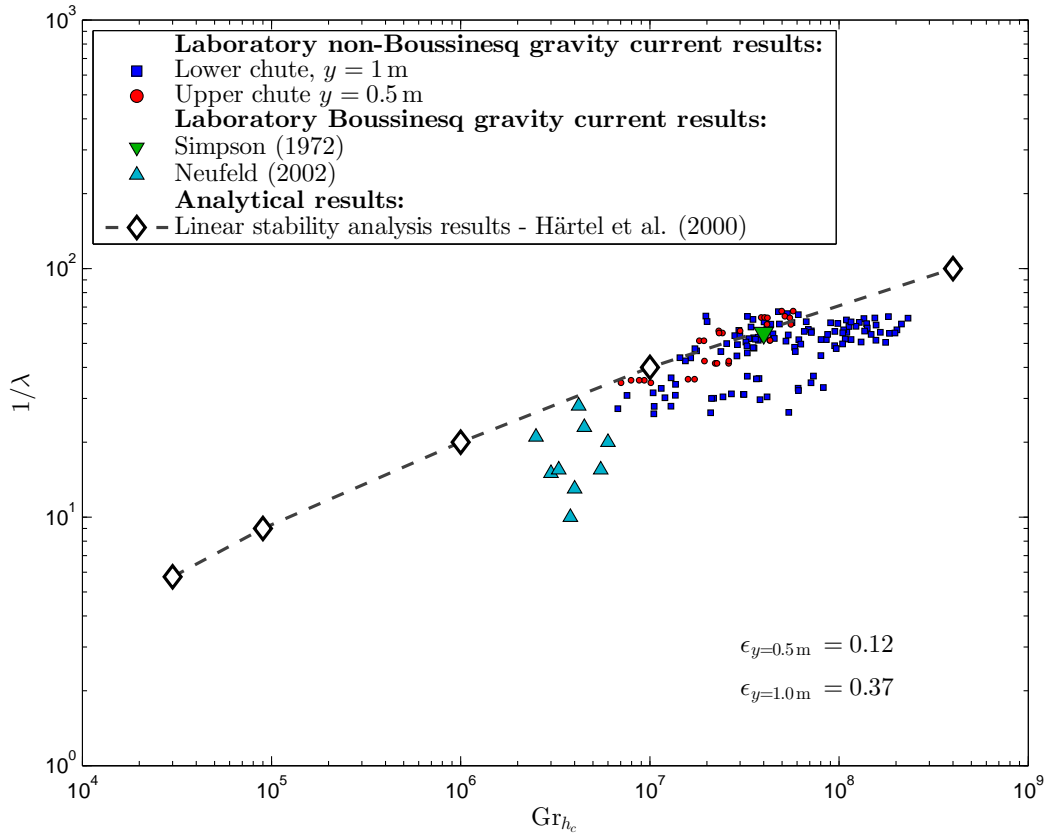


Figure 4.19: Wavenumber,  $1/\lambda$ , versus Grashof number,  $Gr_{hc}$ . Results from experiments conducted using non-Boussinesq gravity currents are compared with experimental and analytical results obtained from Boussinesq gravity currents.

#### 4.4. FLOW FRONT PATTERNS

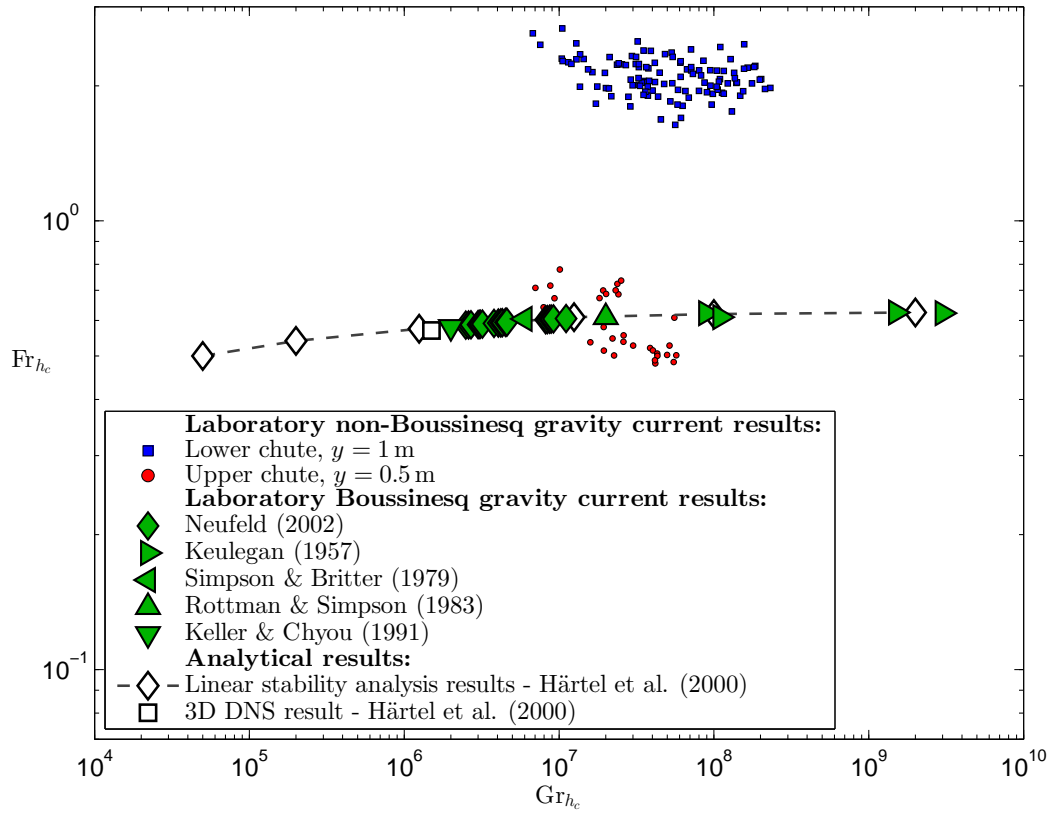


Figure 4.20: Froude number,  $Fr_{hc}$ , versus Grashof number,  $Gr_{hc}$ . Results from experiments conducted using non-Boussinesq gravity currents are compared with experimental and analytical results obtained from Boussinesq gravity currents.

lower chute results generally showing slightly larger wavelengths than would be expected for flows displaying the classic lobe-and-cleft instability.

A relationship between Froude number and Grashof number for flows displaying the classic lobe-and-cleft instability has also been observed (§1.4.1). The Froude number, representing the ratio of kinetic forces (i.e. front velocity) to buoyancy forces, is defined as

$$\text{Fr}_{h_c} = \frac{u}{\sqrt{g'h_c}}, \quad (4.4)$$

and the Grashof number, representing the ratio of buoyancy to viscous forces, is defined as

$$\text{Gr}_{h_c} = \left( \frac{u_b h_c}{\nu} \right)^2, \quad (4.5)$$

where the buoyancy velocity  $u_b = \sqrt{g'h_c}$ . When the EPS-air gravity current upper chute results are compared with results obtained from Boussinesq gravity currents, reasonable agreement is again shown (Figure 4.20). However, the lower chute EPS-air gravity current results have significantly higher Froude numbers than Boussinesq gravity currents with equivalent Grashof numbers, suggesting that the EPS-air gravity currents reach higher front velocities and that buoyancy forces are less significant.

These results appear to further support the qualitative observations made from Figures 4.13, 4.14 & 4.15, that during the early stages of the flows motion the classic lobe-and-cleft instability is dominant and it is this that causes the initial fluctuations at the moving front. As the flows progress down the chute and the front velocity increases, the classic lobe-and-cleft instability becomes insignificant and another type of instability, most likely one of the fingering instabilities observed in unsuspended granular flows, becomes dominant.

### Granular flow instability mechanisms

As previously mentioned, it seems unlikely that the granular fingering mechanism observed by Pouliquen et al. [1997] and Pouliquen and Vallance [1999] is responsible for the development of the frontal pattern of the EPS-air gravity currents during the later stages of the flows' motion (when  $U_f \approx \text{constant}$ ) as the polydispersity of the EPS bead used in this study is less than 10%. Instead it seems more likely that the development of the frontal pattern is determined

#### 4.4. FLOW FRONT PATTERNS

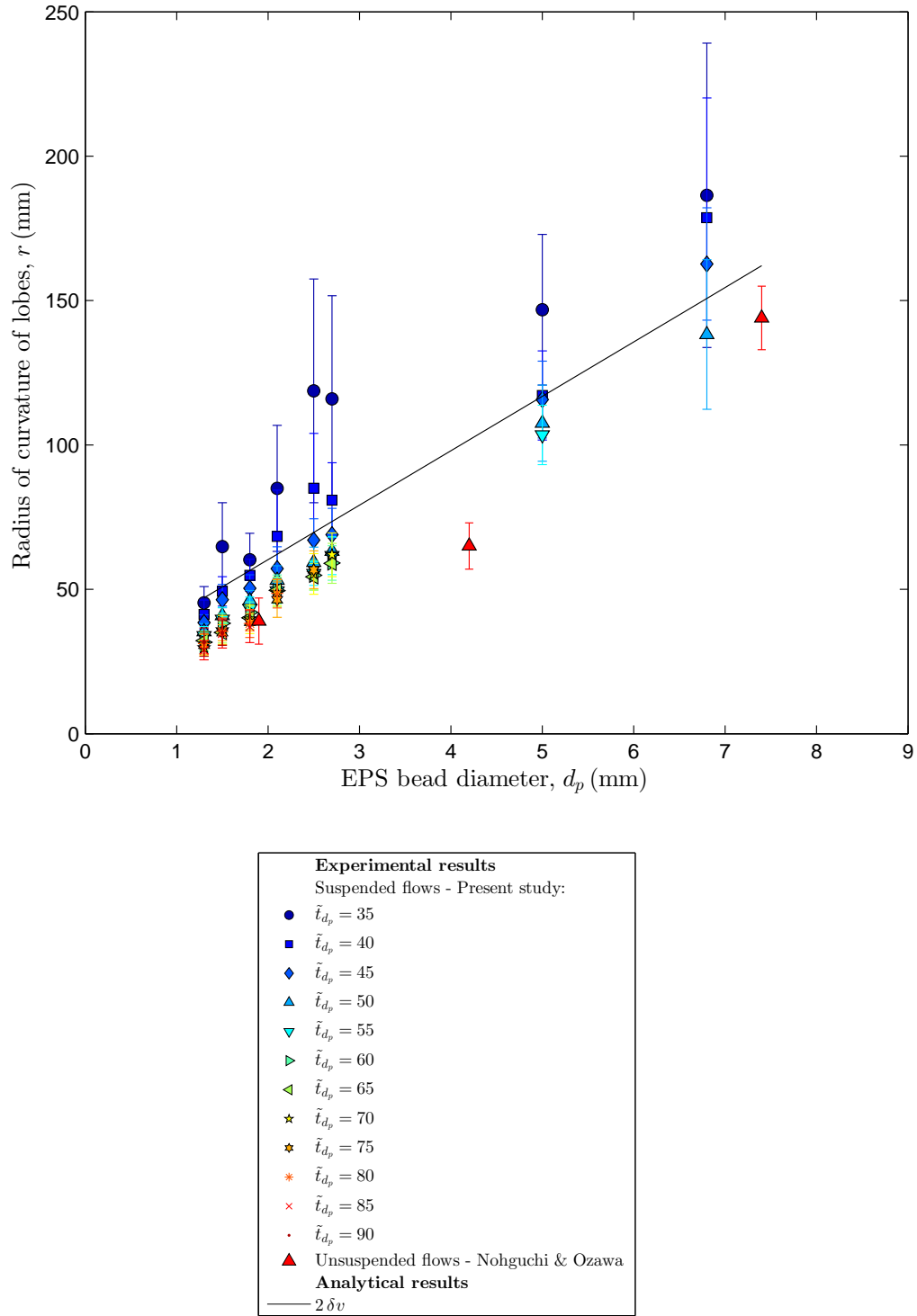


Figure 4.21: Radius of curvature,  $r$ , of lobes versus EPS bead diameter,  $d_p$ , at different values of  $\tilde{t}_{d_p}$ . Results of fully-suspended EPS bead-air gravity currents are compared with experimental and analytical results of unsuspended EPS bead flows [Nohguchi and Ozawa, 2008]. Error bars have length equal to  $\pm 1$  standard deviation from the mean.

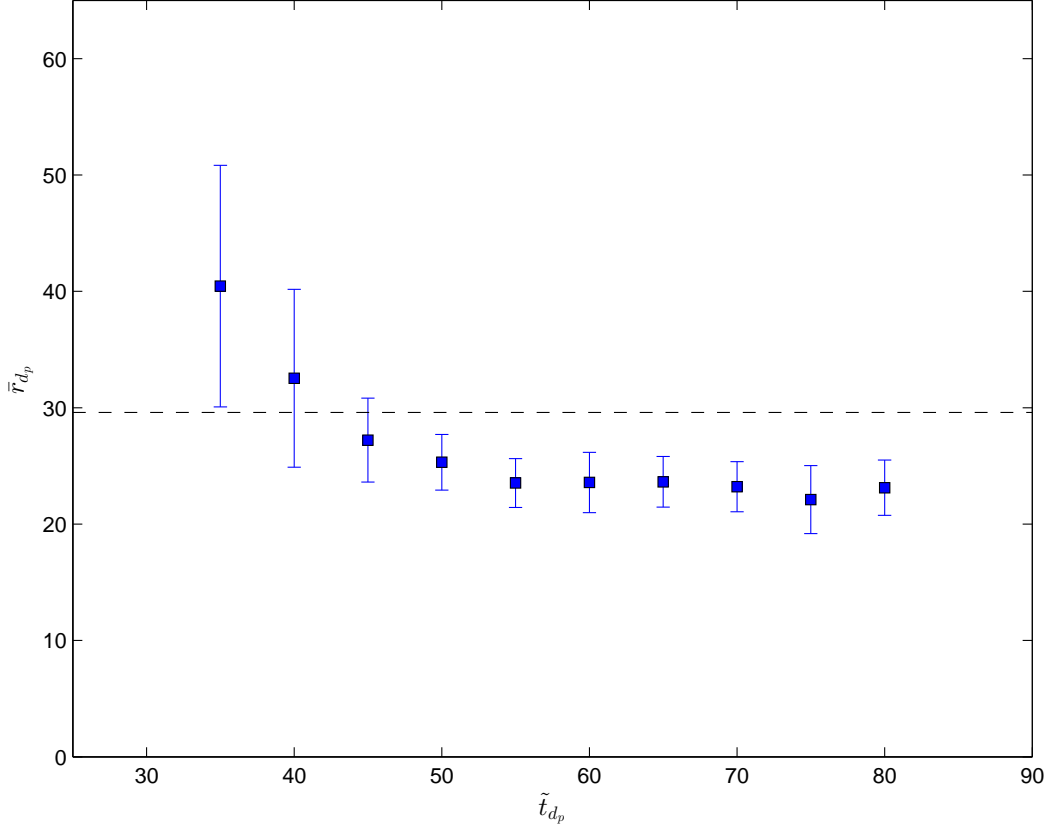


Figure 4.22: Mean non-dimensional radius of curvature,  $\tilde{r}_{d_p}$  versus non-dimensional time,  $\tilde{t}_{d_p}$  for experiments conducted using  $d_p = 2.1$  mm EPS beads. The dotted line represents the analytical result ( $2\delta v$ ) for  $d_p = 2.1$  mm EPS beads [Nohguchi and Ozawa, 2008], and the error bars are  $\pm 1$  standard deviation from the mean value in length.

by drag forces created by the interaction between a flow's particles and the ambient fluid.

For comparison with the results of Nohguchi and Ozawa [2008], the mean radius of curvature (§3.10) of the lobes for each particle size was calculated (Figure 4.21). These values were calculated from the level set contours at all available values of  $\tilde{t}_{d_p}$  for each EPS bead size.

The lobes at the leading edge of the flows consisting of smaller particles had smaller radii of curvature (Figure 4.21), consistent with the observations of sharper lobes and smaller wavelengths for these flows. For each EPS bead size, the lobe radii of curvature were initially ( $\tilde{t}_{d_p} < \approx 50$ ) larger than the value predicted by the velocity boundary layer theory and there is a large amount of scatter in the data (Figures 4.21 and 4.22). This again suggests that in the

#### 4.4. FLOW FRONT PATTERNS

---

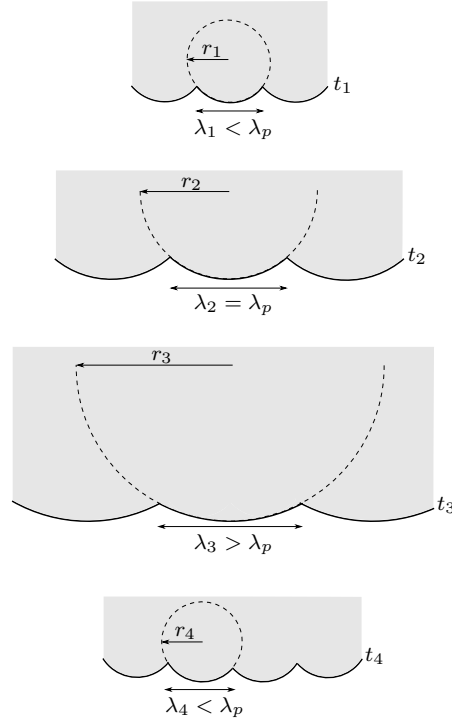


Figure 4.23: Variation in radius of curvature of a lobe  $r$  as wavelength  $\lambda$  increases.  $t_1 < t_2 < t_3 < t_4 < \tilde{t}_{d_p} \approx 50$  and  $\lambda_p$  represents the preferred wavelength of the classic lobe-and-cleft instability, above which the lobe will bifurcate into two smaller lobes ( $t_4$ ).

early stages, lobe size is determined by the classic lobe-and-cleft instability, resulting in the formation of a shifting lobe and cleft pattern with shallow clefts or small amplitude lobes. Classic lobe-and-cleft instability theory suggests the existence of a preferred wavelength  $\lambda_p$  for the flow. Figure 4.23 illustrates the evolution of a lobe over time; showing how a lobe grows until it reaches  $\lambda_p$ , whereupon it bifurcates, and the resulting variation in lobe radius of curvature that occurs throughout this process. For lobe and cleft patterns with relatively small amplitudes, increases in amplitude will also cause variation in lobe radius of curvature, as illustrated in Figure 4.24.

At later stages in the flows' motion ( $\tilde{t}_{d_p} > \approx 50$ ), lobe radius of curvature for each EPS bead size becomes approximately constant as  $\tilde{t}_{d_p}$  increases, and there is much less scatter in the data (Figures 4.21 and 4.22). This is in agreement with observations and lobe and cleft amplitude measurements during the later stages of the flows motion that show that there is less shifting of the lobe-and-cleft-type pattern, and that the clefts become deeper and the lobes more extended. Figure 4.25 illustrates how, for this type of lobe and cleft pattern, as the flow progresses and the lobe and cleft amplitude increases, the radius

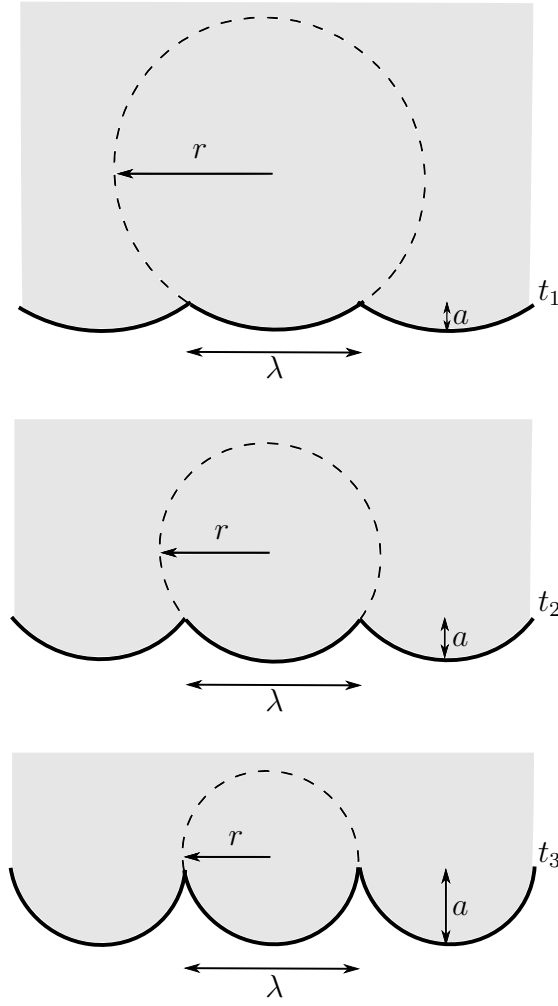


Figure 4.24: Variation in radius of curvature of a lobe  $r$  of wavelength  $\lambda$  as amplitude  $a$  increases for  $\tilde{t}_{dp} < \approx 50$ .

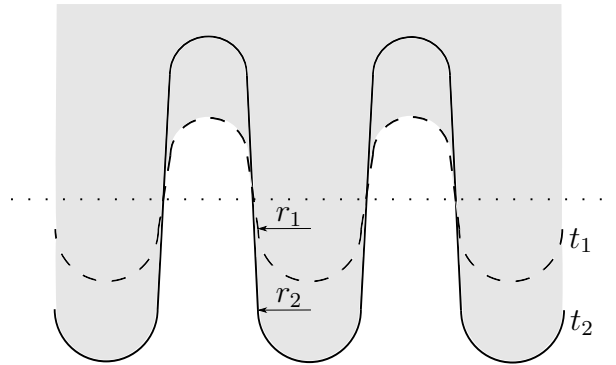


Figure 4.25: Pattern of extended lobes and clefts observed at  $\tilde{t}_{dp} > \approx 50$ . Frontal patterns at  $t_1$  and  $t_2$  ( $t_1 < t_2$ ) are overlaid with the dotted line representing the centreline of the lobe and cleft pattern. Lobe radius of curvature  $r$  remains approximately constant as  $t$  increases.



#### 4.4. FLOW FRONT PATTERNS

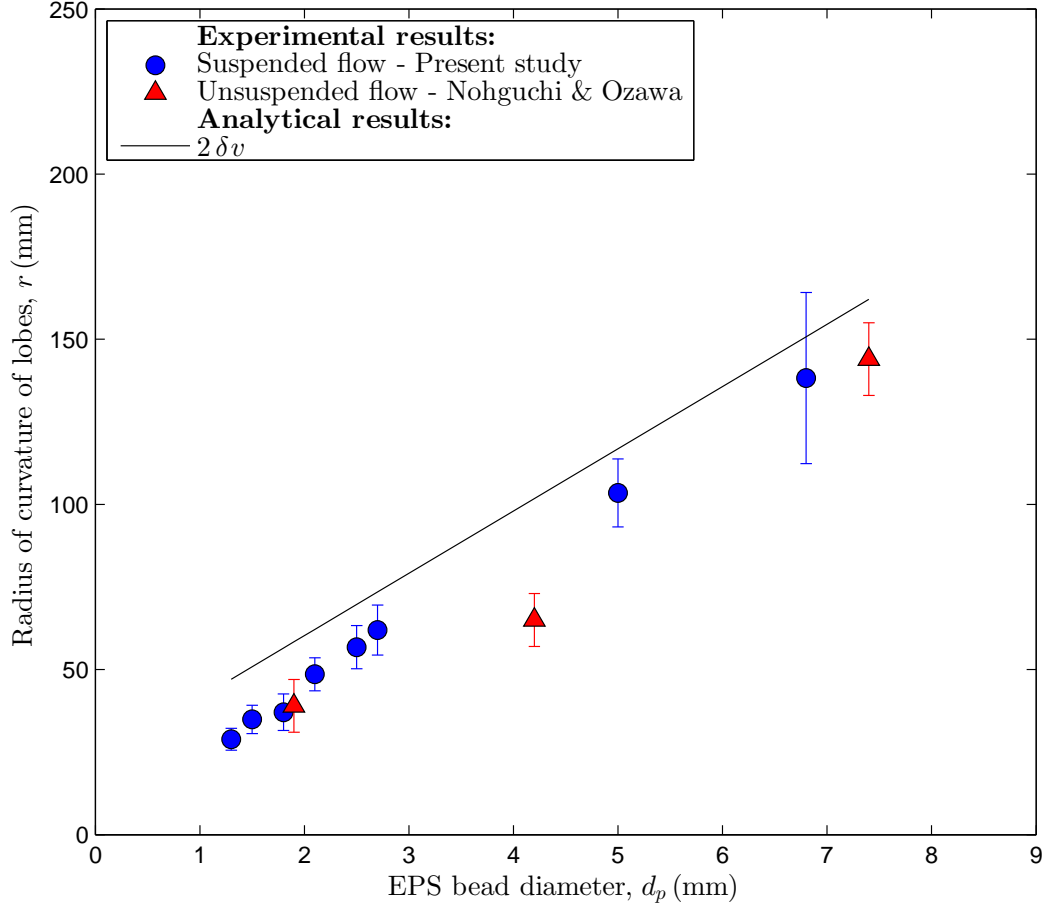


Figure 4.26: Radius of curvature,  $r$ , of lobes versus EPS bead diameter,  $d_p$ , at maximum available values of  $\tilde{t}_{dp}$ . Results of fully-suspended EPS bead-air gravity currents (●) are compared with experimental (▲) and analytical results (solid line) of unsuspended EPS bead flows [Nohguchi and Ozawa, 2008]. Error bars have length equal to  $\pm 1$  standard deviation from the mean.

of curvature remains approximately constant.

The lobe radii of curvature at later values of  $\tilde{t}_{dp}$  show good agreement with Nohguchi and Ozawa’s experimental data (Figures 4.26 and 4.22), and suggest that the dominant mechanism for the development of the lobe-and-cleft-type pattern is no longer the classic lobe-and-cleft instability but is instead a velocity boundary layer forming at the moving front. However both sets of data are slightly below the analytical estimate  $r \approx 2\delta_v$ . When deriving the expression for boundary layer thickness Nohguchi and Ozawa ignored inter-particle collisions in the velocity boundary layer for simplification. In reality, a particle moving through the velocity boundary layer is likely to experience collisions with other particles, reducing the distance that it can move against the drag

force of the ambient fluid. Therefore the analytical results are likely to overestimate the velocity boundary layer thickness which may explain the discrepancy seen between the theoretical and experimental results.

### Rayleigh-Taylor instability mechanisms

The Rayleigh-Taylor instability should be the limiting case as we tend towards a vertical chute. Hydrodynamically, the growth of the Rayleigh-Taylor instability is predicted by a perturbation analysis that shows that the growth rate of the fingers depends on the perturbation wavelength [Chandrasekhar, 1961, Youngs, 1984, Duff et al., 1962, Sharp, 1984]. In the presence of a stabilising influence e.g. viscosity or surface tension, some wavelengths are damped and a dominant mode develops. In the EPS suspension experiments, neither viscosity nor surface tension is present. However, it can be speculated that the air drag experienced by the particle clusters, and the restrictions on lobe shape that this imposes [Bush et al., 2003], would play a similar role in allowing a dominant wavelength to grow. This should provide a rich focus for future modelling.

## 4.5 Scaling of lobe-and-cleft-type patterns

Both granular fingering [Pouliquen et al., 1997] and velocity boundary layer [Nohguchi and Ozawa, 2008] theories suggest that the velocity of the moving front could play a role in determining the wavelength of the pattern that forms at the front. Fingers are created due to differences in velocity between smaller particles and larger particles that slow down due to higher levels of friction as they bunch up around clefts. A velocity boundary layer's thickness will also be affected by the front velocity, which could in turn affect the wavelength of the pattern.

Using the variables shown in the schematic (Figure 4.1), the non dimensional group, which is the Froude number

$$\text{Fr} = \frac{U_f}{\sqrt{g'L \sin \theta}}, \quad (4.6)$$

can be formed, where  $L$  is an appropriate length scale. The theory of a ve-

#### 4.5. SCALING OF LOBE-AND-CLEFT-TYPE PATTERNS

---

locity boundary layer at the moving front (§1.4.2) suggests that there is a relationship between front velocity and wavelength which is determined by an individual particle's interaction with the ambient air. As previously mentioned, Nohguchi and Ozawa [2008] have proposed that the wavelength of the frontal pattern is determined by the size of pairs of vortices that form at the moving front. The size of these vortices is in turn determined by the thickness of the velocity boundary layer. Faster moving flows will have thicker velocity boundary layers as the particles can move a greater distance against the drag force of the static air, resulting in the formation of larger vortices and therefore a larger wavelength pattern. From Equation 1.8 it can be seen that the particle diameter  $d_p$  is a key variable in determining the boundary layer thickness  $\delta_v$ , therefore we will look for a relationship between Froude number and wavelength based on the length scale  $L = d_p$ .

Alternatively, the front velocity of homogenous Boussinesq gravity currents has been found to scale with current height,  $h_c$  [Simpson, 1997]. A relationship between the wavelength of classic lobe-and-cleft instability-induced frontal patterns and current height-based Grashof numbers has also been found for homogenous Boussinesq gravity currents [Härtel et al., 2000, Neufeld, 2002]. This length scale represents the interaction with the ambient air of the current as a whole. Therefore, in order to investigate the effects of this interaction, or any further role played by the classic lobe-and-cleft instability in these non-Boussinesq particle-laden gravity currents we will also look for a relationship between Froude number and wavelength based on the length scale  $L = h_c$ .

Finally, given the success of the initial release volume,  $V_i$ , in scaling the front velocities of the currents studied in this work (§4.1), we will also look for a relationship between Froude number and wavelength based on the length scale  $L = V_i$ . This length scale represents the effect of initial conditions on the subsequent front velocity and lobe-and-cleft-type pattern wavelength.

The dimensionless wavelength ( $\tilde{\lambda}_{d_p} = \lambda/d_p$ ) is plotted against Froude number in Figure 4.27. Interestingly, when scaled with a length scale characterised by the particle diameter there appears to be a monotonically increasing relationship between Froude number and wavelength. The limiting cases of this relationship are determined by the particle diameter ( $\lambda_{\min} = d_p$  therefore  $\tilde{\lambda}_{d_p} = 1$ ) and chute width ( $\lambda_{\max} = 2W$  therefore  $\tilde{\lambda}_{d_p} \approx 2000$ ). A linear fit

#### 4.5. SCALING OF LOBE-AND-CLEFT-TYPE PATTERNS

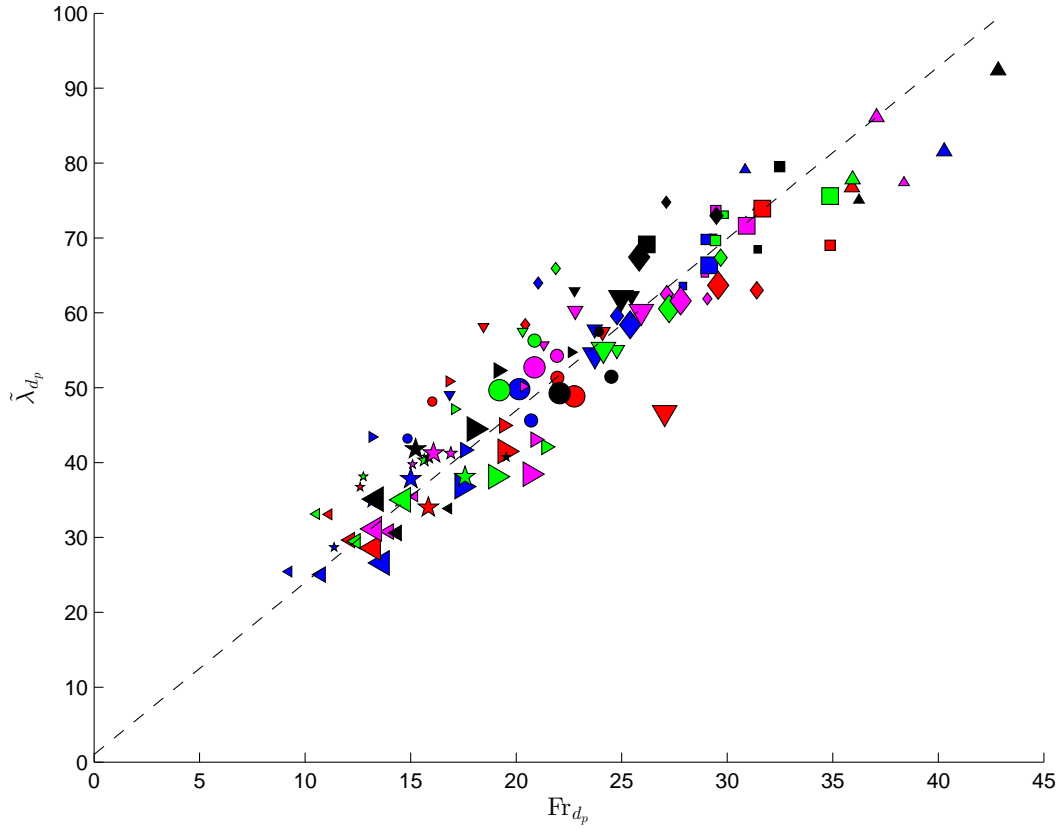


Figure 4.27: Non-dimensional wavelength ( $\tilde{\lambda}_{d_p}$ ) versus Froude number ( $Fr_{d_p}$ ). Particle sizes: 1.3 mm ( $\triangle$ ), 1.5 mm ( $\square$ ), 1.8 mm ( $\diamond$ ), 2.1 mm ( $\nabla$ ), 2.5 mm ( $\circ$ ), 2.7 mm ( $\triangleright$ ), 5.0 mm ( $\star$ ) and 6.8 mm ( $\triangleleft$ ). Slope angles: 65° (blue), 70° (red), 75° (green), 80° (magenta) and 85° (black). Marker size corresponds to the size of the release volume. Dashed line shows linear fit,  $\tilde{\lambda}_{d_p} = 2.3 Fr_{d_p} + 1$  (Equation (4.7)).

## 4.6. CHUTE SURFACE FRICTION

---

of the data,

$$\tilde{\lambda}_{d_p} = 2.3 \text{Fr}_{d_p} + 1, \quad (4.7)$$

is shown in Figure 4.27, with a residual of 0.12, indicating a good level of fit. This is in contrast to the other two length scales considered,  $L = h_c$  &  $L = V_i$ , for which no clear collapse of the scaled data was observed.

The dimensionless rendering of the data show in Figure 4.27 seems to offer good agreement with the concept of a velocity boundary layer determining the wavelength of the frontal pattern. The data shows that when scaled with respect to particle diameter, the smaller particles have higher velocities and therefore thicker boundary layers, resulting in wider lobes and a larger wavelength.

It therefore appears that flows of fully suspended, lightweight granular material exhibit characteristics of the instabilities found at the leading edge of both homogenous particle-laden gravity currents and flows of unsuspended granular material. During the early stages of motion a classic lobe-and-cleft instability mechanism, similar to that observed in homogenous particle-laden gravity currents, appears to be dominant. As the flow propagates down the slope the pattern of lobes and clefts becomes more stable, suggesting that the dominant instability mechanism is now more similar to those observed in unsuspended granular flows. Particle diameter of the granular material plays a central role in determining the wavelength of the lobe-and-cleft-type pattern, as hypothesised by Nohguchi and Ozawa [2008]. When scaled with particle diameter, a relationship between Froude number of the flow and wavelength of the lobe-and-cleft-type pattern is found. This relationship highlights the importance of the role played by drag forces acting on the individual particles in determining the wavelength of the frontal pattern, and appears to support the concept of a velocity boundary layer at the moving front of the flow.

## 4.6 Chute surface friction

The raised nose of a gravity current is caused by friction between the current and the surface that it is flowing over. Given the potential importance of the unstable region generated by the raised nose and the effect that it may have on the instability that develops at the moving front [Härtel et al., 2000], several

## 4.6. CHUTE SURFACE FRICTION

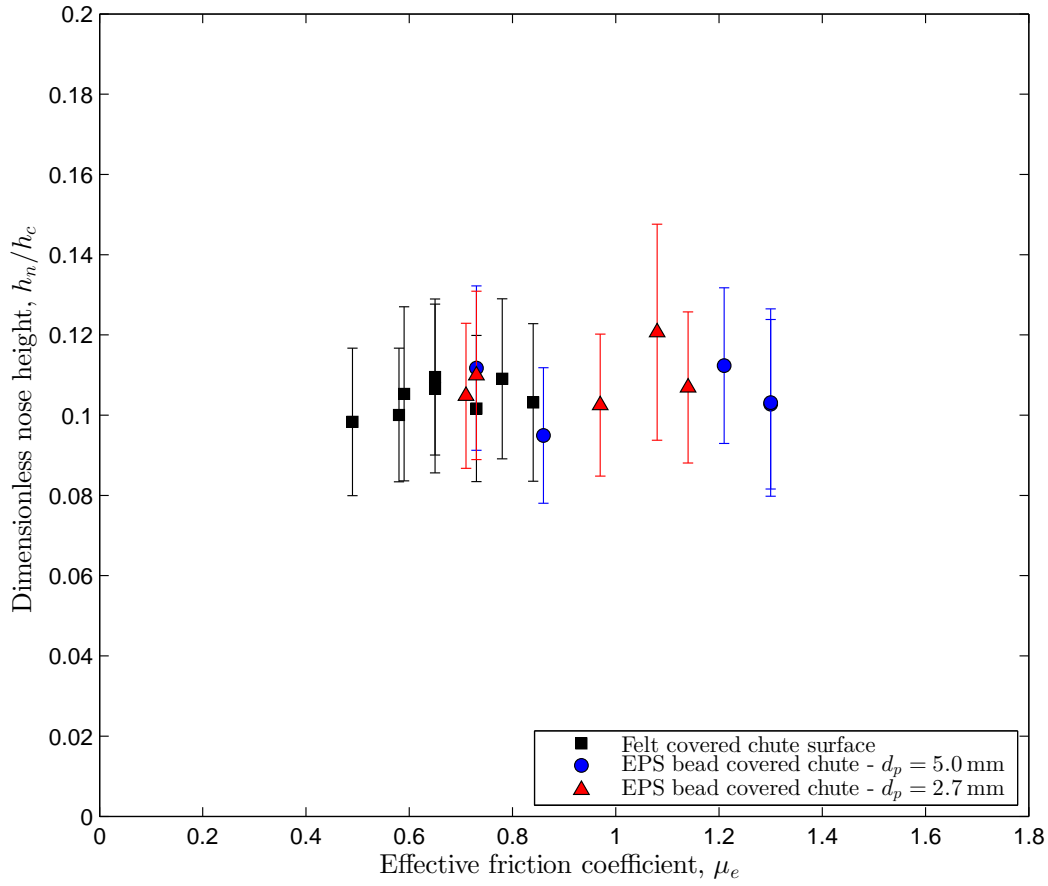


Figure 4.28: Dimensionless nose height,  $\frac{h_n}{h_c}$  versus effective friction coefficient,  $\mu_e$  for experiments conducted using different chute surfaces. Markers represent mean values of  $\frac{h_n}{h_c}$ , with error bar lengths equal to  $\pm 1$  standard deviation from the mean.

#### 4.6. CHUTE SURFACE FRICTION

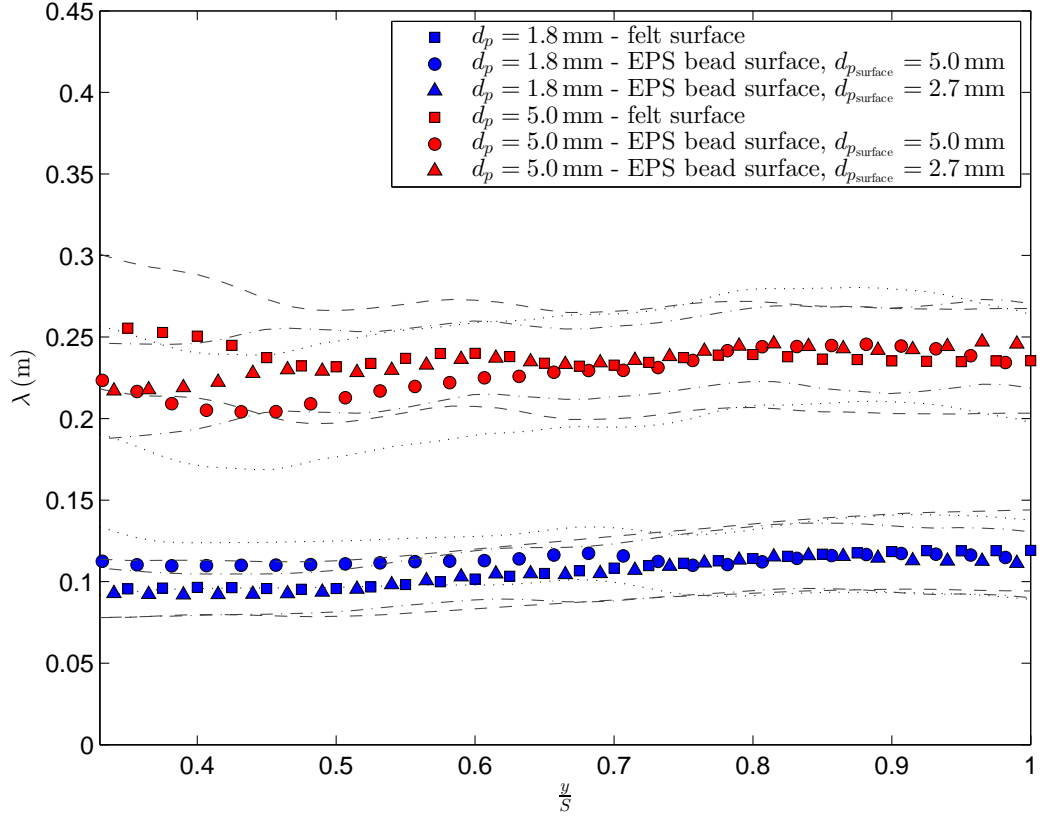


Figure 4.29: Wavelength,  $\lambda$ , versus distance from line release,  $y/S$  for experiments conducted using EPS beads with diameter,  $d_p = 1.8$  mm and  $d_p = 5.0$  mm on different chute surfaces. Dashed lines represent  $\pm 1$  standard deviation from the mean.

different chute surfaces were prepared in order to vary the effective friction coefficient between the current and the chute surface (§2.2.3). However, the dimensionless nose height data collected from experiments using these different surfaces shows no dependence on the effective friction coefficient for the EPS bead gravity currents (Figure 4.28).

Chute surface roughness also had no visible effect on the wavelength of the lobe-and-cleft-type pattern at the moving front of the EPS bead gravity currents (Figures 4.29 & 4.30). The relatively low density and viscosity of these gravity currents mean that the boundary layer over which chute surface friction forces have an effect is likely to be very thin ( $\approx 1 d_p$ ), and therefore variations in chute roughness have no effect on the velocity of particles within the flow.

#### 4.6. CHUTE SURFACE FRICTION

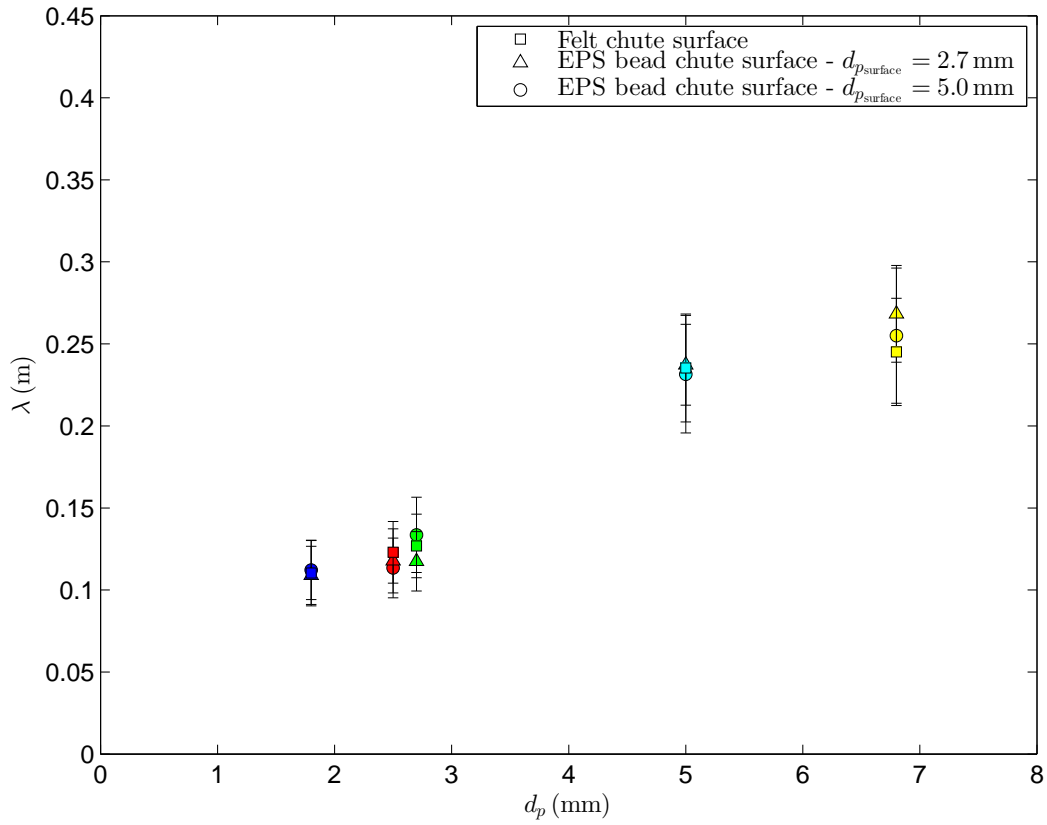


Figure 4.30: Wavelength,  $\lambda$ , versus EPS bead diameter,  $d_p$  for experiments conducted using different chute surfaces. Markers represent mean value of  $\lambda$  at a distance of 1 m from the line release, with error bar lengths equal to  $\pm 1$  standard deviation from the mean.



#### 4.7. POLYDISPERSITY OF EPS BEADS

	Small EPS beads	Large EPS beads	Difference in mean $d_p$
Mixture 1	95% $1.5 \pm 0.06$ mm	5% $1.8 \pm 0.09$ mm	20%
Mixture 2	95% $1.5 \pm 0.06$ mm	5% $2.1 \pm 0.07$ mm	40%
Mixture 3	95% $1.5 \pm 0.06$ mm	5% $2.5 \pm 0.09$ mm	67%
Mixture 4	95% $1.5 \pm 0.06$ mm	5% $5.0 \pm 0.13$ mm	233%
Mixture 5	95% $1.5 \pm 0.06$ mm	5% $6.8 \pm 0.20$ mm	353%

Table 4.1: Mixtures of EPS beads used polydisperse particle experiments. The percentages are in release volume ( $V_i$ ).

### 4.7 Polydispersity of EPS beads; granular fingering instability

For the majority of the experiments conducted in this study care was taken to minimise the effects of polydispersity by sieving the EPS beads into narrow size distributions. The spread of these distributions was typically  $\approx \pm 4\%$  of the mean particle diameter  $d_p$  for the distribution. Pouliquen et al. [1997] and Pouliquen and Vallance [1999] found that for unsuspended flows of granular material, the addition of a small amount ( $\approx 5\%$ ) of another granular material could lead to the formation of a finger-like pattern at the leading edge of the flow. However, this effect was only observed when the mean particle diameter of the added material was at least 14% larger than the mean diameter of the bulk material. In order to investigate whether this granular fingering instability could potentially play a role in fully-suspended, particle-laden gravity currents, five different mixtures of EPS beads were prepared (Table 4.1). Similar to the mixtures used by Pouliquen et al. [1997] and Pouliquen and Vallance [1999], 5% of the release volume,  $V_i$ , was made up of material with a larger particle diameter than the bulk material. The size of the added material ranged from 20 – 350% larger than the mean diameter of the bulk material, providing a good comparison with the range used by Pouliquen et al. [1997], Pouliquen and Vallance [1999] of 14 – 500%. Once prepared, the mixtures were placed in the release hopper ( $V_i = 2100 \text{ cm}^3$ ) and experiments conducted using the same procedure as used for monodisperse EPS beads, described in Chapter 2.

Comparing the wavelength and amplitude of the frontal pattern formed at the leading edge of these flows with those of flows consisting of quasi-monodisperse EPS beads (Figures 4.31 and 4.32), it appears that the poly-

## 4.7. POLYDISPERSITY OF EPS BEADS

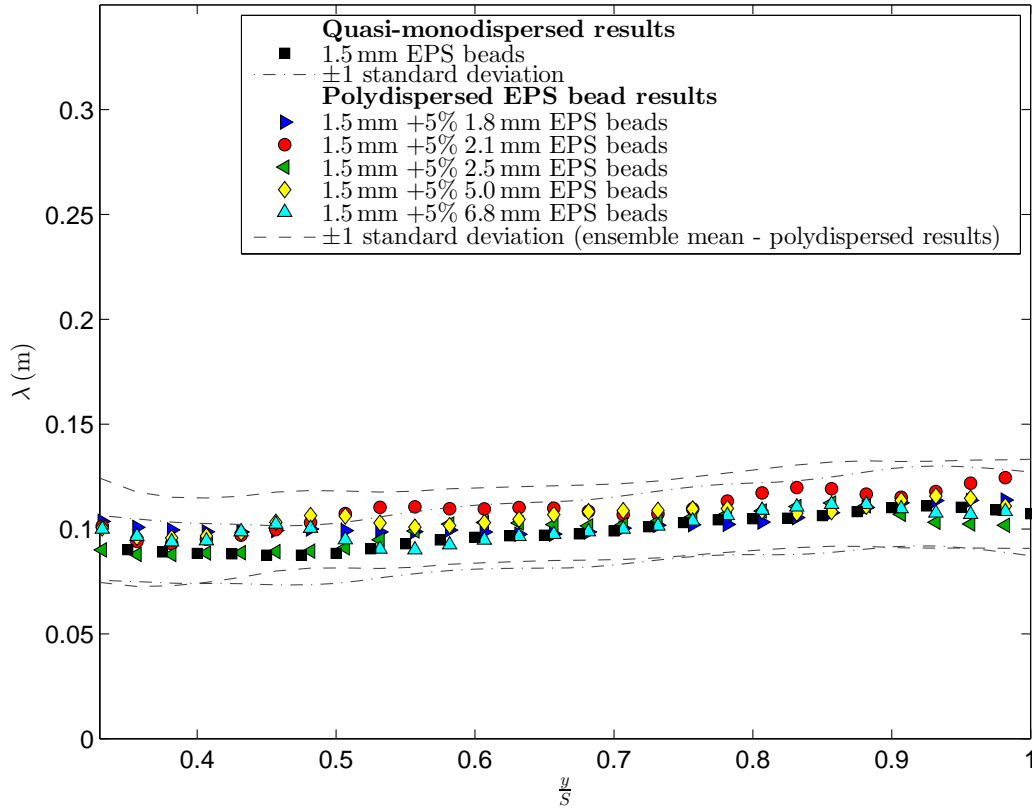


Figure 4.31: Comparison of wavelength versus distance results from experiments conducted using quasi-monodisperse and polydisperse EPS beads. Note: for clarity  $\pm 1$  standard deviation data for polydisperse EPS beads is presented as the ensemble mean of standard deviation data for all polydisperse EPS bead mixtures.

#### 4.7. POLYDISPERSITY OF EPS BEADS

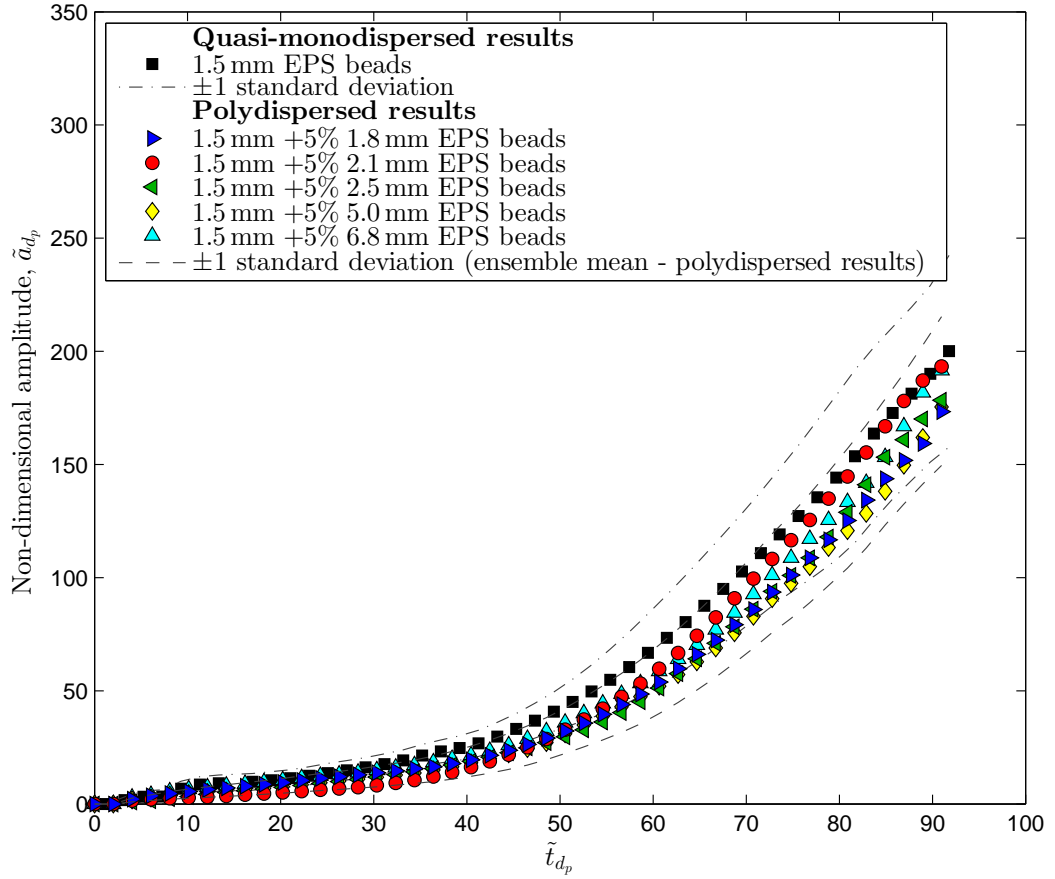


Figure 4.32: Comparison of non-dimensionalised amplitude versus time results from experiments conducted using quasi-monodisperse and polydisperse EPS beads. Note: for clarity  $\pm 1$  standard deviation data for polydisperse EPS beads is presented as the ensemble mean of standard deviation data for all polydisperse EPS bead mixtures.

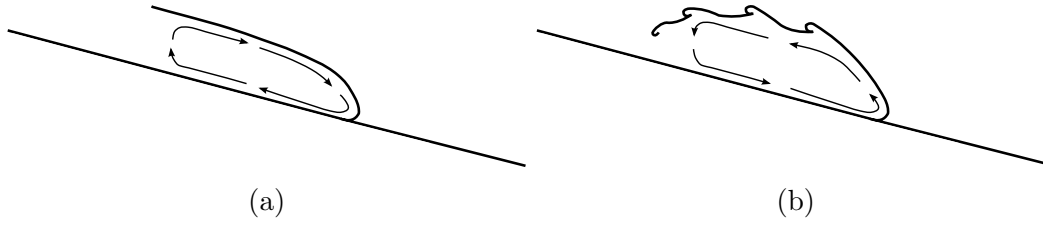


Figure 4.33: Motions of particles within (a) unsuspended and (b) suspended flows.

dispersity of the granular material does not make any significant difference. The instability that leads to the formation of finger-like patterns in flows of unsuspended granular material is either absent from, or has no significant effect on, fully-suspended, particle-laden gravity currents. This is most likely due to the particles being suspended and their motion within the flow. In unsuspended flows larger particles tend to rise to the upper surface of the flow through a kinetic sieving mechanism. Smaller particles percolate downward through a granular medium more often than large particles because they more often encounter sufficiently large voids beneath them. Once at the upper surface the large particles are transported to the leading edge of the flow because the velocities at the surface of unsuspended flows are higher than the average flow velocity. The larger particles then collect in the vicinity of small perturbations in the flow front, leading to an increase in inter-particle friction in that area, which in turn leads to the formation of the finger-like patterns. In the present study the particles are fully suspended within the flow, meaning that inter-particle friction and kinetic sieving mechanisms will have a less significant effect. Additionally, the motion of the large vortex-like structure that dominates the flow dynamics inside the head of the current (§1.5 & §1.3) is such that particles arriving at the upper surface of the flow are transported away from the moving front (Figure 4.33) instead of towards it.

Whilst the granular fingering instability didn't have any significant effect on the fully developed flows in this study, for future studies it would be worth closer investigation of its possible effect immediately after release when the current is still unsuspended, and also the effects of increasing the volume fraction of the larger material.

### 4.8 Summary

In agreement with other theoretical and experimental studies of gravity currents, the approximately steady front velocity reached by the particle-laden, fully suspended flows used in this study was found to be independent of slope angle (provided the slope angle is great enough for the current to become fully suspended) and scales with the volume of particulate material released. Interestingly, given the differences in individual particle settling velocities, the front velocity was also found to be independent of particle diameter. However, the smaller particles' lower settling velocity was found to lead to higher values of flow height. Additionally, the smaller component of settling velocity perpendicular to the chute was found to result in higher values of flow height as slope angle was increased. Increasing the volume of material released also leads to some increase in the flow height. However there appears to be a limit to the amount of particulate material that can be maintained in suspension, and once reached the increase in flow height levels off and rear detrainment increases.

A lobe-and-cleft-type pattern was found to quickly develop at the leading edge of the flows, the initial perturbations that lead to the formation of which are likely to result from a region of unstable stratification at the front of the currents. This region of unstable stratification is caused by the current having a raised nose, which itself is due to friction between the current and the chute surface. The nose of these currents has been found to be geometrically similar to those found in homogenous Boussinesq gravity currents. The relationship between the wavelength of the lobe-and-cleft-type pattern and the Grashof number of the flows also shows reasonable agreement with that of homogenous Boussinesq gravity currents and provides further evidence for the classic lobe-and-cleft instability causing, and determining the wavelength of the initial lobe-and-cleft-type pattern. However, whilst scaled front velocities during the early stages of the flows' motion show good agreement with those of homogenous Boussinesq gravity currents, at later stages they are much higher than we would expect to see for flows where the classic lobe-and-cleft instability is dominant. Instead of the continuously shifting pattern of lobes and clefts that is a feature of homogenous Boussinesq gravity currents, a much more laterally stable pattern emerged, the amplitude of which increases once the currents reach an approximately steady velocity. This suggests that the

dominant instability mechanism is now more similar to those observed in unsuspended granular flows. Particle diameter of the granular material has been found to play a central role in determining the wavelength and development of the lobe-and-cleft-type pattern, as hypothesised by Nohguchi and Ozawa. When scaled with particle diameter, a relationship between Froude number of the flow and wavelength of the lobe-and-cleft-type pattern has been found. This relationship highlights the importance of the role played by drag forces acting on the individual particles in determining the wavelength and development of the frontal pattern, and appears to support the concept of a velocity boundary layer at the leading edge of the flow.

## Bibliography

- R. Britter and P. Linden. The motion of the front of a gravity current travelling down an incline. *Journal of Fluid Mechanics*, 99, 1980.
- J. W. M. Bush, B. A. Thurber, and Blanchette F. Particle clouds in homogeneous and stratified environments. *Journal of Fluid Mechanics*, 489:29–54, 2003. doi:10.1017/S0022112003005160.
- S. Chandrasekhar. *Hydrodynamic and Hydromagnetic Stability*. Oxford University Press, Oxford, UK, 1961.
- R. E. Duff, F. H. Harlow, and C. W. Hirt. Effects of diffusion on interface instability between gases. *Physics of Fluids*, 5:417–425, 1962.
- C. Härtel, F. Carlsson, and M. Thunblom. Analysis and direct numerical simulation of the flow at a gravity-current head. Part 2. The lobe-and-cleft instability. *Journal of Fluid Mechanics*, 418:213–229, 2000.
- J. J. Keller and Y. P. Chyou. On the hydraulic lock exchange problem. *Journal of Applied Mathematics and Physics*, 42:874–909, 1991.
- M. H. Keulegan. An experimental study of the motion of saline water from locks into fresh water channels. 13th progress report on model laws for density currents. *U.S. National Bureau of Standards*, 5168, 1957.
- T. J. Lawson. Haboob structure at Khartoum. *Weather*, 26:105–112, 1971.
- G. V. Middleton. Experiments on density and turbidity currents, I. Motion of the head. *Canadian Journal of Earth Sciences*, 3:532–546, 1966.

## BIBLIOGRAPHY

---

- J. Neufeld. Lobe-cleft patterns in the leading edge of a gravity current. Master's thesis, Department of Physics, University of Toronto, Toronto, Canada, 2002.
- Y. Nohguchi and H. Ozawa. On the vortex formation at the moving front of lightweight granular particles. *Physica D*, 238:20–26, 2008. doi:10.1016/j.physd.2008.08.019.
- O. Pouliquen and J. W. Vallance. Segregation induced instabilities of granular fronts. *Chaos*, 9(3):621–629, 1999.
- O. Pouliquen, J. Delour, and S. B. Savage. Fingering in granular flows. *Nature*, 386:816–817, 1997.
- J. W. Rottman and J. E. Simpson. Gravity currents produced by instantaneous releases of a heavy fluid in a rectangular channel. *Journal of Fluid Mechanics*, 135:95–110, 1983.
- D. H. Sharp. An overview of Rayleigh-Taylor instability. *Physica D*, 12:3–18, 1984.
- J. E. Simpson. Effects of the lower boundary on the head of a gravity current. *Journal of Fluid Mechanics*, 53(4):759–768, 1972.
- J. E. Simpson. *Gravity Currents in the Environment and the Laboratory*. Cambridge University Press, 2nd edition, 1997.
- J. E. Simpson and R. E. Britter. The dynamics of the head of a gravity current advancing over a horizontal surface. *Journal of Fluid Mechanics*, 94:477–495, 1979.
- B. Turnbull and J. N. McElwaine. A comparison of powder-snow avalanches at Vallée de la Sionne, Switzerland, with plume theories. *Journal of Glaciology*, 53(180):30–40, 2007.
- B. Turnbull and J. N. McElwaine. Experiments on the non-Boussinesq flow of self-igniting suspension currents on a steep open slope. *Journal of Geophysical Research*, 113(F01003), 2008. doi:10.1029/2007JF000753.
- D. L. Youngs. Numerical simulation of turbulent mixing by Rayleigh-Taylor instability. *Physica D*, 12:32–34, 1984.





# Chapter 5

## Air pressure

The air pressure sensors mounted on the chute (§2.1) recorded the temporal variation of basal pore pressure as each gravity current passed. In this chapter we find appropriate parameters for scaling these data and use these data to reveal more about the internal dynamics of the gravity current head.

It has been demonstrated both theoretically [McElwaine, 2004] and experimentally [Turnbull and McElwaine, 2008] that a gravity current head consists of a large rotating, vortex-like structure. This structure causes a large positive peak in basal pore pressure quickly followed by a negative peak of approximately equal magnitude as the gravity current passes over a sensor. This pressure signal is therefore significantly different than the signal just consisting of a positive pressure peak that we would expect to see if the pressure was purely hydrostatic.

### 5.1 Air pressure signal noise removal

#### 5.1.1 Discrete Fourier Transform

A typical example of a signal obtained from one of the chute-mounted pressure sensors is shown in Figure 5.1. Whilst this signal displays the features that we would expect to see for a flow of this kind, namely a large positive pressure peak (Figure 5.1 - segment B) quickly followed by a negative peak (Figure 5.1 - segment C), the signal also contains a couple of features that are not

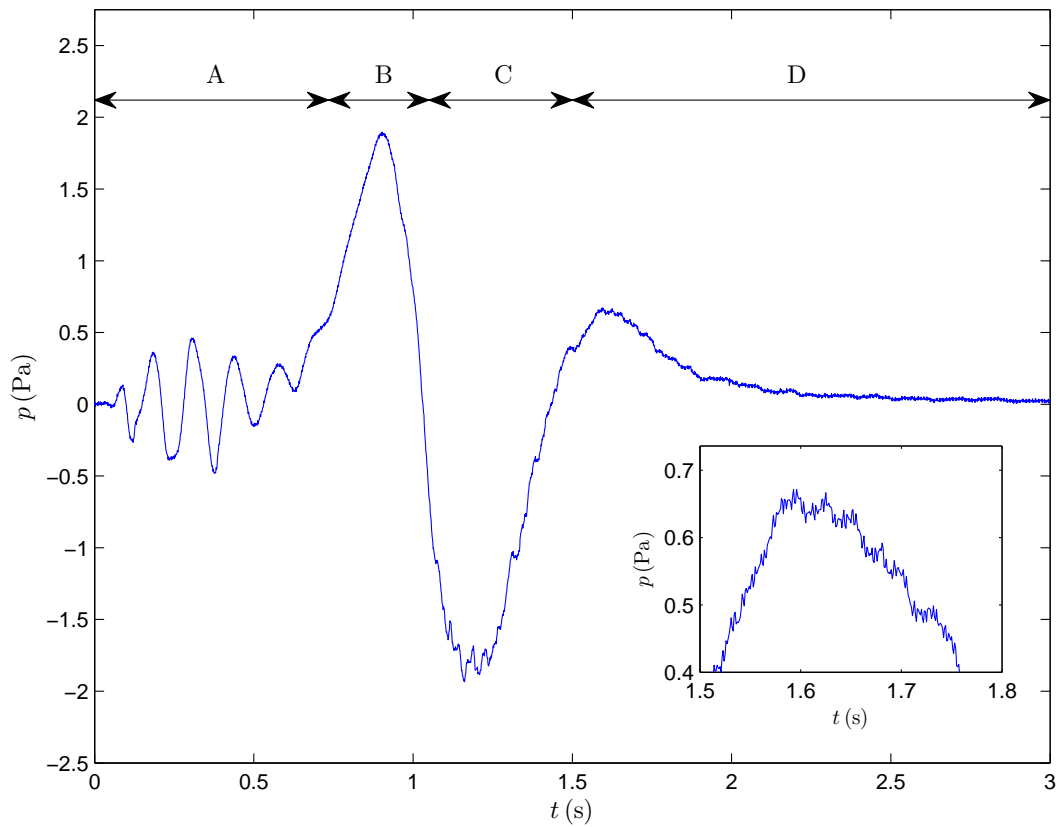


Figure 5.1: Example of an unprocessed pressure signal obtained from one of the pressure sensors mounted on the chute. Inset: close up of part of the signal in which the effect of high frequency noise on the signal can be clearly seen.

## 5.1. AIR PRESSURE SIGNAL NOISE REMOVAL

---

related to the dynamics of the flow. The first of these is low-amplitude, high-frequency electronic noise along the entire length of the signal (Figure 5.1 - segments A→D). The other is a wave of peak amplitude approximately 0.5 Pa and frequency approximately 8 Hz that occurs during the first 0.75 s after the release mechanism is triggered (Figure 5.1 - segment A). This is about the same amount of time that the release mechanism continued in motion for after the initial trigger. Whilst separating the mechanism from the chute (Chapter 2) eliminated vibrations being transmitted being passed directly to the chute, low-frequency pressure waves emitted by the release mechanism (most likely from the sliding runners) are still detected by the pressure sensors. The pressure signals therefore first need to be processed in order to remove these features before they can be used to study the dynamics of the flows.

Initially the signals were processed using a Fourier transform-based technique. This involves transforming the signals from a time-domain representation to a frequency-domain representation. For a pressure signal  $p(k)$  of length  $N_p$  this is achieved using a discrete Fourier transform (DFT), given by

$$P(j) = \sum_{k=1}^{N_p} p(k) \omega_{N_p}^{(k-1)(j-1)} \quad (5.1)$$

where

$$\omega_{N_p} = e^{(-2\pi i)/N_p} \quad (5.2)$$

is an  $N_p$ th root of unity. In order to increase speed and efficiency the signals are first zero padded so that their length is equal to a power of 2, this allows the implementation of a Fast Fourier transform (FFT) algorithm, reducing the number of operations required from  $N_p^2$  to approximately  $N_p \log_2(N_p)$  [Duhamel and Vetterli, 1990].

The DFT of the signal is a complex number; the power in each frequency component represented by the DFT can be obtained by squaring the magnitude of that frequency component. Thus, the power in the  $j$ th frequency component is given by  $|P(j)|^2$ . The power spectrum (Figure 5.2) obtained from the signal displayed in Figure 5.1 shows a peak at approximately 1 Hz which corresponds to the large positive and negative pressure peaks seen in the signal. The signal also contains a wide range of higher frequency ( $\approx 10 - 500$  Hz) components whose power is close, but not equal, to zero. Generally speaking, electronic noise is made up of constantly fluctuating high frequency components. As

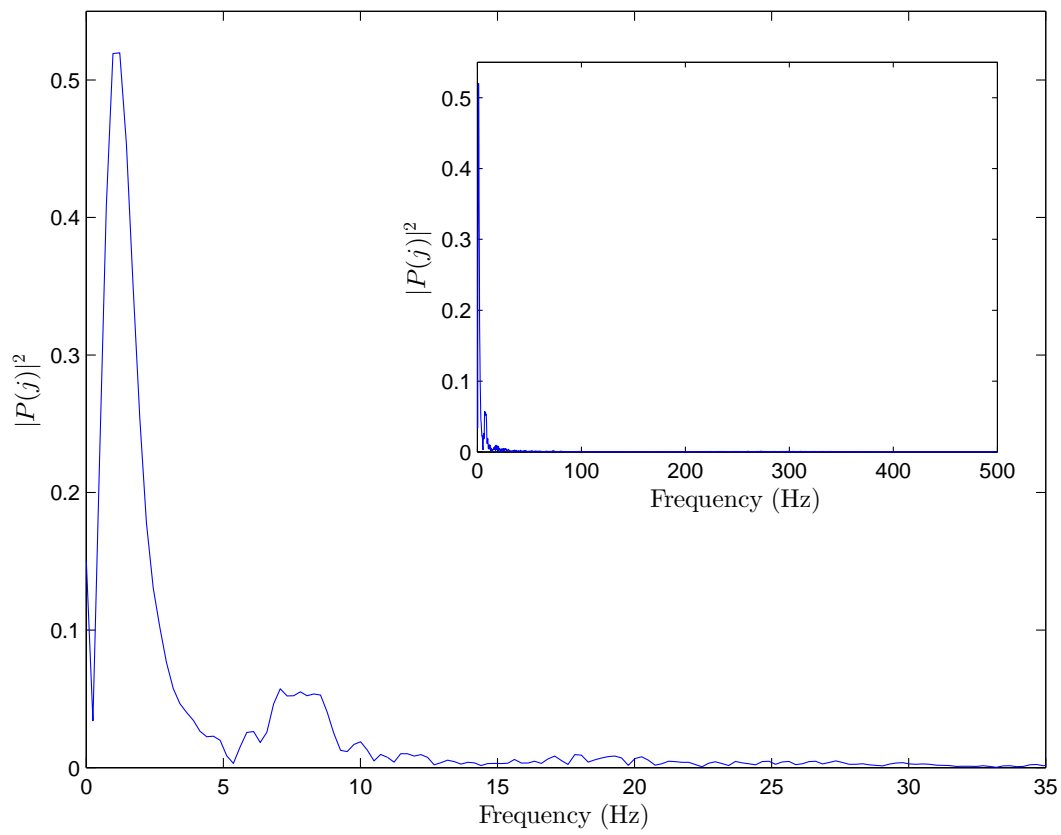


Figure 5.2: Single-sided power spectrum of  $p(t)$ , main:  $x$ -axis shortened for clarity, inset: full  $x$ -axis shown.

## 5.1. AIR PRESSURE SIGNAL NOISE REMOVAL

---

a consequence of this constant fluctuation and wide range of frequencies involved, the power associated with each frequency component remains low. It can be deduced that the high frequency, low power components of the power spectrum shown in Figure 5.2 represent the electronic noise present in the signal. The power spectrum can therefore be used to filter out the electronic noise by identifying and removing the low power frequency components from the signal. This is achieved by setting a threshold power level,  $\Phi$ , and identifying the frequency components for which  $|P(j)|^2 < \Phi$ . Once identified, these components are set to zero,  $P(j) = 0$ , and the inverse DFT,

$$p(k) = \frac{1}{N_p} \sum_{j=1}^{N_p} P(j) \omega_{N_p}^{-(k-1)(j-1)}, \quad (5.3)$$

is applied in order to convert the signal, with the low power frequency components removed, back into the time-domain.

The effect on the output of the inverse DFT of applying different values of  $\Phi$  to the power spectrum is shown in Figure 5.3, and it highlights the importance of selecting an appropriate value for  $\Phi$ . Setting the value too low will mean that the electronic noise is not completely removed from the signal (Figure 5.3(a)). Whereas setting it too high will result in low power frequency components that are not necessarily electronic noise being removed from the signal (Figure 5.3(e)). It is reasonable to expect that the pressure signals obtained from the experiments will contain some higher frequency components arising from fluctuations in the flow caused by turbulence. The nature of the turbulence is such that these fluctuations are likely to be over short timescales and a wide range of frequencies and therefore, as with electronic noise, the power levels of these frequency components will be low. A drawback of using a DFT-based filtering technique to remove electronic noise is that it is extremely difficult to identify which of the lower power frequency components relate to noise and which relate to genuine flow features, and set an appropriate value of  $\Phi$  accordingly. Another drawback of this technique is that in order to remove the  $\approx 8$  Hz wave in the early part of the signal the value of  $\Phi$  needs to be relatively high. This also results in features with the same frequency, and frequencies with the same or lower power levels, that occur later in the signal being filtered out.

Applying a power-level based threshold in the frequency domain is not the

## 5.1. AIR PRESSURE SIGNAL NOISE REMOVAL

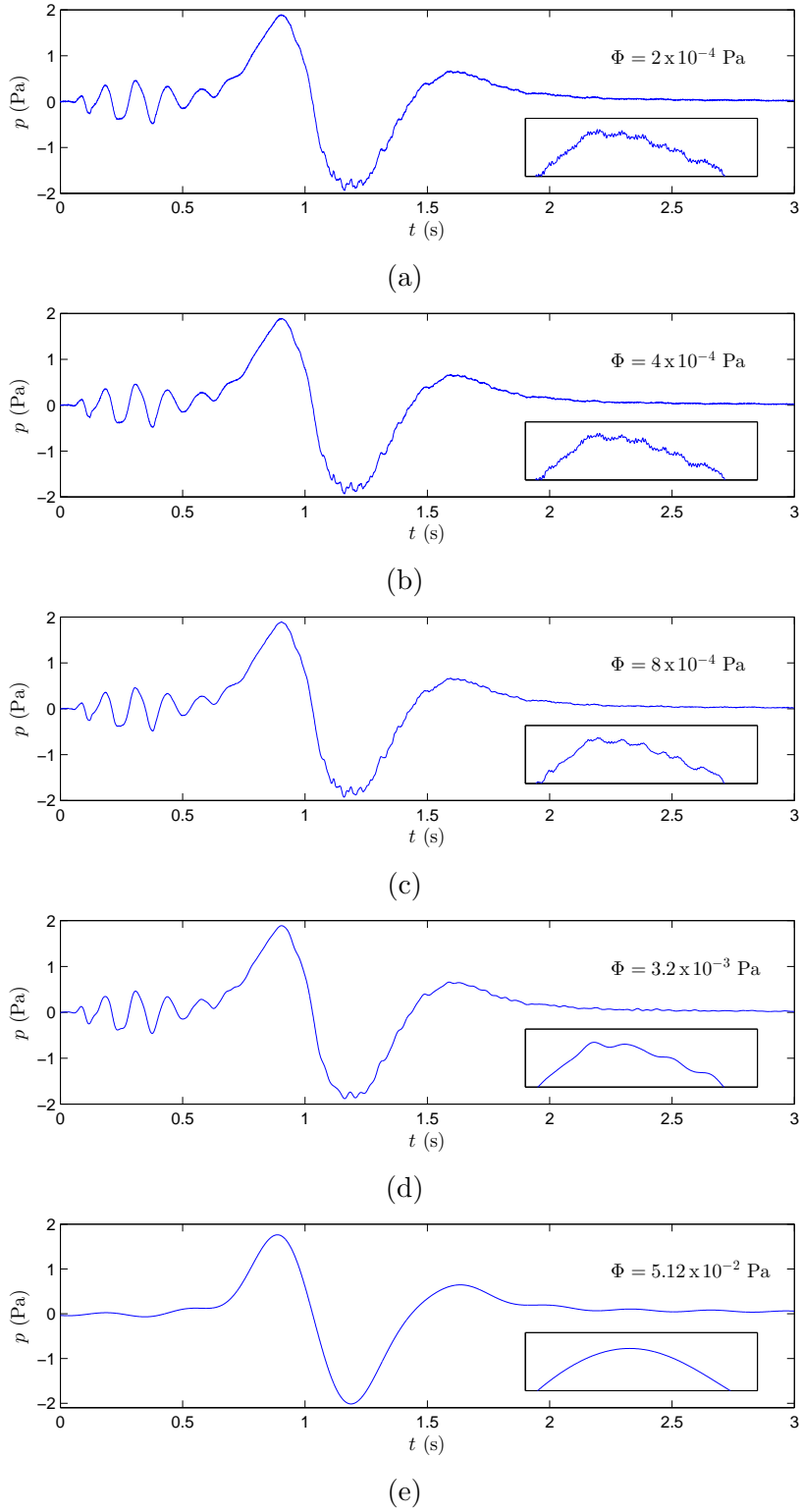


Figure 5.3: Pressure versus time plots using data obtained from inverse DFT. Values of power spectrum threshold,  $\Phi$ , used for (a)-(e) range from  $2 \times 10^{-4}$  to  $5.12 \times 10^{-2}$  Pa.

## 5.1. AIR PRESSURE SIGNAL NOISE REMOVAL

---

only available method of filtering using the DFT of a signal. A frequency-level based threshold whereby any frequencies above a certain value are removed can also be applied to the output of the DFT. Whilst this avoids the problem of unwanted removal of low-power, low-frequency signal features, the problem of setting a threshold that retains low-power, higher frequency signal features while removing unwanted electronic noise still remains.

### 5.1.2 Wavelet analysis

The drawbacks of the DFT-based filtering technique stem from the fact that once the signal has been transformed into the frequency domain, all time information is lost. Electronic noise is present at all points in time along the pressure signal. Therefore if in addition to frequency and power, time information was also available, electronic noise would be easily identifiable as the low power, high frequency components that occur at all points in time along the signal. This is in contrast to other high-frequency components, such as those relating to turbulence, that only occur at certain periods of time along the signal. Similarly, time information could be used to easily remove the pressure wave at the beginning of the signal by identifying all of the frequency components of  $\approx 8$  Hz that occur during the first 0.75 s of the signal.

Attempts can be made to address these drawbacks by adapting the Fourier transform to analyse only a small section, or window, of the signal at a time. The short-time Fourier transform (STFT), maps a signal into a two-dimensional function of time and frequency, providing a compromise between the time- and frequency-based views of the signal. Different values of  $\Phi$  could then be applied when filtering different parts of the signal. However, the information about when and at what frequencies a signal feature occurs at can only be obtained with limited precision, and that precision is determined by the size of the window [Allen, 1977]. Once a particular size for the time window has been chosen, that window is the same for all frequencies. A more flexible approach is required where the window size can be varied in order to determine more accurately time or frequency data relating to signal features.

This more flexible approach exists in the form of wavelet analysis. Wavelet analysis allows the use of long time intervals where more precise low-frequency is required, and shorter regions where high-frequency information is required

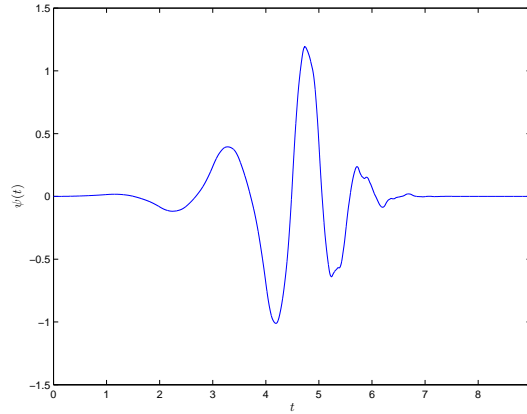


Figure 5.4: Daubechies Db5 wavelet function.

[Mallat, 1998]. Where Fourier analysis consists of breaking up a signal into sine waves of various frequencies, wavelet analysis is the breaking up of a signal into shifted and scaled versions of a mother wavelet. A wavelet is a waveform of limited duration that has an average value of zero. Unlike smooth and predictable sinusoids, they tend to be irregular and asymmetric.

The wavelet basis function used here is a Daubechies wavelet with 5 vanishing moments (Figure 5.4), which was selected as a good compromise between time and frequency localization. Wavelets that have ‘sharp edges’ in the time domain (e.g. Daubechies type 2) have excellent temporal localization. This means that the properties of the signal at a point in time will correspond closely to the values for the wavelet coefficients at that point in time, with little smearing of the coefficients across neighbouring time positions. However, the frequency localization for this type of wavelet basis function is poor. Wavelets with higher numbers of vanishing moments (e.g. Daubechies type 10) have the opposite tendency, with good frequency localization and poor temporal localization [Daubechies, 1992].

Wavelet analysis is performed by the translation and dilation of the mother wavelet along a signal and the convolution of this function with the signal. The continuous wavelet transform (CWT) for a signal  $p$  that varies with time  $t$  based on a mother wavelet  $\psi$  is given by

$$CWT(j, k) = \frac{1}{\sqrt{j}} \int_{-\infty}^{+\infty} p(t) \psi \left( \frac{t - k}{j} \right) dt, \quad (5.4)$$

where  $j$  and  $k$  are the dilation and translation parameters of the mother wavelet



## 5.1. AIR PRESSURE SIGNAL NOISE REMOVAL

---

$\psi$ . If the length of the signal is  $N_p$ , the CWT produces  $N_p$  coefficients at every scale analysed.

Wavelet analysis can be performed more efficiently by replacing the CWT with the discrete wavelet transform (DWT). In this case, the dilation is performed in powers of two, with the mother wavelet starting at its minimum width and is doubled at each dyadic scale  $j$ . The DWT is calculated using a hierarchical cascade of filter banks, making it more efficient numerically, while dramatically reducing the number of wavelet coefficients produced.

The DWT of a time series sampled at  $N_p = 2^J$  points can be formulated over the dyadic scales  $2^j$ ,  $j = 1, \dots, J$  using a filter bank of high and low pass quadrature mirror filters of even filter width,  $\Lambda$ , where  $h_l$  ( $l = 0, \dots, \Lambda - 1$ ) is the high pass (or wavelet) filter,  $g_l$  is the low pass (or scaling) filter and

$$g_l \equiv (-1)^{l+1} h_{\Lambda-1-l} \quad (5.5)$$

At the first stage of the algorithm,  $j = 1$ , these filters are circularly convolved with  $p(t)$  and the downsampled by a factor of 2 to give a set of wavelet,  $w$ , and approximation,  $A$ , coefficients of length  $N_p/2$ :

$$\begin{aligned} w_{1,k} &\equiv \sqrt{2} \tilde{w}_{1,2k+1} \quad k = 0, \dots, \frac{N_p}{2} - 1 \\ \sqrt{2} \tilde{w}_{1,k} &\equiv \sum_{l=0}^{\Lambda-1} h_l p_{t-l \bmod N_p} \quad k = 0, \dots, N_p - 1 \end{aligned} \quad (5.6)$$

$$\begin{aligned} A_{1,k} &\equiv \sqrt{2} \tilde{A}_{1,2k+1} \quad k = 0, \dots, \frac{N_p}{2} - 1 \\ \sqrt{2} \tilde{A}_{1,k} &\equiv \sum_{l=0}^{\Lambda-1} g_l p_{t-l \bmod N_p} \quad k = 0, \dots, N_p - 1 \end{aligned} \quad (5.7)$$

At subsequent stages of the algorithm,  $j$ , the approximation from the previous stage of the algorithm,  $A_{j-1,k}$  is used instead of  $p(t)$  in Equations 5.6 and 5.7 to give wavelet coefficients over all scales  $j = 1, \dots, J$  and a final approximation coefficient.

A drawback of the DWT is that as the scale doubles, the number of wavelet coefficients halves, which makes comparative analysis between scales problematic. Therefore the stationary wavelet transform (SWT) is instead used, which

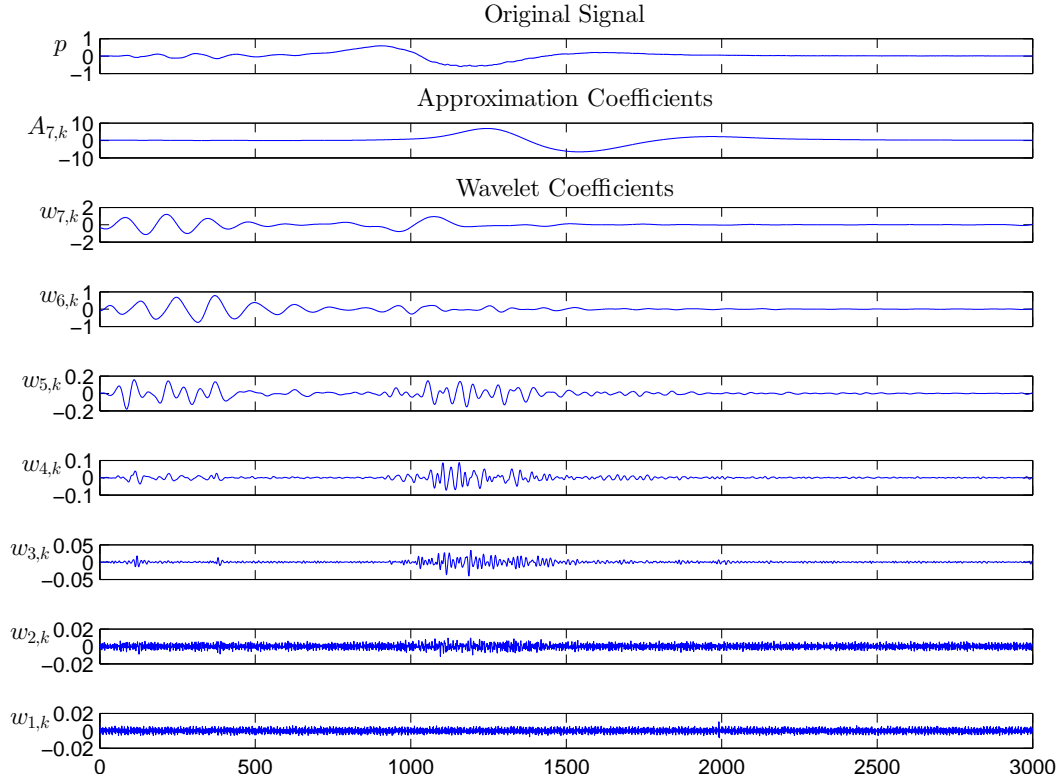


Figure 5.5: Approximation ( $A$ ) and wavelet ( $w$ ) coefficients resulting from a multiscale SWT decomposition of the pressure signal shown in Figure 5.1. The wavelet filter used is a Daubechies wavelet with 5 vanishing moments.

retains the efficiency of working with dyadic scales only but is an undecimated transform, as the downsampling undertaken in the DWT is eliminated. This means that each point in time has a unique coefficient for each scale, i.e. there are  $N_p$  wavelet coefficients at each scale, making between-scale analysis easier. A detailed description of the implementation of the SWT can be found in Appendix A.

A minor drawback of the SWT is that  $2^j$  has to be a factor of the length of the signal,  $N_p$ , for  $j = 1, \dots, J$ . However, this can be overcome in this situation by extending the signal up to the next dyadic scale using zero padding at the end of the signal. The fact that the signal already starts and finishes with values of approximately zero, the addition of zero padding does not cause any significant discontinuities in the signal that may affect the SWT, and the padding can be removed after the filtering has been performed.

Figure 5.5 shows the output of multiscale SWT when applied to the pressure signal shown in Figure 5.1. The signal has been decomposed into approxi-

## 5.1. AIR PRESSURE SIGNAL NOISE REMOVAL

---

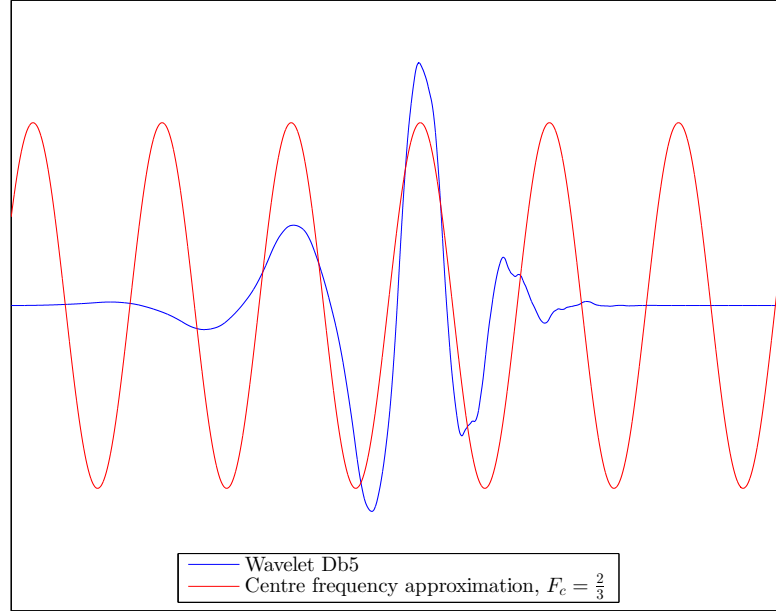


Figure 5.6: Comparison of wavelet db5 and centre frequency based approximation.

Scale, $j$	Pseudo-frequency, $F_j$ (Hz)
1	333
2	167
3	83
4	41
5	21
6	10
7	5

Table 5.1: Wavelet scales and their equivalent pseudo-frequencies.

mation coefficients at scale  $j = 7$  and wavelet coefficients at scales  $j = 1, \dots, 7$ . Although it is impossible to directly convert a wavelet scale into a frequency, a pseudo-frequency corresponding to a scale can be calculated in order to give an approximate associated frequency. This is done by associating with the wavelet a purely periodic signal of frequency  $F_c$  (Figure 5.6), known as the centre frequency.  $F_c$  is equal to the frequency that maximises the fast Fourier transform of the wavelet modulus, which for the Db5 wavelet is  $\frac{2}{3}$  Hz. The pseudo-frequency,  $F_j$ , in Hz is then given by

$$F_j = \frac{F_c}{j \cdot \Delta}, \quad (5.8)$$

where  $j$  is the scale and  $\Delta$  is the sampling period. The pseudo-frequencies corresponding to the wavelet scales from the SWT decomposition in Figure 5.5 are shown in Table 5.1.

Looking at the multiscale SWT decomposition of the pressure signal (Figure 5.5), it can be seen that the high-frequency components of the signal that are filtered into wavelet scales  $w_{1,k}$  and  $w_{2,k}$  are rapidly fluctuating but with approximately constant magnitude throughout the entire length of the signal  $N_p$ . Wavelet scales  $w_{3,k}$ ,  $w_{4,k}$  and  $w_{5,k}$  also contain some low-amplitude, time-invariant components. The fact that the components are high-frequency, time-invariant and present throughout the entire length of the signal, suggests that they correspond to the effects of electronic noise on the signal.

Given that it has the lowest variation in magnitude and corresponds to the highest frequencies present in the signal, wavelet scale  $w_{1,k}$  is likely to contain the most components that correspond to electronic noise. This wavelet scale is therefore used to set a threshold value that is used to filter out the electronic noise from the signal. The mean value of the wavelet scale  $w_{1,k}$  coefficients is approximately zero and they follow an approximately Gaussian distribution (Figure 5.7), so it is therefore assumed that the electronic noise is Gaussian white noise. The threshold value is obtained using estimates of the wavelet scale  $w_{1,k}$  coefficients' standard deviation. The estimator used is based on the median absolute deviation, and has been shown to be well suited to zero mean Gaussian white noise [Donoho and Johnstone, 1994]. The median absolute deviation is then used as part of a penalization method [Birge and Massart, 1997] applied to the wavelet scale  $w_{1,k}$  coefficients in order to determine the threshold value.

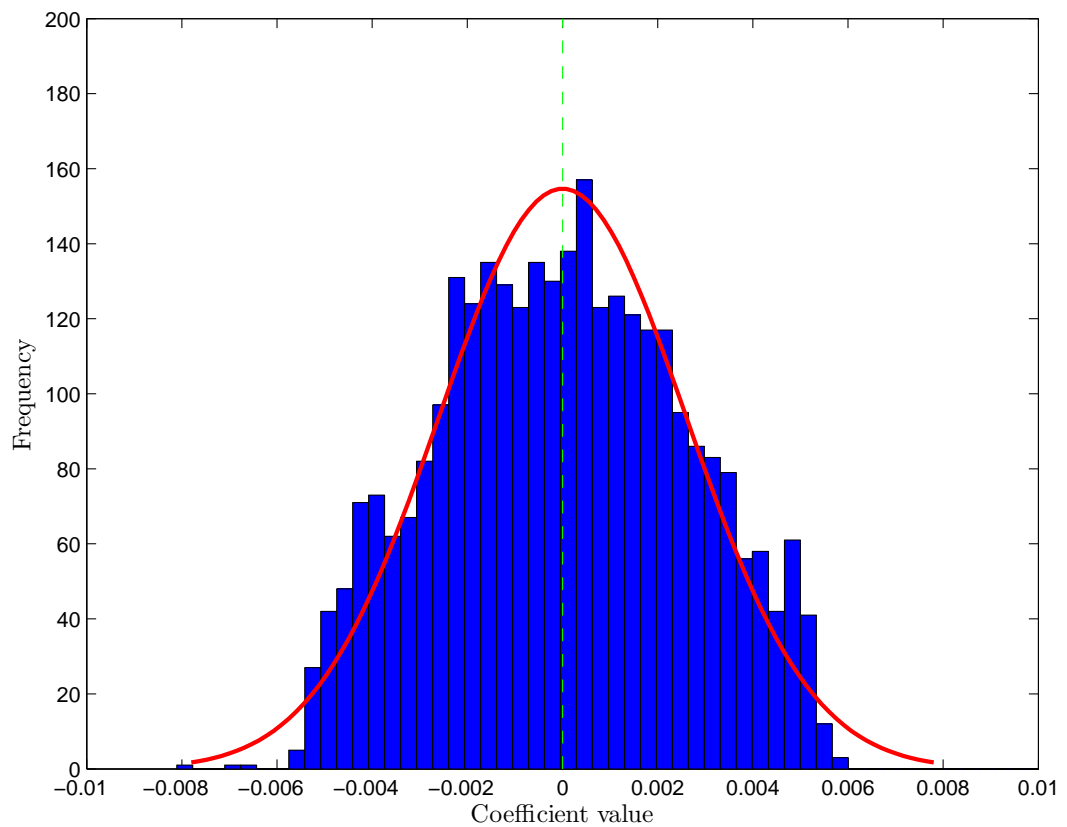


Figure 5.7: Histogram of wavelet scale  $w_{1,k}$  coefficient values (blue bars) corresponding to electronic noise. Red line shows a normal (Gaussian) density function fitted to the data. The dashed green line represents the mean value of the data.

## 5.1. AIR PRESSURE SIGNAL NOISE REMOVAL

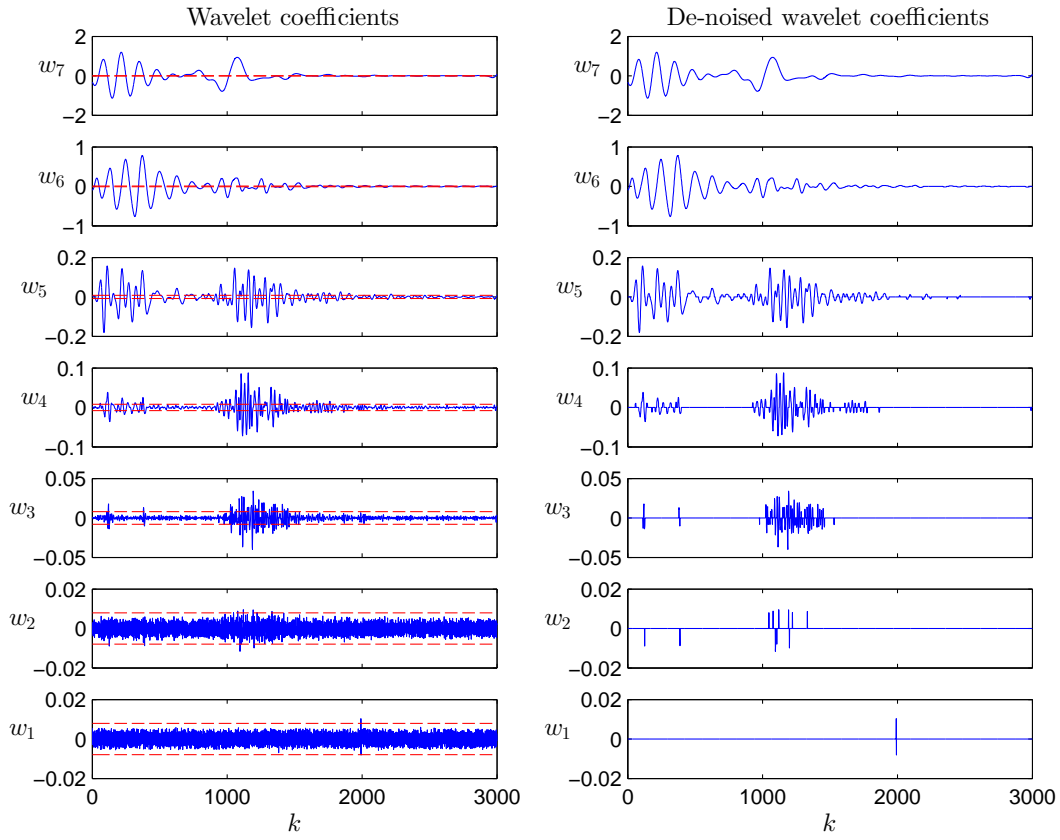


Figure 5.8: Original (left hand column) and de-noised (right hand column) wavelet coefficients at all scales. Red dashed lines indicate threshold value.

## 5.1. AIR PRESSURE SIGNAL NOISE REMOVAL

---

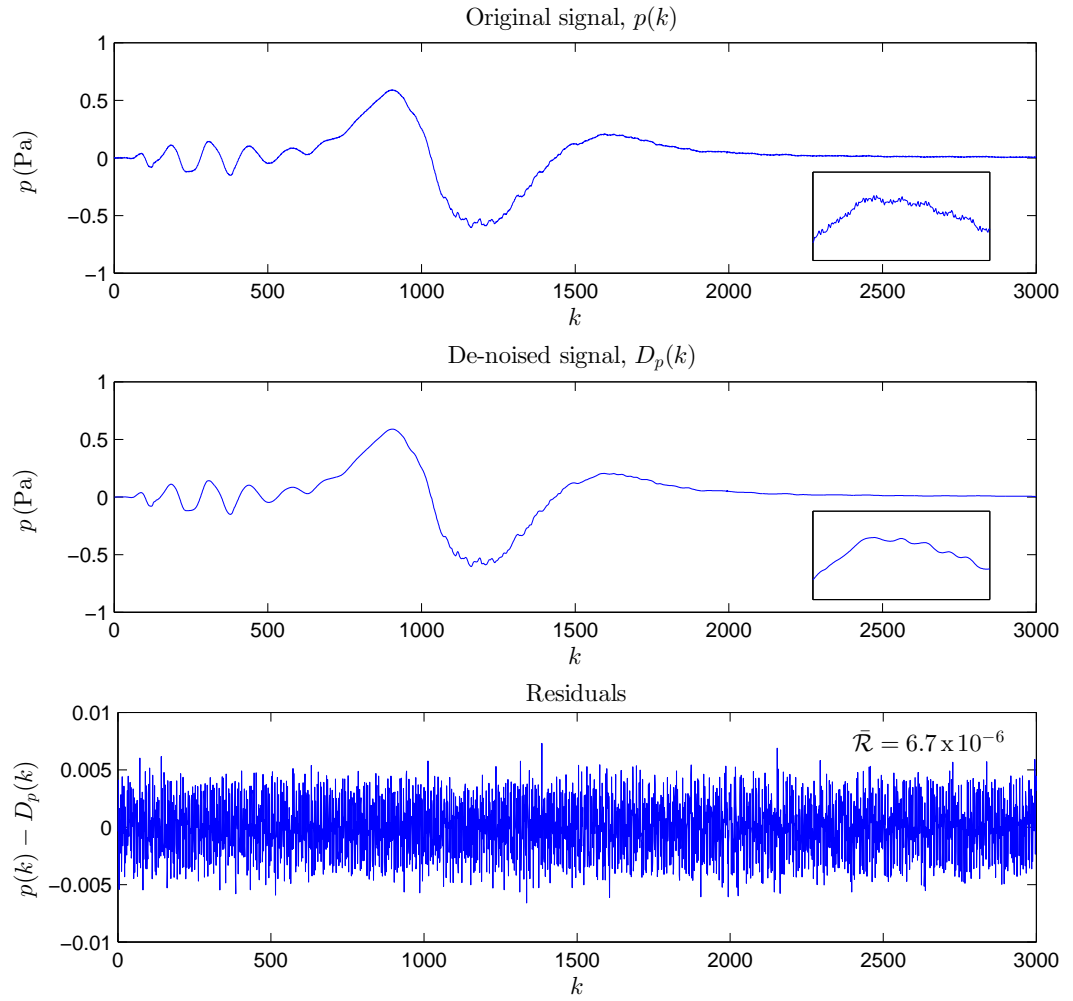


Figure 5.9: Original signal (top), de-noised signal (middle) and residuals of the de-noised signal (bottom).

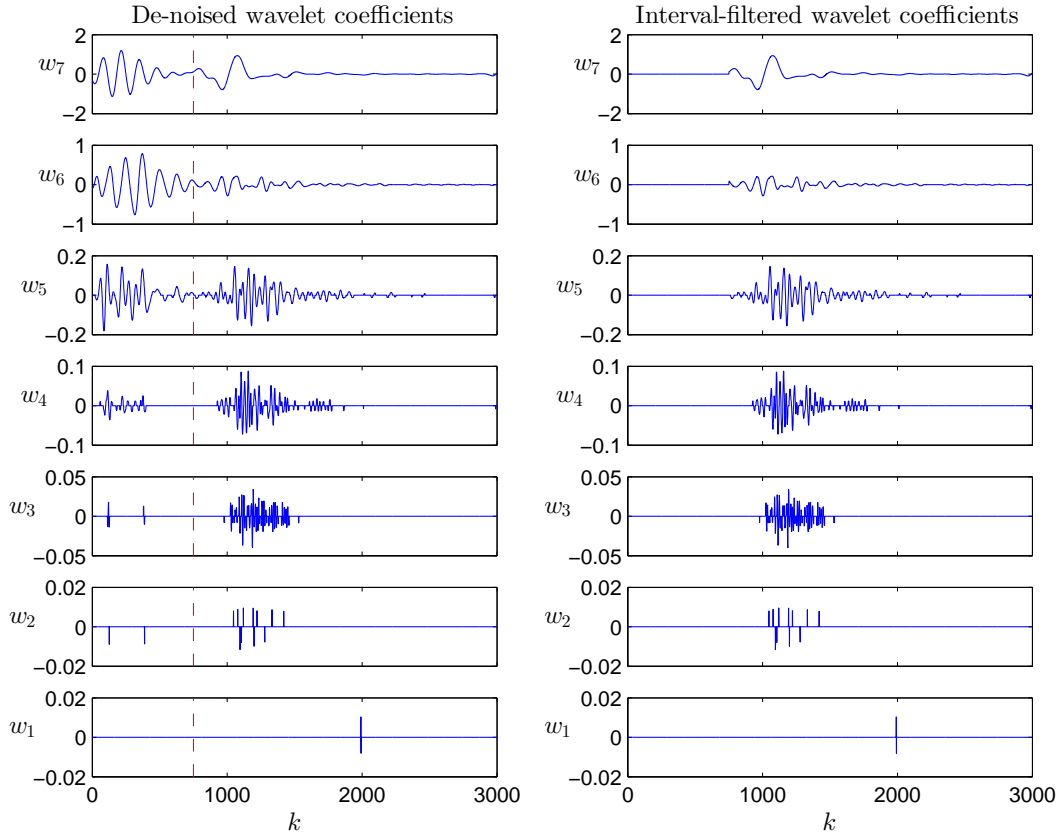


Figure 5.10: De-noised (left hand column) and interval-filtered (right hand column) wavelet coefficients at all scales. Red dashed lines indicate the interval separation point.

Once the threshold value has been obtained it is applied to all the wavelet scales, but not the approximation coefficients, and coefficients with magnitude less than the threshold value are set to zero (Figure 5.8). The de-noised signal and residuals (calculated by subtracting the de-noised signal from the original signal) are shown in Figure 5.9. The mean value of the residuals,  $\bar{\mathcal{R}}$ , is approximately zero and the approximately constant level of variation across the entire length of the signal, indicate that the wavelet coefficients of the signal removed during the de-noising process correspond only to the electronic noise present in the signal and that no other signal features have been lost.

Attention is now turned to the removal of the low-frequency pressure waves that appear at the beginning of the signal. Conversely to the electronic noise, the bulk of the coefficients that correspond to these pressure waves are found in wavelet scales  $w_{7,k}$  and  $w_{6,k}$ , and a minority are found in wavelet scales  $w_{5,k}$ ,  $w_{4,k}$  and  $w_{3,k}$  (Figure 5.5). This is to be expected as, as previously



## 5.1. AIR PRESSURE SIGNAL NOISE REMOVAL

---

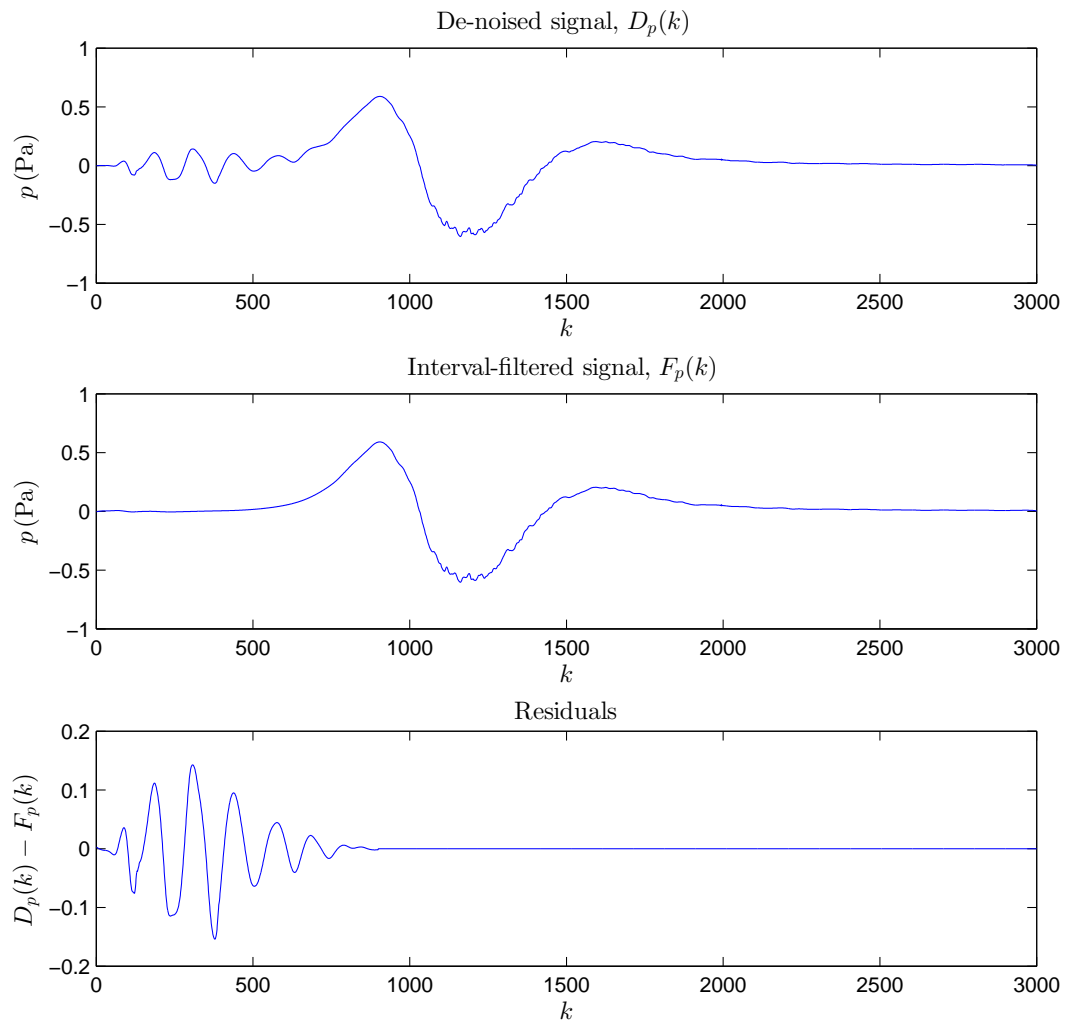


Figure 5.11: De-noised signal (top), interval-filtered signal (middle) and residuals of the interval-filtered signal (bottom).

noted, the pressure wave has a frequency of  $\approx 8$  Hz and wavelet scales  $w_{7,k}$  and  $w_{6,k}$  correspond to a frequency range of  $\approx 5$ -10 Hz. The fact that the effects of the pressure wave are only observed during the early part of the signal means that the wavelet scales can be split by introducing an interval at a certain value of  $t$  (or  $k$ ), and filtering only applied to pre-interval wavelet coefficients. While sophisticated automated interval identification algorithms do exist [Lavielle, 1999, Donoho and Johnstone, 1994], scrutinisation of a large number of pressure signals revealed that the pressure wave consistently occurred during the first 0.75 s of the signal, additionally the earliest positive pressure peaks caused by the current arriving at the first (lowest value of  $s$ ) sensor occurred at  $\approx 0.85$  s. Given these observations, coupled with the fact the main aim of studying these pressure signals is to gain information about the internal dynamics of the currents (i.e. from the positive pressure peak and onwards), use of automated interval identification algorithms was deemed unnecessary, and instead a fixed interval separation point was placed at 0.75 s (or  $k = 750$ ) for all wavelet scales. All wavelet coefficients occurring before this interval separation point were then set to zero (Figure 5.10). The interval-filtered signal and residuals are shown in Figure 5.11, and it can be seen that this method has successfully removed the low frequency pressure wave from the early part of the signal without effecting the rest of the signals features.

## 5.2 Air pressure signals

Air pressure measurements from a series of experiments of the same EPS bead size, release volume and at the same slope angle have been superimposed in Figure 5.12. Similar to other air pressure measurements collected from both field and laboratory experiments [Turnbull and McElwaine, 2008], the vortex behind the head was found to be a very repeatable flow feature.

Current air pressure data from series' of experiments conducted with different combinations of variables is presented in Figure 5.13. The data presented for each series of experiments (i.e. where all variables are kept constant) consists of an ensemble average of the air pressure data collected from each of the experiments in the series, plus or minus the standard deviation from the mean. The repeatability of the vortex behind the head is again highlighted by the lack of scatter in the ensemble data. This is especially true up to the

## 5.2. AIR PRESSURE SIGNALS

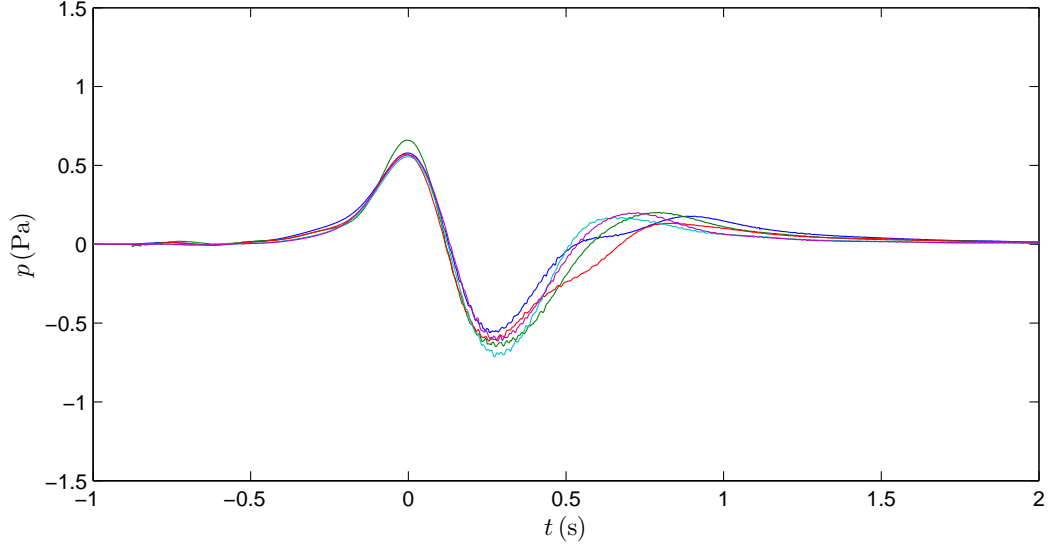


Figure 5.12: Air pressure measurements from five  $3300 \text{ cm}^3$  of 2.7 mm diameter EPS bead currents at a slope angle of  $80^\circ$ . The time origin,  $t = 0$ , corresponds to the arrival of the currents at a sensor positioned a distance  $y_p = 1 \text{ m}$  from the release mechanism.

negative pressure peak, after this the level of scatter increases, indicating a higher level of turbulence in the tail of the current. Several other trends can be identified in the data presented in Figure 5.13. As slope angle  $\theta$  increases ((i)→(iii)), the magnitude of both the positive and negative pressure peaks decreases. Additionally, there is a slight decrease in the positive and negative pressure peak magnitudes as EPS bead diameter  $d_p$  increases ((a)→(c)). For all values of  $d_p$  and  $\theta$ , it can be observed that increasing the release volume  $V_i$  causes a slight increase in positive and negative pressure peak magnitudes.

### 5.2.1 Scaling of pressure signals

Based on rotational theory of the head of a gravity current, modelled as a wedge flow with vortex-like recirculation, a series of expressions have been derived that describe the pressure along the surface through the centre of a gravity current [McElwaine, 2004]. The expression that describes the pressure along the surface between the moving front of the current and the centre of the vortex (i.e. the positive pressure peak to the negative pressure peak) is

$$p = \frac{1}{2}\rho_a u^2 \left(1 - \xi \frac{\eta}{L}\right) + 2g(\rho_c - \rho_a) \eta \sin\left(\frac{1}{2}\phi\right) \cos\left(\theta + \frac{1}{2}\phi\right), \quad (5.9)$$

## 5.2. AIR PRESSURE SIGNALS

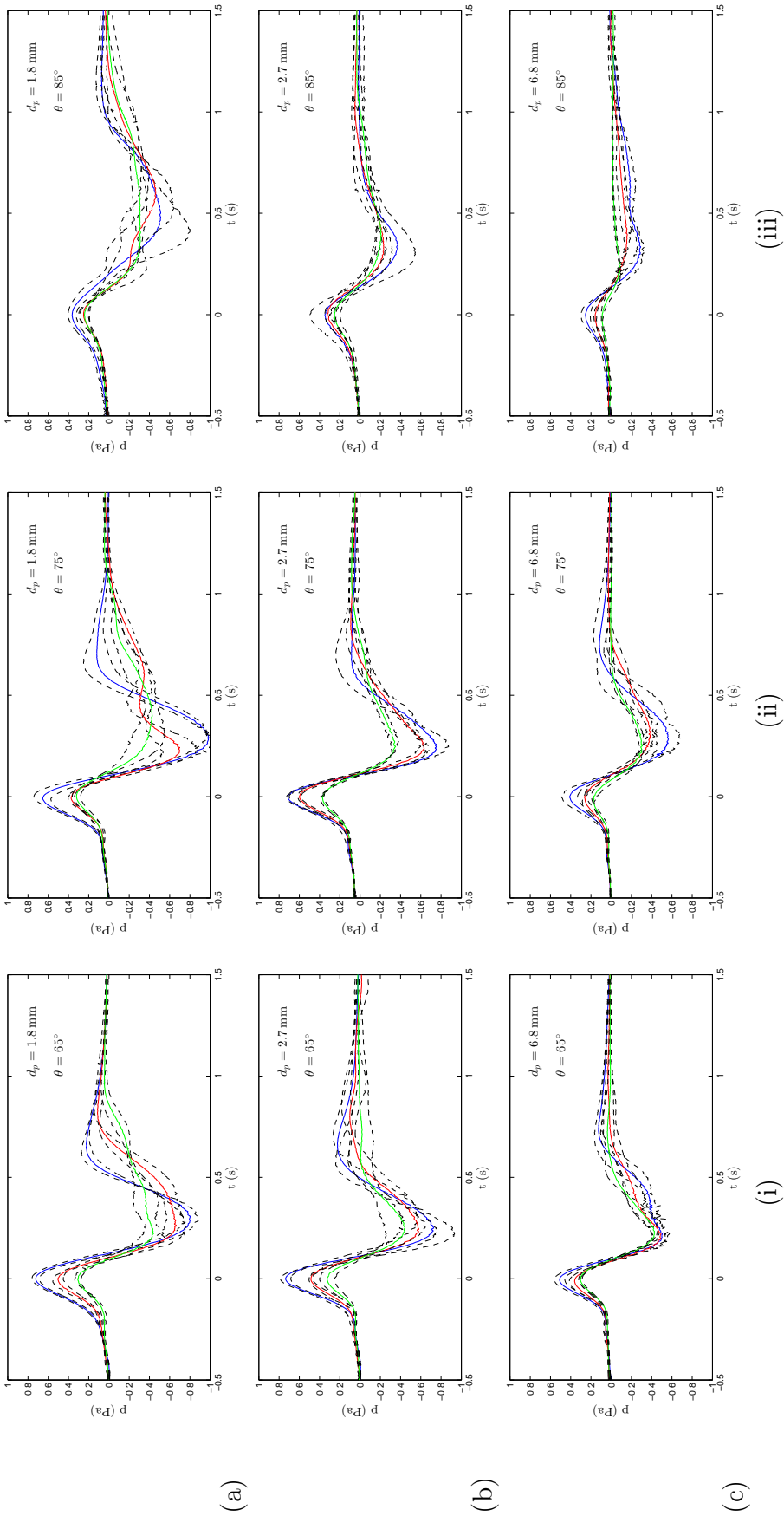


Figure 5.13: Ensemble mean air pressure signals collected from experiments (solid lines), plus or minus the standard deviation from the ensemble mean (dashed lines). Rows (a)→(c) show increasing EPS bead diameter  $d_p$  experiments and columns (i)→(iii) show increasing slope angle  $\theta$  experiments. Line colour indicates initial volume of release  $V_i$ , where blue -  $V_i = 3300 \text{ cm}^3$ , red -  $V_i = 2100 \text{ cm}^3$  and green -  $V_i = 1000 \text{ cm}^3$ .

## 5.2. AIR PRESSURE SIGNALS

---

where  $\xi \approx 1.01$ ,  $L$  is the effective length scale of the flow and  $\eta = (t_0 - t)U_f$  is the distance from the moving front of the current, where  $t_0$  is the time at which the front arrives at the sensor. The angle  $\phi$  is the acute angle that the moving front makes with the chute surface.

Based on the variables in Equation 5.9, the pressure scale,

$$\tilde{p} = \frac{p}{\frac{1}{2}\rho_a u^2} \quad (5.10)$$

and the timescale,

$$\tilde{t}_p = \frac{t}{\left(\frac{L}{g'}\right)^{\frac{1}{2}}}, \quad (5.11)$$

where  $g' = g((\rho - \rho_a)/\rho_a)$ , can be found. The effective length scale  $L$  is taken to be the aerodynamic flow radius, equal to the current height,  $h_c$ . The pressure versus time signals shown in Figure 5.13 are non-dimensionalised using these pressure and timescales (Figure 5.14). When all of the non-dimensionalised signals for a particular value of  $d_p$  and  $\theta$  are presented as an ensemble average, as they are in Figure 5.15, the lack of scatter indicates that this scaling of the data has succeeded in making the pressure data independent of release volume  $V_i$ . The data in Figures 5.14 and 5.15 also appears to be independent of slope angle  $\theta$  and EPS bead diameter  $d_p$ . In order to further investigate this, individual non-dimensionalised pressure signals are grouped according to EPS bead diameter and ensemble average signals produced for each value of  $d_p$  (Figure 5.16(a)), this process is then repeated for the different values of slope angle used (Figure 5.16(b)). The results indicate that the scaled pressure data is indeed independent of both EPS bead diameter and slope angle, and when all the non-dimensionalised signals are compared together (Figure 5.16(c)), this scaling provides a remarkably good collapse of the data, given the number and range of variables involved and the level of turbulence in parts of the flow.

The success of these pressure and timescales in scaling the data provides further evidence that the air flow inside the head of a gravity current is indeed dominated by a large vortex-like structure and that the dynamic theory of the air flow [McElwaine, 2004] provides a good model (up to the minimum pressure peak) for the pressure through a gravity current.

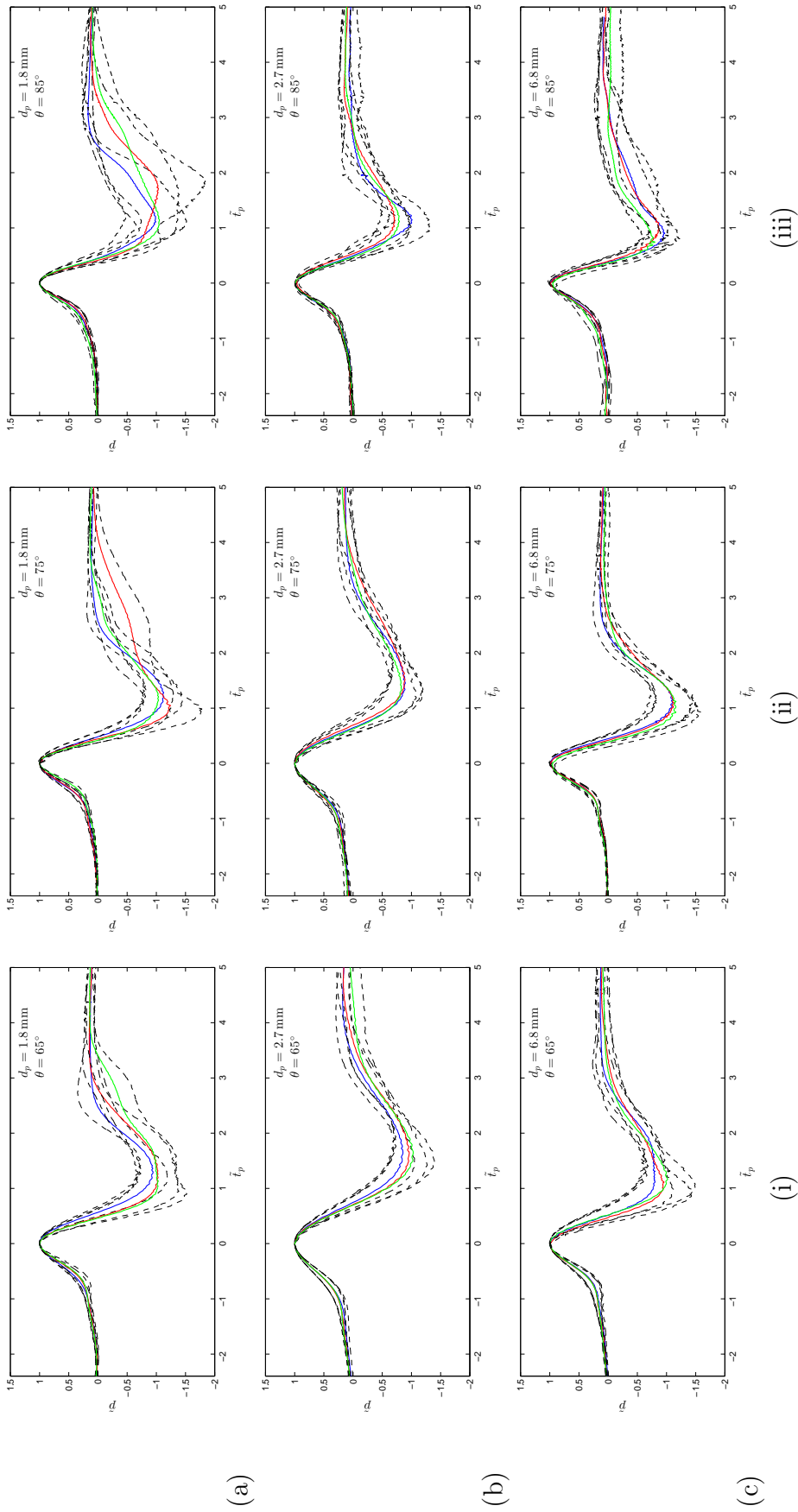


Figure 5.14: Non-dimensional plots of data shown in Figure 5.13. Rows (a)  $\rightarrow$  (c) show increasing EPS bead diameter  $d_p$  experiments and columns (i)  $\rightarrow$  (iii) show increasing slope angle  $\theta$  experiments. Line colour indicates initial volume of release  $V_i$ , where blue -  $V_i = 3300 \text{ cm}^3$ , red -  $V_i = 2100 \text{ cm}^3$  and green -  $V_i = 1000 \text{ cm}^3$ .

## 5.2. AIR PRESSURE SIGNALS

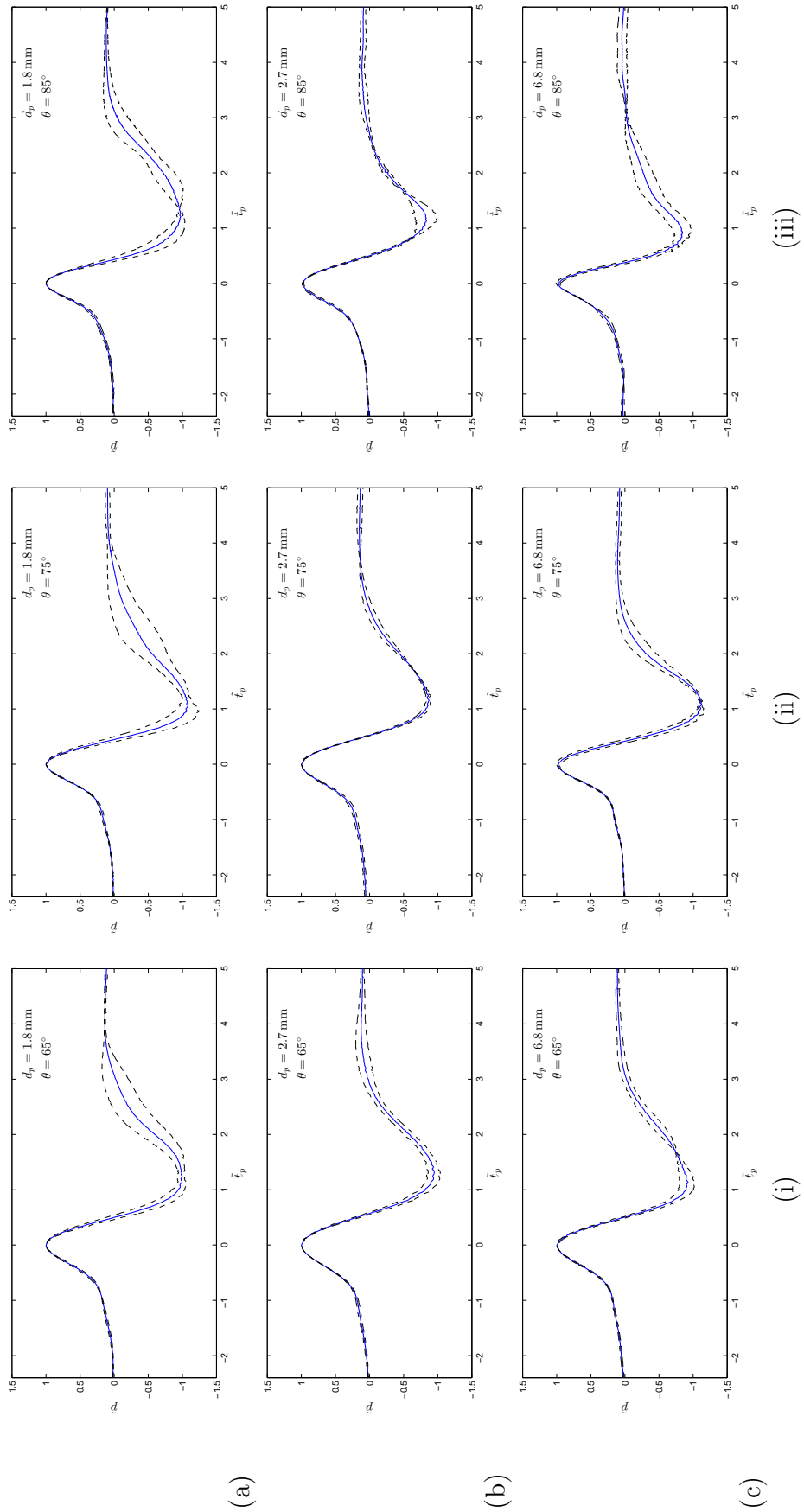


Figure 5.15: Ensemble mean plots of non-dimensional data shown in Figure 5.14. Solid lines represent ensemble mean average of experiments conducted with different initial release volumes  $V_i$ , with plus or minus one standard deviation from the mean shown as dashed lines. Rows (a)  $\rightarrow$  (c) show increasing EPS bead diameter  $d_p$  experiments and columns (i)  $\rightarrow$  (iii) show increasing slope angle  $\theta$  experiments.

## 5.2. AIR PRESSURE SIGNALS

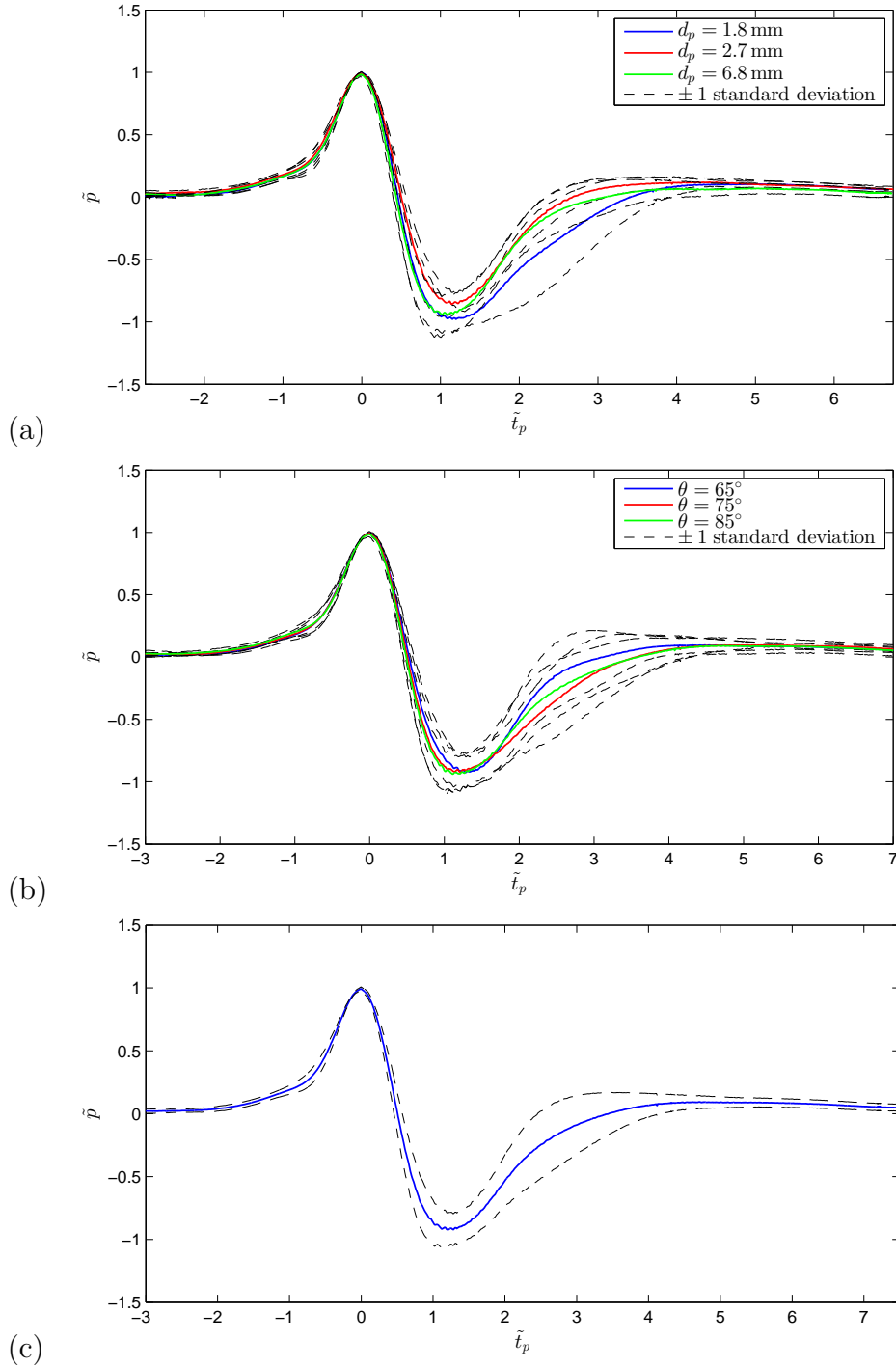


Figure 5.16: Non-dimensional air pressure signals. (a) Solid lines show ensemble mean average signal with different colours representing different EPS bead diameters,  $d_p$ . (b) Solid lines show ensemble mean average signal with different colours representing different slope angles,  $\theta$ . (c) Solid line shows ensemble mean average signal of all experiments. In all plots black dashed lines show plus or minus one standard deviation from the ensemble mean.



### 5.3. CURRENT FRONT ANGLES

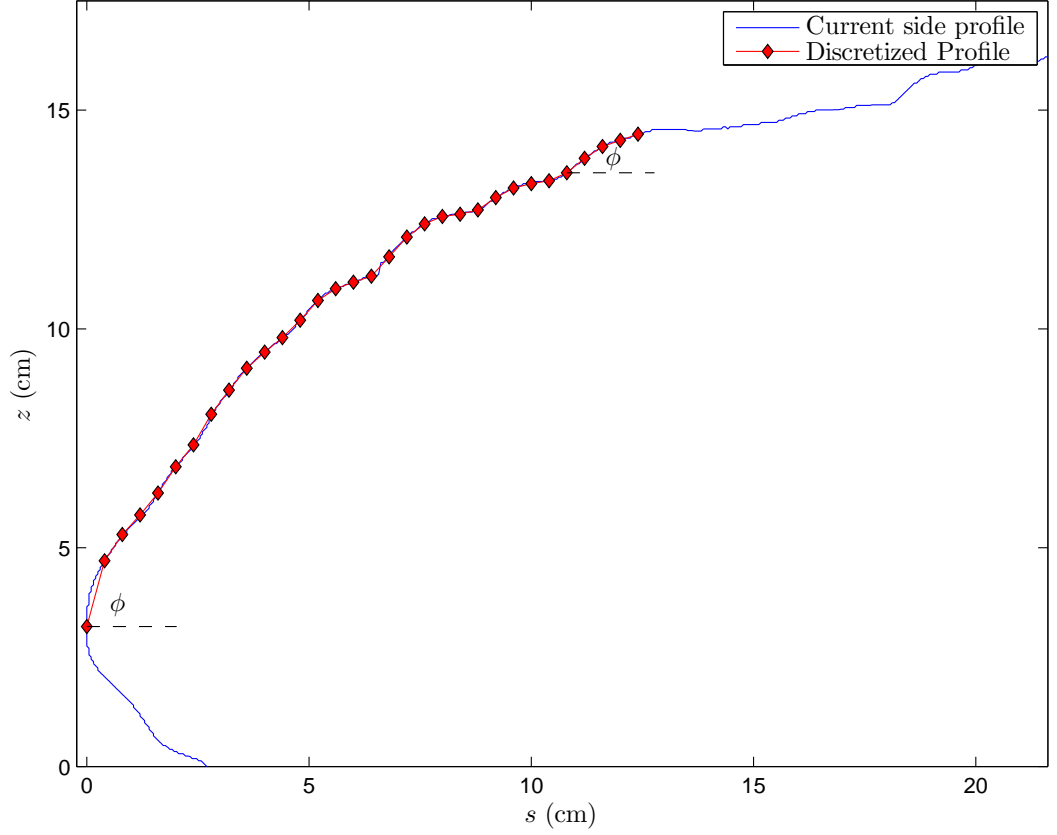


Figure 5.17: Current front edge profile (blue line) with discretization applied (red line).  $s$ -plane separation of discretization points ( $\diamond$ ) is equal to two EPS bead diameters ( $2d_p$ ) and current front angle,  $\phi$ , is the angle between the front edge profile and the  $s$ -plane.

### 5.3 Current front angles

In addition to modelling the air pressure through a gravity current, dynamic theory also states that the acute angle between the front of the gravity current and the chute,  $\phi = 60^\circ$  [von Kármán, 1940, McElwaine, 2004]. Although this result is based on the assumption that the cross-sectional profile of the current is a ‘wedge’, with the foremost point located on the chute surface, as opposed to the raised ‘nose’ profile observed in the currents in this study, it is of interest to measure  $\phi$  for these currents and compare the results with the value suggested by dynamic theory.

McElwaine [2004]’s air flow model is based on an expansion about the stagnation point, and it is therefore at this point that the front angle should be  $60^\circ$ . As previously discussed (§1.4.1), for a gravity current with a raised

### 5.3. CURRENT FRONT ANGLES

---

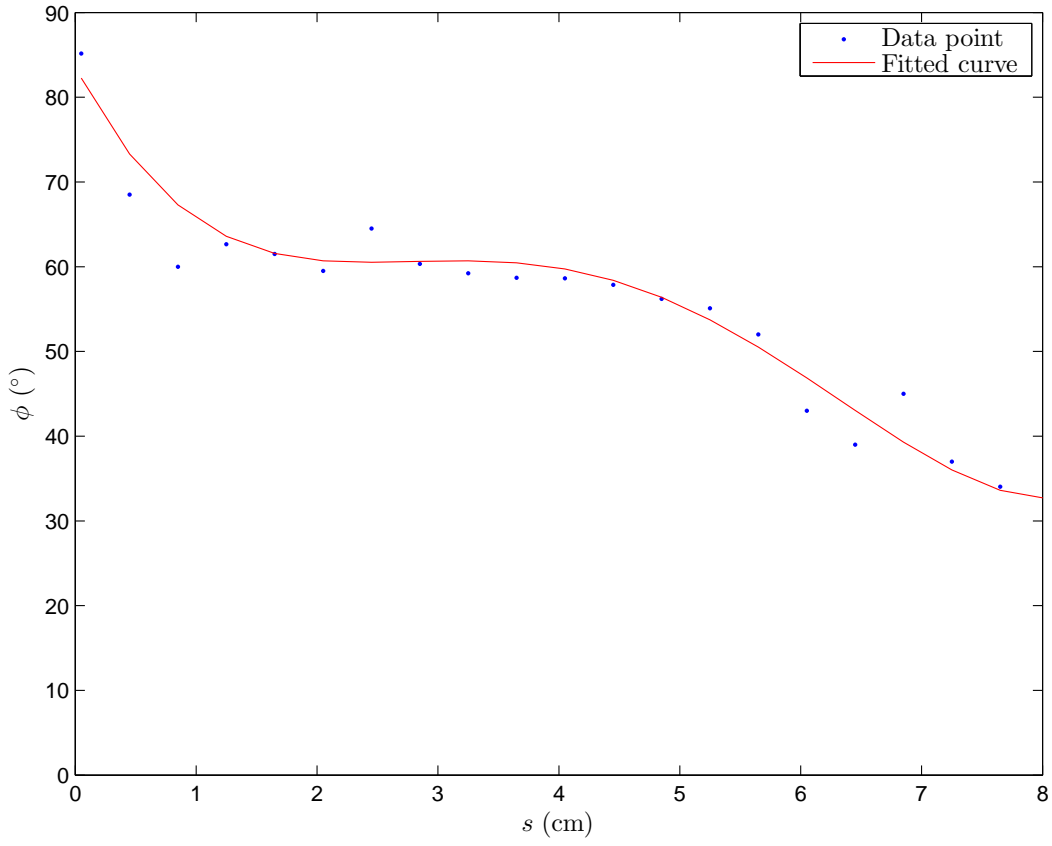


Figure 5.18: Current front angle,  $\phi$ , versus distance from foremost point of the current,  $s$ , for the front edge profile shown in Figure 5.17.

### 5.3. CURRENT FRONT ANGLES

---

nose the stagnation point is located just below the nose of the current [Härtel et al., 2000], therefore in this situation the chute surface is not a suitable datum from which to measure the front angle. As the exact location of the stagnation point for each current is unknown, a line that passes through the nose and is parallel to the chute surface is instead used as the datum (Figure 5.17).

Looking at a front-edge profile taken from one of the side-on images it is clear that the angle that the profile makes with the datum varies greatly along its length (Figure 5.17). Taking a measurement just above the nose gives an angle of  $\phi \approx 90^\circ$ , with this value tending to zero as distance from the nose of the current,  $s$ , increases. It can also be seen that the rate at which  $\phi$  decreases also changes as  $s$  increases, decreasing rapidly immediately behind the nose and less so further away. This variation in rate of decrease is used to select a section of the front profile to be used to measure  $\phi$ . It is desirable to select a section of the front profile above, and as close as possible to the nose. However this section must also provide a good reflection of the angle that a reasonable length of the front profile makes with the datum, therefore the rate of change of  $\phi$  needs to be small around this section. To find such a section the curved front-edge profile is first discretized into a series of small straight-line segments (Figure 5.17). The angle that each of these segments makes with the datum is then calculated and the results plotted against  $s$  (Figure 5.18). All of the front profiles produced  $\phi$  versus  $s$  plots with similar features, rapidly decreasing front angles at low values of  $s$  that then level off before decreasing again as  $s$  increases (and often levelling off again as  $s$  increases further). The first ‘plateau’ of  $\phi$  values is taken as the front angle for the front profile. In order to detect the first plateau in  $\phi$  values a curve is fitted to the points of the  $\phi$  versus  $s$  plot using a least squares method. Stationary points on this curve are then identified, with the first one found to be a saddle point corresponding to the first plateau.

Clearly the front profile needs to be discretized into appropriately sized straight-line sections to ensure accurate results. If the sections are too large then they will not provide a good approximation for the section of curve that they represent, additionally accuracy of the rate of change of  $\phi$  will be lost. Conversely, if the sections are too small the accuracy of the results may be affected by small fluctuations in the profile caused by individual EPS beads. Similar to the discretization applied when detecting lobe and clefts (§3.8), an interval size equal to  $2d_p$  was found to provide an good representation of the

### 5.3. CURRENT FRONT ANGLES

---

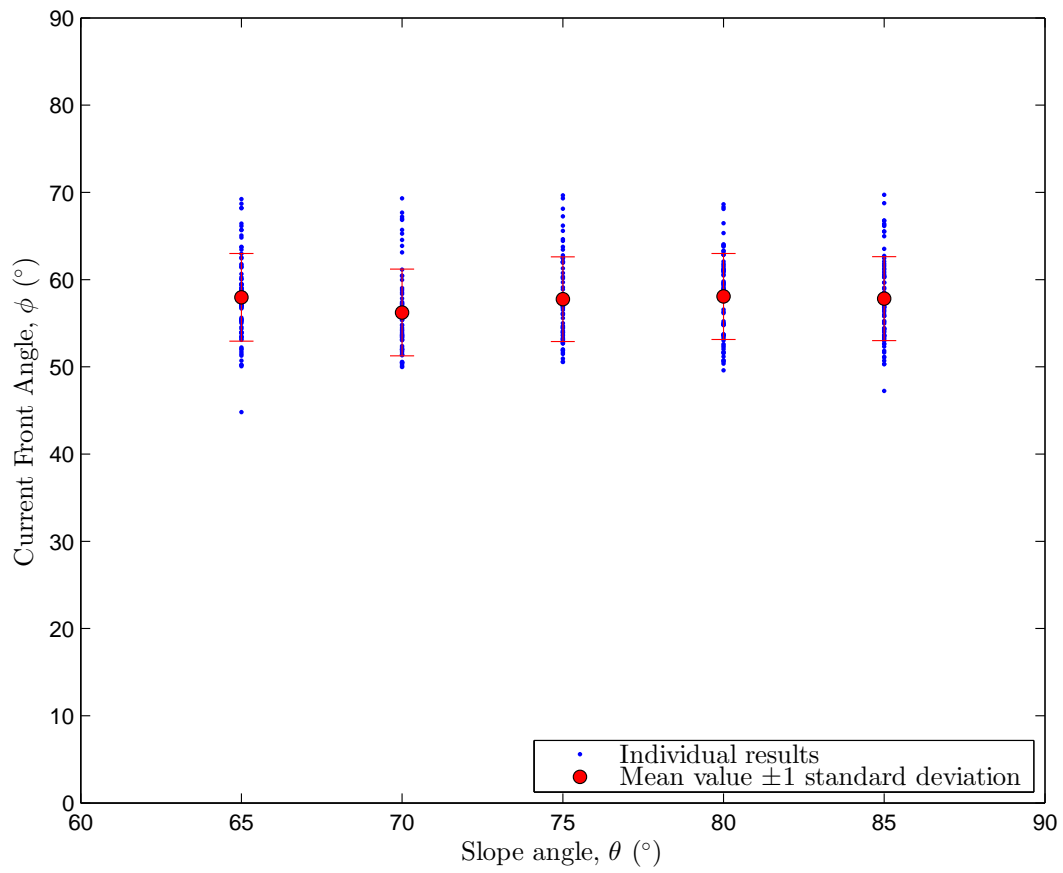


Figure 5.19: Current front angle,  $\phi$ , versus slope angle,  $\theta$

### 5.3. CURRENT FRONT ANGLES

---

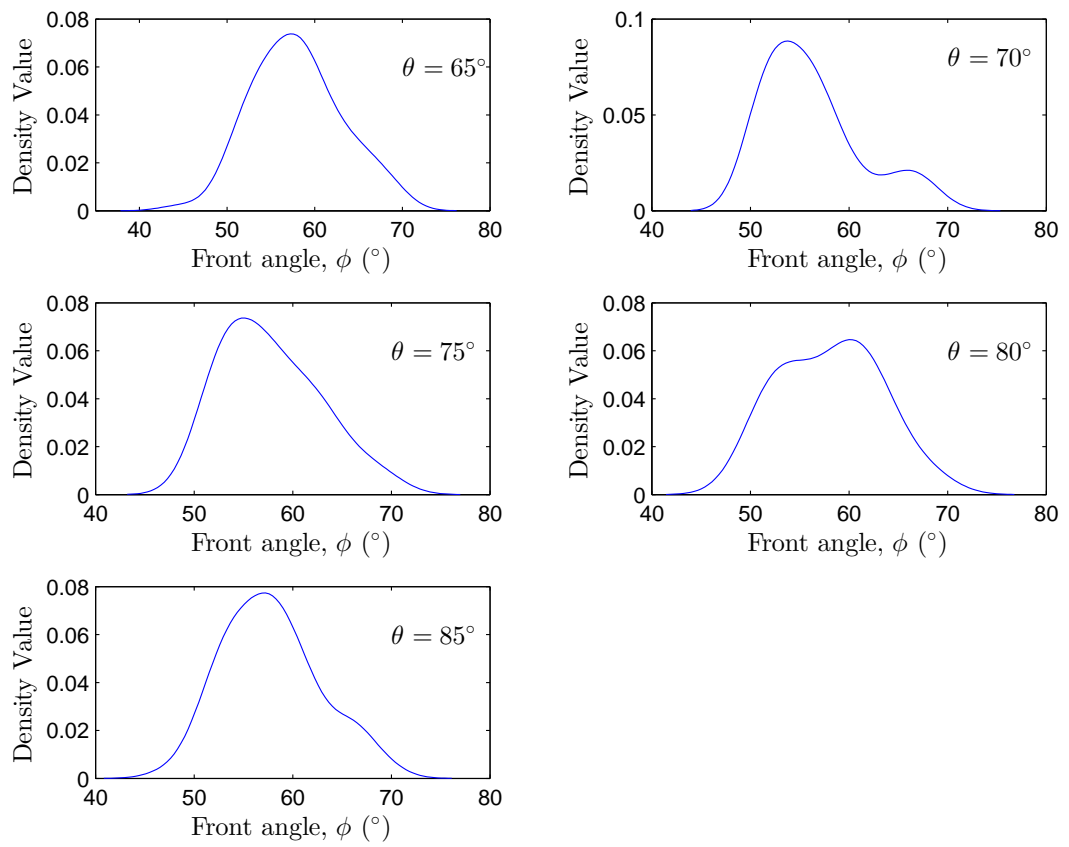


Figure 5.20: Kernel density estimate plots of the front angle data for each slope angle.

## 5.4. VISUALISATION OF PRESSURE SIGNAL FEATURES

---

profile.

The results in Figure 5.19 show that the front angle of the current  $\phi$  is independent of slope angle  $\theta$ , and although there is a reasonably large amount of scatter in the results, the mean value of  $\phi$  for all slope angles plus or minus one standard deviation is  $57.6^\circ \pm 4.9^\circ$ . A normal kernel function was used to obtain a probability density estimate [Bowman and Azzalini, 1997] for the values of  $\phi$  at each slope angle (Figure 5.20). These density estimates show that for the majority of slope angles the front angle is unimodal, with the modal value in the range  $\approx 55-60^\circ$ . The exception is the data from the experiments conducted at a slope angle  $\theta = 70^\circ$ , which is bimodal, with a large peak at approximately  $54^\circ$  and a smaller peak at approximately  $66^\circ$ .

It is unclear whether this high degree of scatter arises naturally from the data itself, or is related to the measurement technique. In the future it would be beneficial to verify this result by refining the technique used here, or developing an improved system.

## 5.4 Wavelet-based visualisation of air pressure signal features

An additional advantage of using the wavelet-based method for de-noising of the signals is that it forms the basis of, and can easily be extended to, a method for visualization of a signal's features developed by Keylock [2007]. This technique makes use of the wavelet decomposition data and allows wavelet coefficients and scales that actively contribute to flow features to be identified. In order to achieve this the variance of the wavelet coefficients, both on a global and scale-by-scale level, is first calculated. All wavelet coefficients are set to zero where the sign of the coefficient at a point in time is opposite that of the sum of the coefficients at that point in time. The remaining coefficients are then normalised by the global (Figure 5.21(b)) or scale-by-scale (Figure 5.21(c)) standard deviations for each component.

The advantage of this method over a standard SWT decomposition, is that only wavelet coefficients that contribute to a particular flow event are shaded, since coefficients with an opposite sign are in white. This makes

## 5.4. VISUALISATION OF PRESSURE SIGNAL FEATURES

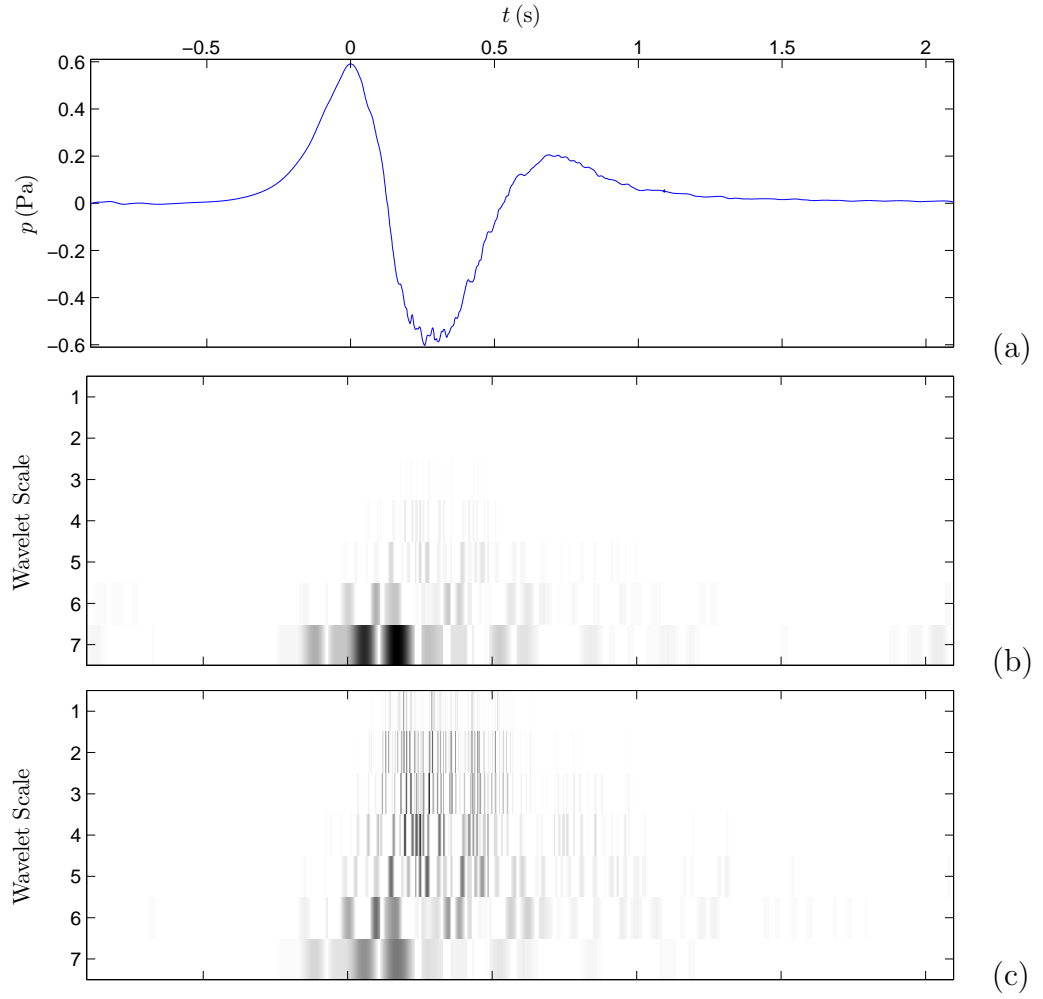


Figure 5.21: Wavelet-based visualisation of flow features. (a) De-noised and filtered pressure signal. (b) Wavelet coefficients normalised by the global wavelet variance. (c) Wavelet coefficients normalised by scale-by-scale wavelet variance. For (b) and (c), darker values indicate a higher value for the coefficients and coefficients that are opposite in sign to the detected fluctuation are set to zero.

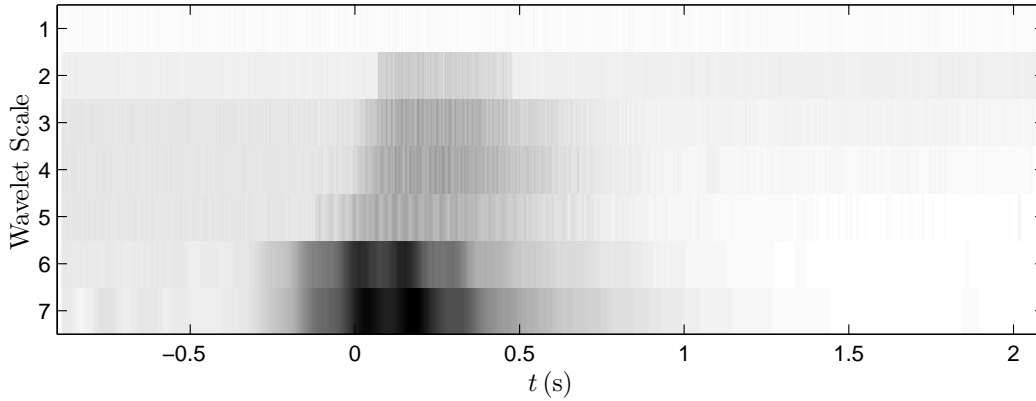


Figure 5.22: Ensemble wavelet-based visualisation of flow features. Wavelet coefficients normalised by scale-by-scale wavelet variance. Darker values indicate a higher value for the coefficients and coefficients that are opposite in sign to the detected fluctuation are set to zero.

it easier to focus upon the relevant scales for generating a particular flow event and hence the likely processes in operation. Scaling with respect to the global variance indicates the scales that dominate the whole flow (Figure 5.21(b)), but makes it harder to determine the importance of a contribution at a particular scale to the detected flow event. Normalising with respect to scale-by-scale variances (Figure 5.21(c)) compensates for differences in energy between scales and produces a wavelet spectrum analogous to the Fourier spectrum. It can be seen in Figure 5.21(b) that overall the flow is dominated by the high amount of energy at level 7, correlating with the peak at  $\approx 1$  Hz in the power spectrum produced from the DFT of the signal. This energy corresponds to the large positive and negative pressure peaks caused by the large vortex-like structure at the centre of the flow. However when differences in energy between scales are accounted for, it is found that higher frequency (scales 2–6) components that occur around and after the negative pressure peak are equally significant (Figure 5.21(c)). It seems likely that these high frequency components correspond to fluctuations in the flow velocity caused by turbulence.

## 5.5 Summary

The non-dimensionalisation of the pressure signals was found to provide good scaling of the vortex-like structure behind the head and allowed ensemble sig-



## 5.5. SUMMARY

---

nals consisting of data from different experiments to be produced (§5.2.1). However the turbulent fluctuations in air pressure observed around and after the negative pressure peak are not well accounted for, and the process of producing ensemble signals causes a significant loss of information about these fluctuations. By applying the wavelet-based visualisation technique to non-dimensionalised air pressure signals from individual experiments, information about the scale of the coefficients that contribute to flow events is obtained. The wavelet coefficient data collected from each individual experiment can then be used to produce an ensemble of all the experiments conducted (Figure 5.22), and general trends in the scale and occurrence of flow features identified.

Similar to the results from an individual experiment (Figure 5.21(b)) there are peaks in the energy levels of wavelet coefficient scales 6 and 7 that coincide with the occurrence to the positive and negative air pressure peaks. The strength of these peaks in coefficient energy level and the short time period over which they occur in the ensemble plot suggest that they were a regular, repeatable feature in the signals. The lower scale (3–5) coefficients appear over approximately the same time period, but are more evenly distributed and less significant (when compared with scales 6 and 7) than those seen in the individual experiment result. The scale (corresponding to high frequencies) and temporal position of these relatively high energy level wavelet coefficients provides further evidence for them relating to the turbulent fluctuations observed in the air pressure signals. This is further backed-up by the differences in distribution and significance when the ensemble result is compared to an individual result. By its very definition a turbulent fluctuation will not always occur at a certain time, therefore when looking at ensemble data of a turbulent process we would expect to see occurrences spread across the time period where turbulence is expected. This spreading of occurrences leads to a reduction in peak wavelet coefficient energy levels and a reduction in significance in the ensemble data. However, despite the reduction of significance caused by the averaging of the data, the contribution made to the air pressure signals by the lower scale wavelet coefficients is still significant and represents a regularly occurring process in the flow, which is most likely turbulent.

Wavelet-based analysis techniques have been demonstrated to be an extremely useful and powerful tool for processing and studying air pressure signals obtained from laboratory-scale powder snow avalanches. As well as denoising and filtering the signals, wavelet-based analysis has been demonstrated

to be capable of enabling visualisation of flow data and identification of important flow events. Information about both the time and frequency levels of these events can be obtained as well as their energy levels relative to both the energy of other events with similar frequencies and to the total energy of the signal as a whole. In addition to being applied to data obtained from laboratory-scale experiments, these wavelet-based techniques could also be applied to field or large-scale model powder snow avalanche air pressure data, or indeed any other kind of time series data.

## Bibliography

- J. B. Allen. Short time spectral analysis, synthesis, and modification by discrete Fourier transform. *IEEE Transactions on Acoustics, Speech, and Signal Processing*, 25(3):235–238, 1977.
- L. Birge and P. Massart. *Festschrift for Lucien Le Cam*, chapter From model selection to adaptive estimation, pages 55–87. Research Papers in Probability and Statistics. Springer, New York, 1997.
- A. W. Bowman and A. Azzalini. *Applied Smoothing Techniques for Data Analysis*. Oxford University Press, Oxford, U.K., 1997.
- I. Daubechies. *Ten Lectures on Wavelets*. CBMS-NSF Regional Conference Series in Applied Mathematics. Society for Industrial and Applied Mathematics, 1992.
- D. L. Donoho and I. M. Johnstone. Ideal spatial adaptation by wavelet shrinkage. *Biometrika*, 81:425–455, 1994.
- P. Duhamel and M. Vetterli. Fast Fourier transforms: A tutorial review and a state of the art. *Signal Processing*, 19:259–299, 1990.
- C. Härtel, F. Carlsson, and M. Thunblom. Analysis and direct numerical simulation of the flow at a gravity-current head. Part 2. The lobe-and-cleft instability. *Journal of Fluid Mechanics*, 418:213–229, 2000.
- C. J. Keylock. The visualization of turbulence data using a wavelet-based method. *Earth Surface Processes and Landforms*, 32:637–647, 2007.
- M. Lavielle. Detection of multiple changes in a sequence of dependent variables. *Stochastic Processes and their Applications*, 83:79–102, 1999.

## BIBLIOGRAPHY

---

- S. Mallat. *A Wavelet Tour of Signal Processing*. Academic Press, 1998.
- J. N. McElwaine. Rotational flow in gravity current heads. *Philosophical Transactions of the Royal Society*, 363:1603–1623, 2004.
- B. Turnbull and J. N. McElwaine. Experiments on the non-Boussinesq flow of self-igniting suspension currents on a steep open slope. *Journal of Geophysical Research*, 113(F01003), 2008. doi:10.1029/2007JF000753.
- T. von Kármán. The engineer grapples with nonlinear problems. *Bulletin of the American Mathematical Society*, 46:615–683, 1940.



## Chapter 6

# Identification of flow patterns using Particle Image Velocimetry

The image and air pressure data examined so far in this study has suggested the presence of various flow patterns within the currents. In this chapter we seek to provide further evidence for the existence of such patterns by attempting to visualise and measure them. These data will then enable further investigation, and potentially direct quantification, of the effect that these flow features have on the development of lobe-and-cleft-type patterns and flow dynamics.

### 6.1 Particle Image Velocimetry

In order to visualise flow patterns within the EPS bead-air currents, the images collected during the experiments were analysed using DigiFlow image processing software [Dalziel, 2002–2013]. Particle velocimetry can be conducted using two different techniques, Particle Tracking Velocimetry (PTV) or Particle Image Velocimetry (PIV). Particle Image Velocimetry is based on pattern matching in an essentially Eulerian way, and has the advantages of excellent velocity resolution and being fairly robust to noise. The disadvantages of this technique are its inability to cope with any structure across the plane being analysed (i.e. velocity gradients parallel to the viewing direction) and that it does not allow individual particles to be tracked, and hence Lagrangian de-

## 6.1. PARTICLE IMAGE VELOCIMETRY

---

scriptions of particle motion cannot be obtained. The advantages of Particle Tracking Velocimetry are that it does allow tracking of individual particles, enabling description of some of the Lagrangian flow features, and that it can be used to analyse flows with significant velocity gradients parallel to the direction of viewing. However, these advantages are best realised in, and will henceforth be referred to as, a ‘typical’ PTV set-up. This typical set-up involves using transparent seeding particles that are suspended in, and closely follow, the flowing fluid. The volume or area of the fluid under investigation is then illuminated (normally with a laser), causing light to scatter off the seeding particles and making them visible to the camera recording the experiment [Grue et al., 2004]. The density of the seeding particles is dense enough such that there is a sufficient number of particles in all parts of the fluid to capture and reflect all of the flow features, but not so dense that individual particles cannot be identified. The flows in this study are likely to have significant velocity gradients normal to the chute (i.e. parallel to the direction of viewing for the plan view images) and would therefore suggest that the PTV-based technique would be better suited to analysing our images [Grue et al., 2004]. However, rather than tracking specifically added seeder particles, this study is attempting to track the EPS beads that are modelling powder snow. The density of the EPS beads means that the PTV algorithms struggle to identify individual particles, the opacity of the beads means that only beads on the flow surface can potentially be identified, and the three-dimensional velocity field means that beads only remain on the surface for very brief time periods. These factors make the PTV-based technique unsuitable for analysing the images obtained from the experiments in this study, and the PIV-based technique is used instead. Although it is only possible to analyse flow features on the outer surface of the current using this technique, it is nevertheless worthwhile as any features observed on the outer surface of the current will likely extend into, and possibly right through, the current.

To allow the relative motions of the EPS beads to be visualised, the mean downslope velocity of the current is calculated and the images are pre-processed to remove the effects of this averaged downslope motion. This pre-processing first involves selecting a region of interest to which the PIV is to be applied, which in this case is the part of the image that contains all, or part, of the current. The mean velocity in terms of pixels per frame is then calculated and the window is moved down the images in the sequence at this rate, effectively

## 6.1. PARTICLE IMAGE VELOCIMETRY

---

creating a Lagrangian interrogation region in which the Eulerian PIV technique is applied.

The pattern matching algorithm used in the PIV process is applied to a certain area, known as the interrogation window, of the region of interest at a time. The interrogation window is then shifted to another position within the region of interest and the pattern matching algorithm is again applied, this process is repeated until the entire region of interest has been covered. The size of the interrogation window and the spacing between the points where it is applied are adjustable, and appropriate values need to be selected in order to produce meaningful results. The overall quality of the output data is a compromise between velocity a spatial resolution [Grue et al., 2004]. A good balance was found to be achieved when the size of the interrogation was set to twice the size of the spacing value. As the patterns being matched by the algorithm are made up of EPS beads, it is therefore the size of these beads that determine the size of the interrogation window, and consequentially the spacing value. After testing various values based on multiples of the EPS bead diameter  $d_p$  used, it was found that an interrogation window size of  $4d_p$  and spacing value of  $2d_p$  gave the most coherent results.

The velocity<sup>1</sup> and vorticity fields obtained from PIV analysis of the plan view images (Figures 6.1, 6.2, 6.3 and 6.4) show that lobes consist of two regions rotating in opposite directions, with the left hand side of the lobe having negative (clockwise) and the right hand side positive (anticlockwise) vorticity. These observations are consistent with the theory of twin vortices proposed by Nohguchi and Ozawa [2008]. During the earlier stages of the currents motion down the chute (Figures 6.1 and 6.3) these regions are relatively small, don't extend back behind the front very far and are rapidly shifting. During the later stages (Figures 6.2 and 6.4) the regions of rotation are more stable and extend further back into the flow, especially for the currents consisting of the smaller diameter EPS beads. This longitudinal extension of the regions of rotation is not just due to the more extended lobes observed in the currents consisting of smaller diameter EPS beads, the large regions of approximately constant vorticity also extend further beyond the lobe and into the main body of the current. The levels of vorticity observed in the flows consisting of smaller diameter EPS beads are also stronger than those of the flows consisting of larger

---

<sup>1</sup>Note for increased clarity of velocity fields the image intensity,  $I$ , has been inverted and made 50% lighter throughout this chapter.

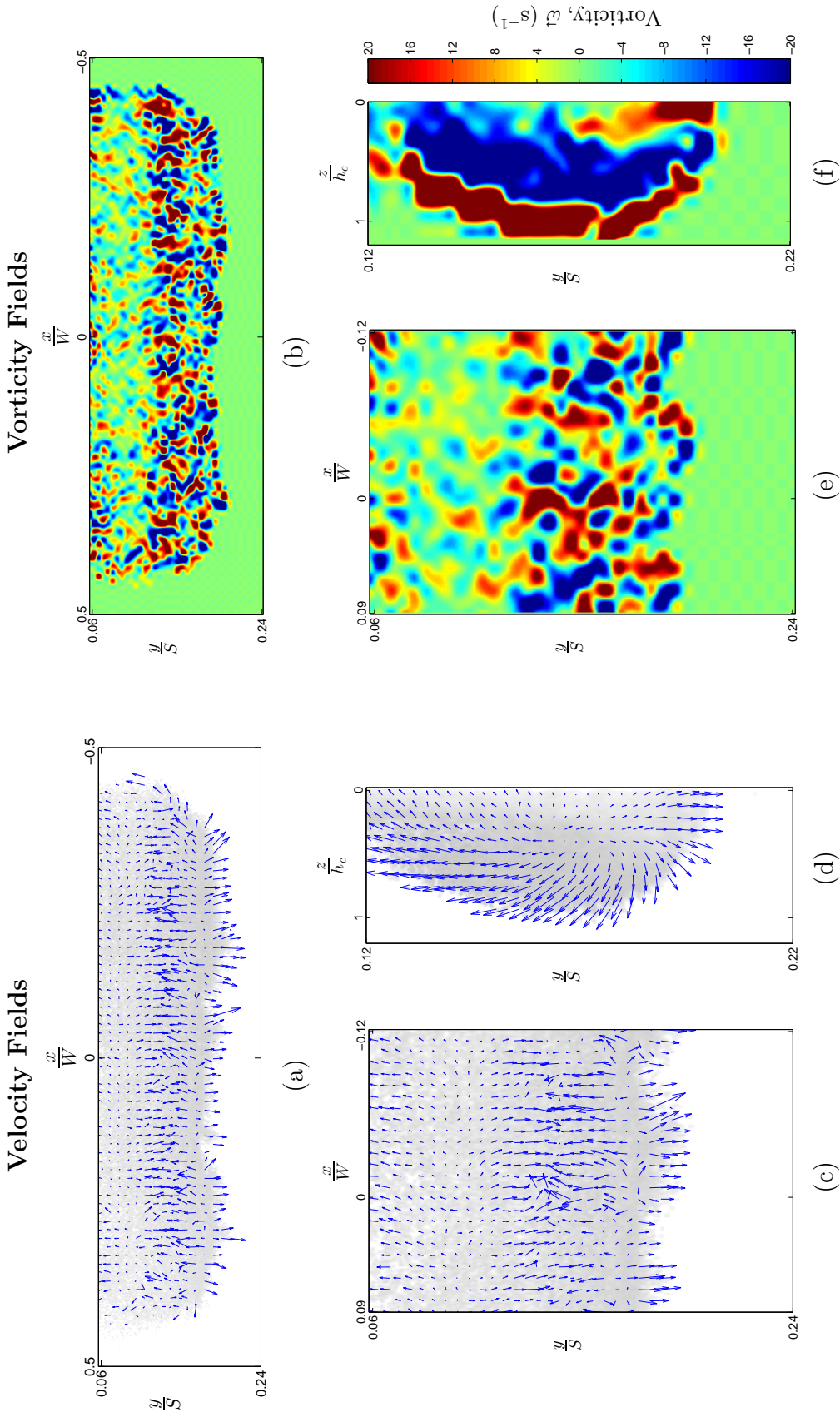


Figure 6.1: Velocity and vorticity fields obtained from PIV analysis of images obtained at  $t = 0.5$  s from an experiment conducted using  $1000\text{ cm}^3$  of 2.1 mm diameter EPS beads on a slope at an angle of  $70^\circ$  to the horizontal. (a) & (b) Plan view of the entire current, (c) & (e) plan view of part of the current, (d) & (f) side view of the current.



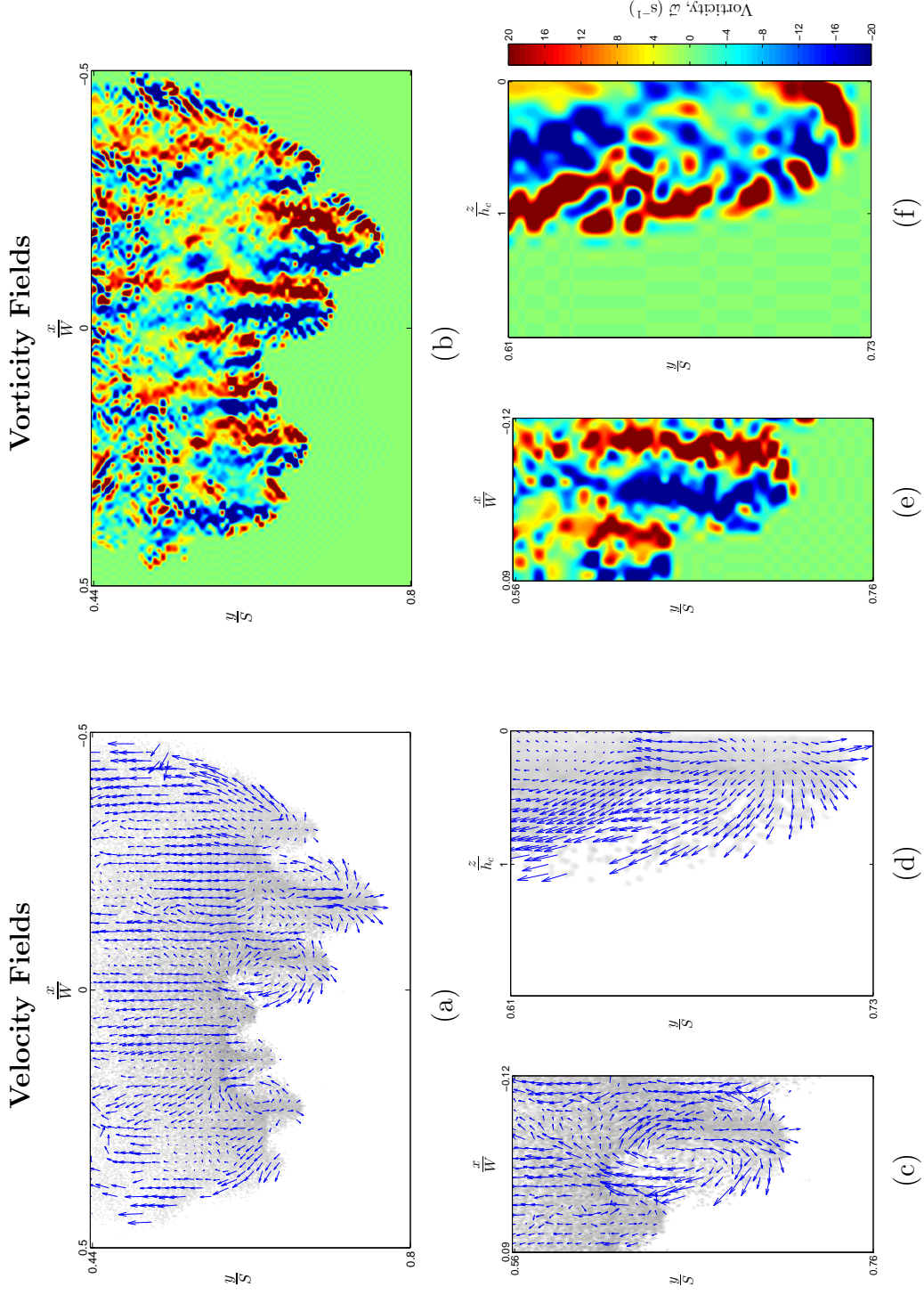


Figure 6.2: Velocity and vorticity fields obtained from PIV analysis of images obtained at  $t = 1.0$  s from an experiment conducted using  $1000\text{ cm}^3$  of 2.1 mm diameter EPS beads on a slope at an angle of  $70^\circ$  to the horizontal. (a) & (b) Plan view of the entire current, (c) & (e) plan view of part of the current, (d) & (f) side view of the current.

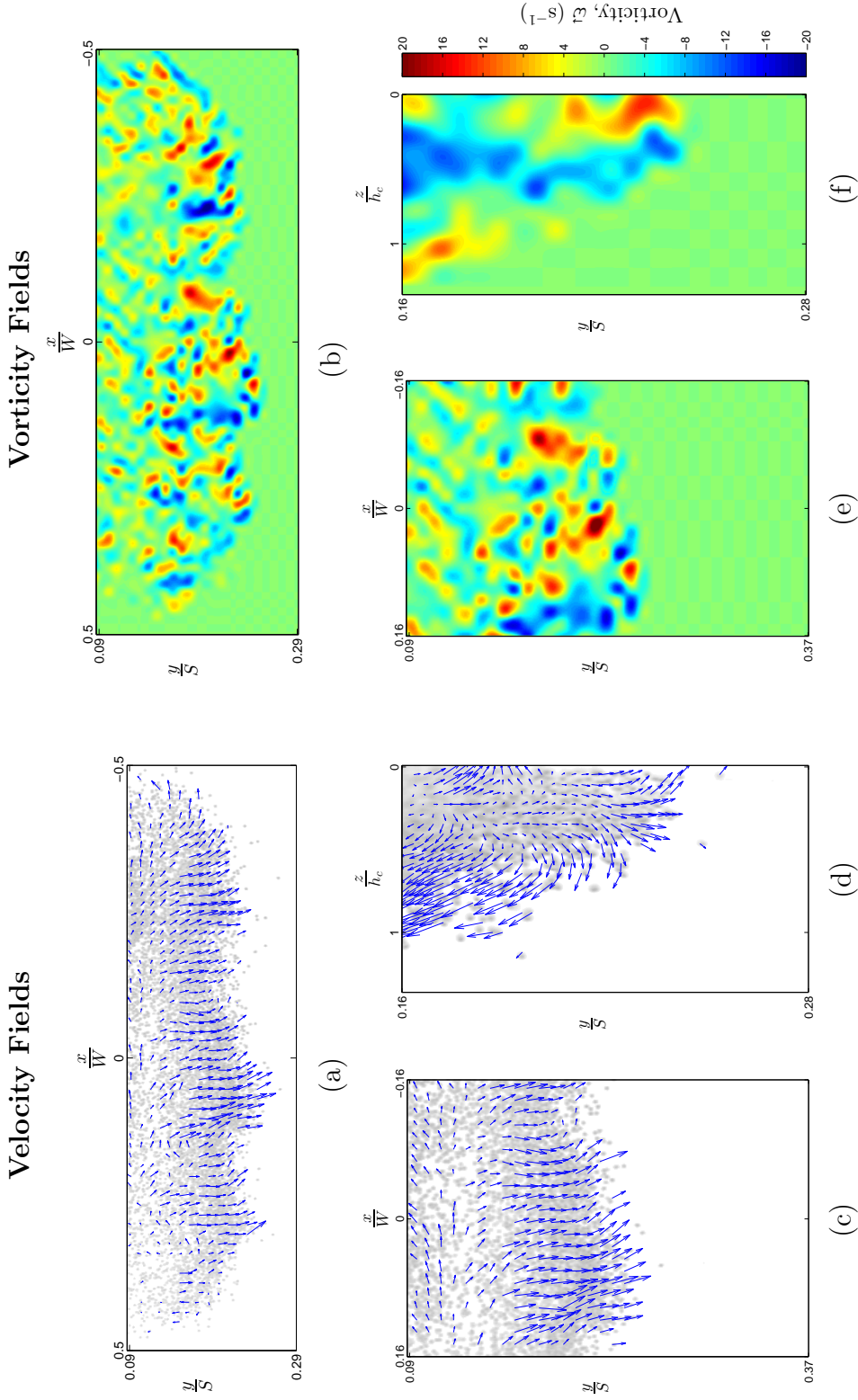


Figure 6.3: Velocity and vorticity fields obtained from PIV analysis of images obtained at  $t = 0.5$  s from an experiment conducted using  $1000\text{ cm}^3$  of 5.0 mm diameter EPS beads on a slope at an angle of  $70^\circ$  to the horizontal. (a) & (b) Plan view of the entire current, (c) & (e) plan view of part of the current, (d) & (f) side view of the current.

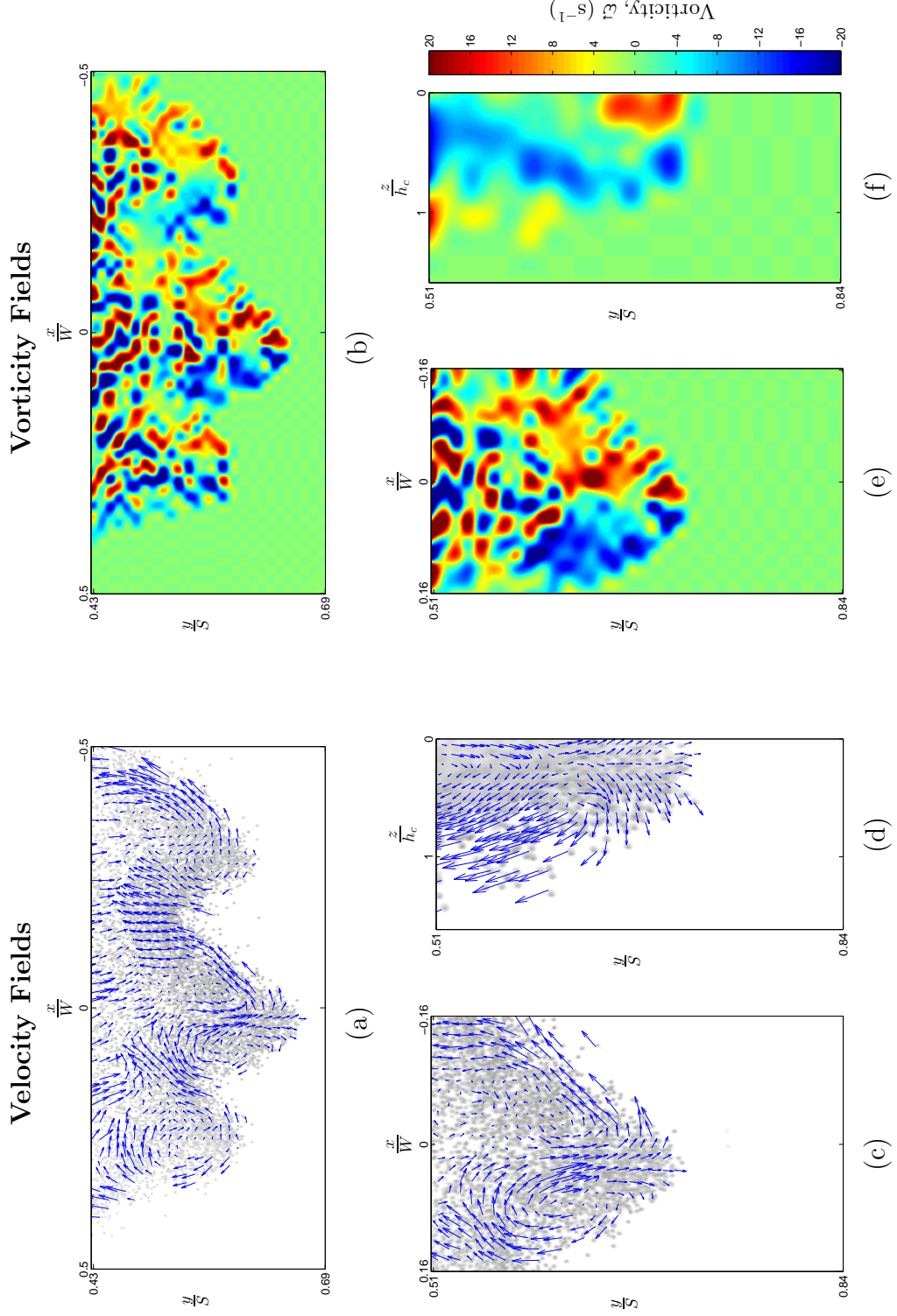


Figure 6.4: Velocity and vorticity fields obtained from PIV analysis of images obtained at  $t = 1.0$  s from an experiment conducted using  $1000 \text{ cm}^3$  of 5.0 mm diameter EPS beads on a slope at an angle of  $70^\circ$  to the horizontal. (a) & (b) Plan view of the entire current, (c) & (e) plan view of part of the current, (d) & (f) side view of the current.

diameter EPS beads.

The velocity and vorticity fields obtained from PIV analysis of the side view images (Figures 6.1, 6.2, 6.3 and 6.4) show that in the central part of the current, in the plane normal to the chute ( $y$ - $z$ ), there is clockwise rotational motion consistent with there being a large vortex-like structure at the centre of the current. A small region of anticlockwise rotational motion can also be seen below the nose of the current head. This is probably caused by the unstable stratification in this region, which is thought to be the origin of the classic lobe-and-cleft instability. Note that in this analysis this region of anticlockwise rotational motion probably appears to extend further back from the nose (increasing values of  $s$ ) than it actually does in reality, due to the cameras position and the uneven nature of the front. The region of positive vorticity of the most extended (greatest value of  $y$  position) lobe can end up appearing to merge with the region of positive vorticity of a lesser extended lobe that is closer to the camera. Small regions of anticlockwise vorticity also appear on the upper outer edge of the current, and appear to be caused by individual EPS beads being thrown clear of the main body of the current. All of these flow features that appear in the  $y$ - $z$  plane appear to be fairly consistent in terms of size and magnitude between both the stage of the current's motion and the size of the EPS beads used.

### 6.1.1 Lobe bifurcation

PIV analysis was conducted on images showing the bifurcation of lobes in order to try and gain more information on the mechanisms behind, and the potential causes of, this process. Figure 6.5 shows the vorticity fields produced from PIV analysis of a typical sequence of images. The left hand side of the lobe has largely negative (clockwise) vorticity and the right hand side of positive (anticlockwise), however small regions of vorticity acting in the opposite direction frequently appear in both sides of the lobe. Often these regions remain small and quickly disappear, however sometimes they grow in both size and magnitude and develop into a new lobe. Figure 6.5 shows such a region forming on the left hand side of the lobe at  $t = 1.025$  s, it subsequently increases in size and magnitude as a separate lobe is formed.

Whilst it would be of interest to also analyse sequences of side on images



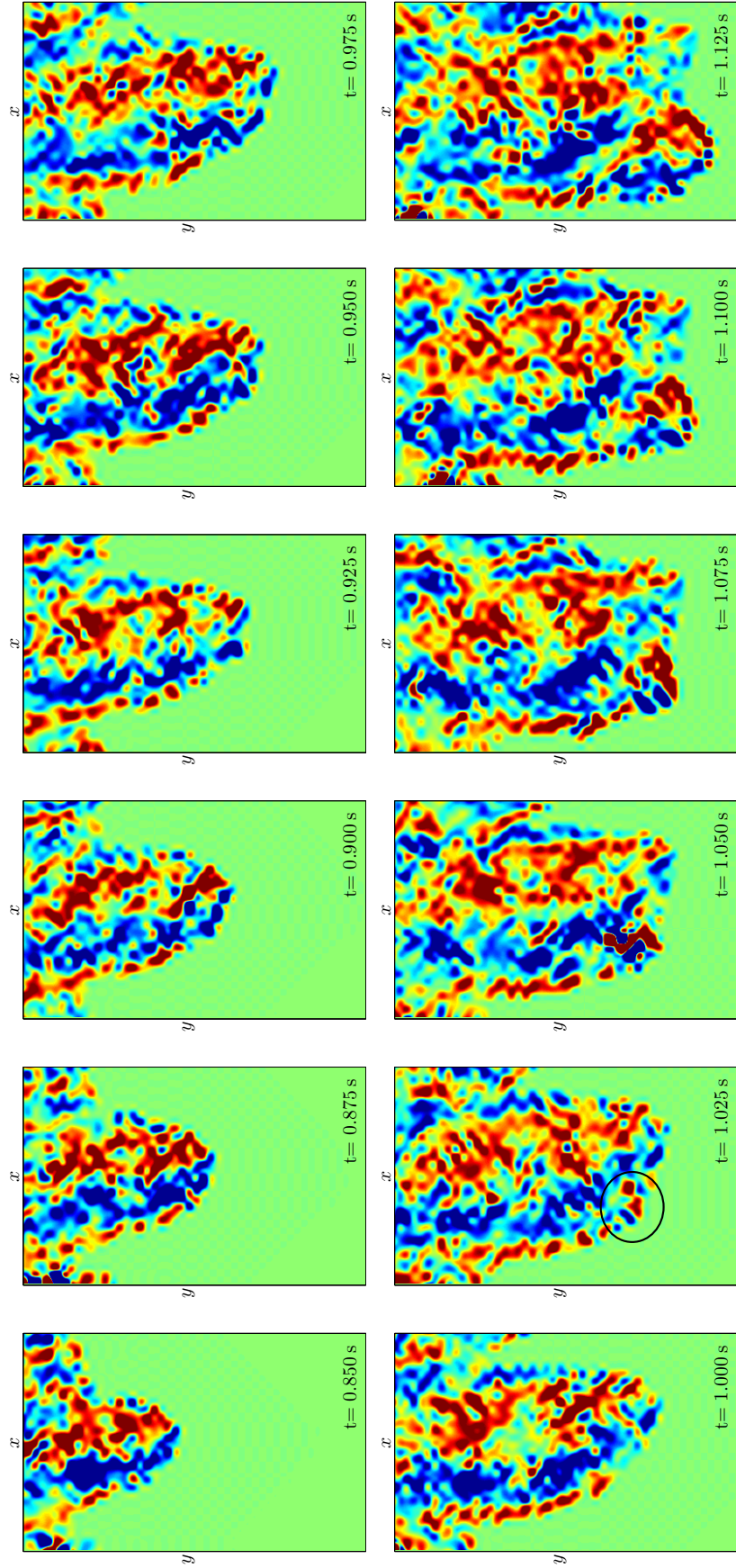


Figure 6.5: Vorticity Fields from PIV analysis of image sequence showing a bifurcating lobe. A small region of opposing vorticity that develops into a new lobe is circled at  $t = 1.025$  s

of lobes bifurcating using PIV, unfortunately no image sequences that clearly capture this process are available due to either the obstruction or distortion of the PIV analysis in the region of interest caused by other lobes located closer to the camera. Even if such data were available, we can only speculate how informative it would be because this form of PIV analysis is heavily biased towards the motion of the outer edges of the current (§6.1), and it may well be that the mechanism that leads to lobe bifurcation originates and is only observable in the centre of the lobe. This limitation of the current PIV set-up is also applicable to the analysis of the plan view image sequences discussed in the previous paragraph. This is an issue that would need to be addressed before it can be clearly determined whether the previously discussed features observed at the outer edge of the current are the cause or a symptom of the bifurcation of a lobe.

### 6.1.2 PIV and pressure signal comparison

The coordination of the collection of air pressure and image data allowed direct comparisons to be made between the air pressure signal and the PIV analysis. The aim of this comparison was to try and establish whether any of the air pressure signal features, most notably the small fluctuations found between the positive and negative peaks, could be directly attributed to flow velocity or vorticity features identified by the PIV analysis. Additionally, any potential effects that the lobe and cleft pattern may have on the air pressure signal were also investigated by identifying and selecting experiments where either the centre of a lobe, cleft or the eye of one of the twin vortices located in a lobe passes directly over a pressure sensor. In order to avoid the issues of PIV obstruction or distortion by other lobes on the side view images (as discussed in §6.1), only experiments where one of the lobes was significantly more extended than the rest were used for the lobe and eye of vortex comparisons. For the cleft comparisons it is clearly impossible to obtain unobstructed side view ( $y$ - $z$  plane) PIV data using this set-up, and these experiments were limited to plan view ( $x$ - $y$  plane) comparisons only.

Once suitable data sets had been identified, each front and side (where available) frame of velocity and vorticity data, along with breakdowns of down ( $y$ ) and cross-chute ( $x$ ) velocity components at the sensor location, was compared with the section of the air pressure signal that they correspond to (see

## 6.1. PARTICLE IMAGE VELOCIMETRY

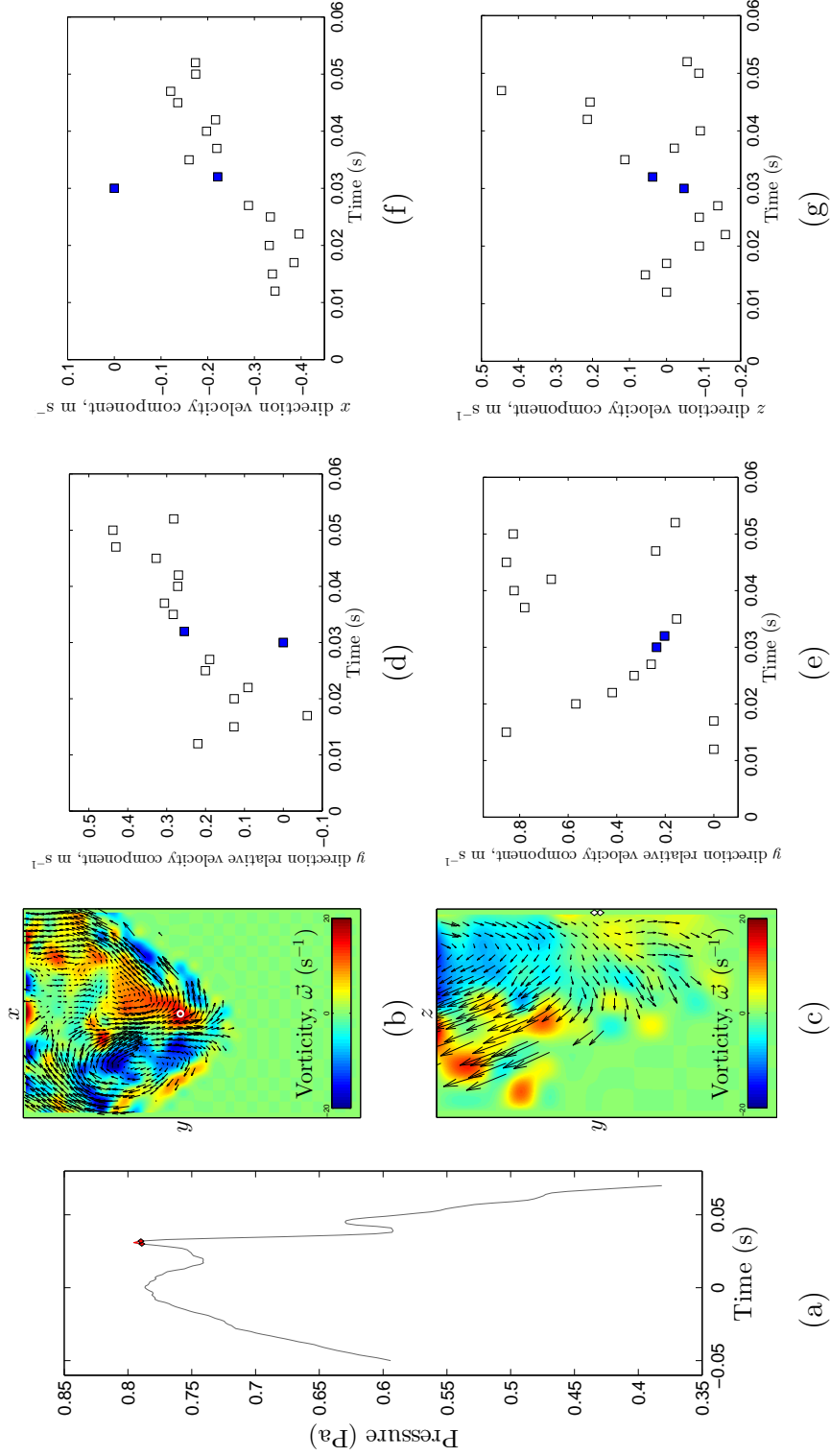


Figure 6.6: Comparison of air pressure signal and PIV analysis data between  $t = 0.03$ – $0.0325$  s for an experiment conducted using  $1000\text{ cm}^3$  of 5 mm diameter EPS beads on a  $70^\circ$  slope. (a) Air pressure signal with section corresponding to  $t = 0.03$ – $0.0325$  s highlighted red. (b) & (c) Vorticity field (colour) overlaid with velocity vector field (black arrows) from plan ( $x$ - $y$  plane) and side view ( $y$ - $z$  plane) images at  $t = 0.03$ – $0.0325$  s respectively, white circle/diamonds indicate position of air pressure sensor tube on chute surface. (d) & (e) Relative (mean front velocity subtracted)  $y$  direction velocity component at pressure sensor location from front and side view PIV data respectively, data corresponding to  $t = 0.03$ – $0.0325$  s is highlighted blue. (f) and (g)  $x$  and  $z$  direction velocity component at pressure sensor location from front and side view PIV data respectively, data corresponding to  $t = 0.03$ – $0.0325$  s is highlighted blue, positive values indicate motion to the left/downwards and negative values to the right/upwards.

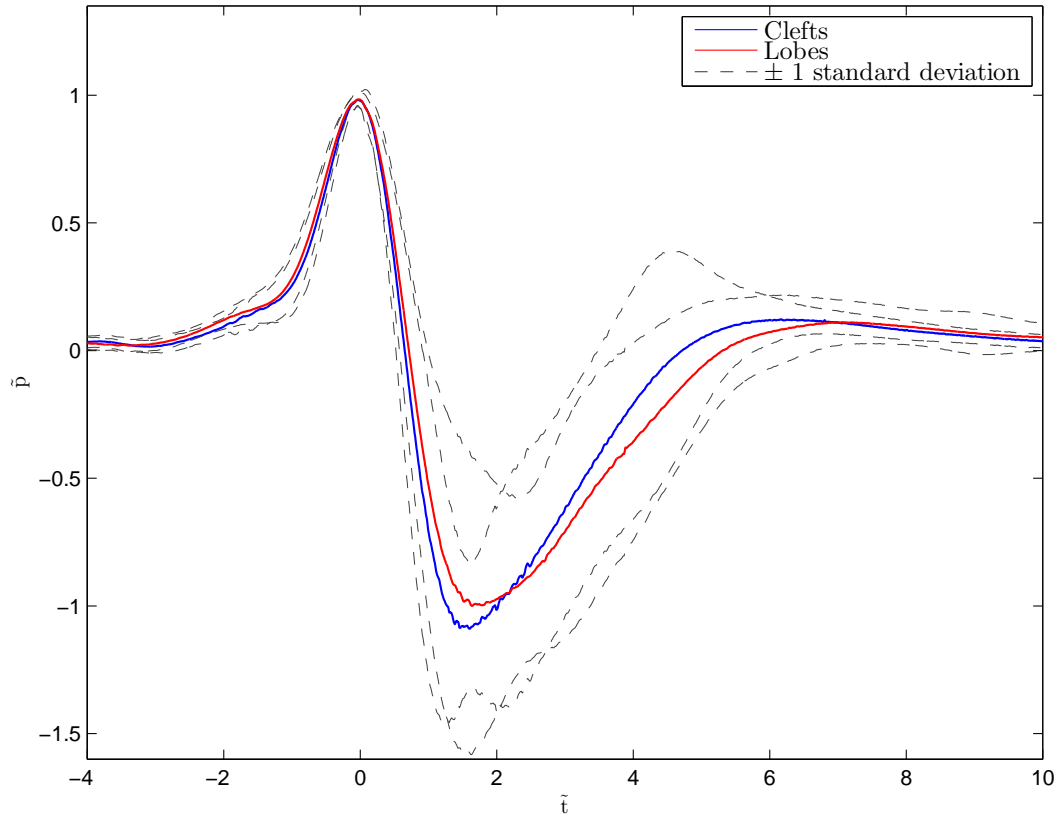


Figure 6.7: Non-dimensional air pressure signal plots (scaling is the same as that used in Chapter 5). Solid lines represent ensemble mean average of experiments where a lobe passes directly over a pressure sensor (red) or where a cleft passes directly over a pressure sensor (blue). Dashed lines represent plus or minus one standard deviation from the mean.



## 6.2. SUMMARY

---

Figure 6.6 for an example). Unfortunately, no consistent patterns between air pressure and PIV data features were observed, either between data sets from different experiments or even between data collected at different times during an individual experiment. A potential explanation for this is the fact that this PIV set-up is tracking the motion of particles on the outer edges of the current (§6.1) and may not be identifying the flow features inside the current that are causing the fluctuations in air pressure detected by the sensor. Additionally, ensemble scaled air pressure signals (Figure 6.7) show no significant difference between those obtained from experiments where a lobe passed directly over a sensor and those where a cleft passed directly over. Which again indicates that the large vortex-like structure at the centre of the current is the dominant influence on the air pressure signal and the influence of the formation and dynamics of lobe and cleft structures on the air pressure signal are likely to be either negligible or extremely subtle.

## 6.2 Summary

Particle Image Velocimetry has been used in order to provide qualitative evidence of the existence of regions of opposing vorticity within the lobes that form at the leading edge of fully suspended, non-Boussinesq particle-laden gravity currents. The size of these areas of opposing vorticity have been shown to increase with both the size of particles that make up the current and its position on the chute. Qualitative evidence of a large rotational motion in the main body of the current has also been shown, along with a smaller area of rotation in the opposite direction just below the nose of the current.

Whilst attempts were made to quantify and link local aspects of these features to fluctuations in the corresponding air pressure signals, this unfortunately proved unsuccessful. In order to perform a full quantitative analysis it is likely that the experimental set-up and procedure would need significant adjustment so that detailed image data relating to the internal flow conditions could be obtained.

Nevertheless, the flow features observed in the Particle Image Velocimetry analysis of the flows surface show good quantitative agreement with the findings of the lobe-and-cleft-type pattern (Chapter 4) and air pressure signal analysis (Chapter 5) conducted in this study. The large rotational motion

in the main body of the current suggests that the flow dynamics are indeed dominated by a large vortex-like structure; with the smaller area of opposite rotation below nose indicating a region of unstable stratification, likely to be the source of the classic lobe and cleft instability. The small, rapidly shifting regions of opposing vorticity observed in the plan view PIV analysis of the early stages of motion suggest that it is this instability that is initially dominant. While the larger, more stable regions of opposing vorticity observed in the PIV analysis of the later stages, coupled with the fact that the size of these regions increases with particle diameter, provides further evidence for the existence of a velocity boundary layer which determines the size of the regions of opposing vorticity, and in turn the wavelength of the lobe-and-cleft-type pattern.

## Bibliography

- S. B. Dalziel. DigiFlow. Dalziel Research Partners, 2002–2013.
- J. Grue, P. L. F. Liu, and G. K. Pedersen. *PIV and Water Waves*. River Edge, New Jersey, USA, 2004.
- Y. Nohguchi and H. Ozawa. On the vortex formation at the moving front of lightweight granular particles. *Physica D*, 238:20–26, 2008. doi:10.1016/j.physd.2008.08.019.

# Chapter 7

## Conclusions

The aim of this work was to gain a better understanding of the dynamics of powder snow avalanches, with a specific focus on the mechanisms behind, and the development of the lobe-and-cleft-type pattern at the leading edge of these particle-laden gravity currents. This was achieved through the physical modelling of powder snow avalanches on a laboratory scale using gravity currents consisting of expanded polystyrene beads and air. These currents have the required similarity criteria to model powder snow avalanches well, including the transition from dense granular flow to fully suspended gravity current and the formation of lobe and cleft type patterns at the leading edge. The experimental set-up allowed key parameters and variables to be adjusted in order to investigate their effects on the formation and features of the lobe-and-cleft-type patterns. A level set-based technique has been developed and successfully applied to image data collected from experiments in order to accurately track the position of the leading edge of the current and measure frontal pattern features such as wavelength, amplitude and lobe radius of curvature. Processing of the image data also allowed various other flow features to be measured, including front velocity and flow and nose height. Additionally, Particle Imaging Velocimetry analysis was conducted using the image data, which enabled visualisation and qualitative comparison of flow features.

Analysis of leading edge profiles and PIV data revealed that these currents initially behave in a similar manner to homogenous Boussinesq gravity currents with regard to formation of patterns at their leading edge. A classic lobe-and-cleft instability, characterized by rapidly shifting patterns of low amplitude

---

lobes and clefts, is observed during the early stages of the flows' motion. Geometric similarity of the currents' profiles and agreement in the relationship between the wavelength of the lobe-and-cleft-type pattern and the Grashof number of the flows, confirms that it is the same classic lobe-and-cleft instability observed in homogenous Boussinesq gravity currents that causes, and determines the wavelength of the initial lobe-and-cleft-type pattern in these non-Boussinesq, particle-laden gravity currents.

At later stages of motion, the scaled front velocities of these currents were found to be much higher than those of flows where the classic lobe-and-cleft instability is dominant. The leading edge profiles and PIV data revealed a much more laterally stable pattern, the amplitude of which increased once the flows reached an approximately steady velocity. Particle diameter of the granular material has been found to play a central role in determining the wavelength and development of the lobe-and-cleft-type pattern, as hypothesised by Nohguchi and Ozawa. When scaled with particle diameter, a relationship between Froude number of the flow and wavelength of the lobe-and-cleft-type pattern has been found,

$$\tilde{\lambda}_{d_p} = 2.3 \text{Fr}_{d_p} + 1 \quad (7.1)$$

that is applicable to these non-Boussinesq, particle-laden gravity currents when  $t_{d_p} > 50$ , where

$$\tilde{t}_{d_p} = t / \sqrt{d_p / g}. \quad (7.2)$$

This relationship highlights the importance of the role played by drag forces acting on the individual particles in determining the wavelength and development of the frontal pattern after the initial stages of the flows' motion. It supports the concept of a velocity boundary layer at the leading edge of the flow and the formation of twin vortices within each lobe, the existence of which have been observed in the PIV analysis of the image data.

Air pressure data were also collected from the chute surface during the experiments in order to provide information on the internal structure and velocities of the currents, as well as alternative methods of measuring the front velocity. Scaling of these air pressure signals, along with PIV data was found to provide good evidence that the air flow inside the head of a gravity current is indeed dominated by a large vortex-like structure and that the dynamic theory of the air flow [McElwaine, 2004] provides a good model for the pressure through a gravity current. Application of a wavelet-based visualisation

---

technique to scaled air pressure data revealed the regular occurrence of high frequency pressure fluctuations within the flow, which we hypothesise are caused by turbulence.

Attempts were made to quantify and link local aspects of flow features identified in PIV analysis to fluctuations in the corresponding air pressure signals, however these proved unsuccessful. In order to perform a full quantitative PIV analysis in future studies, it is likely that the experimental set-up and procedure would need significant adjustment so that detailed image data relating to the internal flow conditions could be obtained.

---

# Appendix A

## The Stationary Wavelet Transform

In order to implement the stationary wavelet transform (SWT), the filters first need to be rescaled to account for the lack of downsampling. Defining the filter width at scale  $j$  as  $\Lambda_j \equiv (2^j - 1)(\Lambda - 1) + 1$ , the  $j$ th level SWT high and low pass filters are expressed as

$$\begin{aligned}\tilde{h}_{j,l} &\equiv h_{j,l}/2^{j/2} \\ \tilde{g}_{j,l} &\equiv g_{j,l}/2^{j/2}.\end{aligned}\tag{A.1}$$

The SWT wavelet and approximation coefficients (equivalent to the DWT expressions in Equations 5.6 and 5.7) are then given as

$$\begin{aligned}w_{j,k} &\equiv \sum_{l=0}^{\Lambda_j-1} \tilde{h}_{j,l} p_{k-l \bmod N_p} \\ A_{j,k} &\equiv \sum_{l=0}^{\Lambda_j-1} \tilde{g}_{j,l} p_{k-l \bmod N_p}.\end{aligned}\tag{A.2}$$

The filters then require periodization so that, instead of an explicit circular convolution with Equation A.1, implicit circular filtering using a standard convolution and a periodized filter is performed, where

$$\tilde{h}_{j,l}^\circ \equiv \sum_{n=-\infty}^{+\infty} \tilde{h}_{j,l} + nN_p.\tag{A.3}$$

---

Expressing Equation A.2 in terms of Equation A.3 gives

$$\begin{aligned}
w_{j,k}^{\circ} &\equiv \sum_{l=0}^{N_p-1} \tilde{h}_{j,l}^{\circ} p_{k-l \bmod N_p} \\
A_{j,k}^{\circ} &\equiv \sum_{l=0}^{N_p-1} \tilde{g}_{j,l}^{\circ} p_{k-l \bmod N_p}.
\end{aligned} \tag{A.4}$$

Equation A.4 can then be evaluated from a recursion which states that, given the approximation  $A_{j,k}^{\circ}$ ,  $w_{j+1,k}^{\circ}$  and  $A_{j+1,k}^{\circ}$  can be obtained from

$$\begin{aligned}
w_{j+1,k}^{\circ} &= \sum_{l=0}^{\Lambda-1} \tilde{h}_l^{\circ} A_{j,k-2^j l \bmod N_p}^{\circ} \\
A_{j+1,k}^{\circ} &= \sum_{l=0}^{\Lambda-1} \tilde{g}_l^{\circ} A_{j,k-2^j l \bmod N_p}^{\circ}
\end{aligned} \tag{A.5}$$



# Appendix B

## Published work

The following paper, based on the work presented in this thesis, was published in the journal *Nonlinear Processes in Geophysics*, volume 20, February 2013.



## Scaling for lobe and cleft patterns in particle-laden gravity currents

A. Jackson, B. Turnbull, and R. Munro

Process and Environmental Research Division, Faculty of Engineering, University of Nottingham, Nottingham, UK

Correspondence to: A. Jackson (evxaj@nottingham.ac.uk)

Received: 15 November 2012 – Accepted: 10 January 2013 – Published: 18 February 2013

**Abstract.** Lobe and cleft patterns are frequently observed at the leading edge of gravity currents, including non-Boussinesq particle-laden currents such as powder snow avalanches. Despite the importance of the instability in driving air entrainment, little is known about its origin or the mechanisms behind its development. In this paper we seek to gain a better understanding of these mechanisms from a laboratory scale model of powder snow avalanches using lightweight granular material.

The instability mechanisms in these flows appear to be a combination of those found in both homogeneous Boussinesq gravity currents and unsuspended granular flows, with the size of the granular particles playing a central role in determining the wavelength of the lobe and cleft pattern. When scaled by particle diameter a relationship between the Froude number and the wavelength of the lobe and cleft pattern is found, where the wavelength increases monotonically with the Froude number.

### 1 Introduction

Both homogeneous particle-laden gravity currents and flows of unsuspended granular material typically feature characteristic three-dimensional wavy patterns at their leading edge (as illustrated by Fig. 5). An example of this instability can be found at the leading edge of a powder snow avalanche. Although this lobe-and-cleft-type structure contributes significantly to air entrainment (Simpson and Britter, 1979), and thus the dynamics of powder snow avalanches, little is known about the mechanisms that cause the formation of these patterns. Here we attempt to gain a better understanding of the instability in particle-laden flows by experimentally modelling powder snow avalanches on a laboratory scale. A powder snow avalanche is an inclined gravity current consisting of fully suspended, lightweight granular material (pow-

der snow) which has much greater density than the ambient fluid (density ratio  $\approx 10$ ), and exhibits characteristics of both homogeneous gravity currents and unsuspended granular flows. Several instability mechanisms have been identified in gravity currents and unsuspended granular flows that may also play a role in powder snow avalanches.

For homogenous Boussinesq gravity currents flowing along a horizontal surface a shifting pattern of lobes and clefts has been observed at the leading edge (Simpson, 1972; Neufeld, 2002; Härtel et al., 2000). Clefts merge together whilst new ones form when a lobe reaches a certain size, as a result the total number of lobes and clefts remains roughly constant. Linear-stability analysis and direct numerical simulations (Härtel et al., 2000) have shown that the stagnation point at the front of a gravity current is located below the nose. The formation of the lobe and cleft pattern is the result of a local instability at the leading edge of the front caused by the area of unstable stratification in the flow region between the nose and the stagnation point. In this paper we will henceforth refer to this instability as the classical lobe and cleft instability. For clarity it should be pointed out that we will refer to the wavy patterns observed at the front of the flows as lobe-and-cleft-type patterns, however the formation of these patterns is not necessarily caused by the classic lobe and cleft instability. There are several other mechanisms that could be causing the formation of a lobe-and-cleft-type pattern, which we shall now introduce.

In contrast to homogenous Boussinesq gravity currents, flows of dense granular material moving down an inclined plane exhibit different forms of wave-like patterns at the moving front (Nohguchi and Ozawa, 2008; Pouliquen et al., 1997). While it is possible that the classic lobe and cleft instability causes the initial fluctuations in the moving front, the aforementioned continuously shifting pattern of lobes and clefts is not present in these cases. Instead a more stable pattern develops with lobes developing into fingers that

accelerate downslope ahead of the remainder of the flow. This pattern is similar in appearance to the instability seen in viscous fluids flowing down an incline (Huppert, 1982); however, in the latter case the instability is driven by surface tension, which is not present in a granular material.

Nohguchi and Ozawa (2008) hypothesise that pairs of vortices form between clefts in the front of a granular flow. These vortices rotate in a manner that reduces the air drag force at the moving front, causing the vortices to grow and deform the initial perturbation into a finger-like pattern. The existence of a velocity boundary layer at the moving front has been proposed, the thickness of which is assumed to be equal to the distance that a single particle travelling at the flow velocity can move against the drag force of the static air. The velocity boundary layer thickness  $\delta_v$  is therefore defined as

$$\delta_v = \frac{2\rho_p d}{3C_d \rho_a}, \quad (1)$$

where  $\rho_p$  and  $\rho_a$  are the densities of the particle and the surrounding air respectively,  $d$  is the diameter of a single particle, and  $C_d$  is the drag coefficient. In order to maintain steady-state vortex motion the radius of each lobe would need to be twice the thickness of the velocity boundary layer. This then suggests that the size of the lobes will be related to the drag forces acting on the particles as drag force plays a key role in determining the velocity boundary layer thickness.

A further mechanism that leads to the formation of lobe-and-cleft-type patterns is caused by polydispersity of the granular medium (Pouliquen et al., 1997). The high concentration of large particles located in the vicinity of a cleft leads to a local increase of the friction in these areas. The material thus locally slows down, amplifying the perturbation and leading to the formation of fingers.

Finally, the Rayleigh–Taylor instability is a fingering instability that occurs at an interface between two fluids of different density, for example a heavy fluid initially lying on top of light fluid in a gravitational field (Lord Rayleigh, 1900; Taylor, 1950). For inviscid fluids the interface will always be unstable, with the growth rate of the unstable modes increasing as their wavelengths decrease (Chandrasekhar, 1961).

This paper focuses on studying the development of lobe-and-cleft-type patterns at the leading edge of a laboratory scale avalanche, using line releases of expanded polystyrene beads suspended in air. Following the findings of Nohguchi and Ozawa (2008), we assume the granular material is homogeneous with narrow size distribution (see Table 1), that there is minimal lateral spreading at the edges of the flow, negating the need for sidewalls, and that the base of the chute is flat. We present detailed measurements of the wavelength of the pattern found at the leading edge of the flow, and consider how the wavelength depends on the key experiment parameters.

**Table 1.** Properties of EPS beads used in our experiments.

Diameter*, $d$ (mm)	Bulk Density, $\rho_p$ (kg m <sup>-3</sup> )	Particle Reynolds Number*, $Re_p$	Settling Velocity*, $v_t$ (m s <sup>-1</sup> )
$1.3 \pm 0.05$	22	$175 \pm 15$	$0.5 \pm 0.05$
$1.5 \pm 0.06$	22	$200 \pm 17$	$0.6 \pm 0.06$
$1.8 \pm 0.09$	21	$225 \pm 22$	$0.7 \pm 0.07$
$2.1 \pm 0.07$	21	$250 \pm 24$	$0.7 \pm 0.07$
$2.5 \pm 0.09$	20	$325 \pm 28$	$0.8 \pm 0.07$
$2.7 \pm 0.08$	19	$325 \pm 29$	$0.8 \pm 0.09$
$5.0 \pm 0.13$	11	$525 \pm 51$	$1.1 \pm 0.08$
$6.8 \pm 0.20$	10	$750 \pm 72$	$1.1 \pm 0.09$

\* Mean value  $\pm 1$  standard deviation.

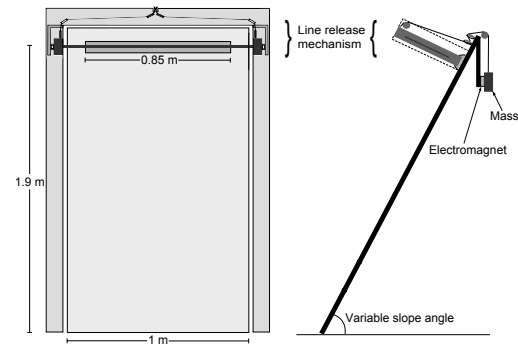


**Fig. 1.** Front and side view schematic of the chute used for experiments.

## 2 Experiments

The lightweight granular material used in this study is expanded-polystyrene (EPS) bead which has been shown (Turnbull and McElwaine, 2008) to provide a good model for powder-snow avalanches by matching important similarity criteria. The bulk density of the EPS bead is  $\rho_p \approx 20 \text{ kg m}^{-3}$ , with a relative density  $\rho_p/\rho_a \approx 17$ , where  $\rho_a = 1.20 \text{ kg m}^{-3}$  denotes air density (at 20 °C and 1 atm) and is here assumed throughout to be a constant. Eight different sizes of particles are used in the experiments, the properties of which are shown in Table 1. The relative density of the EPS beads means that the relatively high level of momentum carried by the snow particles in a powder-snow avalanche is well modelled.

The experiments were carried out using a 1 m wide, 1.9 m long, flat chute (Fig. 1). The chute was covered in a black felt cloth and inclined at slopes between 60° and 90°, where  $\theta$  denotes the angle between the chute and the horizontal. The EPS beads were released using an electromagnetically controlled hopper attached to the top of the chute (see Fig. 1). In

order to create a pseudo two-dimensional line release, a linear hopper was used which had a semi-elliptical cross section (with aspect ratio = 0.9) and a length of 0.85 m. Three different sized linear hoppers were used so that the release volume could be varied between 1000 cm<sup>3</sup>, 2100 cm<sup>3</sup> and 3300 cm<sup>3</sup>. Each flow was observed using two high-speed digital video cameras sampling at 400 Hz. One camera was positioned normal to the transverse plane of the chute to capture the plan view of the flow, ensuring that the full width of the release hopper and the full length of the chute were in view. The second camera was positioned to the side and aligned to view across the transverse plane of the chute, which allowed the head height of the avalanche to be measured. Schematic diagrams of a laboratory-scale avalanche, including the relevant parameters and variables, are shown in Fig. 2.

The particle Reynolds number for a bead of diameter  $d$  moving with velocity  $u$  is

$$Re_p = \frac{\rho_a u d}{\mu}, \quad (2)$$

where  $\mu$  is the dynamic viscosity of the ambient fluid. The particle Reynolds number determines whether the drag acting on the particle is dominated by viscous or pressure forces. Particle Reynolds numbers for powder snow avalanches are typically of the order  $3 \times 10^3$  (Turnbull et al., 2007) and the drag force exerted on the particles from the ambient fluid will largely be due to the form drag of the particles. For values  $500 < Re_p < 10^5$  the drag coefficient for a spherical particle is essentially independent of the particle Reynolds number (Massey, 2006). Typical values of  $Re_p$  for the EPS beads used in the experiments reported are shown in Table 1, and lie on the lower boundary of this range, but correspond to the case where the pressure forces are dominant compared to the viscous forces.

The sedimentation velocity of a particle normal to the slope,  $v_t$ , needs to be taken into account in order to ensure that suspension is maintained over the length of the chute. The length scale

$$L = \frac{v_t^2}{g}, \quad (3)$$

determines the size of the experiment.  $v_t$  was measured by releasing individual EPS beads with the chute inclined at 90° to the horizontal. Using the captured images, the particles were tracked and their terminal velocity calculated. Typical values of  $L$  for our experiments are  $\approx 0.1$  m, much less than the vertical length of the chute, meaning suspension will be maintained and a steady-state powder snow avalanche will be well modelled.

The Richardson number for a layer of height  $h$  and velocity  $u$  on a slope at angle  $\theta$  is

$$Ri = \frac{g' h \cos \theta}{u^2}, \quad (4)$$

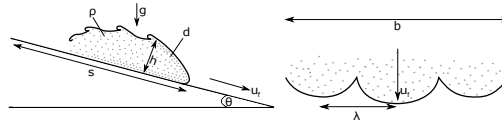


**Fig. 2.** Schematic diagrams of a particulate gravity current of height  $h$ , width  $b$ , density  $\rho$  travelling a distance  $s$  down an inclined plane with a front velocity  $u_f$ . The particulate material has a diameter  $d$  and a lobe and cleft pattern with wavelength  $\lambda$  forms at the moving front.

where the reduced gravity  $g' = g(\rho - \rho_a)/\rho_a$  with  $\rho$  the density of the current. The density ratio  $(\rho - \rho_a)/\rho_a$  is typically used to calculate reduced gravity for fully suspended gravity currents (Turner, 1973) and is comparable to the Atwood number used for other types of density stratified flow. By using steep slope angles the values of  $Ri$  in our experiments ( $Ri \approx 2$ ) were comparable to those observed in full-scale powder-snow avalanches ( $Ri \approx 1$ ). In order to calculate  $\rho$ , the head of the current is assumed to be semi-circular in cross section, with radius equal to the current head height,  $h$ . The volume of the current can then be calculated as  $V_c = (\pi b h^2)/2$  where  $b$  is the width of the release hopper. The proportion of  $V_c$  that is made up of entrained air is then obtained by subtracting the initial release volume,  $V_i$  from  $V_c$ . For the purpose of calculating  $\rho$  it is also assumed that all of the EPS beads released are contained within the current head, meaning that the proportion of  $V_c$  made up of EPS bead will be equal to  $V_i$ . The density of the current is then calculated as  $\rho = [(1 - \alpha)\rho_a + \alpha\rho_p]$ , where  $\alpha = V_i/V_c$ .

### 3 Method for tracking the moving front and lobe and cleft formation

The captured images were analysed using a level set method (McElwaine et al., 2004) to accurately track the front position of the flow and determine the formation of lobes and clefts. For each sequence of images the arrival time  $T(x, y)$  of the flow is detected for each pixel. The matrix  $T(x, y)$  of first arrival times is classified as a level set, with the contours  $T(x, y) = t$  corresponding to the front of the flow at a particular time. This technique was applied to both the plan view and side view images. The contours were used to measure flow properties, such as current head height, front position and velocity.

Calculating the gradient of the level set ( $\nabla T$ ) produces a vector field where each vector is normal to the surface of the moving front. The divergence of the vector field can be used to calculate the curvature of the level set,

$$\kappa = \nabla \cdot \frac{\nabla T}{|\nabla T|}. \quad (5)$$

In the next section we show how the curvature can be used to provide a robust and repeatable method for detecting and

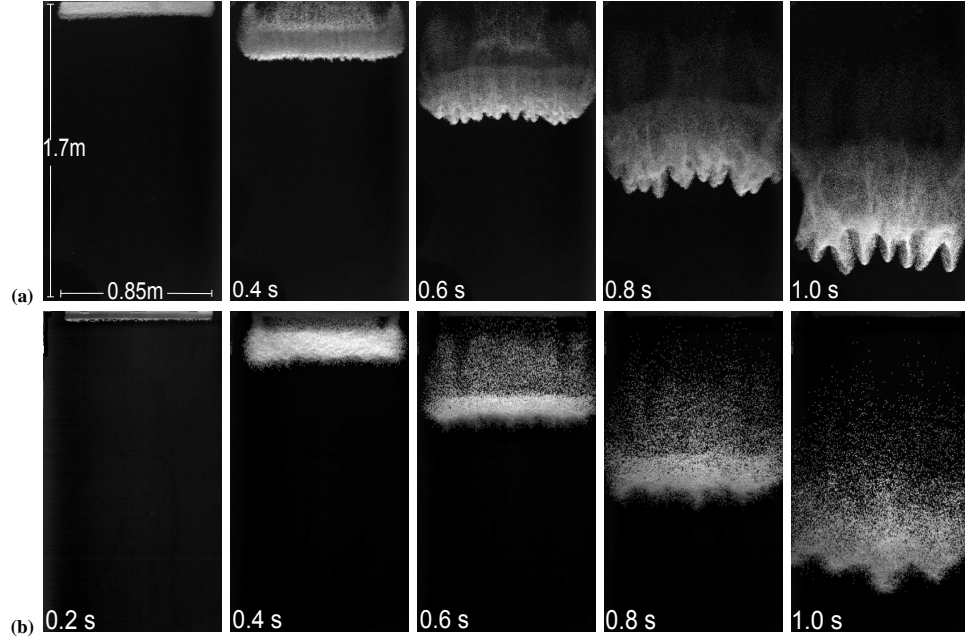


**Fig. 3.** Video stills taken at 0.2 s intervals from experiments conducted at a slope angle of  $65^\circ$  using: (a)  $2100 \text{ cm}^3$  of 1.8 mm diameter EPS beads and (b)  $3300 \text{ cm}^3$  of 5.0 mm diameter EPS beads.

tracking lobes and clefts, with lobes corresponding to regions of small positive curvature and clefts to lines of large negative curvature.

#### 4 Results

For each particle diameter,  $d$ , shown in Table 1 and for each initial release volume,  $V_i$ , experiments were carried out at five different slope angles:  $65^\circ$ ,  $70^\circ$ ,  $75^\circ$ ,  $80^\circ$  and  $85^\circ$ . Figure 3 shows images from two separate experiments: (a) for  $d = 1.8 \text{ mm}$  and a release volume of  $2100 \text{ cm}^3$ ; and (b) for  $d = 5.0 \text{ mm}$  and a release volume of  $3300 \text{ cm}^3$ . In both cases the slope angle was set at  $65^\circ$ . In each experiment a well-defined front is observed that propagates down the slope. Immediately after the release the front is seen to accelerate down the slope for a short distance ( $\approx 0.5 \text{ m}$ ) before reaching an approximately constant velocity.

Although the particles start from a pseudo two-dimensional linear distribution, a wavy pattern quickly appears in the moving front. As the fronts continue to propagate downslope these fluctuations grow in amplitude. Clear qualitative differences can be observed between the two flows shown in Fig. 3. One of the most striking is the difference in wavelength of the lobe-and-cleft-type pattern created by the fluctuations in the moving front during the later stages

of the flows motion. That is, the lobe and cleft structure in Fig. 3a (for  $d = 1.8 \text{ mm}$ ), has a noticeably smaller wavelength than that observed for the larger particles shown in Fig. 3b (for  $d = 5.0 \text{ mm}$ ). Also, the lobes that form in Fig. 3a (for  $d = 1.8 \text{ mm}$ ) have a greater amplitude than those in Fig. 3b (for  $d = 5.0 \text{ mm}$ ).

By taking particle diameter  $d$  as our lengthscale, a non-dimensional timescale can be calculated,

$$\tilde{t} = t / \sqrt{d/g}. \quad (6)$$

Images taken at the same non-dimensional time,  $\tilde{t} = 50$ , from four experiments using the same release volume, but different sized particles are shown in Fig. 4. It can be shown that for a given value of  $\tilde{t}$ , as particle diameter increases the wavelength of the lobe-and-cleft-type pattern and the downslope position of the front also increase, but the ratio of the wavelength to amplitude remains approximately constant.

Front profiles generated from the flows in Fig. 3a and b are shown in Fig. 5, with the curvature of the corresponding level sets shown in Fig. 6. These figures show an initially shifting pattern of lobes and clefts. Lobes develop and grow in size, occasionally bifurcating, whilst clefts regularly merge together. This indicates that the lobe and cleft instability observed in fully suspended, Boussinesq gravity currents is dominant during the early phases of the flow. In the

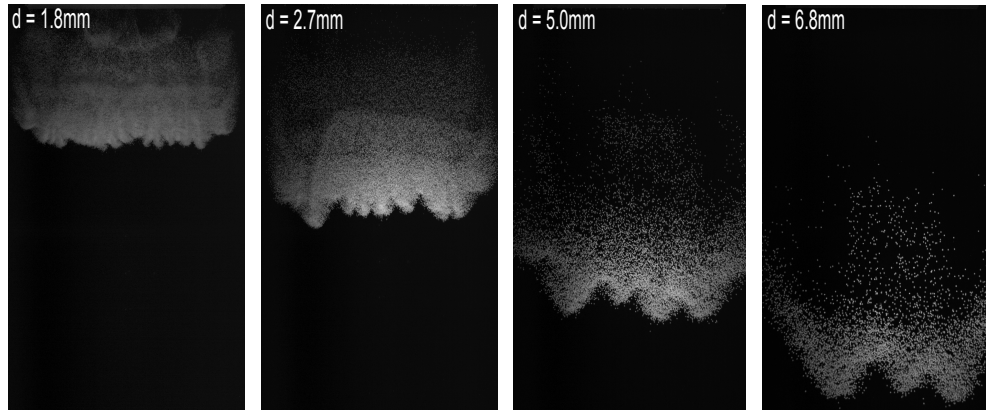


**Fig. 4.** Video stills taken at  $\bar{t} = 50$  from experiments conducted at a slope angle of  $65^\circ$  using  $2100 \text{ cm}^3$  of: 1.8 mm, 2.7 mm, 5.0 mm and 6.8 mm diameter EPS beads.

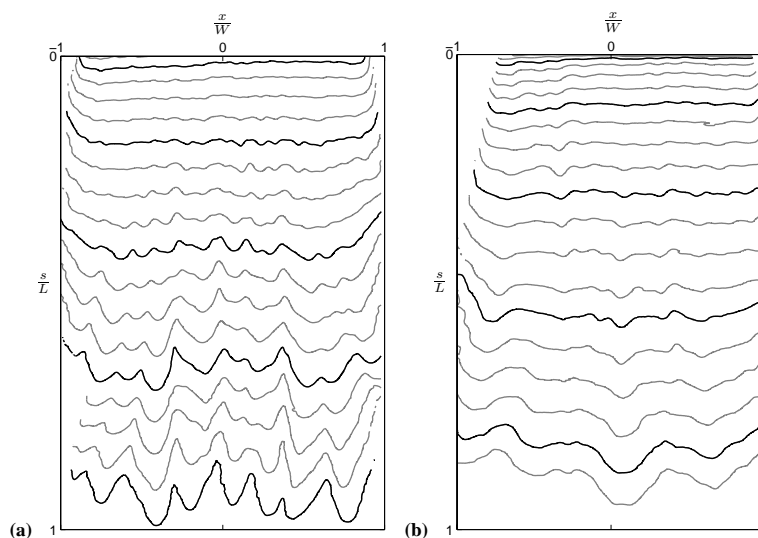


**Fig. 5.** (a) and (b) front profiles at 0.05 s intervals taken from the flows shown in Fig. 3a and b, respectively. The highlighted profiles correspond to the position of the fronts at the times shown in Fig. 3.

later stages of the flow, the position of the lobes is much more stable and there is less merging and bifurcation. As already noted, at later times the amplitude of the lobes has increased, this is particularly apparent for the flows consisting of smaller particles. This indicates that the fingering instabilities observed in unsuspended granular flows become more dominant in the later phases of the flow.

In order to investigate the effects of changing the release volume, wavelength against average distance from the line

release ( $s$ ) for one particle size (2.7 mm) is shown in Fig. 7. Results from each of the three different release volumes are plotted separately and it can be seen that the volume of granular material released has no effect on the wavelength of the pattern in the moving front. Changing the volume of material released did have an observable effect towards the rear of the flows; as the volume was increased, the amount of detrainment at the rear of the flow also increased.

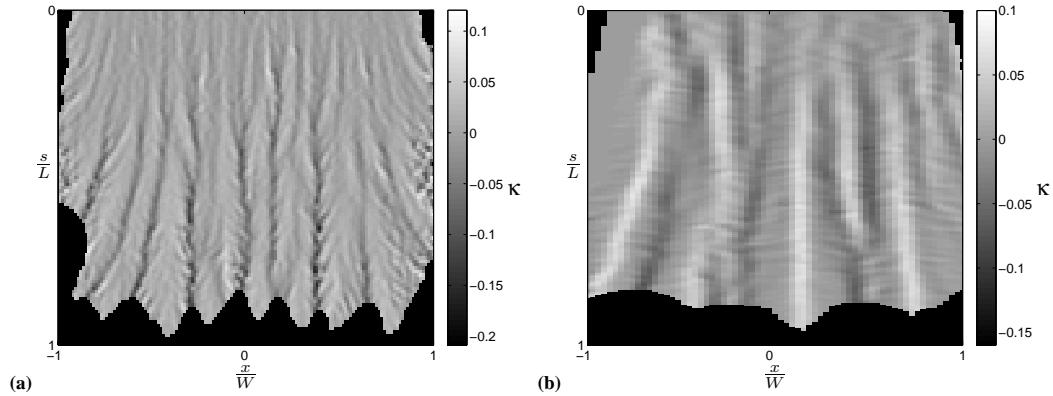


**Fig. 6.** (a) and (b) curvature ( $\kappa$ ) of the level set  $T(x, y)$  calculated from the flows shown in Fig. 3a and b, respectively. Areas of negative curvature (dark) indicate the location of clefts, whilst areas of positive curvature (light) indicate the location of lobes.

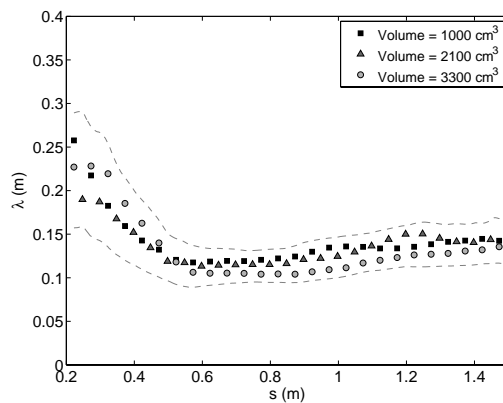


**Fig. 7.** Average wavelength ( $\lambda$ ) versus distance from line release ( $s$ ) for experiments using  $2.7 \pm 0.08$  mm diameter particles, plus or minus the standard deviation from the mean (dashed lines).

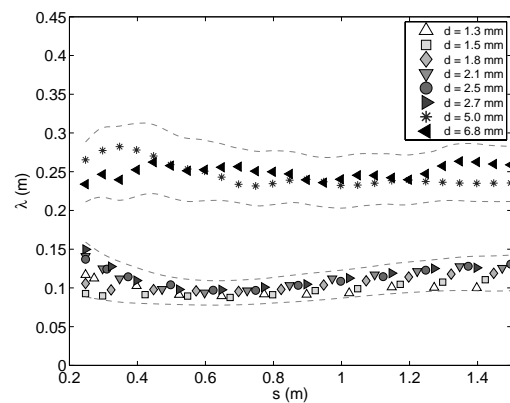


**Fig. 8.** Average wavelength ( $\lambda$ ) versus distance from line release ( $s$ ), plus or minus the standard deviation from the mean (dashed lines).

Figure 8 shows average wavelength ( $\lambda$ ) plotted against average distance from the line release for each particle size. The wavelength values for each particle size are obtained by taking the average from experiments conducted using the three release volumes. The results verify the observation that the pattern observed in the flows made up of smaller particles had a smaller wavelength than those made up of larger particles. It can also be seen that the wavelength remains relatively stable once the flow has reached an approximately constant velocity.

Current head heights for flows consisting of 1.8 mm and 6.8 mm diameter EPS beads are shown for each release volume and slope angle in Fig. 9. Several trends can be seen in the data; current height increases monotonically with in-

creasing slope angle and release volume, but with decreasing particle diameter. That is, currents consisting of smaller particles have larger heads, and therefore higher levels of suspension, due to the particles having lower settling velocities resulting in lower levels of particle sedimentation. Larger heads and greater levels of suspension are observed at higher slope angles as the component of the particles settling velocity normal to the slope is reduced. The data in Fig. 9 shows agreement with qualitative observations of detrainment levels at the rear of the flow. That is, it was observed that as the release volume was increased, higher levels of rear detrainment were observed, especially for currents consisting of smaller diameter EPS beads. Increased detrainment was also observed at higher slope angles. These observations are supported by Fig. 9 where the data for the smaller particles

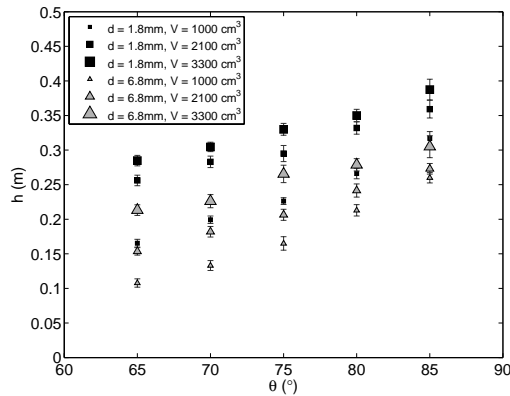


**Fig. 9.** Current head height ( $h$ ) versus slope angle ( $\theta$ ) for currents consisting of 1.8 mm and 6.8 mm diameter EPS beads. Head height was measured at a distance of 1 m from the line release. Error bars have length equal to the standard deviation from the mean.

shows a much smaller increase in current head height between the middle and largest size of release volume than that between the smallest and middle size. For both particle sizes the difference in current head height between the three release volume sizes decreases as slope angle increases. These observations and results indicate that there may be a limit to the amount of material that can be suspended within the head of the current, and as this limit is approached the amount of material detrained from the rear of the head increases.

In Fig. 10 the average wavelength at a distance of 1 m from the line release is plotted against slope angle for each of the particle sizes used. It was observed during the experiments that increasing the angle of the slope increased the level of suspension within the flow. At higher slope angles, more air was entrained into the current and its height ( $h$ ) perpendicular to the slope visibly increased. As the slope angle becomes steeper, the increased component of gravity driving the current is counteracted by an increase in air entrainment (Turnbull and McElwaine, 2007). However, it can be seen from Fig. 10 that the wavelength of the pattern is independent of the slope angle, indicating that level of suspension or air entrainment has no effect on the formation of the pattern. Interestingly, in Fig. 10 there appears to be a bifurcation in the data between the smaller particles ( $d = 1.5$ – $2.7$  mm) and the larger particles ( $d = 5.0$ – $6.8$  mm). This bifurcation could be due to the higher levels of polydispersity of the smaller particles (standard deviation  $\approx 5\%$  of mean particle diameter) compared with the larger particles (standard deviation  $\approx 2.5\%$  of mean particle diameter). Whilst it is possible that the granular fingering mechanism observed by Pouliquen et al. (1997) could play a more significant role in the flows consisting of smaller particles, this seems unlikely as in the experiments conducted by Pouliquen et al. this

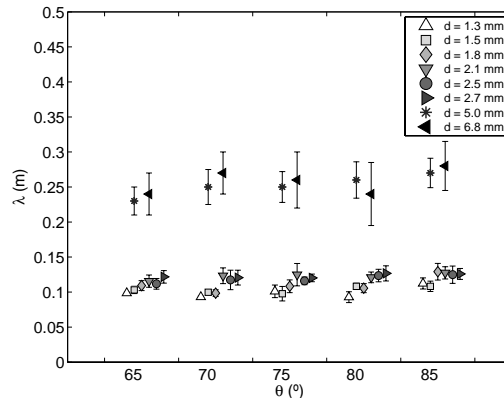


**Fig. 10.** Average wavelength ( $\lambda$ ) 1 m from the line release versus slope angle ( $\theta$ ). Error bars have length equal to the standard deviation from the mean. Results are offset horizontally for clarity.

mechanism was only observed when the standard deviation of the mean particle diameter was greater than 10 %. Another potential explanation for the bifurcation in the data could be the role played by viscous drag forces for the different particle sizes. As previously mentioned, the values of  $Re_p$  are high enough for pressure drag forces to constitute the bulk of the total drag force. However, whilst the larger particle's  $Re_p$  values are within the region where the drag coefficient for a spherical particle is independent of  $Re_p$ , the smaller particle's values lie just below this region. Therefore, although pressure drag forces are still dominant, viscous forces will have a more significant effect on the drag force acting on the particles.

The Rayleigh–Taylor instability should be the limiting case as we tend towards a vertical chute. Hydrodynamically, the growth of the Rayleigh–Taylor instability is predicted by a perturbation analysis that shows that the growth rate of the fingers depends on the perturbation wavelength (Chandrasekhar, 1961; Youngs, 1984; Duff et al., 1962; Sharp, 1984). In the presence of a stabilising influence, e.g. viscosity or surface tension, some wavelengths are damped and a dominant mode develops. In our EPS suspension experiments, we have neither viscosity nor surface tension present. However, we speculate that the air drag experienced by the particle clusters, and the restrictions on lobe shape that this imposes (Bush et al., 2003), would play a similar role in allowing a dominant wavelength to grow. This should provide a rich focus for future modelling.

For comparison with the results of Nohguchi and Ozawa (2008), the mean radius of curvature of the lobes for each particle size was calculated (Fig. 11). These values were calculated from the level set contours corresponding to when the flows had reached a distance of 1 m down the chute ensuring



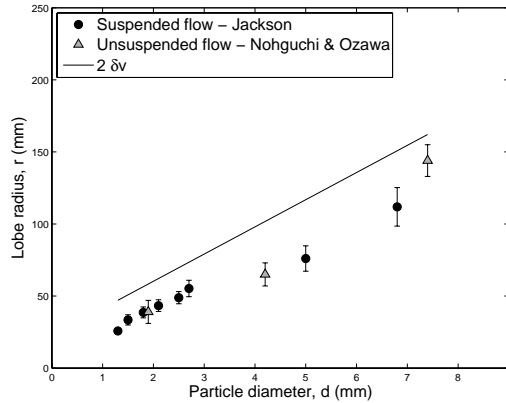


**Fig. 11.** Radius of curvature of lobes versus particle diameter. Results from the experiments presented in this paper (●) are compared with the experimental results (△) and analytical results (solid line) of Nohguchi and Ozawa (2008).

that, as with the results of Nohguchi and Ozawa (2008), the flows had reached an approximately steady velocity. The lobes at the leading edge of the flows consisting of smaller particles had smaller radii of curvature, consistent with the observations of sharper lobes and smaller wavelengths for these flows. The results show good agreement with Nohguchi and Ozawa's experimental data (which are also shown in Fig. 11), however both sets of data are slightly below the analytical estimate  $r \approx 2\delta_v$ . When deriving the expression for boundary layer thickness Nohguchi and Ozawa ignored inter-particle collisions in the velocity boundary layer for simplification. In reality, a particle moving through the velocity boundary layer is likely to experience collisions with other particles, reducing the distance that it can move against the drag force of the ambient fluid. Therefore, the analytical results are likely to overestimate the velocity boundary layer thickness which may explain the discrepancy seen between the theoretical and experimental results.

## 5 Non-dimensionalisation

Both granular fingering (Pouliquen et al., 1997) and velocity boundary layer (Nohguchi and Ozawa, 2008) theories suggest that the velocity of the moving front could play a role in determining the wavelength of the pattern that forms at the front. Fingers are created due to differences in velocity between smaller particles and larger particles that slow down due to higher levels of friction as they bunch up around clefts. A velocity boundary layer's thickness will also be affected by front velocity, which could in turn affect the wavelength of the pattern.

Using the variables shown in the schematic (Fig. 2), the non-dimensional group, which is the Froude number

$$Fr = \frac{u_f}{\sqrt{g' L \sin \theta}}, \quad (7)$$

can be formed where  $L$  is an appropriate length scale. The theory of a velocity boundary layer at the moving front suggests that there is a relationship between front velocity and wavelength which is determined by an individual particle's interaction with the ambient air. As previously mentioned, Nohguchi and Ozawa (2008) have proposed that the wavelength of the frontal pattern is determined by the size of pairs of vortices that form at the moving front. The size of these vortices is in turn determined by the thickness of the velocity boundary layer. Faster moving flows will have thicker velocity boundary layers as the particles can move a greater distance against the drag force of the static air, resulting in the formation of larger vortices and therefore a larger wavelength pattern. From Eq. (1) it can be seen that particle diameter  $d$  is a key variable in determining the boundary layer thickness  $\delta_v$ ; therefore, we will look for a relationship between the Froude number and wavelength based on the length scale  $L = d$ .

The dimensionless wavelength ( $\tilde{\lambda}_d = \lambda/d$ ) is plotted against the Froude number in Fig. 12. Interestingly, when scaled with a length scale characterised by the particle diameter there appears to be a monotonically increasing relationship between the Froude number and wavelength. A linear fit of the data,

$$\tilde{\lambda}_d = 2.3 Fr_d + 1, \quad (8)$$

is shown in Fig. 12, with a residual of 0.12 indicating a good level of fit.

This dimensionless rendering of the data seems to offer good agreement with the concept of a velocity boundary layer determining the wavelength of the frontal pattern. The data shows that when scaled with respect to particle diameter, the smaller particles have higher velocities and therefore thicker boundary layers resulting in wider lobes and a larger wavelength.

## 6 Conclusions

This paper has presented experiments on the flows of fully suspended, lightweight granular material down an inclined surface. These currents have been found to exhibit characteristics of the instabilities found at the leading edge of both homogenous particle-laden gravity currents and flows of unsuspended granular material. During the early stages of motion a lobe and cleft instability mechanism, similar to that observed in homogenous particle-laden gravity currents, appears to be dominant. As the flow propagates down the slope the pattern of lobes and clefts becomes more stable

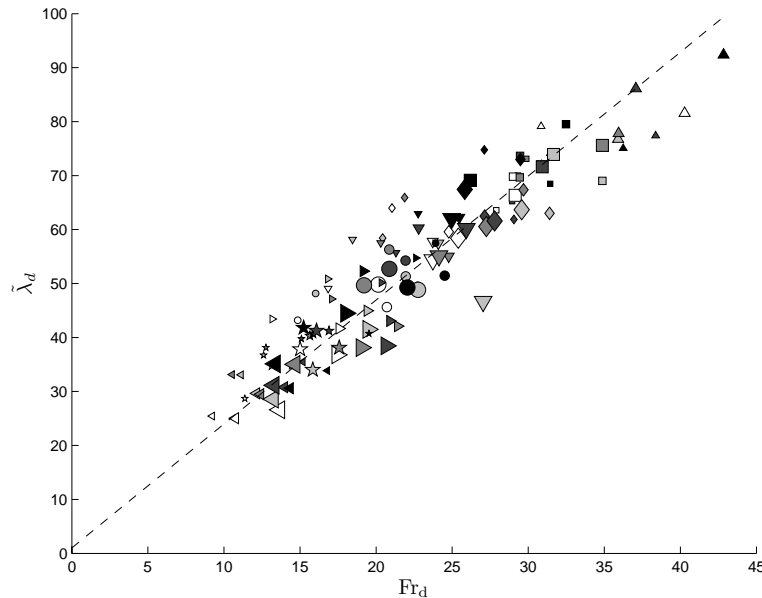


**Fig. 12.** Non-dimensional wavelength ( $\tilde{\lambda}_d$ ) versus the Froude number ( $Fr_d$ ). Particle sizes: 1.3 mm ( $\Delta$ ), 1.5 mm ( $\square$ ), 1.8 mm ( $\diamond$ ), 2.1 mm ( $\nabla$ ), 2.5 mm ( $\circ$ ), 2.7 mm ( $\triangleright$ ), 5.0 mm ( $\star$ ) and 6.8 mm ( $\triangleleft$ ). Marker shades correspond to slope angle: 65° – clear, through to 85° – black. Marker size corresponds to the size of the release volume. Dashed line shows linear fit,  $\tilde{\lambda}_d = 2.3 Fr_d + 1$  (Eq. 8).

suggesting that the dominant instability mechanism is now more similar to those observed in unsuspended granular flows. Particle diameter of the granular material has been found to play a central role in determining the wavelength of the lobe and cleft pattern, as hypothesised by Nohguchi and Ozawa (2008). When scaled with particle diameter, a relationship between the Froude number of the flow and wavelength of the lobe and cleft pattern has been found. This relationship highlights the importance of the role played by drag forces acting on the individual particles in determining the wavelength of the frontal pattern, and appears to support the concept of a velocity boundary layer at the moving front of the flow.

Edited by: J. M. Redondo

Reviewed by: J. McElwaine and one anonymous referee

## References

- Bush, J., Thurber, B., and F., B.: Particle clouds in homogeneous and stratified environments, *J. Fluid Mech.*, 489, 29–54, doi:10.1017/S0022112003005160, 2003.
- Chandrasekhar, S.: *Hydrodynamic and Hydromagnetic Stability*, Oxford University Press, Oxford, UK, 1961.
- Duff, R., Harlow, F., and Hirt, C.: Effects of diffusion on interface instability between gases, *Phys. Fluids*, 5, 417–425, 1962.
- Härtel, C., Carlsson, F., and Thunblom, M.: Analysis and direct numerical simulation of the flow at a gravity-current head. Part 2. The lobe-and-cleft instability, *J. Fluid Mech.*, 418, 213–229, 2000.
- Huppert, H.: Flow and instability of a viscous current down a slope, *Nature*, 300, 427–9, 1982.
- Lord Rayleigh: Investigation of the character of the equilibrium of an incompressible heavy fluid of variable density, in: *Scientific Papers*, vol. II, p. 200, Cambridge University Press, Cambridge, UK, 1900.
- Massey, B.: *Mechanics Of Fluids*, Taylor & Francis, Abingdon, UK, 8th Edn., 2006.
- McElwaine, J., Patterson, M., and Dalziel, S.: Lobe and cleft formation at the head of a gravity current, *Proceedings of the XXI International Congress of Theoretical and Applied Mechanics*, 15–21, 2004.
- Neufeld, J.: Lobe-cleft patterns in the leading edge of a gravity current, M.S. thesis, Department of Physics, University of Toronto, Canada, 2002.
- Nohguchi, Y. and Ozawa, H.: On the vortex formation at the moving front of lightweight granular particles, *Physica D*, 238, 20–26, doi:10.1016/j.physd.2008.08.019, 2008.
- Pouliquen, O., Delour, J., and Savage, S.: Fingering in granular flows, *Nature*, 386, 816–817, 1997.
- Sharp, D.: An overview of Rayleigh-Taylor instability, *Physica D*, 12, 3–18, 1984.

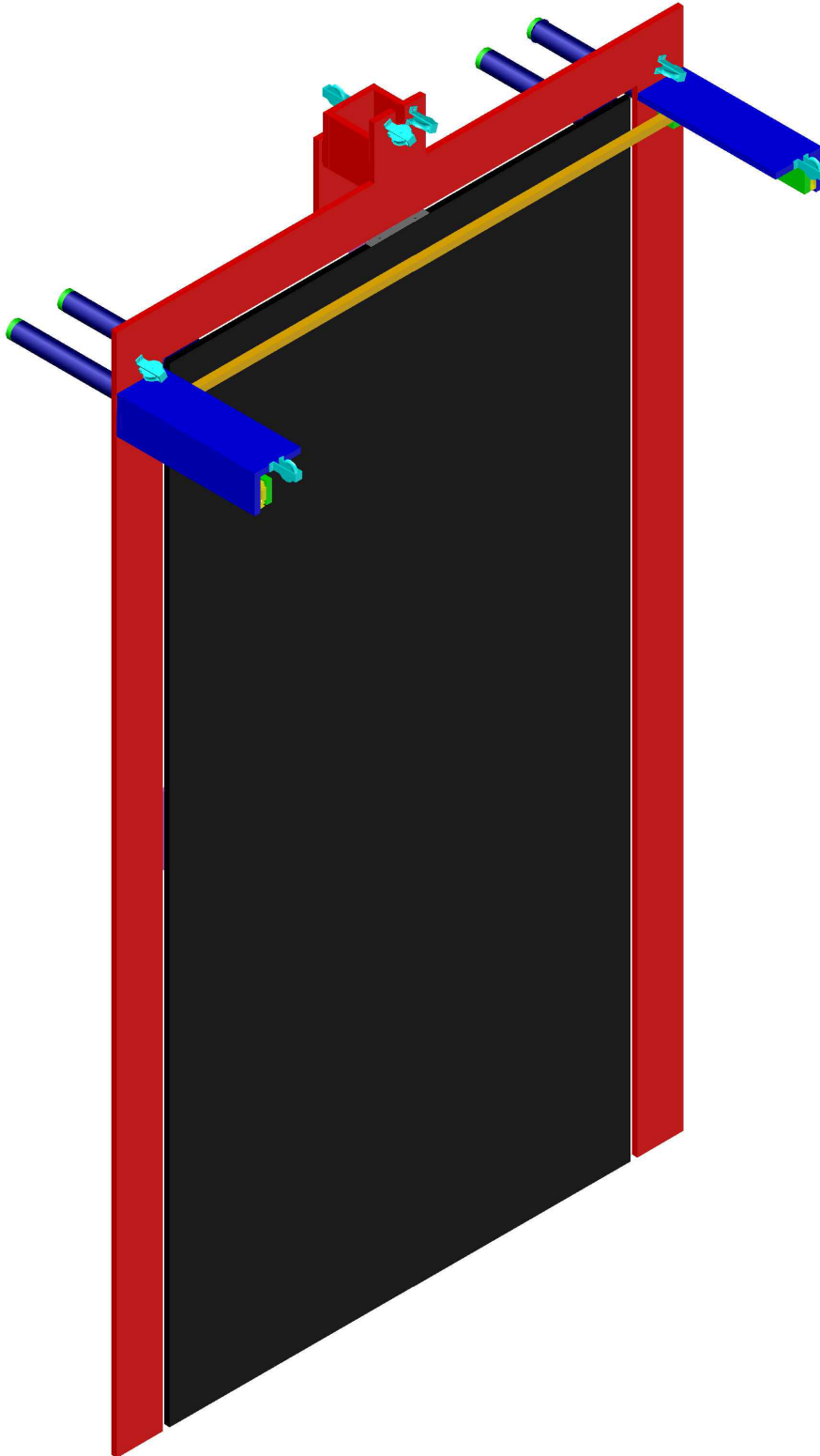
- Simpson, J.: Effects of the lower boundary on the head of a gravity current, *J. Fluid Mech.*, 53, 759–768, 1972.
- Simpson, J. and Britter, R.: The dynamics of the head of a gravity current advancing over a horizontal surface, *J. Fluid Mech.*, 94, 477–495, 1979.
- Taylor, G.: The instability of liquid surfaces when accelerated in a direction perpendicular to their planes, I, *Proc. R. Soc. Lon. Ser. A*, 201, 192–196, 1950.
- Turnbull, B. and McElwaine, J.: A comparison of powder-snow avalanches at Vallee de la Sionne, Switzerland, with plume theories, *J. Glaciol.*, 53, 30–40, 2007.
- Turnbull, B. and McElwaine, J.: Experiments on the non-Boussinesq Flow of Self-Igniting Suspension Currents on a Steep Open Slope, *J. Geophys. Res.*, 113, F01003, doi:10.1029/2007JF000753, 2008.
- Turnbull, B., McElwaine, J., and Ancey, C.: Kulikovskiy-Sveshnikova-Beghin model of powder snow avalanches: Development and application, *J. Geophys. Res.*, 112, F01004, doi:10.1029/2006JF000489, 2007.
- Turner, J.: *Buoyancy Effects in Fluids*, Cambridge University Press, Cambridge, UK, 1973.
- Youngs, D.: Numerical simulation of turbulent mixing by Rayleigh-Taylor instability, *Physica D*, 12, 32–34, 1984.

---

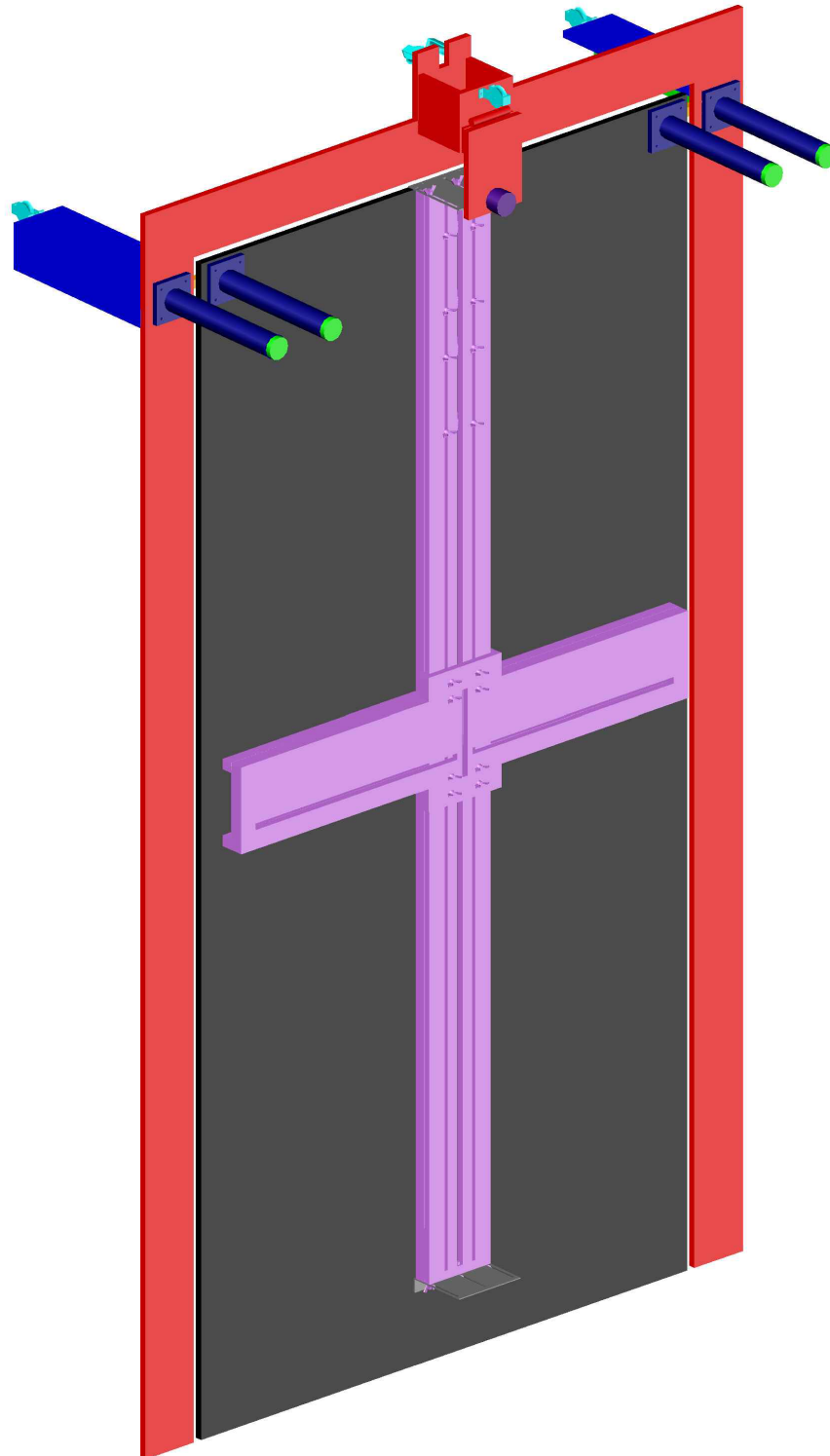
## Appendix C

### Chute design CAD drawings

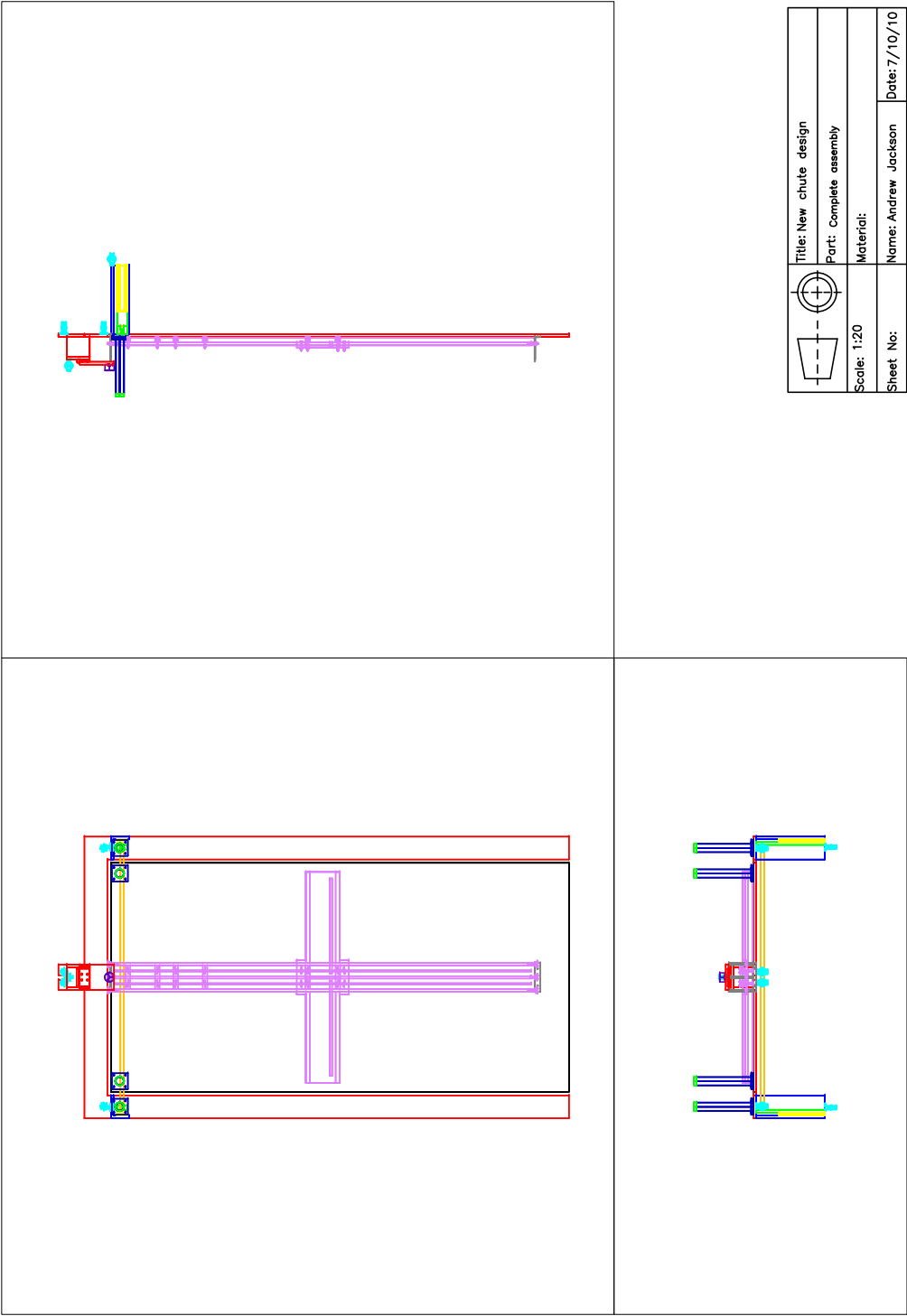
## C.1 Complete chute assembly – front – isometric projection



## C.2 Complete chute assembly – rear – isometric projection

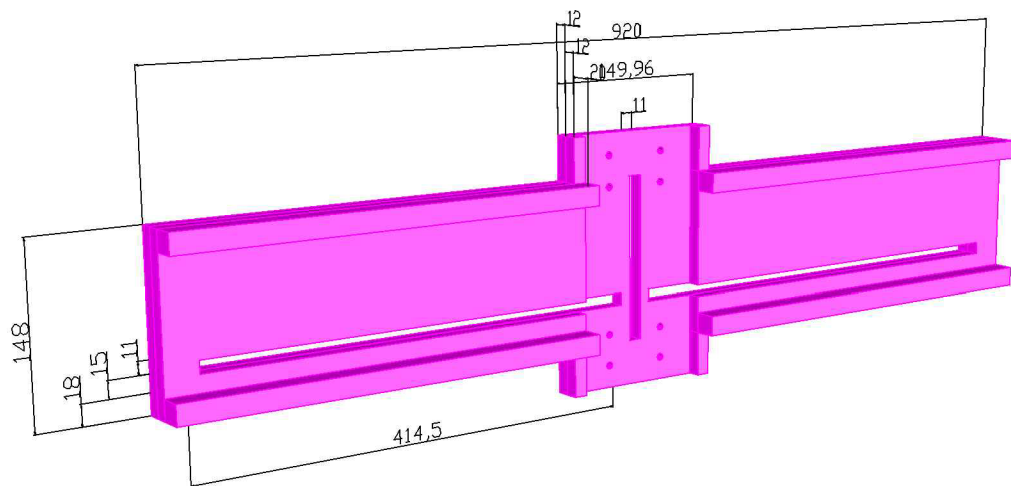


C.3 Complete chute assembly – first angle projection

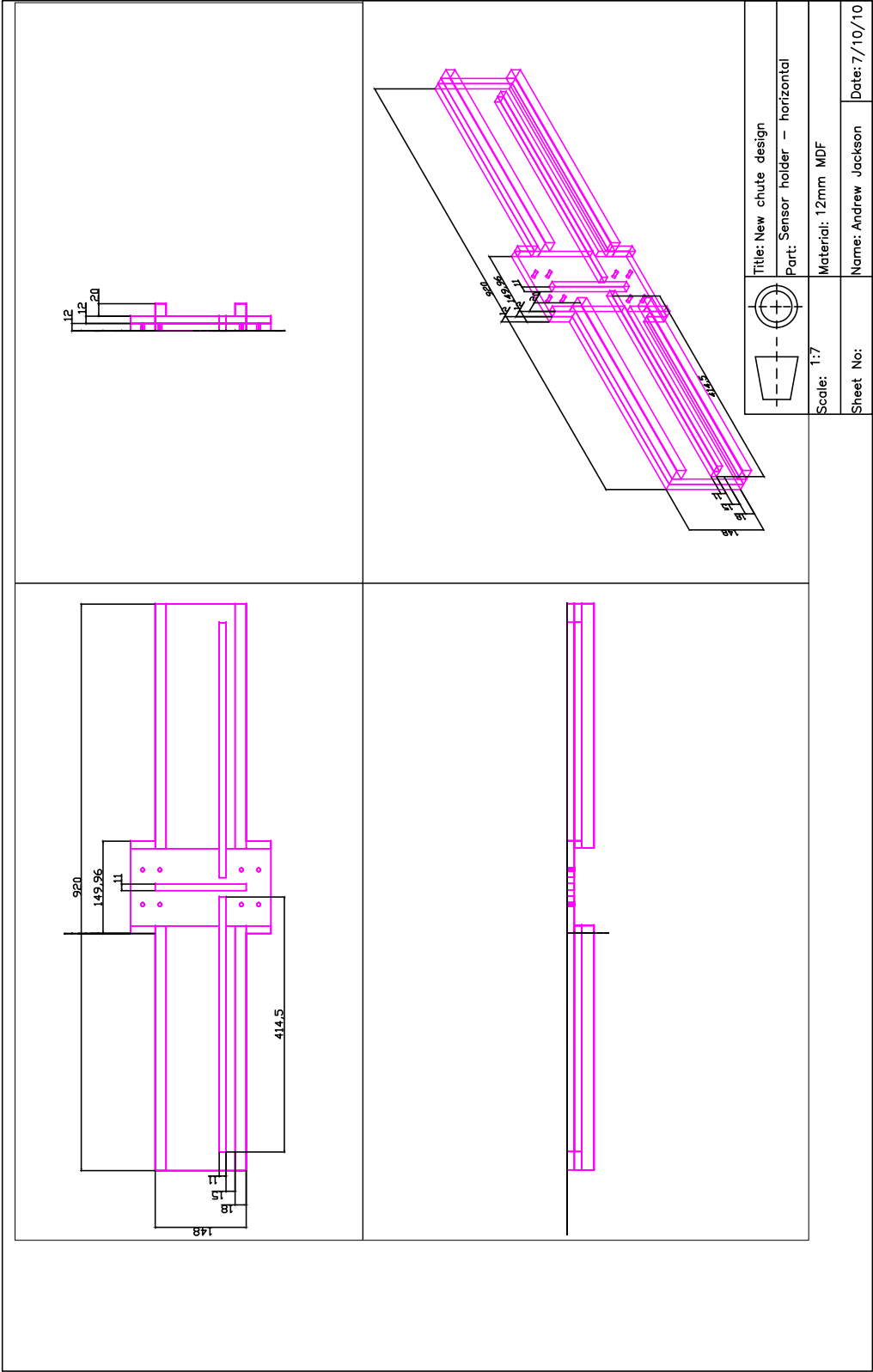




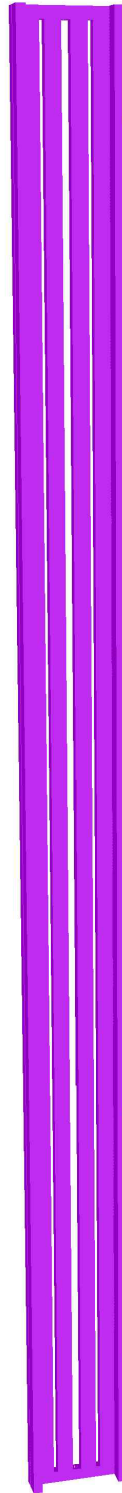
## C.4 Sensor adjustment – horizontal – isometric projection



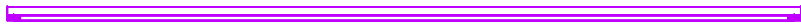
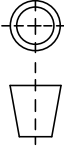


C.5 Sensor adjustment – horizontal – first angle projection



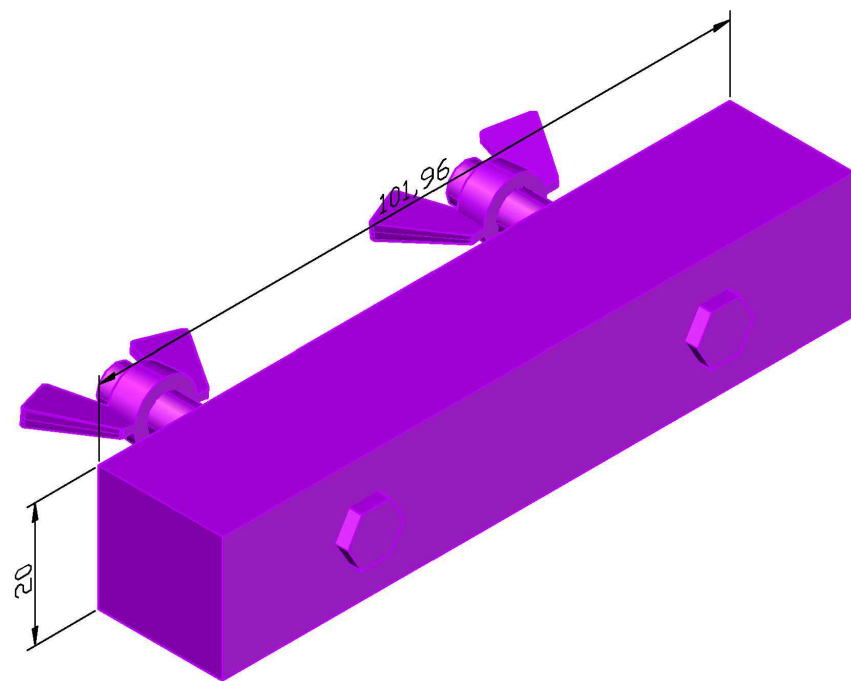
## C.6 Sensor adjustment – vertical – isometric projection



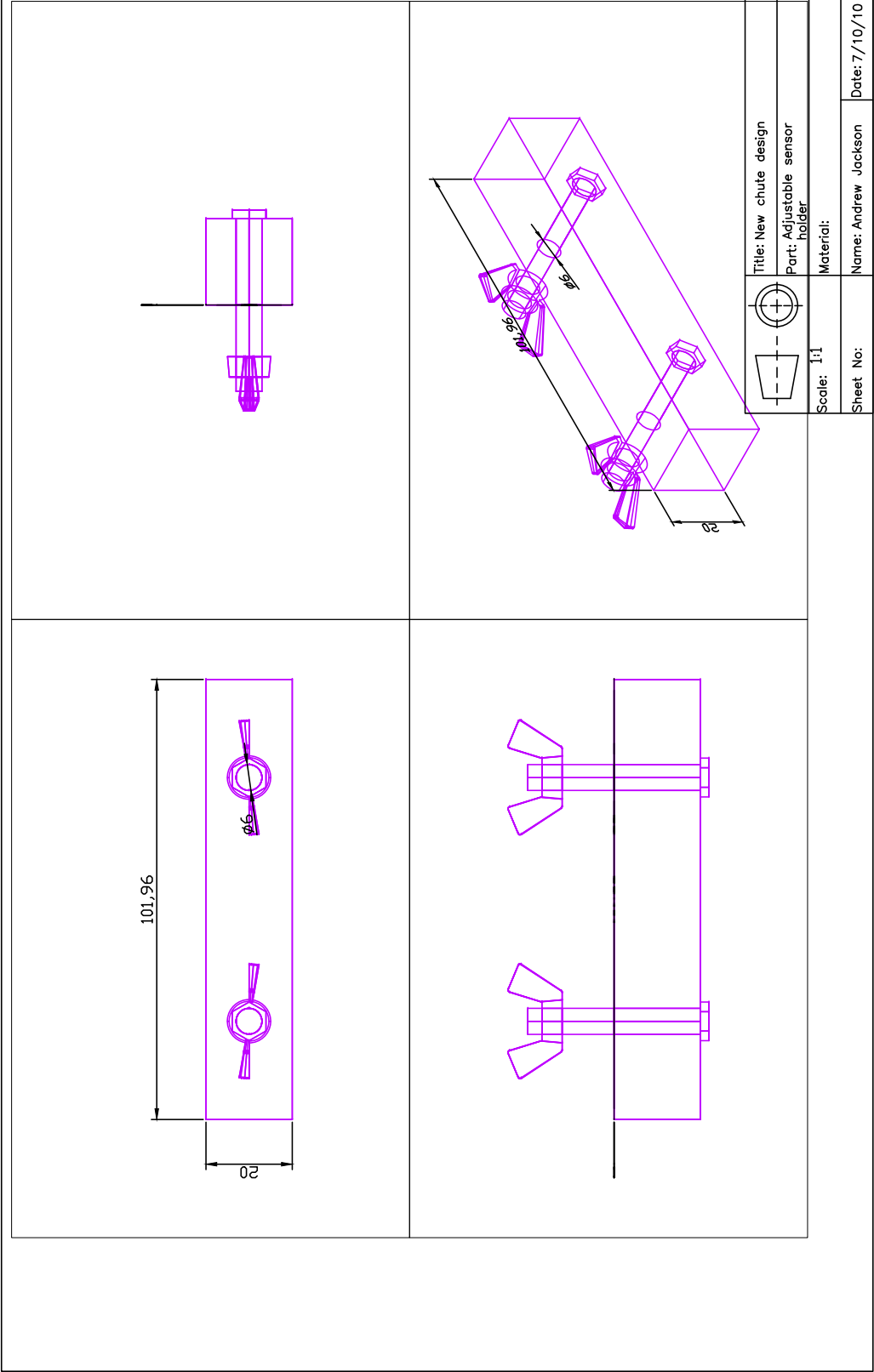
C.7 Sensor adjustment – vertical – first angle projection

		Title: New chute design	
			Part: Sensor adjustment – vertical
Scale: 1:12		Material: 12mm MDF	
Sheet No:		Name: Andrew Jackson	
		Date: 7/10/10	

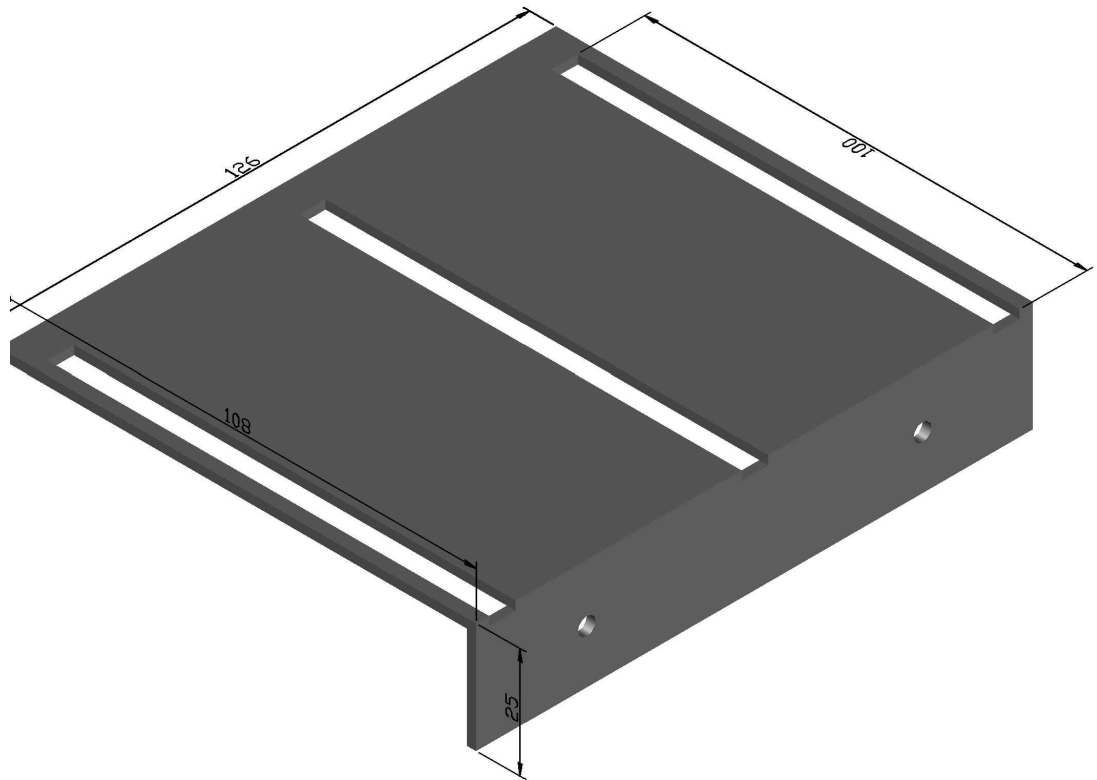
## C.8 Adjustable sensor holder – isometric projection



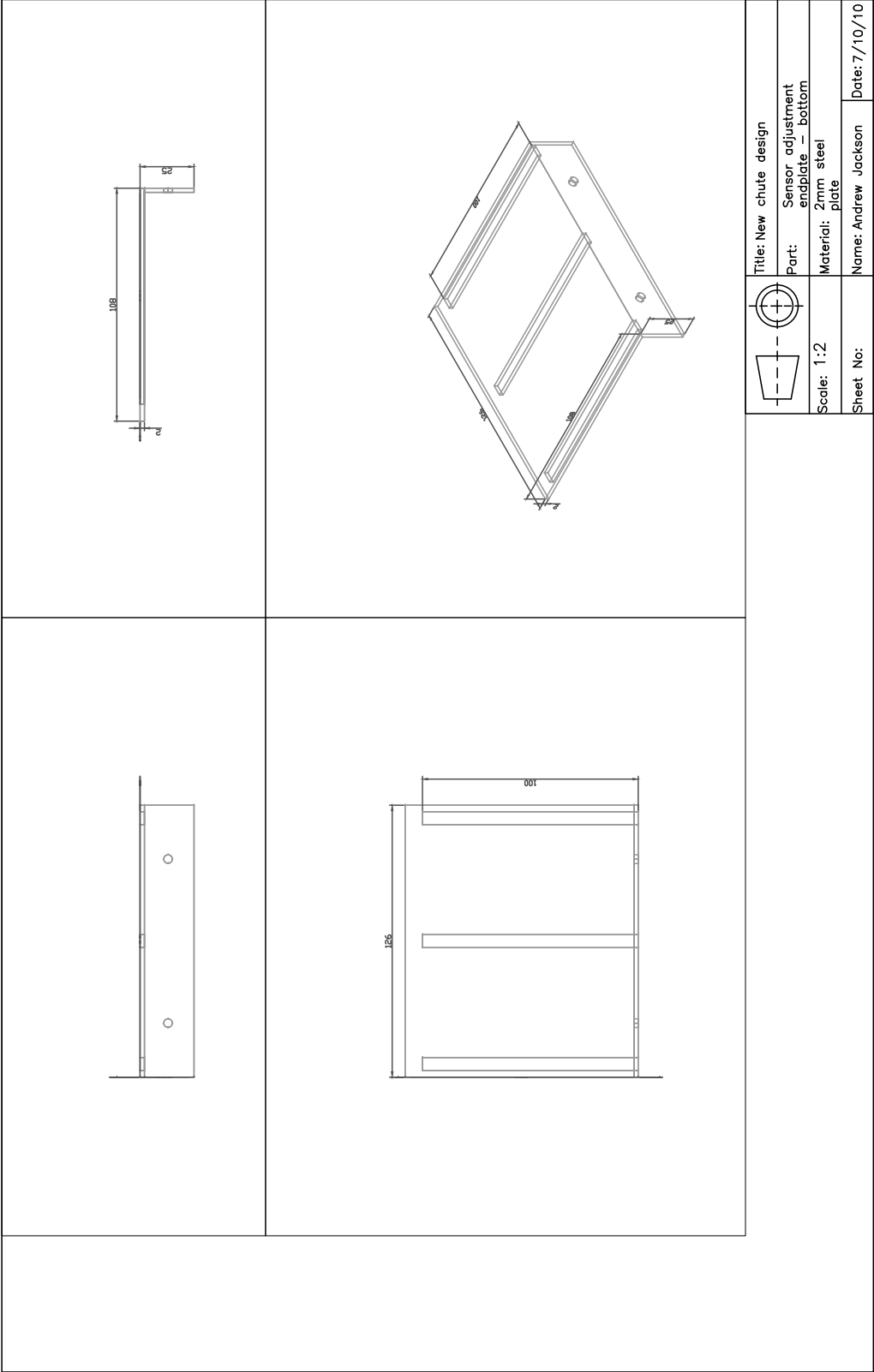
C.9 Adjustable sensor holder – first angle projection



C.10 Sensor adjustment endplate – bottom –  
isometric projection

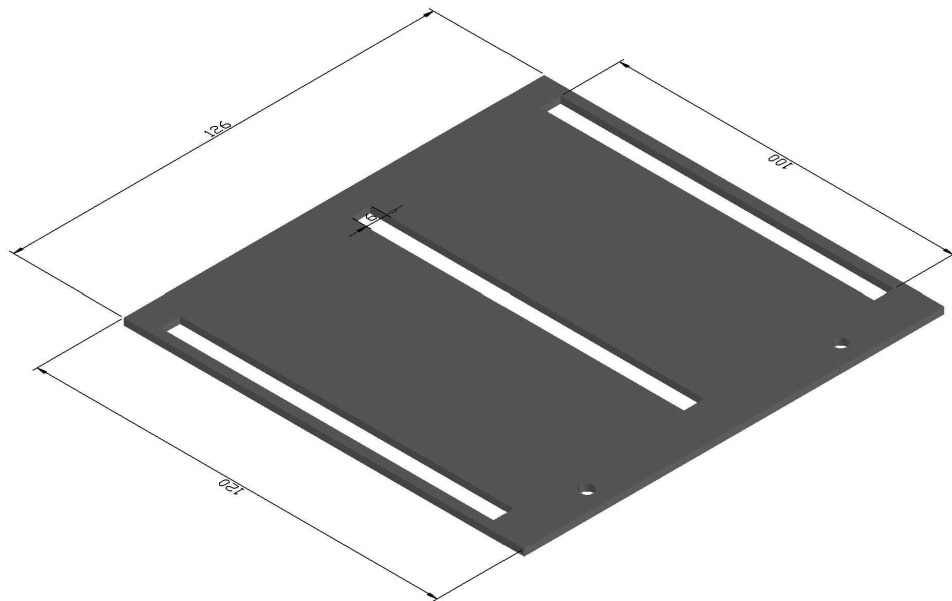


C.11 Sensor adjustment endplate – bottom – first angle projection

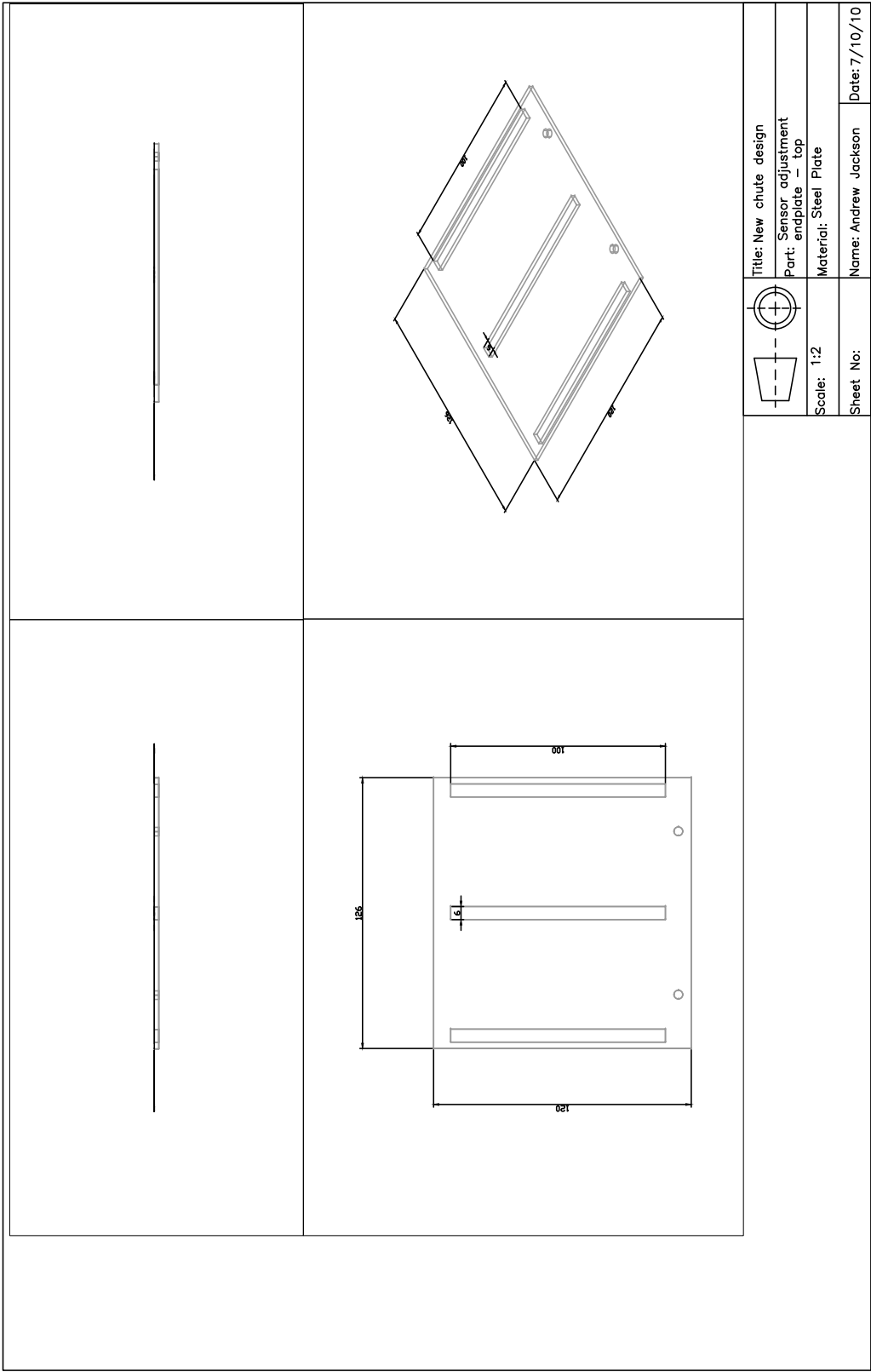




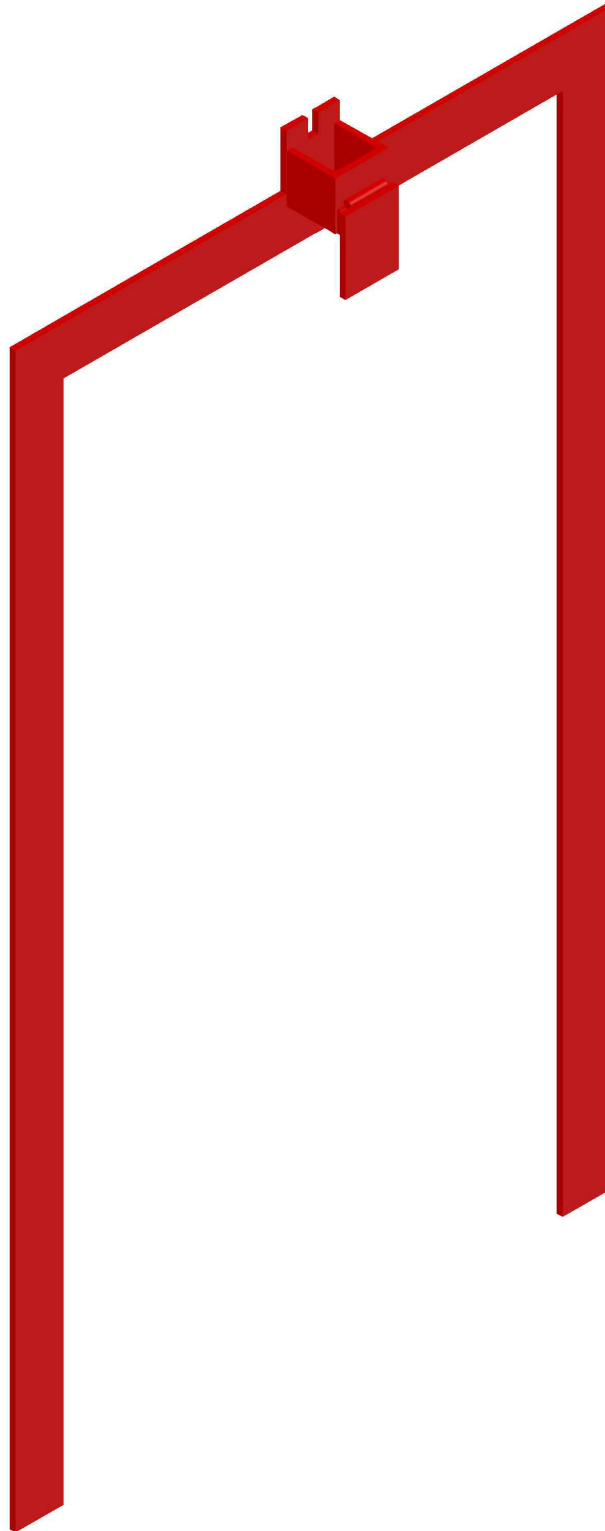
**C.12 Sensor adjustment endplate – top – isometric projection**



C.13 Sensor adjustment endplate – top – first angle projection

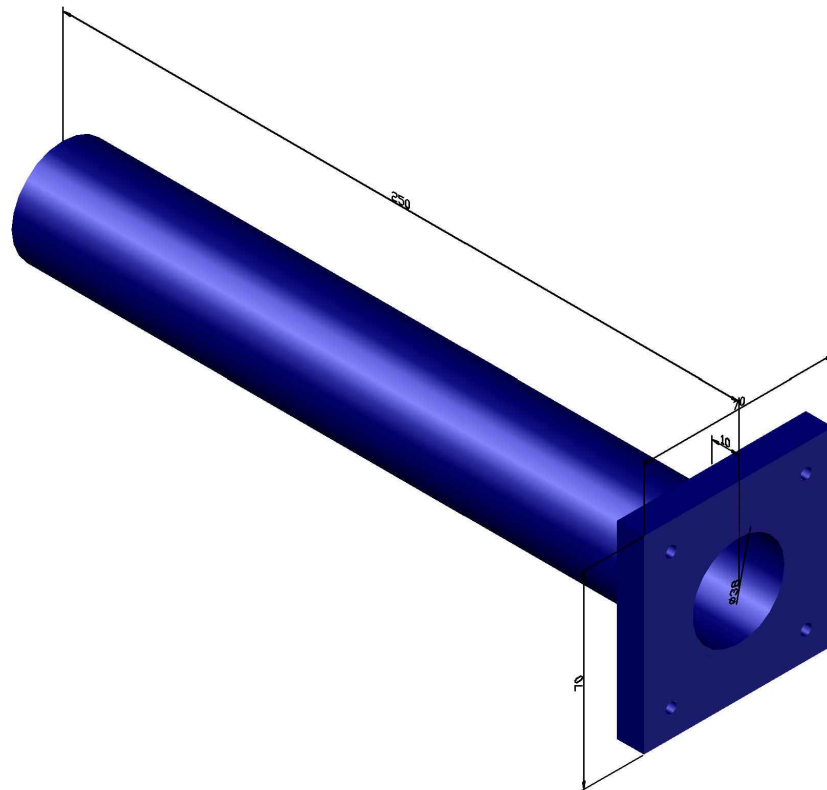


**C.14 Release mechanism surround board – isometric projection**

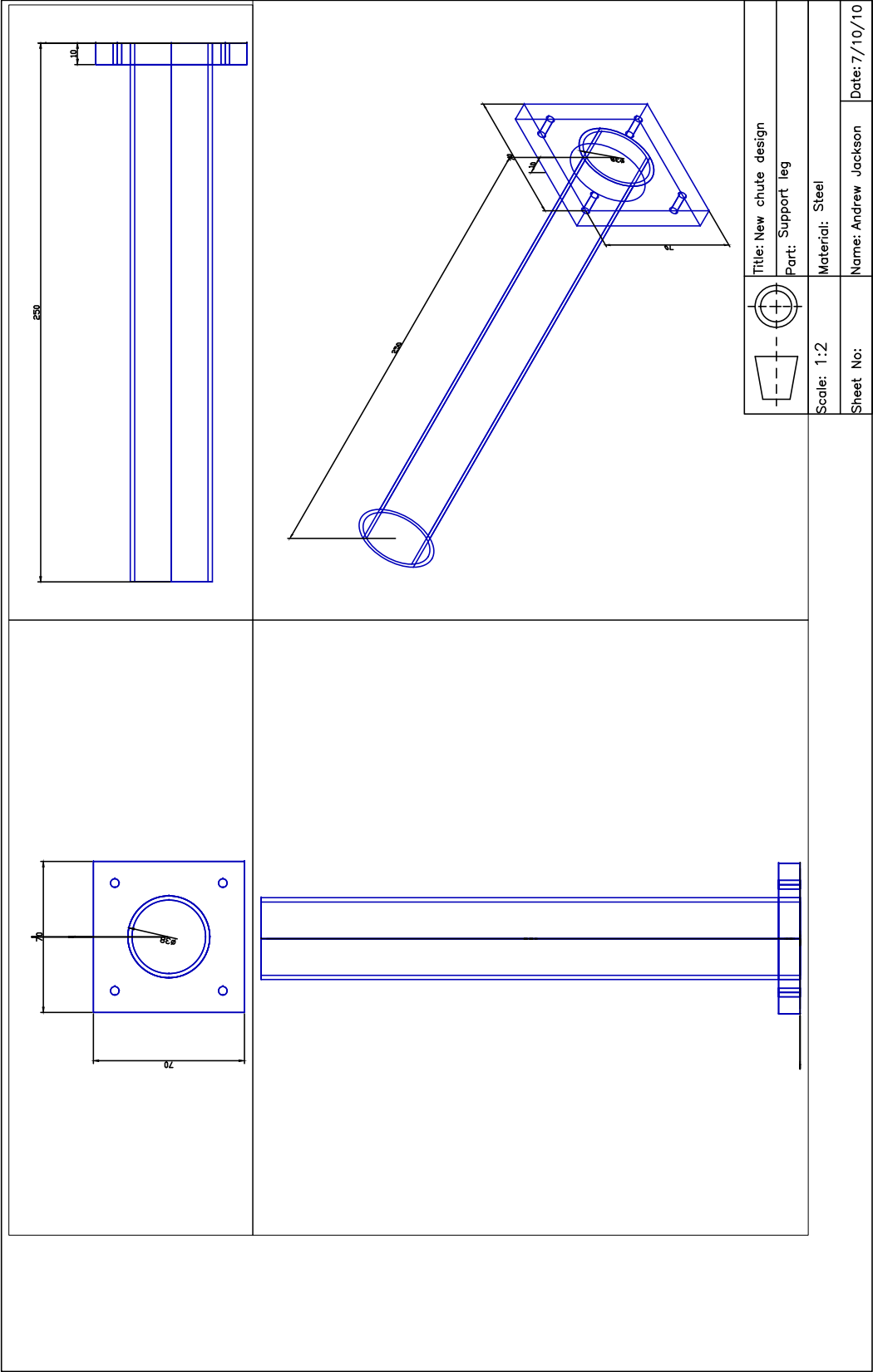




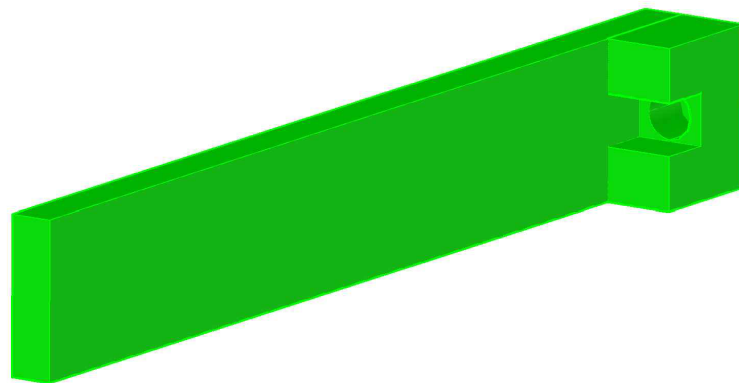
## C.16 Release mechanism support leg – isometric projection



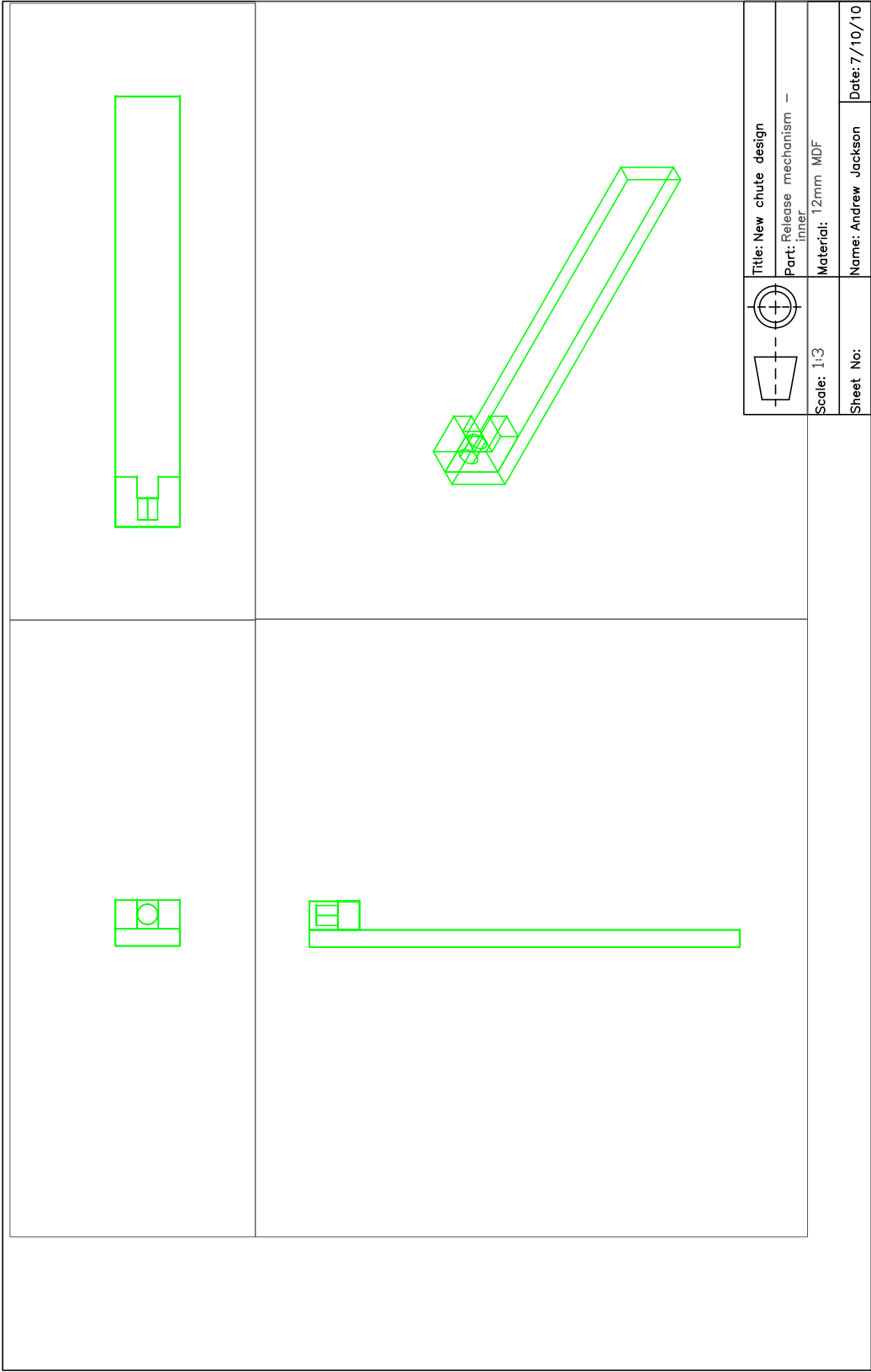
C.17 Release mechanism support leg – first angle projection



## C.18 Release mechanism – inner – isometric projection

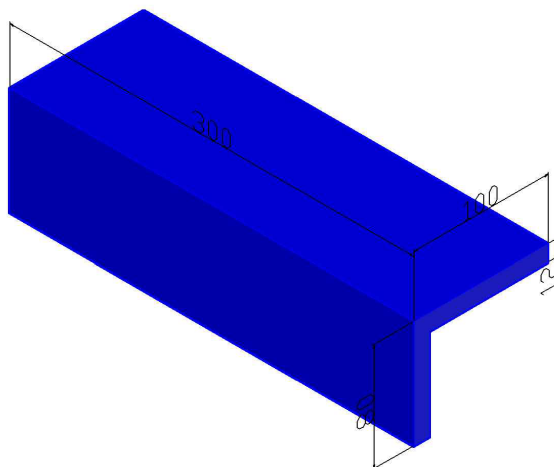


C.19 Release mechanism – inner – first angle projection

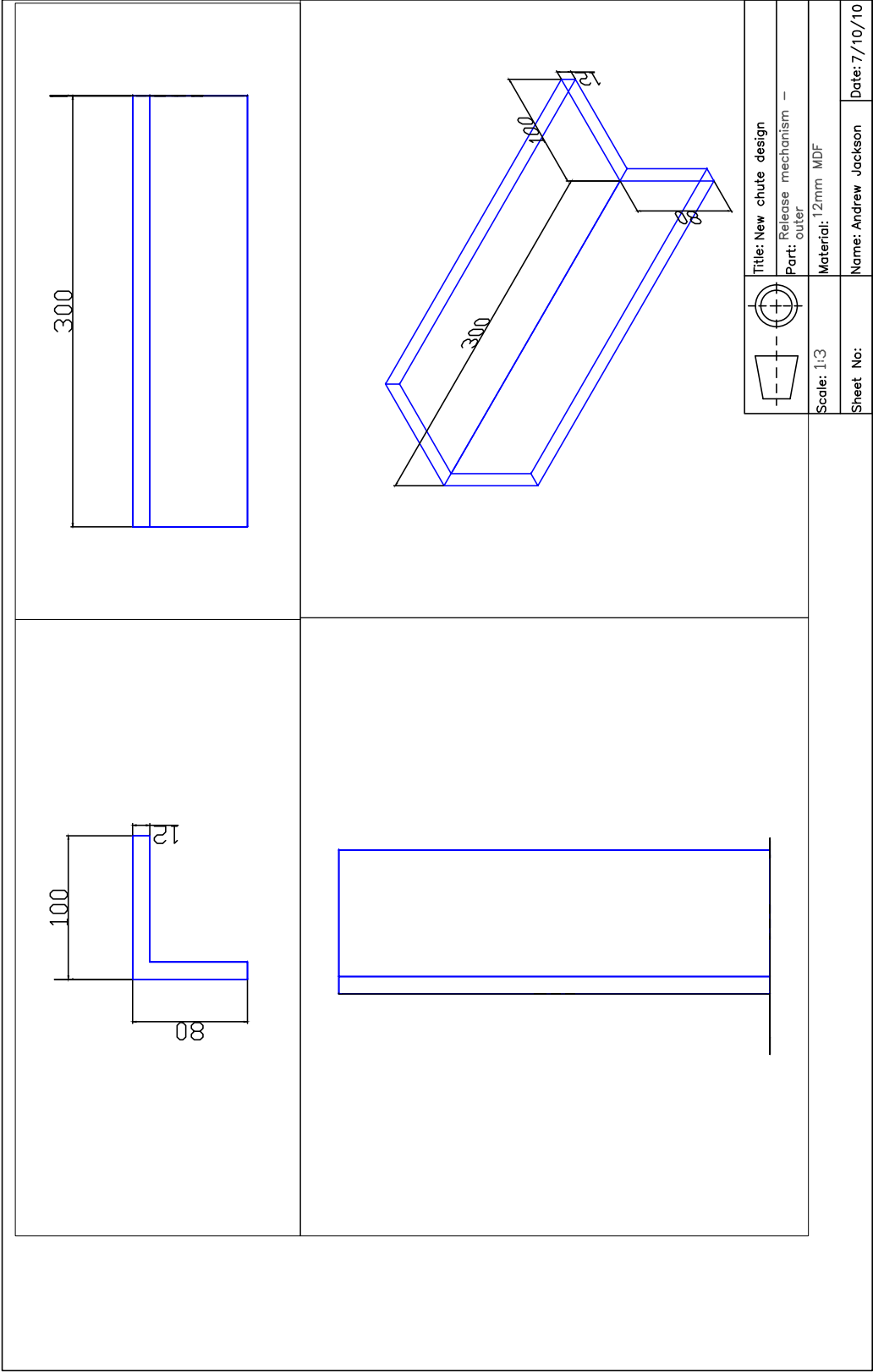




## C.20 Release mechanism – outer – isometric projection



C.21 Release mechanism – outer – first angle projection



# Bibliography

- J. B. Allen. Short time spectral analysis, synthesis, and modification by discrete Fourier transform. *IEEE Transactions on Acoustics, Speech, and Signal Processing*, 25(3):235–238, 1977.
- C. Ancey. Powder snow avalanches: Approximation as non-Boussinesq clouds with a Richardson number-dependent entrainment function. *Journal of Geophysical Research*, 109(F01005), 2004. doi:10.1029/2003JF000052.
- C. Ancey. Plasticity and geophysical flows: A review. *Journal of Non-Newtonian Fluid Mechanics*, 142(4-35), 2007.
- G. K. Batchelor. *An Introduction to Fluid Mechanics*. Cambridge University Press, Cambridge, UK, 1967.
- P. Beghin and G. Brugnot. Contribution of theoretical and experimental results to powder-snow avalanche dynamics. *Cold Regions Science and Technology*, 8:63–73, 1983.
- P. Beghin and X. Olgne. Experimental and theoretical study of the dynamics of powder snow avalanches. *Cold Regions Science and Technology*, 19:317–326, 1991.
- P. E. Beghin, E. J. Hopfinger, and R. E. Britter. Gravitational convection from instantaneous sources on inclined boundaries. *Journal of Fluid Mechanics*, 107:407–422, 1981.
- L. Birge and P. Massart. *Festschrift for Lucien Le Cam*, chapter From model selection to adaptive estimation, pages 55–87. Research Papers in Probability and Statistics. Springer, New York, 1997.
- J. Boussinesq. *Thorie de l’coulement tourbillonnant et tumultueux des liquides dans les lits rectilignes a grande section*, volume 1. Gauthier-Villars, Paris, 1897.

- A. W. Bowman and A. Azzalini. *Applied Smoothing Techniques for Data Analysis*. Oxford Univeristy Press, Oxford, U.K., 1997.
- A. N. Bozhinskiy and K. S. Losev. *The fundamentals of avalanche science*. Eidgenössisches Institut für Schnee- und Lawinenforschung, Davos, Switzerland, 1998.
- A. N. Bozhinskiy and L.A. Sukhanov. Physical modelling of avalanches using an aerosol cloud of powder material. *Annals of Glaciology*, 26:242–394, 1998.
- R. Britter and P. Linden. The motion of the front of a gravity current travelling down an incline. *Journal of Fluid Mechanics*, 99, 1980.
- J. W. M. Bush, B. A. Thurber, and Blanchette F. Particle clouds in homogeneous and stratified environments. *Journal of Fluid Mechanics*, 489:29–54, 2003. doi:10.1017/S0022112003005160.
- S. Chandrasekhar. *Hydrodynamic and Hydromagnetic Stabiltiy*. Oxford University Press, Oxford, UK, 1961.
- S. B. Dalziel. DigiFlow. Dalziel Research Partners, 2002–2013.
- I. Daubechies. *Ten Lectures on Wavelets*. CBMS-NSF Regional Conference Series in Applied Mathematics. Society for Industrial and Applied Mathematics, 1992.
- D. L. Donoho and I. M. Johnstone. Ideal spatial adaptation by wavelet shrinkage. *Biometrika*, 81:425–455, 1994.
- J. A. Drahun and J. Bridgewater. The mechanisms of free surface segregation. *Powder Technology*, 36:39–53, 1983.
- R. E. Duff, F. H. Harlow, and C. W. Hirt. Effects of diffusion on interface instability between gases. *Physics of Fluids*, 5:417–425, 1962.
- P. Duhamel and M. Vetterli. Fast Fourier transforms: A tutorial review and a state of the art. *Signal Processing*, 19:259–299, 1990.
- T. Ellison and J. Turner. Turbulent entrainment in stratified flows. *Journal of Fluid Mechanics*, 6(423-448), 1959.
- J. Grue, P. L. F. Liu, and G. K. Pedersen. *PIV and Water Waves*. River Edge, New Jersey, USA, 2004.

## BIBLIOGRAPHY

---

- M. A. Hampton. The role of sub-aqueous debris flow in generating turbidity currents. *Journal of Sedimentary Petrology*, 42:775–793, 1972.
- C. Härtel, F. Carlsson, and M. Thunblom. Analysis and direct numerical simulation of the flow at a gravity-current head. Part 2. The lobe-and-cleft instability. *Journal of Fluid Mechanics*, 418:213–229, 2000.
- F. Hermann, J. Hermann, and K. Hutter. Laboratory experiments on the dynamics of powder snow avalanches. In *International Symposium on Avalanche Formation, Movement and Effects, Proceedings of the Davos Symposium, Sept. 1986*, volume IAHS-Publ. No. 162, pages 431–439, 1987.
- R. C. Hibbeler. *Engineering Mechanics: Statics and Dynamics*. Pearson, Prentice Hall, 11th edition, 2007.
- E. J. Hopfinger and J. C. Tochon-Danguy. A model study of powder snow avalanches. *Journal of Glaciology*, 81:343–356, 1977.
- K. Hutter, S. B. Savage, and Y. Nohguchi. Numerical, analytical, and laboratory experimental studies of granular avalanche flows. *Annals of Glaciology*, 13:109–116, 1989.
- A. Jackson, B. Turnbull, and R. Munro. Scaling for lobe and cleft patterns in particle-laden gravity currents. *Nonlinear Processes in Geophysics*, 20:121–130, 2013.
- K. Kawada, K. Nishimura, and N. Maeno. Experimental studies on a powder-snow avalanche. *Annals of Glaciology*, 13:129–134, 1989.
- J. J. Keller and Y. P. Chyou. On the hydraulic lock exchange problem. *Journal of Applied Mathematics and Physics*, 42:874–909, 1991.
- M. H. Keulegan. An experimental study of the motion of saline water from locks into fresh water channels. 13th progress report on model laws for density currents. *U.S. National Bureau of Standards*, 5168, 1957.
- C. J. Keylock. The visualization of turbulence data using a wavelet-based method. *Earth Surface Processes and Landforms*, 32:637–647, 2007.
- M. Lavielle. Detection of multiple changes in a sequence of dependent variables. *Stochastic Processes and their Applications*, 83:79–102, 1999.
- T. J. Lawson. Haboob structure at Khartoum. *Weather*, 26:105–112, 1971.

- J. S. Lim. *Two-Dimensional Signal and Image Processing*, pages 469–476. Prentice Hall, Englewood Cliffs, NJ, 1990.
- M. Y. Louge, C. S. Carroll, and B. Turnbull. Role of pore pressure gradients in sustaining frontal particle entrainment in eruption currents - the case of powder snow avalanches. *Journal of Geophysical Research: Earth Surface*, 116(F04030), 2011. doi:10.1029/2011JF002065.
- S. Mallat. *A Wavelet Tour of Signal Processing*. Academic Press, 1998.
- S. Margreth. Gutachten betreffend unglückslawinen in Galtür vom 23.2.1999 und in Valzur vom 24.2.1999. In *SLF Gutachten G2000*, pages 15–18. Swiss Federal Institute for Snow and Avalanche Research (SLF), Davos Dorf, Switzerland, 2000. In German.
- B. S. Massey. *Mechanics of Fluids*. Taylor & Francis, Abingdon, UK, 8th edition, 2006.
- J. N. McElwaine. Rotational flow in gravity current heads. *Philosophical Transactions of the Royal Society*, 363:1603–1623, 2004.
- J. N. McElwaine and K. Nishimura. *Particulate Gravity Currents*, volume 31 of *Special Publication of the International Association of Sedimentologists*, chapter Ping-pong Ball Avalanche Experiments, pages 135–148. Blackwell Science, Malden, Massachusetts, USA, 2001.
- J. N. McElwaine and M. D. Patterson. Lobe and cleft formation at the head of a gravity current. Technical report, Department of Applied Mathematics and Theoretical Physics, Centre for Mathematical Sciences, University of Cambridge, 2004.
- J. N. McElwaine, M. D. Patterson, and S. B. Dalziel. Lobe and cleft formation at the head of a gravity current. *Proceedings of the XXI International Congress of Theoretical and Applied Mechanics*, pages 15–21, 2004.
- J. L. Meriam and L. G. Kraige. *Engineering Mechanics: Statics*, page 330. Wiley and Sons, 2002.
- G. V. Middleton. Experiments on density and turbidity currents, I. Motion of the head. *Canadian Journal of Earth Sciences*, 3:532–546, 1966.

## BIBLIOGRAPHY

---

- J. Neufeld. Lobe-cleft patterns in the leading edge of a gravity current. Master's thesis, Department of Physics, University of Toronto, Toronto, Canada, 2002.
- K. Nishimura and Y. Ito. Velocity distribution in snow avalanches. *Journal of Geophysical Research*, 102(B12):27297–27303, 1997.
- K. Nishimura, F. Sandersen, K. Kristensen, and K. Lied. Measurements of powder snow avalanche - Nature. *Surveys in Geophysics*, 16(5-6), 1995.
- Y. Nohguchi and H. Ozawa. On the vortex formation at the moving front of lightweight granular particles. *Physica D*, 238:20–26, 2008. doi:10.1016/j.physd.2008.08.019.
- N. Otsu. A threshold selection method from gray-level histograms. *IEEE Transactions on Systems, Man, and Cybernetics*, 9(1):62–66, 1979.
- O. Pouliquen. Scaling laws in granular flows down rough inclined planes. *Physics of Fluids*, 11(3):542–548, 1999.
- O. Pouliquen and J. W. Vallance. Segregation induced instabilities of granular fronts. *Chaos*, 9(3):621–629, 1999.
- O. Pouliquen, J. Delour, and S. B. Savage. Fingering in granular flows. *Nature*, 386:816–817, 1997.
- Lord Rayleigh. Investigation of the character of the equilibrium of an incompressible heavy fluid of variable density. In *Scientific Papers*, volume II, page 200. Cambridge University Press, Cambridge, UK, 1900.
- J. W. Rottman and J. E. Simpson. Gravity currents produced by instantaneous releases of a heavy fluid in a rectangular channel. *Journal of Fluid Mechanics*, 135:95–110, 1983.
- S. B. Savage and C. K. K. Lun. Particle size segregation in inclined chute flow of dry cohesionless granular solids. *Journal of Fluid Mechanics*, 189:311–335, 1988.
- J. P. Serra. *Image analysis and mathematical morphology*. Academic Press, London, 1982.
- D. H. Sharp. An overview of Rayleigh-Taylor instability. *Physica D*, 12:3–18, 1984.

- J. E. Simpson. Effects of the lower boundary on the head of a gravity current. *Journal of Fluid Mechanics*, 53(4):759–768, 1972.
- J. E. Simpson. *Gravity Currents in the Environment and the Laboratory*. Cambridge University Press, 2nd edition, 1997.
- J. E. Simpson and R. E. Britter. The dynamics of the head of a gravity current advancing over a horizontal surface. *Journal of Fluid Mechanics*, 94(3):477–495, 1979.
- C. Solomon, S. Gibson, and T. Breckon. *Fundamentals of Digital Image Processing: A Practical Approach Using MATLAB*. Wiley, Hoboken, New Jersey, USA, 2010.
- G. I. Taylor. The instability of liquid surfaces when accelerated in a direction perpendicular to their planes, I. *Proceedings of the Royal Society A*, 201:192–6, 1950.
- B. Turnbull and J. N. McElwaine. A comparison of powder-snow avalanches at Vallée de la Sionne, Switzerland, with plume theories. *Journal of Glaciology*, 53(180):30–40, 2007.
- B. Turnbull and J. N. McElwaine. Experiments on the non-Boussinesq flow of self-igniting suspension currents on a steep open slope. *Journal of Geophysical Research*, 113(F01003), 2008. doi:10.1029/2007JF000753.
- B. Turnbull and J. N. McElwaine. Potential flow models of suspension current air pressure. *Annals of Glaciology*, 51(54), 2010.
- B. Turnbull, J. N. McElwaine, and C. Ancey. Kulikovskiy-Sveshnikova-Beghin model of powder snow avalanches: Development and application. *Journal of Geophysical Research*, 112(F01004), 2007. doi:10.1029/2006JF000489.
- J. S. Turner. *Buoyancy Effects in Fluids*. Cambridge University Press, Cambridge, UK, 1973.
- J. Vallet, B. Turnbull, S. Joly, and F. Dufour. Observations on powder snow avalanches using videogrammetry. *Cold Regions Science and Technology*, 39:153–159, 2004.
- J. L. Vinningland, Ø. Johnsen, Flekkøy E. G., R. Toussaint, and K. J. Måløy. Experiments and simulations of a gravitational granular flow instability. *Physical Review E*, 76(051306), 2007.



## BIBLIOGRAPHY

---

- J. L. Vinningland, Ø. Johnsen, Flekkøy E. G., R. Toussaint, and K. J. Måløy. Size invariance of the granular Rayleigh-Taylor instability. *Physical Review E*, 81(041308), 2010.
- C. Völtz, W. Pesch, and I. Rehberg. Rayleigh-Taylor instability in a sedimenting suspension. *Physical Review E*, 65(011404), 2001.
- T. von Kármán. The engineer grapples with nonlinear problems. *Bulletin of the American Mathematical Society*, 46:615–683, 1940.
- D. L. Youngs. Numerical simulation of turbulent mixing by Rayleigh-Taylor instability. *Physica D*, 12:32–34, 1984.